Dissertation
submitted to the
Combined Faculty of Natural Sciences and Mathematics
of Heidelberg University, Germany
for the degree of
Doctor of Natural Sciences

Put forward by
Christoph Engler
born in: Bruchsal
Oral examination: 14.12.2021

Populations of satellite galaxies with the IllustrisTNG simulations: from galaxy clusters to the Local Group

Referees:

Prof. Dr. Eva K. Grebel

Prof. Dr. Björn Malte Schäfer

Abstract

In this thesis, I study populations of satellite galaxies in a ΛCDM context using the IllustrisTNG suite of cosmological magneto-hydrodynamical simulations. Utilising the entire range of IllustrisTNG allows for an unprecedented combination of statistical sample size and numerical resolution, resulting in mass ranges that cover multiple orders of magnitude for both host and satellites samples, as well as the first statistical sample of 198 high-resolution Milky Way-/Andromeda-like (MW/M31) hosts. I investigate the galaxy-halo connection for satellite and central galaxies across the mass spectrum in the stellar-to-halo mass relation as the most fundamental relationship of galaxy evolution in the cosmological standard model. I analyse the abundance of past and present-day satellite and subhalo populations around MW/M31-like hosts, find a remarkable degree of diversity, and put them into context with both observational surveys and previous simulations of similar systems. Their satellites become increasingly quenched towards smaller stellar masses as they lose their gas reservoirs more easily after infall. Thus, I not only give a detailed view on the evolution of satellite galaxies after infall and the environmental effects they experience but overcome one of the remaining challenges to the ΛCDM model: there is no missing satellites problem according to IllustrisTNG.

Zusammenfassung

Diese Doktorarbeit untersucht Populationen von Satellitengalaxien im Kontext des ΛCDM Modells mit der kosmologischen, magneto-hydrodynamischen Simulationssuite IllustrisTNG. Der Umfang der IllustrisTNG Simulationen ermöglicht eine noch nie da gewesene Kombination von statistischer Samplegröße und numerischer Auflösung: Massebereiche von Hosts und Satelliten erstrecken sich über mehrere Zehnerpotenzen und ich verfüge über das erste statistische Sample von 198 hochaufgelösten Hosts ähnlich zur Milchstraße oder Andromeda. Ich erforsche die Verbindung von Galaxien und Dunkler-Materie-Halos für Satelliten und zentrale Galaxien im verfügbaren Massespektrum mit der Relation von Stern- und Halomasse – der grundlegendsten Beziehung für die Entstehung von Galaxien im kosmologischen Standardmodell. Ich analysiere das Aufkommen von vergangenen und gegenwärtigen Satelliten- und Subhalopopulationen um Hosts wie der Milchstraße und Andromeda, finde ein bemerkenswertes Ausmaß an Vielfältigkeit und setze sie in Kontext zu Beobachtungssurveys und vorherigen Simulationen ähnlicher Systeme. Ihre weniger massereichen Zwerggalaxien betreiben fast ausschließlich keine aktive Sternentstehung mehr, da sie nach ihrem Einfall schnell ihrer Gasreservoirs entzogen werden. Somit gebe ich nicht nur einen detaillierten Überblick zur Entwicklung von Satellitengalaxien nach ihrem Einfall, sowie zu den Umgebungseffekten, die auf sie einwirken, sondern bewältige sogar eine der verbliebenen Herausforderungen für das ΛCDM Modell: Laut IllustrisTNG gibt es keine fehlenden Zwerggalaxien in Systemen wie der Milchstraße.

Acknowledgements

It does not seem that long ago that I started my PhD, moved into my offices at MPIA and ARI, and tried to learn more about galaxies – or to figure out how to even access the simulation data. Three and a half years, two and a half papers, and many, many coffees later, I have written up this thesis and somehow I am very close to actually finishing my PhD. All of this would not have been possible without the help, influence, and support of my colleagues, friends, and family. My heartfelt gratitude goes to the following people.

First and foremost, I want to say thank you to my supervisors and advisers. To Annalisa Pillepich: you have taught me much over the last years: from galaxy clusters and environmental effects to dwarf galaxies and missing satellites; how to make good-looking plots, how to write well-structured papers, and how to give decent talks. Thank you for all your honest feedback and that you have continued to push me to grow as a scientist. Thank you to Eva Grebel: for taking me into your research group a year into my PhD, for the financial support, and for all the valuable feedback and comments. Thank you to Anna Pasquali: for continuing to give me advise throughout all my projects, all our conversations and discussions, and for letting me help and learn as a tutor in the Astronomical Techniques lectures. And to Thorsten Lisker: thanks for getting me into science and into my PhD in the first place! Our discussions and your advise throughout my Master thesis and the first year of my PhD have continued to influence me.

I would also like to thank Björn Malte Schäfer for acting as the second referee for my thesis. I hope this makes for a good read! And thank you to Jochen Heidt and Simon Glover for joining my PhD defence as committee members.

A big thank you to Gandhali, Martina, and Elad from our GC Theory group at MPIA: for your scientific advise, lunch times, and for making me feel welcome since day one. Thank you to the people from our galaxy star formation history group at ARI: Tom, Bahar, Josefina, and Nico. For your feedback, company, and for listening to me vent about papers and referees.

Thank you to my office mates that I have had the pleasure to share my working days with: Christian, Hector, Sven, Hans, Caro, Ania, Arianna, Josha, Johanna, Manuel, and Giancarlo. For all the conversations and distractions, all the lunch and coffee/tea times. Thank you to IMPRS and my generation for the retreats and Thursday nights. And a big thank you to my friend Victor for proofreading my thesis on pretty short notice. Thanks for helping me with all the science problems throughout our Bachelors', Masters', and PhD's; for all the lunches and dumb jokes.

Finally, I want to thank my family – especially my parents, my brother Fabian, my sister-in-law Tanja, my niece Rosalie, and my grandma Bäwi – for all the support over the years. Thanks for distracting me from work when it was needed and for understanding when things were a little too stressful to stop by. And especially for all the food.

Last – and most importantly – I want to thank my partner Sam for her love, her kindness, and her never-ending support. Thank you for being so understanding when I had to spend so many evenings to work on this thesis. Thank you for calming me down and for taking as much pressure off me as you could. I'll be happy to return the favour when its your turn.

Contents

List of Figures

List of Tables

Dedicated to the memory of
Anna Heil, Lothar Egler, and Franz Berenz

Chapter 1

Introduction

1.1 Galaxy evolution in a cosmological context

1.1.1 ΛCDM: origins and fundamental principles

In recent decades, ΛCDM – with Λ denoting the cosmological constant, i.e. dark energy for the accelerated expansion of the Universe, and CDM corresponding to cold dark matter – has emerged as the standard model of cosmological structure formation, predicting the matter content and geometry of the Universe. Starting from a near-uniform state after the Big Bang, small-scale density perturbations are driven by the period of cosmic inflation and – accelerated by the gravitational pull of non-baryonic, cold dark matter – collapse to form the first non-linear objects in the Universe. Ultimately, galaxies of various morphologies and sizes form from gas that cools and condensates in the potential wells of dark matter haloes and accumulate to groups and clusters in the large-scale structure of the cosmic web.

Throughout the 20th century, multiple observational findings hinted at the existence of dark matter as an additional mass component of galaxies. Zwicky (1933) found a surprisingly large velocity dispersion from seven galaxies in the Coma cluster. Taking only visible matter (i.e. stellar mass) into account, this system should not have remained bound. The flat rotation curve of the Andromeda galaxy (Babcock 1939; Rubin and Ford 1970) suggested more mass to be found in its outer regions. Furthermore, the measured stellar masses of the Milky Way and Andromeda were actually found to be too small to cause them to approach each other (Kahn and Woltjer 1959). Later observations suggested that mass around the Milky Way and other, similar spiral galaxies seemed to be missing (Einasto et al. 1974; Ostriker et al. 1974).

After numerical studies found that spiral galaxies could be stabilised by a massive halo component (Ostriker and Peebles 1973), a population of dark matter haloes was theorised as the fundamental environment for galaxy formation (White and Rees 1978, also White and Frenk 1991, as well as Frenk and White 2012 for a review). Based on the analytic model of Press and Schechter (1974) for self-gravitating and self-similar masses, these haloes grow hierarchically through mergers and provide the gravitational potential wells in which gas cools and condenses to form galaxies.

In subsequent years, the theory of cosmic inflation became the basis for the initial formation of structure (Guth 1981; Linde 1982; Starobinsky 1982). During this

period, quantum fluctuations seed a Gaussian, scale-free distribution of small-scale, adiabatic density fluctuations. The resulting overdensities ultimately collapse to form the first non-linear structures. While the growth of structures is initially regulated by the dominant radiation component, the growth of these perturbations decelerates due to the Meszaros effect (Meszaros 1974): as the Universe expands, it becomes harder for the perturbations to accumulate more matter. Once the Universe evolves from radiation to matter dominated, dark matter begins to regulate the growth of structure instead.

1.1.2 Dark matter: properties and particle candidates

Therefore, the properties and characteristics of the non-baryonic dark matter particle dictate the appearance of the structures that ultimately form from these perturbations. Particle candidates can be broadly grouped into three categories according to their typical mass and velocity at early times: hot, warm, and cold dark matter (Bond et al. 1984; Primack and Blumenthal 1984). Dark matter fluctuations below the typical free-streaming scale of these particles are washed out by random thermal motions. This dictates what kind of objects form from these fluctuations, including their size and how they evolve to form the Universe we observe today.

Hot dark matter

For hot dark matter with a typical mass of $\sim$ 30 eV, the free-streaming length translates to the characteristic mass of a supercluster or a large galaxy cluster of at least 10^{15} $M_{\odot}$. These systems would then need to fragment in order to form individual galaxies. Although light neutrinos, such as electron neutrinos, appear as suitable particle candidates due to their mass being in agreement with that of a hot dark matter particle (Lubimov et al. 1980), simulations have revealed such a neutrino-dominated universe to differ drastically from ours. As the present-day galaxy population would have originally formed in superclusters, which subsequently fragment into smaller systems, their current distribution would be significantly more clustered (White et al. 1983).

Warm dark matter

In a warm dark matter scenario with a typical particle mass of $\sim$ 2 keV, dark matter haloes of dwarf galaxies are the first non-linear objects to form. Particle candidates include a non-standard gravitino (Blumenthal et al. 1982; Bond et al. 1982; Pagels and Primack 1982) or a sterile neutrino (Dodelson and Widrow 1994; Shi and Fuller 1999; Laine and Shaposhnikov 2008; Shaposhnikov 2008; Lovell et al. 2016).

Cold dark matter

In the case of cold dark matter with a typical mass of $\sim$ 100 GeV, the first structures to form are even smaller, with a characteristic mass similar to Earth's mass. Multiple particle types have been theorised to make up cold dark matter: supersymmetric, weakly interacting particles (WIMPs, Ellis et al. 1984) such as supersymmetric neutralinos created as heavy thermal remnants from annihilation processes, or axions like cold Bose condensates or quantum chromodynamics axions (Preskill et al. 1983; Turner and Wilczek 1991). Further alternatives include other, axion-like particles behaving as fuzzy dark matter (Bose-Einstein condensates, Suárez et al. 2014; Marsh 2016; Mocz et al. 2017), self-interacting dark matter particles (Spergel and Steinhardt 2000), as well as dark photons (Buckley et al. 2014; Vogelsberger et al. 2016) and particles interacting with relativistic standard model particles (Boehm et al. 2014; Schewtschenko et al. 2015).

Hierarchical structure growth

For either warm or cold dark matter, smaller objects are the first to form. They become non-linear, decouple from the universal expansion and collapse. The resulting dark matter haloes continue to grow hierarchically into larger structures by either merging with other existing haloes or by accreting the diffuse dark matter surrounding them. While major mergers of similar mass haloes are the only events to cause a nearly complete mixing of old and newly added dark matter, most of their growth stems from either minor mergers or the accretion of diffuse material (Guo and White 2008; Fakhouri et al. 2010; Wang et al. 2011).

In order to obtain a full analytic description of the formation and evolution of dark matter halo populations, the original model of Press and Schechter (1974) was extended to include descriptions for halo abundance, halo merger rates, as well as distributions of halo formation time and halo formation histories (Bower 1991; Bond et al. 1991; Lacey and Cole 1993; Kauffmann and White 1993). Whereas both warm and cold dark matter structures grow hierarchically, dark matter objects in a cold dark matter scenario can be significantly smaller. This results in a far more detailed substructure, with a larger number of low-mass subhaloes around a given host dark matter halo. Figure 1.1, taken from Lovell et al. (2012), illustrates this by contrasting simulations of a Milky Way-mass halo in cold dark matter (left panel, based on the Aquarius simulations, Springel et al. 2008) and warm dark matter scenarios (right panel). Furthermore, cold dark matter subhaloes have been found to be more concentrated than in warm dark matter scenarios (Lovell et al. 2012; Bose et al. 2017; Newton et al. 2021).

1.1.3 The galaxy-halo connection

As baryons follow the overall distribution of dark matter due to its gravitational pull, they are contained within the potential well of dark matter haloes. Gas cools

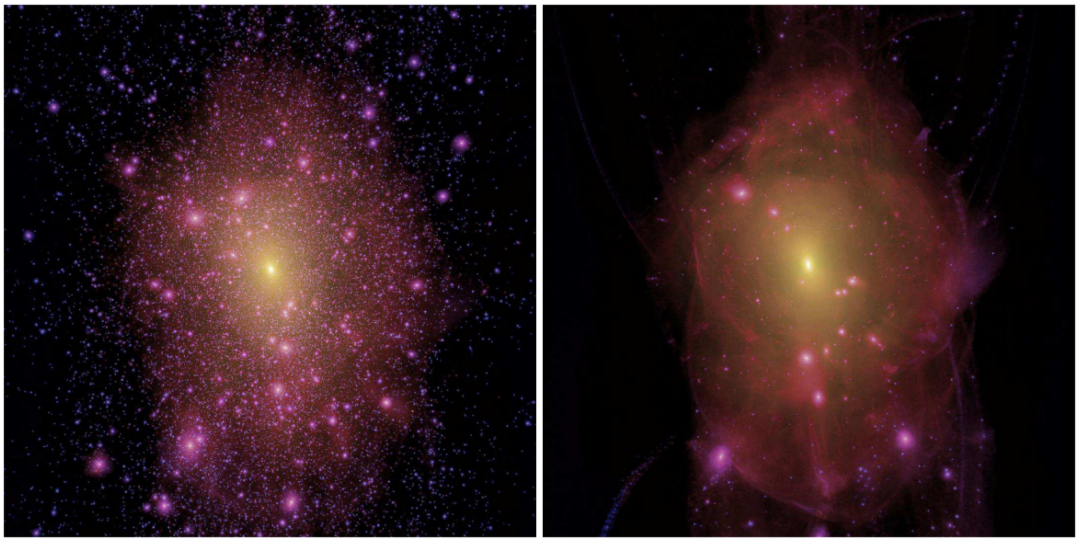

Figure 1.1: Milky Way-mass haloes in cold dark matter (left panel) and warm dark matter scenarios (right panel). The cold dark matter halo on the left is taken from the Aquarius simulations (Springel et al. 2008). The image intensity signifies the line-of-sight projected square of the density whereas the hue denotes the projected density-squared velocity dispersion, from blue for low to yellow for high velocity dispersion. SOURCE: Lovell et al. (2012).

and condenses to ultimately form galaxies at the haloes' cores. The anisotropic collapse of the initial density fluctuations as well as the subsequent clustering of baryonic and non-baryonic matter causes the large-scale distribution of dark matter haloes and galaxies to form a web-like pattern.

This cosmic web consists of a hierarchy of interconnected structures that formed from gravitational instabilities (Zel'Dovich 1970; Bond et al. 1996; Schmalzing et al. 1999; Furlanetto et al. 2003): knots, filaments, sheets, and voids. Knots mark gravitational collapses along three principal axes, forming dark matter haloes and ultimately galaxies. They contain most observable objects in the Universe. These knots are connected by filaments, i.e. structures that collapsed along two principal axes. Cold gas is transported along filaments and fed onto the dark matter haloes in knots, fuelling star formation processes in the galaxies they contain (Katz et al. 2003; Kereš et al. 2005; Dekel and Birnboim 2006; Ocvirk et al. 2008; Dekel et al. 2009; van de Voort et al. 2011; Nelson et al. 2016; Martizzi et al. 2019). Sheets correspond to structures that are collapsed along one principal axis; their intersections form the filaments. Finally, cosmic voids encompass the regions between knots, filaments, and sheets.

Throughout cosmic time, the cosmic web and its components, as well as the distribution of mass therein, evolve significantly, providing the large-scale environment for galaxy formation and evolution (Hahn et al. 2007; Sousbie et al. 2009; Cautun et al. 2014a). In recent years, theoretical studies have, therefore, started to analyse the imprint of the local cosmic web morphology on halo (Pichon et al. 2011; Libeskind et al. 2012; Forero-Romero et al. 2014; Goh et al. 2019) and galaxy populations (Metuki et al. 2015; Gheller et al. 2016; Codis et al. 2018; Martizzi et al. 2020).

1.1.4 The large-scale structure in observations

On the observational side, galaxy redshift surveys provide the most precise information on the large-scale structure. Although Jõeveer et al. (1978) already found the majority of galaxy clusters on the southern hemisphere to form chains, it was the CfA survey – the first extensive 3D galaxy survey with a sample size of 2,400 galaxies – that provided the first clear picture of the large-scale distribution of galaxies and the cosmic web (Davis et al. 1982). The CfA2 survey extended these findings with the detection of the first "Great Wall" – the largest sheet structure detected at the time (de Lapparent et al. 1986; Geller and Huchra 1989). By raising questions about the origin and evolution of such structures and the overall distribution of matter in the Universe, these surveys played a key role in the development of a cosmological model.

In subsequent years, larger surveys increased the sample sizes of both galaxies and the structures they form. This includes the 2-degree Field Galaxy Redshift Survey with 220,000 galaxies (2dFGRS, Colless et al. 2001), large-scale power spectra from 205,000 galaxies of the Sloan Digital Sky Survey (SDSS, Tegmark et al. 2004), the Sloan Great Wall, which increased the size of the largest observed structure in the Universe (previously the CfA Great Wall) by 80 per cent, as well as the 2MASS Redshift survey that covers 91 per cent of the sky with a sample size of 45,000 galaxies (Huchra et al. 2005). Figure 1.2, taken from Springel et al. (2006), summarises these advances by illustrating the large-scale galaxy distributions obtained from the CfA2 survey (top cone, small), SDSS (top cone, large), and 2dFGRS (left cone) – including the CfA2 and Sloan Great Walls – and contrast them with simulated large-scale galaxy distributions (right and bottom cones). Here, halo and subhalo populations from the Millennium simulation (Springel et al. 2005b) have been populated with galaxies using semi-analytic techniques and were subsequently matched to the geometries and magnitude limits of the observational surveys in the opposite cones.

Observing gas filaments

However, direct observations of the cold gas filaments that are traced by the large-scale distribution of galaxies remain challenging due to their low surface brightness levels. Their low density mostly prevents star formation activity. While theoretical works predict Lyman α emission (Hogan and Weymann 1987; Gould and Weinberg 1996; Cantalupo et al. 2005; Laursen et al. 2009; Faucher-Giguère et al. 2010; Rosdahl and Blaizot 2012), it remains difficult to detect in observations: at low redshifts, filaments exhibit a fairly low density since they have been stretched out by cosmic expansion. At higher redshifts, on the other hand, the Universe is in a more homogeneous state and the features of the cosmic web appear less pronounced. With the UV background as the only source of ionising radiation, Lyman α emission is significantly below current detection limits. Therefore, additional sources of ionisation, such as quasars (Arrigoni Battaia et al. 2019) or feedback from star formation and

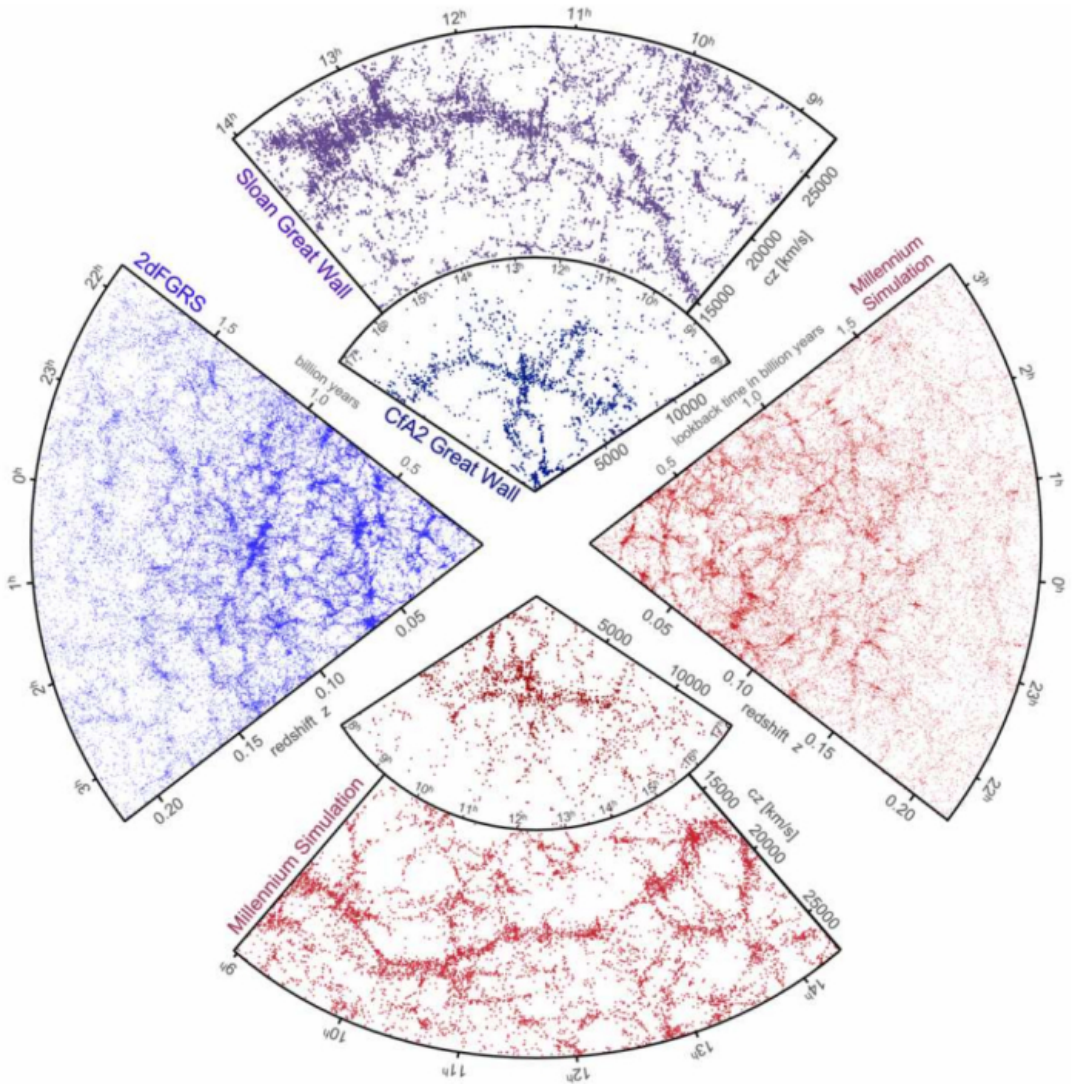

Figure 1.2: Large-scale distribution of galaxies from spectroscopic redshift surveys and the Millennium simulation. The small top cone depicts the CfA2 Great Wall centred on the Coma cluster (Geller and Huchra 1989) where the large top cone shows a part of SDSS drawn to the same scale, including the Sloan Great Wall (Gott et al. 2005). The cone on the left illustrates galaxies from one half of the 2-degree Field Galaxy Redshift Survey (2dFGRS, Colless et al. 2001). The bottom and right slices show mock galaxy surveys constructed by combining haloes from the Millennium simulation (Springel et al. 2005b) with semi-analytic models for galaxy formation and evolution, matched to the geometries and magnitude limits of the surveys in their opposite slices. SOURCE: Springel et al. (2006).

black hole activity (Umehata et al. 2019), are required. Although simulations still predict current and future observations to remain challenging (Cantalupo et al. 2005; Kollmeier et al. 2010; Bertone and Schaye 2012; Rosdahl and Blaizot 2012; Smith et al. 2019a; Corlies et al. 2020; Elias et al. 2020), first observations have been used to perform tomography of the cosmic web, identifying baryonic filaments at redshift $z < 0.5$ by stacking Lyman α emission signals (Lee et al. 2014; Gallego et al. 2018; Lee et al. 2018).

Alternatively, gas filaments may be observed through thermal Sunyaev-Zel'dovich signals (de Graaff et al. 2019; Tanimura et al. 2019) or detected directly in X-ray wavelengths. While attempts at the detection of cosmic filaments and the missing baryons therein (the amount of observed baryons in the local Universe is too small by up to 40 per cent compared to theoretical expectations) in the X-ray regime have been challenging (Nicastro et al. 2005; Kaastra et al. 2006; Rasmussen et al. 2007; Nicastro et al. 2008; Zappacosta et al. 2010), they have become more successful in recent years: Nicastro et al. (2018) were able to observe two absorbers of highly ionised oxygen in the spectrum of a quasar in the filamentary intergalactic medium. The next generation of X-ray and radio telescopes, such as the Cosmic Web Explorer ATHENA observatory, might enable significant progress for observational reconstructions of the baryonic cosmic web (Kaastra et al. 2013; Horii et al. 2017; Vazza et al. 2016; Cui et al. 2018; Simionescu et al. 2021).

Galaxies & the large-scale environment

Detailed features in the large-scale distribution of galaxies can be categorised using a multitude of cosmic web identification methods based on models and simulations such as Spineweb (Aragón-Calvo et al. 2010), DisPerSE (Sousbie 2011; Sousbie et al. 2011), ORIGAMI (Falck et al. 2012; Falck and Neyrinck 2015), or NEXUS+ (Cautun et al. 2013). Combined with sizeable galaxy samples from surveys like SDSS or the Galaxy And Mass Assembly survey (GAMA, Driver et al. 2009; Driver et al. 2011), these analysis tools can connect individual galaxies to different components of the cosmic web (i.e. knots, filaments, sheets, or voids), providing insights into the environmental impact of the large-scale structure on the evolution of galaxy populations.

Quenching mechanisms – processes that bring the star formation activity of galaxies to a halt – may already be exerted here: in cosmic voids, galaxies tend to be less massive, bluer (i.e. with higher star formation activity), and more compact (Rojas et al. 2004; Beygu et al. 2016). The closer they get to filaments and sheets, the more massive and passive they become, with specific star formation rates decreasing in the vicinity of cosmic web features and red fractions increasing further towards knots, as galaxies move along filaments into cluster environments (Porter et al. 2008; Martínez et al. 2016; Kraljic et al. 2018; Winkel et al. 2021). Furthermore, galaxy properties such as their stellar-to-halo mass ratio, morphology, stellar age, and size can be affected by their large-scale environment (Chen et al. 2017; Kuutma et al. 2017; Tojeiro et al. 2017). Massive galaxies near filament structures exhibit systematically

higher HI fractions (Kleiner et al. 2017) as filaments contain gas that they feed onto the knots of the cosmic web.

1.2 Galaxies & halo environment

While the large-scale structure can already leave an imprint on galaxies, the dark matter haloes that galaxies inhabit as either centrals (i.e. the dominant galaxy in the halo centre) or as satellites (i.e. less massive galaxies orbiting the central) serve as a more immediate environment with more direct effects on galaxy populations – especially for satellite galaxies. These halo environments range from systems like the Local Group with a total mass of a few 10^{12} $M_\odot$ to massive galaxy clusters such as Virgo or Coma with total masses on the order of 10^{14} $M_\odot$ and 10^{15} $M_\odot$, respectively. Field galaxies, on the other hand, tend to evolve relatively undisturbed within their own dark matter halo without the presence and influence of other galaxies. This raises a fundamental question: is galaxy evolution predominantly driven by nature (i.e. their internal processes and the initial conditions from which they originate) or nurture (i.e. the environmental effects they experience inside their host halo)?

While the formation and evolution of most galaxies is governed by a blend of both nature and nurture, the kind of environment they inhabit plays a key role in dictating which of the two dominates. Whether a galaxy spends its lifetime in the field or whether it is bound to a more massive group or cluster environment sets it on a different evolutionary path. Although environmental effects act on satellite galaxies in environments of all masses, they are particularly strong in galaxy clusters – the most massive, gravitationally bound structures in the Universe – and for the most abundant galaxies in the Universe, low-mass dwarf galaxies (Baldry et al. 2008; Li and White 2009; Pozzetti et al. 2010; Baldry et al. 2012).

1.2.1 Environmental effects: observational findings

On the colour, star formation activity, and morphology of satellite galaxies

Observed galaxy populations in groups and clusters appear distinct from their counterparts in the field, resulting in bimodal distributions for galaxy properties such as colour, morphology, or star formation activity. High-density group and cluster environments can shut down star formation processes more efficiently – thereby making galaxies appear red (Balogh et al. 2004; Lisker et al. 2008; van den Bosch et al. 2008; Peng et al. 2010; Prescott et al. 2011) and quenched (Balogh et al. 1999; Lewis et al. 2002; van der Wel et al. 2010; Spindler et al. 2018; Schaefer et al. 2019) – and transform their morphologies from disky late-types into more elliptical early-types (Einasto et al. 1974; Oemler 1974; Dressler 1980; Binggeli et al. 1987; Lisker et al. 2007; Grebel 2011). Galaxies in low-density field environments, on the other hand, tend to be blue spiral galaxies with active star formation (Strateva et al. 2001; Kauffmann et al. 2003; Baldry et al. 2004; Hogg et al. 2004; Kauffmann et al. 2004; Crossett

et al. 2017). In massive galaxy clusters, ram pressure stripping (see Chapter 1.2.2) has been found to be the most dominant process in quenching satellite galaxies (see e.g. Boselli et al. 2014; Boselli et al. 2016 for satellites in the Virgo cluster) – possibly after a final, induced episode of enhanced star formation (Vulcani et al. 2018; Safarzadeh and Loeb 2019). Satellites located closer to the cluster centre exhibit higher quenched fractions than those in cluster outskirts, particularly at lower satellite stellar masses (Presotto et al. 2012; Wetzel et al. 2013; Barsanti et al. 2018). Furthermore, satellite quenched fractions are correlated with the mass of their host: more massive systems, i.e. at larger host-to-satellite mass ratios, tend to host an increasing fraction of passive satellites (Wetzel et al. 2012; Wetzel et al. 2013; Davies et al. 2019).

On the dark matter haloes of satellites

However, not only observable properties of satellite galaxies are altered by their environment. As galaxy stellar mass and luminosity are tightly linked to halo mass and the depth of the halo potential, the respective dark matter haloes of satellite galaxies are affected as well, as they are removed in the gravitational potential of the host halo (Tinker et al. 2013; Hudson et al. 2015; van Uitert et al. 2016; Niemiec et al. 2017; Sifón et al. 2018; Dvornik et al. 2020). While halo mass is not directly observable, it can be observationally constrained using HI line widths (Tully and Fisher 1977), weak lensing measurements (e.g. Mandelbaum et al. 2006; Huang et al. 2019; Sonnenfeld et al. 2019), X-ray observations (e.g. Lin et al. 2003; Lin and Mohr 2004; Yang et al. 2007; Kravtsov et al. 2018), employing galaxy kinematics, stellar velocities, or planetary nebulae as tracers for the halo potential (e.g. Erickson et al. 1987; Ashman et al. 1993; Peng et al. 2004; van den Bosch et al. 2004), or by measuring the mass or abundance of globular clusters (e.g. Spitler and Forbes 2009; Forbes et al. 2018; Prole et al. 2019).

Pre-processing in previous hosts

The environmental effects that satellite populations of groups and clusters are subject to – loss of the dark matter halo, the cessation of star formation activities, as well as morphological transformation – are not necessarily restricted to their present-day environments. As some satellites were previously orbiting smaller subgroups, they already became subject to pre-processing and experienced environmental effects in their previous, less massive host system. Therefore, these satellites may still exhibit shared properties as an imprint of their previous host: they may be particularly quenched considering their spatial position inside their present-day host, share similar kinematics, or still appear clearly connected in phase-space (Zabludoff et al. 1996; Hou et al. 2014; Haines et al. 2015; Bianconi et al. 2018; Lisker et al. 2018; Bidaran et al. 2020).

1.2.2 Environmental effects: numerical interpretations

This section follows up on the previous observational findings with interpretations from theory, i.e. models and simulations. While observations merely offer a momentary snapshot of certain galaxy properties, they can be fully traced throughout a galaxy's lifetime in simulations – within the assumptions and restraints of the adopted physical models. I will introduce different types simulations, including N-body dark matter-only simulations and cosmological hydrodynamical simulations, as well as the physical processes their models include in Chapter 2.

Physical processes acting on satellite galaxies

In group or cluster environments, any galaxy can become subject to galaxy-galaxy interactions such as harassment (Moore et al. 1996; Moore et al. 1998) – high-velocity encounters driving morphological transformation – or various interactions with the host halo's potential. In a starvation scenario, gas accretion from the surrounding halo into the galaxy is cut off. Star formation continues for an extended period of time until the galaxy's gas reservoirs are exhausted (Larson et al. 1980; Balogh et al. 2000; Kawata and Mulchaey 2008; Wetzel et al. 2013). Ram pressure stripping (Gunn and Gott 1972; Moore et al. 1999b) deprives galaxies in the intracluster or intragroup medium of their gas, thereby removing the reservoirs for the formation of new stars and rapidly quenching the galaxies (e.g. Tonnesen et al. 2007; Bekki 2014; Fillingham et al. 2016; Simpson et al. 2018). This process can already act on satellites that are several virial radii outside of their host (von der Linden et al. 2010; Bahé et al. 2013; Zinger et al. 2018). Interactions between the cold interstellar and the hot intergalactic medium can cause the interstellar medium's temperature to increase rapidly, followed by evaporation and removal of the gas therein (e.g. Cowie and Songaila 1977; Boselli and Gavazzi 2006). Finally, tidal stripping in the host cluster potential can remove the surrounding dark matter haloes of satellite galaxies and stars from their outskirts, produce tidal tails, or even lead to their disruption (e.g. Toomre and Toomre 1972; Merritt 1983; Barnes and Hernquist 1992; Bournaud et al. 2004).

While these processes are predominantly responsible for "environmental quenching" of lower-mass satellites, more massive satellites may cease to form stars regardless as they are subject to "mass quenching" from secular, internal processes. For massive galaxies, the latter quenching process is commonly attributed to feedback from active galactic nuclei (AGN). Without appropriate models for AGN feedback, cosmological hydrodynamical simulations have not managed to reproduce quenched fractions and colour distributions of observed galaxy populations (McCarthy et al. 2011; Dubois et al. 2016; Kaviraj et al. 2017; Weinberger et al. 2018). In low-mass galaxies, periods of intense star formation can cause supernova explosions and stellar winds to drive out their gas (Agertz et al. 2013; Emerick et al. 2016) while reionisation can remove gas from dark matter haloes and the galaxies that

form therein in the early Universe (Tollerud and Peek 2018; Rodriguez Wimberly et al. 2019; Kang and Ricotti 2019)

Impacts on satellite galaxy and halo properties

As in observations, simulations and semi-analytic models find the quenched fractions of satellite populations to be correlated with the mass of their host: increasing host-to-satellite mass ratios result in larger quenched fractions (De Lucia et al. 2012; Furlong et al. 2015; Bahé et al. 2017; Henriques et al. 2017; De Lucia et al. 2019; Tremmel et al. 2019). Furthermore, satellites that were accreted at an earlier time, i.e. those that were subject to environmental effects inside their present-day environment for longer, exhibit higher quenched fractions compared to satellites that were accreted just recently (Smith et al. 2015; Rhee et al. 2017; Pasquali et al. 2019; Donnari et al. 2021b).

In addition, simulations have shown that the morphological transformation of satellite galaxies from disky to elliptical, which may accompany the quenching process, can occur due to a multitude of encounters. Tidal interactions of satellites with groups and clusters drive a significant fraction of transformations. However, the degree to which a late-type satellite is affected depends on properties such as disk inclination or its orbital parameters: satellites that achieve smaller pericentric distances on shorter timescales experience more significant morphological transformations (Kazantzidis et al. 2011; Villalobos et al. 2012; Joshi et al. 2020). Other processes driving morphological transformation include harassment in repeated encounters with other member galaxies, which is particularly effective in galaxy clusters (Bekki and Couch 2011; Lisker et al. 2013; Bialas et al. 2015), as well as minor and major mergers. Mergers, however, seem to play a more important role in the transformation of central galaxies than for group and cluster satellites (Feldmann et al. 2011; Martin et al. 2018; Clauwens et al. 2018; Joshi et al. 2020). Figure 1.3, taken from Joshi et al. (2020), illustrates the morphological transformation process for two present-day cluster satellites from the TNG50 simulation as projected stellar composite maps in face-on and edge-on projections from $z = 1.5$ to $z = 0$.

The dark matter haloes of satellite galaxies are largely lost due to the gravitational potential of their host environment after accretion. While stellar and halo mass of central galaxies are tightly correlated in the stellar-to-halo mass relation (SHMR), satellites exhibit significant deviations from the SHMR of the general galaxy population (Rodríguez-Puebla et al. 2012; Rodríguez-Puebla et al. 2013; Bahé et al. 2017; Buck et al. 2019; Niemiec et al. 2019). The removal of their haloes may already start outside the host halo's virial radius (Reddick et al. 2013; Behroozi et al. 2014; Smith et al. 2016) or even in previous, group-like host environments as part of pre-processing (Joshi et al. 2019).

As previously pointed out by observations in Chapter 1.2.1, pre-processing of satellite galaxies that were accreted onto their present-day host as part of a group can already leave an imprint on their properties. Theoretical models covering galaxy

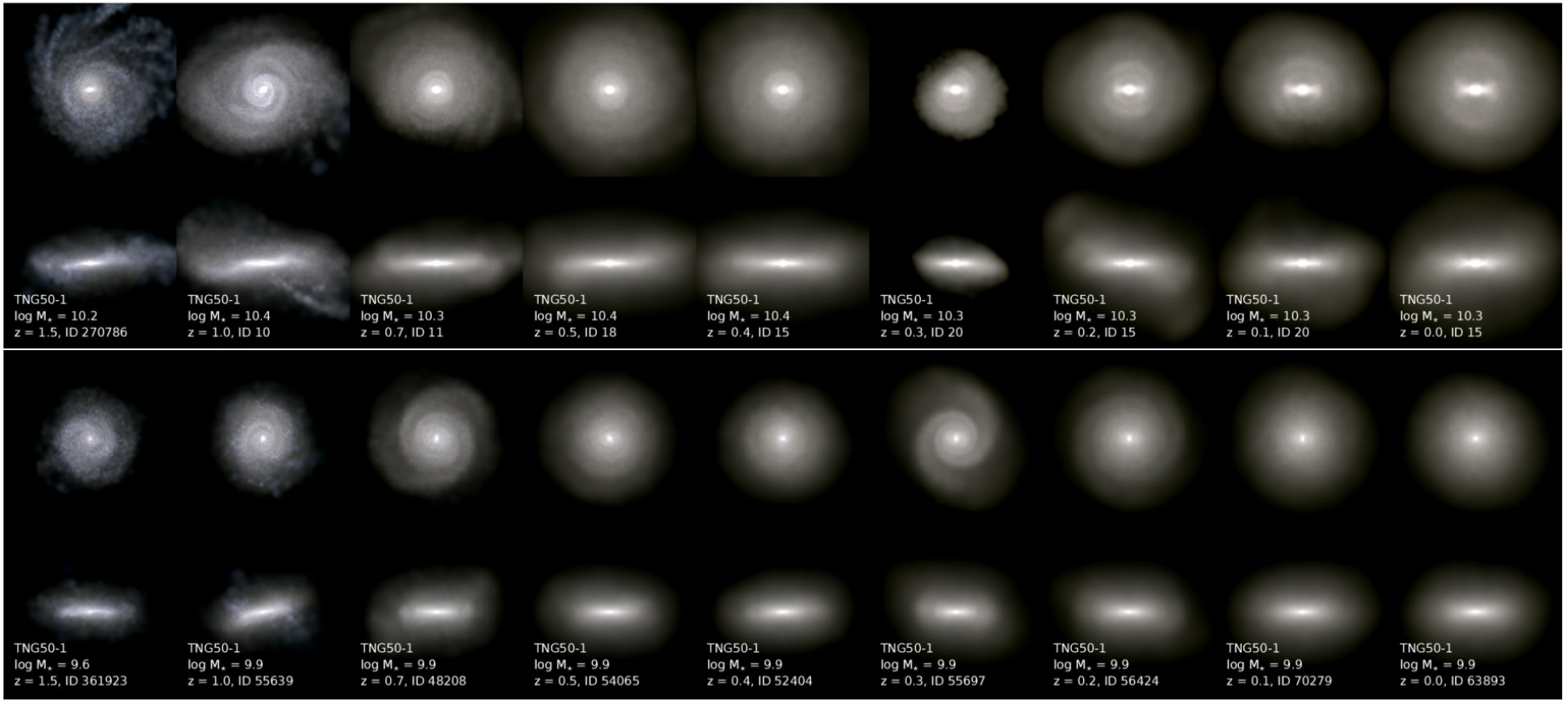

Figure 1.3: Morphological evolution of two present-day cluster satellites in TNG50 from $z = 1.5$ to $z = 0$. Theses satellite galaxies were selected to be disky at their time of accretion and non-disky by $z = 0$. Each panel illustrates projected stellar composite maps in an area of $(40\ \mathrm{kpc})^2$ with James Webb Space Telescope Near Infrared Camera (JWST NIRCam) f200W, f115W, and F070W filters. The first and third row correspond to face-on projections, the second and fourth row to edge-on projections. SOURCE: Joshi et al. (2020).

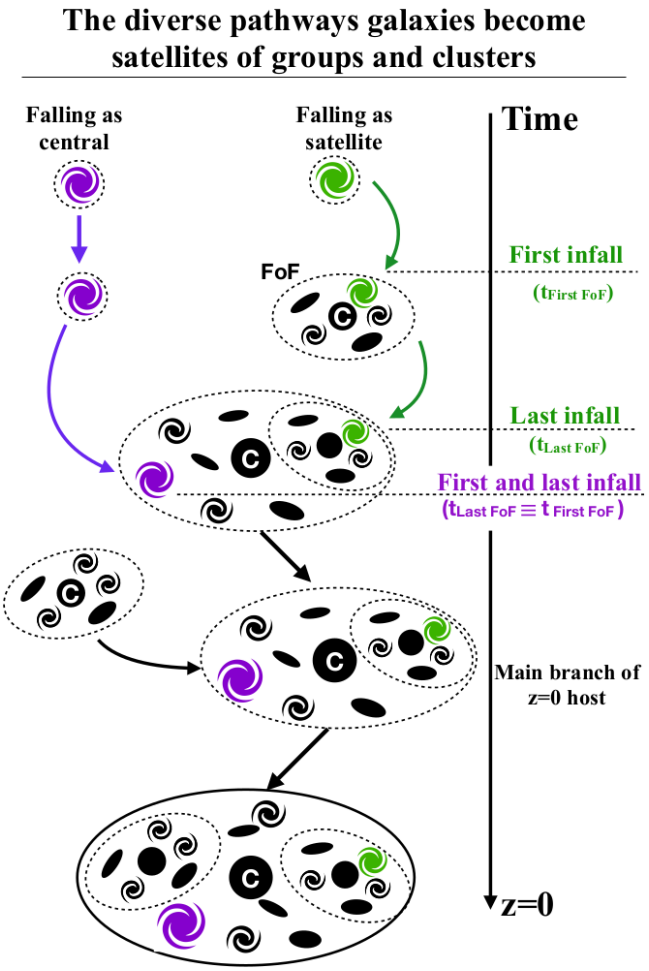

Figure 1.4: The diversity of evolutionary pathways for present-day satellites of groups and clusters, including the concept of pre-processing. This schematic illustrates two possible evolutionary tracks for the infall of galaxies into their present-day host. Galaxies falling as centrals (purple galaxy) spend their early life in isolation until they are directly accreted into their present-day environment. On the other hand, there are galaxies that fall into their present-day host as a satellite (green galaxy): they first become satellites of a smaller group of galaxies, which subsequently falls into their present-day environment together. The green galaxy may already become subject to environmental effects as a satellite of its first host and experience pre-processing. SOURCE: Donnari et al. (2021b).

evolution in a full cosmological context follow present-day satellites throughout their lifetime and through all previous host environments they experienced (Fujita 2004; McGee et al. 2009; Bahé et al. 2019; Joshi et al. 2019). Figure 1.4, taken from Donnari et al. (2021b), illustrates the concept of pre-processing by comparing different evolutionary pathways for satellite galaxies of present-day groups and clusters. Both semi-analytic models and cosmological hydrodynamical simulations reveal that $25 - 45$ per cent of present-day satellites of galaxy clusters were originally accreted into smaller groups before falling into their current host (McGee et al. 2009; De Lucia et al. 2012; Bahé et al. 2013; Donnari et al. 2021b). As they already become subject to environmental effects there, they may cease to form stars within these groups before they reach their present-day environment. The overall fraction of pre-processed satellites, however, is a strong function of host mass: present-day

galaxy clusters host higher fractions of them than less massive galaxy groups (Bahé et al. 2013; Bahé et al. 2019; Pallero et al. 2019).

In conclusion, both observations and theoretical models have repeatedly shown that halo environments – spanning several orders of magnitude in total mass from low-mass groups to massive galaxy clusters – leave a distinct imprint on satellite galaxy populations. The following part of this chapter focuses on a more specific, less massive environment in order to explore and describe its satellite population in more detail: the Local Group, consisting of the Milky Way and Andromeda galaxies as separate yet very similar host systems.

1.3 The Local Group

1.3.1 Satellite abundance around the Milky Way and similar systems

The abundance of dwarf satellite galaxies orbiting the Milky Way (MW) and Andromeda (M31) has helped to inform our understanding of the Universe and the formation of galaxies therein. Yet, these satellite systems – the closest we can study down to as low as a few thousand solar masses in stars – continue to challenge the ΛCDM model of structure formation and the simulations based on it.

For about twenty years, the "missing satellites" problem (Moore et al. 1999a; Klypin et al. 1999; Bullock and Boylan-Kolchin 2017) has attracted notable interest across the astronomical community by pointing towards a seemingly insurmountable tension between observations and theoretical models. According to its original incarnation, dark matter- or gravity-only simulations of the cosmological assembly of MW-like haloes in a ΛCDM scenario predict far more satellites (i.e. subhaloes; Springel et al. 2008; Diemand et al. 2008) than there are actual luminous satellites observed around the Galaxy – particularly at the low-mass end.

From an observational perspective, the number of satellite galaxies that have been detected around the MW has in fact continued to grow into the ultra-faint regime in recent years (stellar masses of $\lesssim 10^5$ $M_\odot$, e.g. Zucker et al. 2006; Belokurov et al. 2006; Sakamoto and Hasegawa 2006; Willman 2010; Drlica-Wagner et al. 2015; Koposov et al. 2015; Torrealba et al. 2016; Torrealba et al. 2018; Drlica-Wagner et al. 2020). On the other hand, the number of bright, classical satellites had initially been constant for two decades after the discovery of the Sagittarius galaxy (Ibata et al. 1994) but additional bright satellites such as Crater 2 and Antila 2 (Torrealba et al. 2016; Torrealba et al. 2019), as well as tidal remnants of former bright satellites, such as Gaia-Enceladus (Belokurov et al. 2018; Helmi et al. 2018; Myeong et al. 2018) and Sequoia (Myeong et al. 2019), have been discovered in recent years.

Characterising the satellite populations of similar galaxies within and beyond the Local Volume is essential in order to understand how representative the MW

and Andromeda are in a cosmological context. Therefore, the study of the abundance of satellite dwarf galaxies has been extended over the last decade, from the MW (McConnachie 2012) and M31 (Martin et al. 2016; McConnachie et al. 2018) to other nearby galaxies, such as Centaurus A (e.g. Crnojević et al. 2014; Müller et al. 2017; Crnojević et al. 2019; Müller et al. 2019), M94 (Smercina et al. 2018), and M101 (e.g. Bennet et al. 2017; Bennet et al. 2019; Carlsten et al. 2019).

However, sample completeness is of the essence when searching for satellite systems to compare to the satellite abundances in the MW and the Local Group. Contamination by foreground and background objects can cause major issues. Carlsten et al. (2020b) and Carlsten et al. (2021) summarise such comparisons using CFHT/MegaCam data from the Canada-France-Hawaii Telescope (CFHT). By utilising surface brightness fluctuations, they obtain reliable distance measurements to confirm satellite candidates around twelve hosts in the Local Volume (i.e. within 12 Mpc).

The "Satellites Around Galactic Analogs" (SAGA) survey extends the search for a "normal" satellite system by aiming for a statistical sample of MW-like hosts beyond the Local Volume at distances of $20 - 40$ Mpc. The first stage of SAGA identified 27 satellites around 8 MW-like systems, revealing a significant degree of host-to-host scatter between satellite systems (Geha et al. 2017). This sample was recently expanded to 127 satellites around 36 MW-like hosts in the survey's second stage (Mao et al. 2021). While the satellite abundance of the MW is consistent with those from the SAGA survey, the systems exhibit a remarkable degree of diversity, ranging from MW-like hosts with no satellites whatsoever to systems with up to 9 satellites, down to an absolute r-band magnitude of $M_\mathrm{r} < -12.3$. Ultimately, SAGA aims to spectroscopically determine the satellite systems of 100 MW-like host galaxies down to satellite stellar masses of about 10^6 $\mathrm{M}_\odot$.

1.3.2 Environmental effects on Local Group satellites

Local Group satellites seem to be subject to particularly strong environmental effects. There is a distinct transition regarding the properties of low-mass dwarf galaxies with stellar masses of $M_* < 10^9$ $\mathrm{M}_\odot$ within 300 kpc of the MW or M31 – approximately within their virial radius. Their morphologies become more spheroidal, they barely contain atomic gas, and their star formation activity is subsequently shut down (Einasto et al. 1974; Grcevich and Putman 2009; McConnachie 2012; Slater and Bell 2014; Phillips et al. 2015; Wetzel et al. 2015). There is a clear correlation between the gas content of dwarf galaxies and the distance to their host galaxy (Blitz and Robishaw 2000; Grebel et al. 2003; Spekkens et al. 2014; Putman et al. 2021): more isolated dwarf galaxies in the outskirts become gas-richer. While isolated dwarfs outside of the Local Group support this picture by exhibiting a richer gas content (Bradford et al. 2015; Stierwalt et al. 2015), the SAGA survey finds significantly different results. Despite the proximity to their respective host galaxy, SAGA satellites appear to retain their gas and continue to form stars (Geha et al. 2017; Mao et al.

2021). Thus, the quenched fractions of satellite galaxies outside of the Local Volume and of those within the Local Group are currently in contradiction to each other.

Star formation histories of dwarf galaxies in the Local Group

In order to learn more about the star formation process of dwarf galaxies and their build-up of stellar mass, cumulative star formation histories (SFH) have been reconstructed in numerous studies. In observations with resolved stellar populations, SFHs can be derived directly from colour-magnitude diagrams of individual stars. By looking for the oldest main-sequence turn-off stars, several single age stellar populations can be separated from each other (Dolphin 2002; Brown et al. 2014; Skillman et al. 2017; Cignoni et al. 2018; Sacchi et al. 2018). Comparisons of the SFHs of dwarf galaxies within and outside the Local Group in the nearby Universe have emphasised the impact of their environment on their evolution. While individual SFHs exhibit a large diversity, the mean SFHs of dwarfs of different morphological types are – for the most part – remarkably similar. Differences are mostly found in the last few Gyr of their evolution as they transform from gas-rich to gas-poor. Dwarf galaxies in the Local Group seem to be representative of other dwarfs in the local Universe (Weisz et al. 2011b; Weisz et al. 2011a). The diversity of SFHs of satellite galaxies in the Local Group stems from both their own stellar mass and their environment – with differences even between the populations of the Milky Way and Andromeda: less massive dwarfs in higher density environments exhibit a more rapid evolution at earlier times than more massive dwarfs as well as those in lower-density environments (Weisz et al. 2014; Gallart et al. 2015; Weisz et al. 2019).

Accurately reproducing MW- or Local Group-like systems and their satellite populations – including their abundance, spatial distribution, as well as gas content and star formation activity – has been a key challenge to theoretical models and one of the major achievements of cosmological hydrodynamical simulations in recent years. These projects and their contributions are summarised in Chapter 2.2.3.

1.4 The rationale and goals of the thesis

In this thesis, I study satellite galaxy populations with the IllustrisTNG suite of cosmological magneto-hydrodynamical simulations (see Chapter 2.3 for details). Utilising the entire range of IllustrisTNG allows for an unprecedented combination of statistical sample size and numerical resolution, resulting in mass ranges that cover multiple orders of magnitude for both host and satellites samples. The host environments I study in this thesis range from massive, Coma- or Virgo-like galaxy clusters to galaxy groups and Milky Way-mass systems, including the first statistical sample of 198 high-resolution Milky Way-/Andromeda-like (MW/M31) hosts. Satellite galaxies range from classical dwarf galaxies like Leo I to Magellanic Cloud-like, or

even MW-like and more massive satellites around cluster hosts. Thus, the IllustrisTNG simulations are capable of bridging the regimes of large-scale volumes and zoom-in simulations (see Chapter 2 for details on types of simulations).

I investigate how – within the framework of the adopted models – different environments affect the mass components of my satellite samples after infall (i.e. dark matter, stars, and gas) and analyse which of the processes listed in Chapter 1.2.2 dominate their respective evolution to the present-day the most. Their environment impacts and changes their galaxy-halo connection, their gas content and star formation activities, as well as their abundance in terms of surviving luminous satellite galaxies and dark matter haloes in general.

Furthermore, I examine their evolution in the context of the ΛCDM model of structure formation. The galaxy-halo connection is described by the most fundamental relationship of galaxy formation and evolution in the cosmological standard model: the stellar-to-halo mass relation. But to what level is it universal between different types of galaxies? And what factors determine its scatter? In the last two decades, astronomers have continued to examine alternative cosmological models, e.g. based on warm dark matter, since the cold dark matter in ΛCDM is still met with crucial challenges, such as the missing satellites problem, which predicts far more satellites than observed around the MW (see Chapter 1.3). But is this still an issue in the light of modern, ΛCDM-based, cosmological hydrodynamical simulations? The dwarf galaxies around the MW and M31 seem to be subject to particularly strong environmental effects as they become almost exclusively gas-poor and quenched within the virial radius of their host. But are these local satellite galaxies representative in a cosmological context compared to the satellite populations of similar hosts? Utilising the IllustrisTNG simulations, I explore these questions in statistically significant samples of satellites throughout cosmic time, as well as across simulation volumes and resolution levels in order to distinguish between actual physical processes and numerical limitations.

1.4.1 The structure of the thesis

In the remainder of this chapter, I summarise the structure of this thesis, as well as the goals and approaches of the research projects that will be presented over the next chapters.

In Chapter 2, I introduce cosmological simulations of galaxy formation as the main tools used in this thesis to study satellite galaxy populations. I give a brief history, categorise different kinds of simulations, and summarise their main advances and achievements in recent years. Furthermore, I present the IllustrisTNG simulation suite, discuss their adopted models, and summarise some of the main findings originating from IllustrisTNG so far.

Chapter 3 presents the results of Engler et al. (2021b), *"The distinct stellar-to-halo mass relations of satellite and central galaxies: insights from the IllustrisTNG simulations"*. I study the galaxy-halo connection of satellite and central galaxies selected above

the same minimum total dynamical mass ($M_{\rm dyn} \geq 10^{10.5}$ M$_\odot$) using their stellar-to-halo mass relation (SHMR). This chapter focuses mostly on $z = 0$ but also entails a discussion on the redshift evolution of the relations and their galaxy-to-galaxy variations up to $z \sim 2$. I define a number of environmental parameters and examine their effects on satellite galaxies in groups and clusters, their locus in the SHMR, and the scatter in stellar mass. Combining all the runs of the IllustrisTNG suite, I explore an unprecedented dynamical range of satellite and host masses. Due to the nature of the simulations (uniform volumes instead of e.g. zoom-in simulations), the shape of the mass distributions of host haloes and their satellite galaxies are replicated closely, similar to how they emerge in the real Universe.

In Chapter 4, I discuss the findings of Engler et al. (2021a), *"The abundance of satellites around Milky Way- and M31-like galaxies with the TNG50 simulation: a matter of diversity"*. Throughout this chapter, I analyse the satellite populations of a statistical sample of 198 MW- and M31-like hosts using the TNG50 simulation. With a baryonic mass resolution of 8×10^4 M$_\odot$, this is the largest host sample at this high level resolution to date. I study the evolution of satellite abundance throughout cosmic time and search for statistically significant correlations between satellite abundance and various properties of their host galaxies and host haloes. I compare the satellite abundance around TNG50 hosts to both observational surveys of MW-like hosts and previous simulations of MW- and Local Group-like hosts. Furthermore, I examine the abundance and evolution of subhalo populations, which may be either luminous or dark, and make comparisons to the abundance of luminous satellite galaxies in order to address the missing satellites problem (see Chapter 1.3) – one of the most significant discrepancies to challenge the ΛCDM model of structure formation over the last two decades.

I take a closer look at the satellites of TNG50 MW/M31-like hosts in Chapter 5. I examine their distribution in phase-space as well as their quenched fractions in comparison to the satellite populations of observed systems. In order to investigate how these satellite galaxies became quenched, I analyse their gas content as a function of distance to their host galaxy and within phase-space, and relate them to their time of accretion. Finally, I study the evolution of the satellites' mass components after infall as a function of satellite stellar mass in order to quantify the contributions of tidal stripping, ram pressure stripping, and quenching processes on their dark matter, gas, and stellar mass.

I present the conclusions of my thesis in Chapter 6. With several statistical samples of both satellite galaxies and the environments in which they reside – spanning up to three orders of magnitude in total host mass – I give an elaborate view of the joined evolution of satellite dark matter and stellar mass, as well as their gas content and how it affects their star formation activity within the framework of the IllustrisTNG simulations. Furthermore, I provide an outlook for further research based on the work in this thesis, which will contribute to the results of Chapter 5 for a future publication.

Chapter 2

The tools of the thesis: cosmological galaxy simulations

Cosmological simulations of galaxy formation have become one of the key instruments to interpret observational results and to understand the evolution of galaxies and their properties throughout time. With a cosmological model as their foundation – in the case of ΛCDM, dark energy for the accelerated expansion of the Universe and cold dark matter as the fundamental component for structure formation (see Chapter 1) – they follow the coupled evolution of dark and baryonic matter, as well as how they interact with each other to form populations of galaxies similar to those observed in the present-day Universe. Despite the fact that baryonic matter in the form of stars and gas constitute merely up to five per cent of the Universe's energy budget, the physical processes occurring throughout their evolution and their interactions with each other are the most complex component of modern cosmological simulations. As they cover both a large range of scales and physics, they need to be carefully implemented. Ultimately, well-defined initial conditions and accurate models are required to predict realistic galaxies – both on the individual level, as well as for entire galaxy populations in a cosmological context (Somerville and Davé 2015; Vogelsberger et al. 2020a).

2.1 Theoretical foundation

The initial conditions of a simulation describe the density perturbations in the early Universe (around redshift $z \sim 100$) that are applied to a homogeneous, expanding background, commonly based on a flat Friedmann-Lemaître-Robertson-Walker space-time. The simulation's matter composition is predefined with the adopted cosmological parameters (e.g. from the Wilkinson Microwave Anisotropy Probe, Hinshaw et al. 2013, or the Planck Collaboration et al. 2016). Furthermore, positions and velocities of dark matter particles and baryons are assigned and subsequently displaced using linear theory approximation (Zel'Dovich 1970) or low-order perturbation theory (Bertschinger 2001). The most common types of initial conditions result in periodic, large-scale volumes or zoom-in conditions. The periodic conditions of the former mimic the cosmological principle for large-scale matter homogeneity and

isotropy. In the latter case, a high-resolution region is embedded and simulated in a low-resolution background in order to gain a more detailed view into the region of interest.

2.1.1 Simulating dark matter

Dark matter is commonly simulated using N-body methods to follow the pure gravitational dynamics of dark matter particles. Their behaviour is described by a combination of the collisionless Boltzmann equation and the Poisson equation. Thus, the mass of each particle remains conserved along its trajectory. On small scales, gravitational interactions are softened using kernel-based smoothing methods or adaptive softening schemes in order to prevent spurious two-body interactions (Price and Monaghan 2007). The latter technique automatically decreases the softening length in high-density regions.

The integration schemes employed to compute the gravitational forces of the N-body system follow two main approaches: using approximations for direct summation or utilising mesh-based methods. The former employ tree structures, possibly improved by fast multipole methods (Barnes and Hut 1986; Dehnen 2000). The latter are based on fast Fourier transforms and include particle-mesh methods, adaptive mesh refinement schemes, and multigrid methods (e.g. Hockney and Eastwood 1981). Typically, modern simulations adopt hybrid methods of these two categories.

2.1.2 Simulating baryonic matter

Simulating the baryonic component and the physical processes between them is more complex. Computing hydrodynamic processes – typically described as an inviscid, ideal gas based on the Euler equation – is numerically demanding. There are several techniques to solve the hydrodynamical equations.

Lagrangian methods employ a sample of particles to approximate continuous fluid dynamics. In this smoothed particle hydrodynamics method, properties such as energy, momentum, and mass are conserved (Lucy 1977; Springel 2010b; Price 2012). Simulation codes employing this technique include GADGET-2/3 (Springel 2005) and Gasoline2 (Wadsley et al. 2017). Eulerian methods, such as adaptive-mesh-refinement schemes, are helpful in dealing with the large dynamic range of cosmological simulations. According to certain refinement criteria, the size of the mesh can be reduced if required (Berger and Oliger 1984; Berger and Colella 1989). This method is employed in codes such as RAMSES (Teyssier 2002) and Enzo (Bryan et al. 2014). Arbitrary Lagrangian-Eulerian methods – used in the AREPO (Springel 2010a), TESS (Duffell and MacFadyen 2011), and SHADOWFAX (Vandenbroucke and De Rijcke 2016) codes – create a Voronoi tessellation of discrete, mesh-generating points. Since these points are able to move freely, the resulting mesh continuously deforms to change its morphology without encountering mesh-tangling effects.

Physical processes of baryons

Regardless of which of these techniques are employed, various baryonic processes need to be taken into account along with the hydrodynamical equations. Most of the following processes are implemented as subgrid models since they occur on scales that are not accessible to simulations due to their limitations in numerical resolution. Different versions of these sub-resolution models are one of the major uncertainties between different simulations of recent years.

Models for gas cooling describe how gas dissipates energy through either primordial or metal-line cooling in a spatially-uniform, time-dependent radiation field. Furthermore, cold-phase gas of the interstellar medium may cool via fine-structure or molecular cooling in simulations that achieve this level of resolution (Wiersma et al. 2009a; Tielens 2010; Haardt and Madau 2012). The complex multi-phase structure of the interstellar medium is an essential part of simulations as it provides the gas and environment for star formation processes. Since modelling the multi-phase structure directly is challenging due to interactions of gas, dust, and radiation, it is generally approximated with an effective polytropic equation of state for an equilibrium two-phase interstellar medium. While the majority of gas mass is part of the cold phase, the rest is part of a volume-filling phase heated by supernovae (Agertz et al. 2011; Dalla Vecchia and Schaye 2012; Hopkins et al. 2012).

Cold gas can ultimately form stars: universally, 1 per cent of molecular gas is converted into stars per free fall time (Bigiel et al. 2011; Krumholz et al. 2012). However, as single stars cannot be resolved, simulation models produce stellar particles that correspond to single-age, single-metallicity stellar populations with an underlying stellar mass function. Throughout their evolution, these stellar populations return mass to the surrounding gas and enrich it via Type Ia and II supernovae, asymptotic giant branch stars, as well as neutron star mergers (Wiersma et al. 2009b; Vogelsberger et al. 2013; Naiman et al. 2018). These interactions with their surrounding gas generates a feedback loop that regulates further star formation. By injecting energy and momentum thermally or kinetically, stellar feedback causes galaxies to eject gas. Processes such as stellar winds, photoionisation, and radiation pressure contribute to these galactic-scale outflows (Agertz et al. 2013; Stinson et al. 2013; Hopkins 2014; Hopkins et al. 2018; Smith et al. 2019b).

Supermassive black holes provide another, essential kind of feedback in more massive galaxies. They typically accrete mass based on a Bondi-Hoyle accretion rate with an Eddington limit. As their formation is not yet well understood, they are seeded numerically (Shlosman et al. 1989; Hopkins and Quataert 2011; Anglés-Alcázar et al. 2013; Davé et al. 2019). As active galactic nuclei (AGN), these supermassive black holes can be the source of relativistic jets, electromagnetic radiation, and non-relativistic outflows, which affect the surrounding gas. This AGN feedback is generally implemented in two modes: the radiative "quasar" mode and the kinetic "radio" mode feedback. The former consists of energy and momentum injections

into the surrounding gas based on the supermassive black hole's bolometric luminosity and its accretion rate. The latter – typically effective at low accretion rates – corresponds to highly-collimated jets of relativistic particles and may be the cause of observed X-ray bubbles (Di Matteo et al. 2005; Springel et al. 2005a; Sijacki et al. 2007; Weinberger et al. 2018; Pillepich et al. 2021). Together, stellar and AGN feedback regulate star formation activity in low- and high-mass galaxies, respectively, cause lower baryon retention fractions, and are required for an appropriate simulation of the galaxy-halo connection (e.g. Behroozi et al. 2010; Moster et al. 2013).

Other, additional models of baryonic processes include magnetic fields, which influence gas motions and provide pressure support in the interstellar medium, implemented with ideal magnetohydrodynamics (Ferrière 2001; Kotera and Olinto 2011), as well as cosmic rays, which may drive galactic outflows (Field et al. 1969; Ferriere 2003; Uhlig et al. 2012; Pakmor et al. 2016; Simpson et al. 2016). Simulations exploring the high-redshift Universe around the epoch of reionisation, such as the Cosmic Reionization on Computers project (Gnedin and Kaurov 2014), the SPHINX (Rosdahl et al. 2018), or the Cosmic Dawn II simulations (Ocvirk et al. 2020), further include models for radiation hydrodynamics that are able to affect the kinetic and thermal state of the gas component.

2.1.3 Cosmological simulations of recent years

Examples for large-scale cosmological hydrodynamical simulations of recent years that employ such physical models include Illustris (Genel et al. 2014; Vogelsberger et al. 2014a; Vogelsberger et al. 2014b; Sijacki et al. 2015), EAGLE (Crain et al. 2015; Schaye et al. 2015), Magneticum (Hirschmann et al. 2014; Dolag et al. 2015; Dolag et al. 2016), MUFASA (Davé et al. 2016), HorizonAGN (Dubois et al. 2016), IllustrisTNG (Marinacci et al. 2018; Naiman et al. 2018; Nelson et al. 2018a; Pillepich et al. 2018a; Springel et al. 2018, see Chapter 2.3 for details), and SIMBA (Davé et al. 2019). All of these simulations offer a large range of group and cluster environments with a particle mass resolution on the order of 10^{6-7} $M_\odot$ and a spatial resolution on the kpc-level.

Recent advancements of such simulations have focused either on more massive or less massive objects and environments. Particularly massive, simulated galaxy clusters are available in large samples in the TNG300 simulation (as part of the IllustrisTNG suite) or in more detail in the zoom-in simulations of Hydrangea (Bahé et al. 2017) and C-EAGLE (Barnes et al. 2017). More detailed, Virgo-like clusters with a particularly high level of numerical resolution are available in the ROMULUSC cluster zoom simulation (Tremmel et al. 2019) and – along with a statistical sample of high-resolution Milky Way- and Andromeda-like hosts – the TNG50 run of the IllustrisTNG suite (Nelson et al. 2019a; Pillepich et al. 2019).

Milky Way- and Local Group-like systems have been of particular interest of zoom-in simulations to study their structure and satellite populations. This includes projects such as APOSTLE (Fattahi et al. 2016a), Latte (Wetzel et al. 2016), Auriga

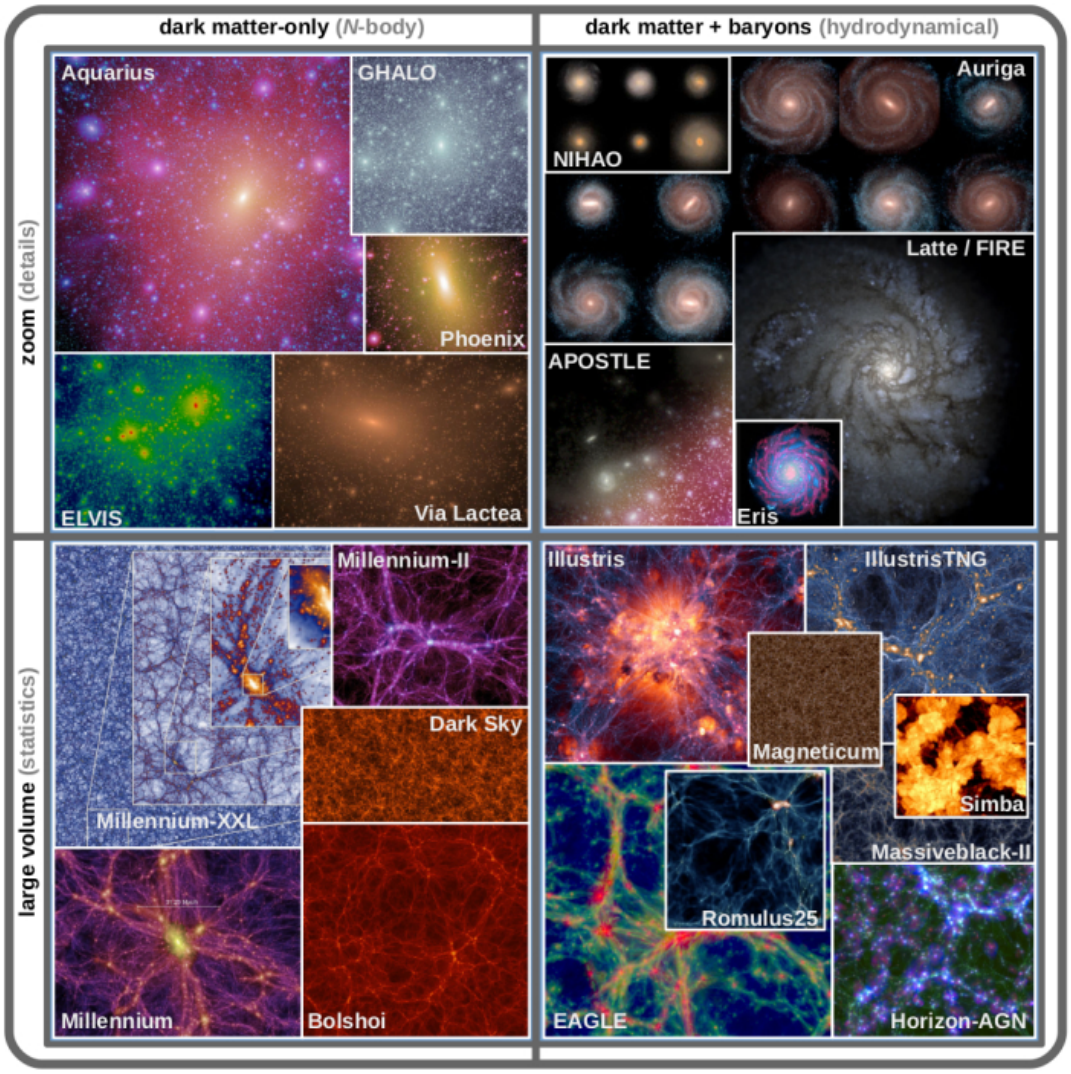

Figure 2.1: Visualisations of various cosmological simulations of structure and galaxy formation. The schematic is divided based on the matter they simulate (dark matter-only vs. dark matter and baryons, i.e. hydrodynamical simulations; left and right quadrants, respectively), as well as according to the volume they encompass (zoom-in vs. large volume simulations; top and bottom quadrants, respectively). While large volumes provide statistical samples of haloes and galaxies, zoom-in simulations allow for a smaller number or even single objects to be studied in greater detail. SOURCE: Vogelsberger et al. (2020a).

(Grand et al. 2017), and FIRE-2 (Garrison-Kimmel et al. 2014; Garrison-Kimmel et al. 2017; Garrison-Kimmel et al. 2019), as well as – most recently – the ARTEMIS (Font et al. 2021a) and DC Justice League simulations (Applebaum et al. 2021).

These simulations and several more are visualised in Figure 2.1 (taken from Vogelsberger et al. 2020a), which provides an overview on cosmological simulations of structure and galaxy formation from recent years. Simulations are divided into quadrants according to the types of matter they include (dark matter-only vs. dark matter and baryons, i.e. hydrodynamical simulations) and the volume they encompass (zoom-in vs. large volumes).

2.2 Key results of dark matter-only & baryonic simulations

With several decades of both N-body, dark matter-only simulations and baryonic, cosmological hydrodynamical simulations, theoretical models have provided numerous insights into the formation and evolution of dark matter halo and galaxy populations. In the following, I summarise some of their key results.

2.2.1 Insights from dark matter-only simulations

On global halo properties

The abundance of dark matter haloes across mass regimes has been studied extensively in N-body simulations. Due to their hierarchical growth via mergers, their resulting halo mass function evolves throughout time. While its high-mass end is exponentially suppressed, its low-mass end follows a power-law slope, i.e. there is a significantly larger abundance of low-mass than of massive dark matter haloes (Press and Schechter 1974; Bond et al. 1991; Jenkins et al. 2001; White 2002; Reed et al. 2003a). A variety of empirical fitting functions have been formulated (e.g. Reed et al. 2003b; Watson et al. 2013; Bocquet et al. 2016). On large scales, the distribution of dark matter can be described by a two-point correlation function whose signal increases with time (Springel et al. 2006; Springel et al. 2018). It is significantly different from the galaxy correlation function as galaxies form in high peaks of the underlying dark matter distribution (Benson et al. 2000).

On individual halo properties

The internal structure of individual dark matter haloes has been described by several functional forms, such as the spherically-averaged Navarro-Frenk-White density profile (Navarro et al. 1996; Navarro et al. 1997) or the Einasto profile whose slope gradually changes to become shallower towards the halo centre (Einasto 1965; Navarro et al. 2004). Furthermore, the concentration of dark matter haloes has been found to be correlated with their formation time (Navarro et al. 1997). Halo shapes – especially the ones of more massive haloes – are typically prolate (Jing 2002; Allgood et al. 2006; Bett et al. 2007). As dark matter-only simulations achieved higher

resolutions, subhaloes – substructures within host haloes – could be detected. Compared to field haloes with similar mass, they appear less extended as they are subject to tidal stripping inside their host halo (Moore et al. 1999a; Diemand et al. 2007; Springel et al. 2008; Navarro et al. 2010). Subhalo abundance has been found to correlate with various host properties, e.g. more concentrated hosts have a lower abundance of subhaloes (Gao et al. 2004).

2.2.2 Insights from baryonic simulations

Individual and global galaxy properties are well explored with cosmological hydrodynamical simulations. While large-scale simulations are suitable to study galaxy populations due to the statistical samples available, characteristics of individual galaxies can by analysed well in zoom-in simulations due to their higher level of numerical resolution. Early baryonic simulations examined the interstellar medium and the Lyman α forest of individual galaxies (Katz and Gunn 1991; Navarro and Benz 1991; Katz 1992; Hernquist et al. 1996).

On galaxy abundance

The galaxy stellar mass function exhibits a similar shape to the dark matter halo function, albeit with a shallower slope at lower masses and with the exponential suppression of massive galaxies occurring at lower volume densities. Observationally, it is described by a Schechter or Double Schechter function (Schechter 1976; Panter et al. 2007; Baldry et al. 2012). In simulations, accurate models for the suppression of star formation are required to reproduce the observed galaxy stellar mass function.

On feedback processes

While supernova feedback regulates the star formation efficiency of low-mass galaxies, more massive galaxies are regulated by AGN feedback (Dekel and Silk 1986; Larson 1974; White and Frenk 1991). Appropriate feedback models result in a reasonably well reproduced stellar-to-halo mass relation (Schaye et al. 2015; Pillepich et al. 2018a). The circumgalactic medium can be utilised to constrain feedback mechanisms since it is directly affected by the resulting galaxy outflows. While it is challenging to resolve due to its small spatial scales and multi-phase structure, circumgalactic gas refinement schemes have been developed to increase the level of numerical resolution (Hummels et al. 2019; Peeples et al. 2019; Suresh et al. 2019; van de Voort et al. 2019). In the intracluster medium, simulations have reproduced observed iron distributions, as well as Sunyaev-Zeldovich and X-ray scaling relations accurately (Planelles et al. 2014; Rasia et al. 2015; Vogelsberger et al. 2018).

On the distribution of galaxies and population properties

The distribution of galaxies and their degree of clustering has been found to be a function of their mass - with larger two-point correlation lengths for more massive galaxies – as well as their colour, star formation activity, and formation time (Meneux et al. 2008; Foucaud et al. 2010; Artale et al. 2017; Springel et al. 2018). Furthermore, various observed scaling relations have been reproduced by simulations in recent years to confirm that their produced galaxy properties are realistic. This includes the mass-metallicity (Davé et al. 2017; De Rossi et al. 2017; Torrey et al. 2018; Torrey et al. 2019) and mass-size (Genel et al. 2018) relations, the relation between supermassive black holes mass and stellar velocity dispersion (Kormendy and Ho 2013), as well as properties like galaxy colour (Trayford et al. 2015; Kaviraj et al. 2017; Nelson et al. 2018a).

On galaxy morphology

Modern simulations produce a range of realistic galaxy morphologies. Disky late-type galaxies form inside their dark matter haloes due to the conservation of angular momentum as their gas cools (Fall and Efstathiou 1980; Mo et al. 1998). Appropriate, efficient stellar feedback models are required to avoid both overcooling and angular momentum catastrophes (Balogh et al. 2001; Brook et al. 2011) to create late-type galaxies with extended, rotationally-supported, and gaseous disks such as in the Eris, NIHAO, FIRE, Latte, Auriga, and FIRE-2 simulations (Guedes et al. 2011; Wang et al. 2015a; Hopkins 2014; Wetzel et al. 2016; Grand et al. 2017; Hopkins et al. 2018, respectively; see also Aumer et al. 2013; Marinacci et al. 2014). Early-type galaxies form in two phases: at early times, they predominantly grow through active in-situ star formation. At later times, mergers and the accretion of external mass dominate their assembly, increasing their size significantly (Wang et al. 2015b; Feldmann et al. 2011; Rodriguez-Gomez et al. 2016; Lagos et al. 2018; Schulze et al. 2018).

2.2.3 Satellite populations of Milky Way-like hosts

One particular topic that has been studied extensively in recent years concerns the satellite and subhalo populations around Milky Way-like (MW) host galaxies and the missing satellites problem (see Chapter 1.3). Dark matter-only simulations had found many more low-mass subhaloes surround MW-mass hosts compared to the observed dwarf satellites around the Galaxy (Moore et al. 1999a; Klypin et al. 1999). However, the abundance of dark matter subhaloes and luminous galaxies is different. Baryonic effects such as supernova feedback (Larson 1974; Dekel and Silk 1986; Mori et al. 2002) and reionisation (Couchman and Rees 1986; Efstathiou 1992; Thoul and Weinberg 1996) are thought to reduce the efficiency of star formation and should hence be able to keep visible galaxies from forming in low-mass dark matter haloes. This has been shown repeatedly with both semi-analytic models (Bullock et al. 2000; Benson et al. 2002a; Benson et al. 2002b; Somerville 2002; Font et al. 2011; Guo et al.

2011) and full hydrodynamical simulations (Okamoto et al. 2005; Governato et al. 2007; Macciò et al. 2007; Sawala et al. 2016a) over the last two decades. Furthermore, satellites can be destroyed by tidal shocks as they pass through their host galaxy's disk (D'Onghia et al. 2010; Yurin and Springel 2015).

Since galaxy formation is expected to be significantly suppressed at low halo masses, a majority of these (sub)haloes should not host a luminous component – from theoretical perspectives in general, as well as specifically within a ΛCDM ansatz. Therefore, a large body of work in the past years has focused on a line of solutions to the missing satellites problem and considered the idea that luminous dwarf galaxies inhabit only a small fraction of these predicted subhaloes (e.g. Nickerson et al. 2011; Shen et al. 2014; Sawala et al. 2015; Sawala et al. 2016b; Benitez-Llambay and Frenk 2020). On the other hand, even for (sub)haloes that are able to host some star formation, the mapping between dark matter (sub)halo mass and galaxy stellar mass remains theoretically uncertain – particularly for systems below 10^{10-11} $M_\odot$ in total mass (e.g. Sawala et al. 2015, and references therein). Large systematic variations exist across galaxy formation models, be it numerical simulations, semi-empirical, or semi-analytical models. Finally, a number of cosmological hydrodynamical simulations have shown that galaxy physics affect the survival of subhaloes (luminous or dark) by generally suppressing the total cumulative abundance of low-mass subhaloes at $z = 0$, regardless of whether they host a luminous galaxy or not (see e.g. Chua et al. 2017 for a recent discussion based on results from the Illustris simulation). However, while different galaxy formation models agree qualitatively on the suppression of subhalo formation and survival, on the shape of the stellar-to-halo mass relation at lower masses, and on the stochasticity of star formation, large quantitative, systematic uncertainties remain across model predictions.

As for observations of MW-like hosts (see Chapter 1.3), searching for the "normal" satellite system of a MW-like host has been an open question for simulations as well. Models for MW-like haloes and their subhalo populations began in dark matter-only simulations (e.g. Aquarius, Springel et al. 2008; Via Lactea II, Diemand et al. 2008; Phat ELVIS, Kelley et al. 2019) and – more recently – have achieved the required numerical resolution to study MW-like galaxies and their abundance of luminous satellite galaxies in cosmological hydrodynamical simulations. So far, these simulations have mostly been performed as zoom-in simulations, focused on either a single or a small sample of MW- or LG-like hosts, with projects such as Latte (Wetzel et al. 2016), FIRE (Hopkins 2014; Hopkins et al. 2018; Garrison-Kimmel et al. 2019), the DC Justice League simulations (Applebaum et al. 2021), or APOSTLE (Fattahi et al. 2016a; Fattahi et al. 2016b; Sawala et al. 2016a). Other projects have managed to take steps towards larger samples: the Auriga simulations are comprised of a suite of 30 isolated MW-like galaxies and their satellite systems (Grand et al. 2017; Simpson et al. 2018), while Font et al. (2021a) have more recently presented satellite abundances of the ARTEMIS simulations, a suite of 45 zoom-in MW-like haloes resimulated with the EAGLE model.

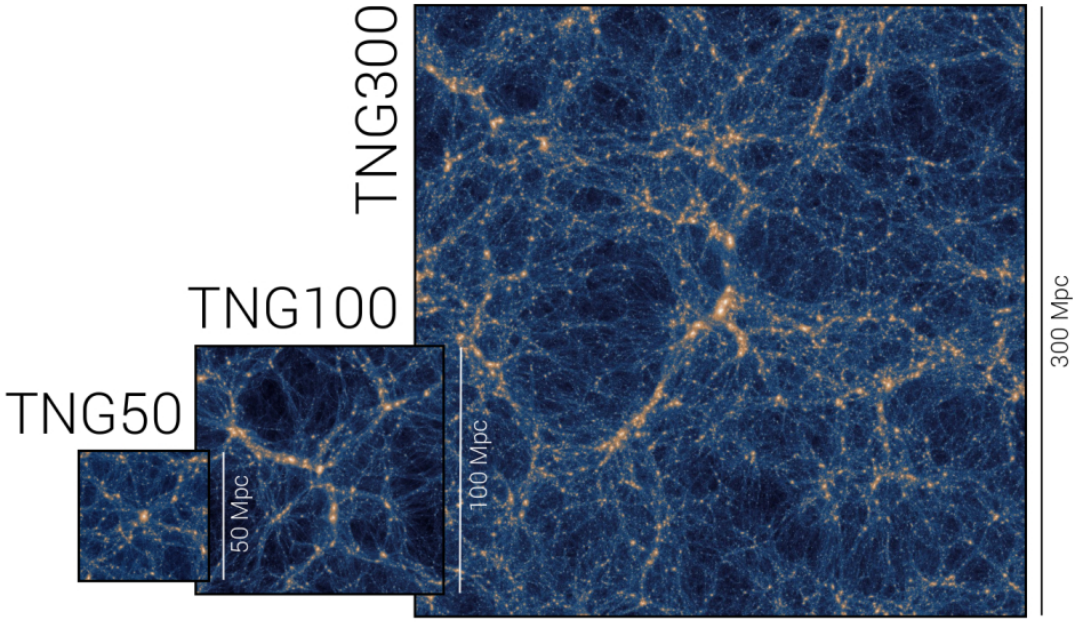

Figure 2.2: The three flagship runs of the IllustrisTNG suite of cosmological magneto-hydrodynamical simulations: TNG50, TNG100, and TNG300. Their names indicate the size of the volume they encompass: $(50\ \mathrm{Mpc})^3$, $(100\ \mathrm{Mpc})^3$, and $(300\ \mathrm{Mpc})^3$, respectively. Each simulation is depicted in projected dark matter density. SOURCE: Nelson et al. (2019b).

2.3 The IllustrisTNG simulations

The results of this thesis are based on data from IllustrisTNG[1], *The Next Generation* suite of state-of-the-art magneto-hydrodynamical cosmological simulations of galaxy formation (Marinacci et al. 2018; Naiman et al. 2018; Nelson et al. 2018a; Pillepich et al. 2018a; Springel et al. 2018; Nelson et al. 2019b; Nelson et al. 2019a; Pillepich et al. 2019). Building on the success of its predecessor Illustris (Genel et al. 2014; Vogelsberger et al. 2014a; Vogelsberger et al. 2014b; Nelson et al. 2015; Sijacki et al. 2015), IllustrisTNG follows the same fundamental approach but includes improved aspects and novel features in its galaxy formation model and expands its scope to several simulated volumes and improved resolution.

The models for galaxy formation include physical processes such as gas heating by a spatially uniform and time-dependent UV background, primordial and metal-line gas cooling, a subgrid model for star formation and the unresolved structure of the interstellar medium (Springel and Hernquist 2003), as well as models for the evolution and chemical enrichment of stellar populations, which track nine elements (H, He, C, N, O, Ne, Mg, Si, Fe) in addition to europium and include yields from supernovae Ia, II, and asymptotic giant branch stars (Vogelsberger et al. 2013; Torrey et al. 2014).

Furthermore, IllustrisTNG incorporates improved feedback implementations for galactic winds caused by supernovae as well as accretion and feedback from black holes. In particular, depending on accretion, black hole feedback occurs in two

[1] http://www.tng-project.org/

Simulation	$L_{\rm box}$ [Mpc]	$N_{\rm DM}$	$m_{\rm DM}$ [$M_\odot$]	$m_{\rm b}$ [$M_\odot$]
TNG300	302.6	2500^3	5.9×10^7	1.1×10^7
TNG100	110.7	1820^3	7.5×10^6	1.4×10^6
TNG50	51.7	2160^3	4.5×10^5	8.5×10^4

Table 2.1: Simulation details for TNG300, TNG100, and TNG50 – the flagship runs of the IllustrisTNG project used in this thesis. Parameters include the side length of the simulation box $L_{\rm box}$, the number of dark matter particles $N_{\rm DM}$, as well as the mass of both dark matter and baryonic particles $m_{\rm DM}$ and $m_{\rm b}$, the latter representing the typical stellar particle mass.

modes: low accretion rates result in purely kinetic feedback, while high accretion rates invoke thermal feedback (Weinberger et al. 2017). Galactic winds are injected isotropically and the wind particles' initial speed scales with the one-dimensional dark matter velocity dispersion (Pillepich et al. 2018b). Magnetic fields are amplified self-consistently from a primordial seed field and follow ideal magnetohydrodynamics (Pakmor and Springel 2013).

The TNG simulations were run using the moving mesh code AREPO (Springel 2010a). Here, concepts from adaptive mesh refinement and smooth particle hydrodynamics are combined to create an unstructured, moving Voronoi tessellation. IllustrisTNG follows the ΛCDM framework, adopting cosmological parameters according to recent constraints from Planck data: matter density $\Omega_{\rm m} = 0.3089$, baryonic density $\Omega_{\rm b} = 0.0486$, cosmological constant $\Omega_\Lambda = 0.6911$, Hubble constant $h = 0.6774$, normalisation $\sigma_8 = 0.8159$, and spectral index $n_{\rm s} = 0.9667$ (Planck Collaboration et al. 2016).

The TNG suite simulates three different cubic volumes with side lengths of approximately 50 Mpc, 100 Mpc, and 300 Mpc, referred to as TNG50, TNG100, TNG300, respectively. While TNG300 has the lowest resolution of the three, its greater volume provides large statistical samples of galaxies and dense environments, including about 270 galaxy clusters exceeding 10^{14} $M_\odot$ (see e.g. Pillepich et al. 2018a, and see Chapters 3.1.1 and 4.1.1 for the definition of cluster/host mass). The intermediate volume TNG100 adopts the same initial conditions as the original Illustris simulation and provides both statistical samples of galaxies in field, groups, and clusters, as well as an adequate mass resolution to study these objects. TNG50 combines a cosmological volume and a statistically significant sample of galaxies and intermediate-mass environments with a zoom-in-like level of mass resolution. (Nelson et al. 2019a; Pillepich et al. 2019). Figure 2.2, taken from Nelson et al. (2019b), illustrates these three simulation volumes side by side in projected dark matter density. Specifics on each simulation are summarised in Table 2.1.

2.3.1 Results of IllustrisTNG

With more than 300 publications making use of data from the IllustrisTNG simulation suite – including TNG300, TNG100, and TNG50, as well as their various lower-resolution runs and dark matter-only analogues – the models adopted in these simulations have been tested against both observations and other simulations. In the following, I give a summary of some of the aspects that have been studied so far.

TNG galaxies exhibit a bimodal colour distribution with a sharp transition from blue to red – predominantly due to the kinetic feedback mode of active galactic nuclei (AGNs) at low accretion rates – that are in quantitative agreement with observations from SDSS (Nelson et al. 2018a). The clustering of both blue and red galaxies over various spatial scales is consistent with observations (Springel et al. 2018). Massive groups and clusters exhibit a realistic stellar mass content distributed between the central galaxy, satellite galaxies, and the diffuse intracluster light (Pillepich et al. 2018a). The simulations produce realistic galaxy sizes and offer insights into the size growth of both quenched and star-forming galaxies (Genel et al. 2018). Furthermore, the abundance of oxygen ions in circumgalactic and intergalactic media, the overall gas-phase mass-metallicity relation at $z < 2$, as well as the metallicity profiles at $z = 0$ and the enrichment histories of TNG galaxy clusters are all in agreement with observations (Nelson et al. 2018b; Torrey et al. 2018; Vogelsberger et al. 2018). The flat circular velocity curves of TNG Milky Way-like galaxies are in good agreement with observational constraints and predict dominating dark matter fractions in their inner regions (Lovell et al. 2018).

Stellar morphologies of star-forming and quenched galaxies – either in synthetic galaxy images or from spheroid-to-total ratios and the concentration of the stellar mass density profiles – are in agreement with observations (Rodriguez-Gomez et al. 2019; Tacchella et al. 2019). Gas stripping phenomena of satellite galaxies in massive groups and clusters can be studied to identify jellyfish galaxies (Yun et al. 2019). The HI content of satellite galaxies as a function of environment is in line with observational surveys of recent years (Stevens et al. 2019). Overall, IllustrisTNG produces a realistic population of quenched galaxies at low, intermediate, and high redshifts (Weinberger et al. 2018; Donnari et al. 2019), however, for proper comparisons it is of the essence to take observational effects and biases into account and to accurately match galaxy and host mass ranges (Donnari et al. 2021a).

The circumgalactic medium around massive hosts emits X-ray signals consistent with observations (Davies et al. 2020; Truong et al. 2020). In the high-resolution run TNG50, an abundance of cold gas structures on scales of kiloparsecs or less can be identified in the circumgalactic medium around elliptical galaxies (Nelson et al. 2020). The evolution of supermassive black holes, central galaxies, and the circumgalactic medium in IllustrisTNG are linked with each other: AGN feedback – especially its low-accretion kinetic mode – effectively ejects gas from the galaxy and prevents it from cooling radiatively and being reaccreted, thereby quenching the galaxy's star formation activity (Zinger et al. 2020). Furthermore, most satellite

galaxies that entered their present-day cluster host with a disky morphology transform to be more elliptical by $z = 0$ due to impulsive tidal shocks that act as gravitational perturbations during pericentric passages (Joshi et al. 2020). A significant fraction of present-day, quenched satellites of groups and clusters actually ceased to form stars in a previous, less-massive group environment as they became subject to pre-processing (Donnari et al. 2021b). The circumgalactic gas of Milky Way- and Andromeda-like galaxies in TNG50 exhibits bubbles, shells, and cavities at X-ray wavelengths, similar to the eROSITA and Fermi bubbles of the observed Milky Way (Pillepich et al. 2021). Finally, TNG50 dwarf galaxies display a large diversity in their cumulative star formation histories over a range of environments, depending on their stellar mass as well as their status as centrals or satellites (Joshi et al. 2021).

Chapter 3

The distinct stellar-to-halo mass relations of satellite and central galaxies

This chapter presents the results of Engler et al. (2021b), *"The distinct stellar-to-halo mass relations of satellite and central galaxies: insights from the IllustrisTNG simulations"*. I examine the stellar-to-halo mass relation (SHMR) across all TNG runs to explore an unprecedented dynamical range of both host and galaxy masses by comparing satellite and central galaxies selected above the same minimum total dynamical mass of $M_{\rm dyn} \geq 10^{10.5}$ M$_\odot$. I focus mostly on $z = 0$ but comment on the redshift evolution of the relations and their galaxy-to-galaxy variations up to $z \sim 2$. Using various environmental parameters, I examine their effects on satellite galaxies in groups and clusters, their locus in the SHMR and the scatter in stellar mass.

This chapter is structured as follows: in Chapter 3.1, I define my selection of galaxies and introduce the parameters I adopt to characterise their environment. I present my results in Chapter 3.2: the SHMR of centrals and satellites, its scatter as a function of dynamical mass, and the influence of various environmental quantities on the SHMR of satellite galaxies. In Chapter 3.3, I discuss the processes that act on satellites after infall into a more massive environment, as well as their transition from the SHMR of centrals. Furthermore, I provide a series of fitting functions for the SHMR in IllustrisTNG and examine the limitations of halo finders and resolution effects, as well as how they affect my results. The results of this chapter are summarised in Chapter 6.1.

3.1 Methods

3.1.1 Galaxy selection and environmental properties

In this chapter, I study galaxies between $z = 0$ and $z = 2$ over a wide range of mass by limiting my sample of galaxies to objects with a total dynamical mass of $M_{\rm dyn} \geq 10^{10.5}$ M$_\odot$. This mass range extends to the dwarf regime without getting into conflict with the simulations' resolution limits. I define dynamical mass as the

sum of all gravitationally bound resolution elements identified by the SUBFIND algorithm (Springel et al. 2001; Dolag et al. 2009, and see Chapter 3.1.2 for more details on my fiducial mass measurements). Within a larger particle group – haloes determined by a friends-of-friends (FoF) algorithm – SUBFIND detects substructures of particles as locally overdense regions that are gravitationally self-bound. The SUBFIND catalogue returns central as well as satellite subhaloes. Centrals are gravitationally bound objects whose position coincides with the centre of FoF haloes, i.e. the minimum of the gravitational potential. This includes both brightest cluster galaxies at the high-mass end, as well as field galaxies at lower masses. Any other SUBFIND objects within a FoF halo are called satellites. A priori, satellite subhaloes may be either dark or luminous (i.e. contain a non-vanishing number of stellar particles, in which case they are called satellite galaxies), and can be members of their parent FoF group regardless of their distance from the centre. In this chapter, I exclusively consider luminous subhaloes (i.e. with at least one stellar particle) and include both centrals and satellites in my sample.

Since I am particularly interested in satellites in groups and clusters, i.e. environments that are expected to leave some sort of imprint on them, I only consider satellite galaxies in hosts of $M_{\rm host} \geq 10^{12}$ $\mathrm{M}_{\odot}$ in the following sections – with hosts being the FoF halo the respective satellite galaxy inhabits. As host mass $M_{\rm host}$, I use its virial mass $M_{\rm 200c}$ – the total mass of a sphere around the FoF halo's centre with a mean density of 200 times the critical density of the universe. Furthermore, I define satellites as only those galaxies found within the virial radius $R_{\rm 200c}$ of their FoF hosts at the time of observation. While this excludes backsplash galaxies – galaxies which are currently located outside the virial radius of the FoF halo after experiencing a first infall and their first pericentric passage – I have verified that their inclusion would not alter my results in a significant manner by using the catalogs from Zinger et al. (2020).

However, not all satellites represent actual galaxies. Some correspond to fragmentations and clumps within other galaxies due to e.g. disk instabilities that SUBFIND identified as independent objects. Since these non-cosmological objects contain little to no dark matter, I only regard subhaloes with a dark matter mass fraction (to total mass, i.e. including stars and gas) of at least 10 per cent in order to remove these clumps (see discussion section 5.2 in Nelson et al. 2019b). Additionally, I require satellites to reside at a cluster-centric distance of at least 0.05 $R_{\rm 200c}$. This way I avoid the innermost host regions, where the identification of subhaloes can become troublesome due to the large density of their surroundings.

At $z = 0$, these selection criteria yield a sample of 62,253 (3,373; 307) satellite galaxies in TNG300 (TNG100; TNG50). However, groups and clusters can act as very different environments. They cover a large range of mass and act differently on satellite galaxies. In order to compare these effects, I further divide the satellites into subsamples according to the virial mass of their host haloes. The demographics of available host haloes and the number of galaxies in each subsample for TNG300,

Host M_{200c}	TNG300	TNG100	TNG50
$10^{12} - 10^{13}$ M$_\odot$	35,464	1,708	183
$10^{13} - 10^{14}$ M$_\odot$	3,453	168	23
$10^{14} - 10^{14.5}$ M$_\odot$	239	11	1
$10^{14.5} - 10^{15.2}$ M$_\odot$	41	3	0

Table 3.1: Number of host haloes in TNG300, TNG100, and TNG50 at z = 0. I divide haloes into bins of virial mass M_{200c} for all simulation volumes to account for lower-mass groups and massive galaxy cluster environments.

Sample	TNG300	TNG100	TNG50
Centrals	624,682	41,824	4,358
Satellites, $M_{200c} \geq 10^{12}$ M$_\odot$	62,258	3,373	307
Satellites, $M_{200c} = 10^{12} - 10^{13}$ M$_\odot$	22,347	1,121	124
Satellites, $M_{200c} = 10^{13} - 10^{14}$ M$_\odot$	24,662	1,367	183
Satellites, $M_{200c} = 10^{14} - 10^{14.5}$ M$_\odot$	9,867	556	40
Satellites, $M_{200c} = 10^{14.5} - 10^{15.2}$ M$_\odot$	5,382	329	0

Table 3.2: Galaxy samples from TNG300, TNG100, and TNG50 at z = 0. This includes centrals (top row) and satellites in group and cluster environments. I study subhaloes with total dynamical masses of $M_{dyn} \geq 10^{10.5}$ M$_\odot$. This limit effectively translates to galaxies with stellar mass of about a few 10^8 M$_\odot$ and above. Satellites are defined as galaxies within their host's virial radius R_{200c}.

TNG100 and TNG50 are summarised in Tables 3.1 and 3.2.

Beyond host mass, I use more specific quantities to assess the immediate environment of satellite galaxies. These are:

1. *Cluster-centric distance:* distance to the central galaxy of the host halo. The gravitational potential and tidal forces grow stronger towards the cluster centre (e.g. Gnedin et al. 1999). Cluster-centric distances are given in units of the host's virial radius.

2. *Infall times:* I use the satellite galaxies' first infall through the virial radius R_{200c} of their present-day host's main progenitor to account for the duration over which they have been subject to environmental effects.

3. *Local luminosity density:* local luminosity density describes the satellites' immediate surroundings and their proximity to other galaxies. I generalise the approach of Sybilska et al. (2017) for a larger range in host mass: for each satellite, I consider other galaxies within a fixed three-dimensional aperture, sum up their *r*-band luminosities and divide by the volume of the sphere. As radius for the aperture I use 10 per cent of the host's virial radius. Furthermore, I only take subhaloes with a stellar mass of at least 10^9 M$_\odot$ (within twice the stellar half-mass radius) into account in order to ensure an appropriate level of resolution for neighbouring galaxies.

Furthermore, I discuss an alternative sample of satellites in Chapters 3.3.1 and 3.3.2 in addition to my fiducial selection. In this case, I do not limit satellite galaxies by their present-day dynamical mass at $z = 0$ but by their peak dynamical mass to all satellites that have ever reached $M_{\mathrm{dyn,\ peak}} \geq 10^{10.5}$ $\mathrm{M}_{\odot}$ throughout their lifetime. This enables me to analyse the impact of environment on the galaxy and halo mass components of present-day satellite populations over an even wider range of masses.

3.1.2 Mass measurements

Throughout this chapter, I compare different operational definitions of a galaxy's stellar mass and total dynamical mass. In either case, I account only for those stellar particles or resolution elements that are labelled as gravitationally bound to a galaxy according to the SUBFIND algorithm. The results presented in this analysis therefore rely on the accuracy of SUBFIND (see e.g. Ayromlou et al. 2019 for a discussion). Other halo finders might return somewhat different mass measurements and I comment on this in Chapter 3.3.5. While I do not expect my qualitative findings to change, quantitative results might be subject to biases. Furthermore, I impose additional 3D radial cuts for mass measurements, which can either represent galaxy-specific structural properties or simply correspond to fixed 3D apertures. It should be noted that I do not employ halo mass descriptors such as $M_{200\mathrm{c}}$ or other spherical-overdensity definitions for my galaxy sample and analysis. Such mass measurements would only work for centrals and would not be meaningful for satellites since the latter merely represent slight enhancements on the overall background density distributions dominated by their underlying cluster or group hosts.

My fiducial choices for galaxy masses read as follows:

- Stellar mass M_{*}: a galaxy's stellar mass is the sum of the mass of all the gravitationally bound stellar particles found within twice the stellar half-mass radius $R^{*}_{1/2}$ from the galaxy centre. While the stellar half-mass radius is calculated from all gravitationally bound stellar particles in the subhalo as identified by SUBFIND, I limit stellar mass in this way since I am specifically interested in the galaxy's main body, not its diffuse outskirts.

- Dynamical mass M_{dyn}: a galaxy's total dynamical mass is the sum of all gravitationally bound resolution elements (dark matter, stellar and black hole particles, gas cells) as identified by SUBFIND.

For other apertures, I follow the approach in Pillepich et al. (2018a) and consider dynamical and stellar masses within 100 pkpc (physical kpc), 30 pkpc, 10 pkpc and 5 pkpc. However, I still only consider particles that are gravitationally bound to the subhalo. I choose these apertures to take different galaxies and their components into consideration: depending on the mass of subhaloes, stellar half-mass radii can range from a few kpc in Milky Way-like haloes to tens of kpc for central galaxies of

group environments. Furthermore, most of the stellar mass of Milky Way-like galaxies is enclosed within 30 kpc – this aperture provides stellar mass estimates roughly comparable with observational measurements within Petrosian radii (Schaye et al. 2015). I include stellar mass measurements in 5 pkpc to account for less massive galaxies in my sample.

Importantly, distinguishing among different mass definitions allows me to characterise how different parts of galaxies are affected by environmental effects such as tidal stripping, and thus how these different mass definitions affect the description and quantification of the stellar-to-halo mass relations for centrals and satellites separately.

Note that unless otherwise stated, I define $M_{\rm dyn}$ as the dynamical mass at the *present day* since I specifically aim to investigate differences of satellite to central galaxies caused by their environment. Other studies have characterised satellite subhalo mass as peak masses, i.e. before they became subject to environmental effects. In this case, most of the differences I find in this chapter comparing the SHMRs of centrals and satellites would be mitigated (e.g. Shi et al. 2020).

In order to account for discrepancies resulting from resolution effects between the three simulation volumes, I rescale stellar mass in both TNG300 and TNG100 to TNG50. Typically, this results in an increase in stellar mass by a factor of $\sim$ 2 ($\sim$ 1.5) in TNG300 (TNG100). However, it reaches up to a factor of a few at the low-mass end. These versions are denoted as rTNG300 and rTNG100, respectively. The rescaling process is described in detail in Appendix A.

3.1.3 Functional form and fit of the stellar-to-halo mass relation

Over the course of this chapter, I quantify the relationship between total dynamical mass $M_{\rm dyn}$ and stellar mass M_* of galaxies by either plotting the latter vs. the former or by plotting their stellar mass fraction – the ratio of stellar to dynamical mass – vs. their dynamical mass. I use the expression stellar-to-halo mass relation (SHMR) for either form and describe the latter version by adopting the parametrization from Moster et al. (2010) and Moster et al. (2013):

$$\frac{M_*}{M_{\rm dyn}} = 2N \left[\left(\frac{M_{\rm dyn}}{M_1} \right)^{-\beta} + \left(\frac{M_{\rm dyn}}{M_1} \right)^{\gamma} \right]^{-1} . \tag{3.1}$$

The four free parameters correspond to the normalisation of the stellar-to-halo mass ratio N, a characteristic mass M_1, and the two slopes at the low- and high-mass ends β and γ. At the characteristic mass M_1, the ratio of stellar and subhalo mass is equal to the normalisation N. I fit this model to the distributions of running medians, as well as the $16^{\rm th}$ and $84^{\rm th}$ percentiles using non-linear least squares minimisation. The fits are applied separately to the SHMRs of centrals and satellites in groups and clusters.

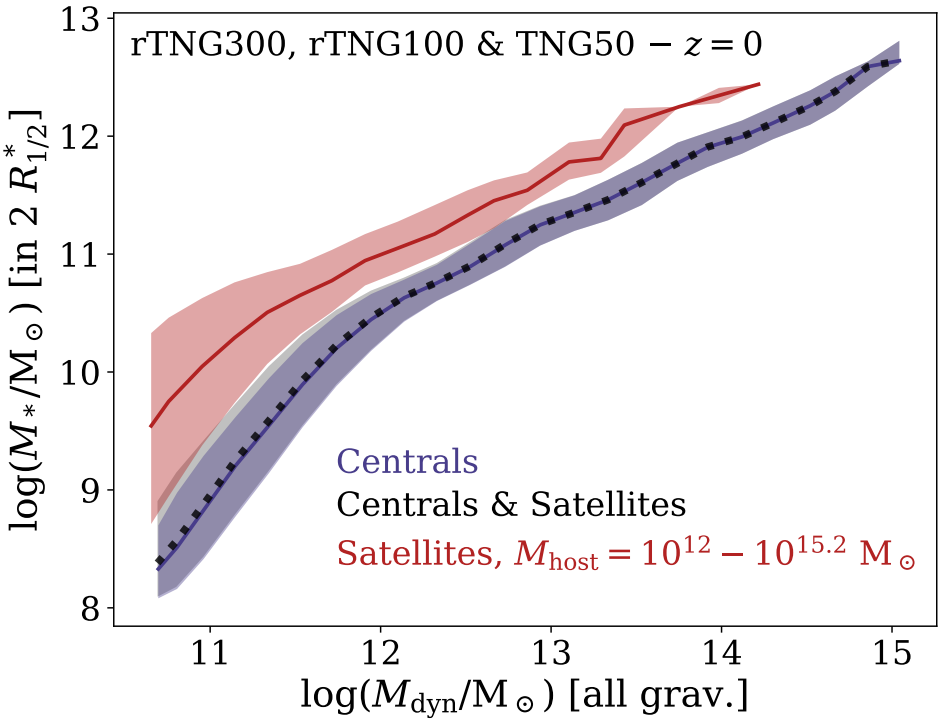

Figure 3.1: Stellar-to-halo mass relation (SHMR) for central and satellite galaxies at z = 0 with total dynamical masses (all gravitationally bound material) of at least $10^{10.5}$ $M_\odot$, combining samples of the rescaled rTNG300 and rTNG100, as well as TNG50 (see text and Appendix A for details). I employ all gravitationally bound material as determined by SUBFIND instead of halo mass as M_{200c} for dynamical mass. Since satellites only correspond to slight enhancements on the overall background density, mass definitions using spherical overdensities would not enable a meaningful comparison between centrals and satellites. Furthermore, dynamical masses are considered *not* at peak mass along each subhalo history but at present-day times, in order to highlight the impact of environmental effects. I present the SHMR as stellar mass as a function of dynamical mass for centrals (solid blue curve), satellites in hosts of $10^{12} - 10^{15.2}$ $M_\odot$ (solid red curve), as well as both centrals and satellites (dotted black curve) at $z = 0$, as medians within bins of 0.5 dex over the range of dynamical masses. Shaded areas denote their scatter as 16$^{\text{th}}$ and 84$^{\text{th}}$ percentiles.

3.2 Results

3.2.1 Stellar-to-halo mass relation at z = 0

In this section, I examine the relationship of total dynamical mass $M_{\rm dyn}$ and stellar mass M_* at $z = 0$, by comparing satellites in groups and clusters with $M_{\rm host} \geq 10^{12}$ $M_\odot$ to central galaxies. Figure 3.1 shows the SHMR of galaxies with $M_{\rm dyn} \geq 10^{10.5}$ $M_\odot$ in TNG50 and the resolution-rescaled rTNG100 and rTNG300 (see Appendix A): centrals (solid blue curve), satellites (solid red curve), as well as both centrals and satellites combined (dotted black curve). I consider masses in my fiducial aperture choice – the sum of all gravitationally bound particles for total dynamical mass and all stellar particles within twice the stellar half-mass radius $R^*_{1/2}$ for stellar mass. There is a systematic offset between central and satellite galaxy populations: at fixed stellar mass, satellites are shifted towards smaller total dynamical mass. Shaded areas show the scatter in the SHMR as 16$^{\text{th}}$ and 84$^{\text{th}}$ percentiles. At all

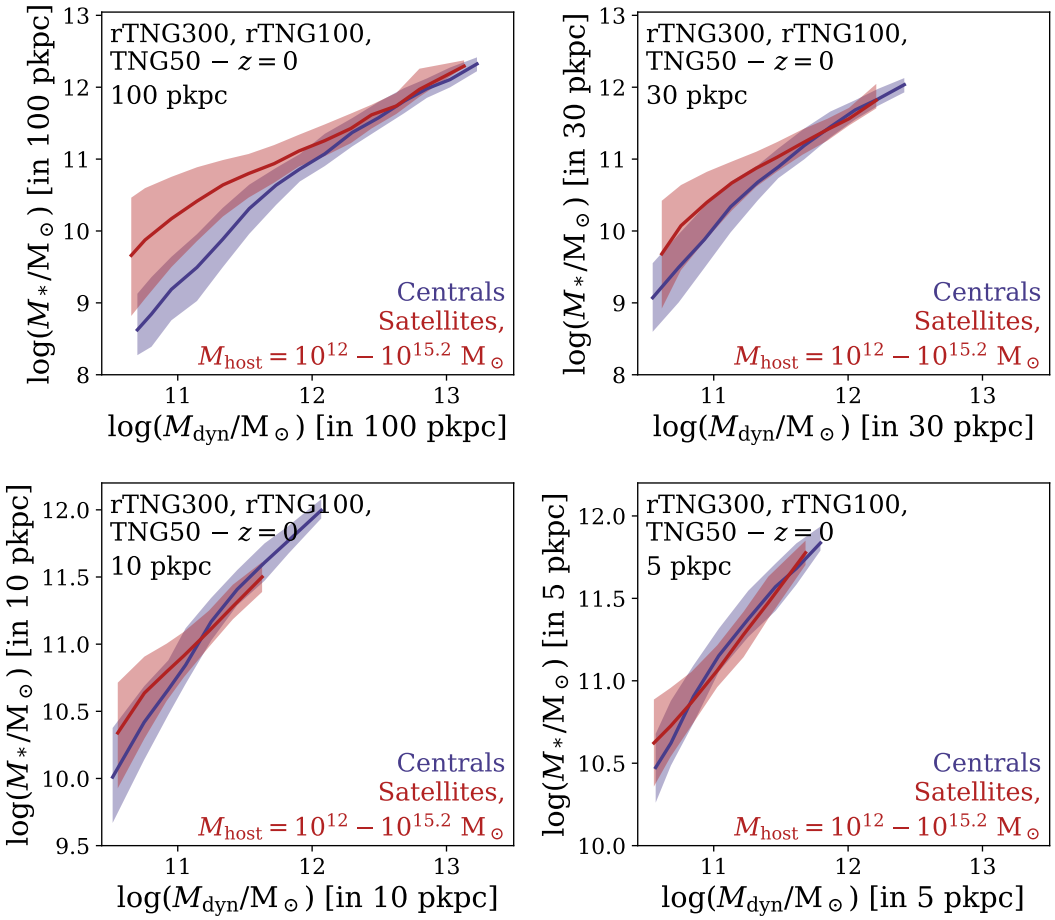

Figure 3.2: As Figure 3.1, SHMR for rTNG300, rTNG100, and TNG50 centrals and satellites at z = 0, however, masses are measured in fixed, physical apertures. In all panels, galaxies are limited to total dynamical masses of at least $10^{10.5}$ $M_\odot$. I present the SHMR as stellar mass as a function of dynamical mass for centrals (solid blue curve), as well as satellites in hosts of $10^{12} - 10^{15.2}$ $M_\odot$ (solid red curve) as medians within bins of 0.5 dex over the range of dynamical masses. Shaded areas denote their scatter as 16th and 84th percentiles. Both dynamical mass and stellar mass are measured in fixed, physical apertures: 100 pkpc (top left panel), 30 pkpc (top right panel), 10 pkpc (bottom left panel), and 5 pkpc (bottom right panel).

dynamical masses, satellites exhibit a larger scatter than centrals, increasing towards the lower mass end.

Additionally, I present combinations of fixed physical apertures in Figure 3.2. Here, both stellar and subhalo mass are confined to the innermost 100 pkpc (physical kpc), 50 pkpc, 10 pkpc and 5 pkpc (from top left to bottom right). Measuring stellar and dynamical masses within fixed physical apertures shows a similar offset for the largest aperture of 100 pkpc. However, the offset between satellites and centrals at the high-mass end is less pronounced than for my fiducial apertures. While 100 pkpc still encompass all gravitationally bound particles in low- and intermediate-mass subhaloes, the upper limit of dynamical mass shifts to a lower value compared to the SHMR in my fiducial aperture choice. Since the dark matter subhalo is more extended than the galaxy's stellar body, this affects the total dynamical mass to a

larger degree than the stellar mass. When the SHMR is examined for progressively smaller apertures, the offset between centrals and satellites becomes less significant over the whole range of dynamical mass – albeit to a lesser degree towards the low-mass end for larger apertures. Environmental effects that cause this offset between the SHMRs of centrals and satellites affect galaxies in an outside-in fashion. Since the inner galaxy regions remain largely unaffected by their environment, the offset between the SHMRs of centrals and satellites decreases when constraining galaxy and subhalo mass to smaller apertures.

3.2.2 Dependence on host mass and redshift

I examine the separation of satellite galaxies more closely in the top panel of Figure 3.3. Here, satellite galaxies of rTNG300, rTNG100, and TNG50 are split into subsamples according to their $z = 0$ host mass: $10^{12} - 10^{13}$ $M_\odot$, $10^{13} - 10^{14}$ $M_\odot$, $10^{14} - 10^{14.5}$ $M_\odot$, and $10^{14.5} - 10^{15.2}$ $M_\odot$. The most massive host mass bin includes exclusively rTNG300 satellites, while the other three bins consist of satellites from rTNG300, rTNG100, and TNG50.

The SHMR is shown as fits to the average distribution of stellar mass fractions at a given dynamical mass for centrals and the four satellite subsamples, following the fitting function in Chapter 3.1.3. I fit Equation (3.1) to the distributions of running medians (solid curves), as well as their 16^{th} and 84^{th} percentiles (dotted curves) to illustrate the differences in scatter between centrals and satellites in groups and clusters.

The SHMR of satellite galaxies generally shows a large offset from the SHMR of centrals, with satellite subhaloes exhibiting larger stellar mass fractions over the whole range of dynamical mass. Measured at the peak of the relation, this offset ranges from stellar mass fractions of about 10 per cent for satellites in $10^{12} - 10^{13}$ $M_\odot$ hosts to 15 per cent in hosts of $10^{14.5} - 10^{15.2}$ $M_\odot$.

While there is a trend with host mass – satellites in more massive hosts tend to have larger median stellar mass fractions at fixed dynamical mass – this correlation is even more pronounced when considering the relation's scatter. While the distribution of 16^{th} percentiles practically shows the same basic offset from the SHMR of centrals for all satellites, the 84^{th} percentiles of SHMRs increase more significantly than the average median relation. Satellites in more massive environments can reach larger stellar mass fractions: up to 28 per cent in hosts of $10^{12} - 10^{13}$ $M_\odot$ or $50 - 60$ per cent in hosts of $10^{13} - 10^{15.2}$ $M_\odot$ at the peak of 84^{th} percentiles. On the other hand, the maximum stellar mass fraction for the 84^{th} percentiles of central galaxies only reaches $2 - 4$ per cent. The fit parameters of the four samples' median SHMRs are summarised in Table 3.3. Although it is not shown here, the same trends hold for general baryonic-to-total mass ratios as well, considering the contributions of both stars and gas. It should be emphasised that the SHMRs for satellites in $10^{14} - 10^{14.5}$ $M_\odot$ and $10^{14.5} - 10^{15.2}$ $M_\odot$ hosts represent lower limits due to effects of numerical resolution: the rescaling process for stellar masses of satellites

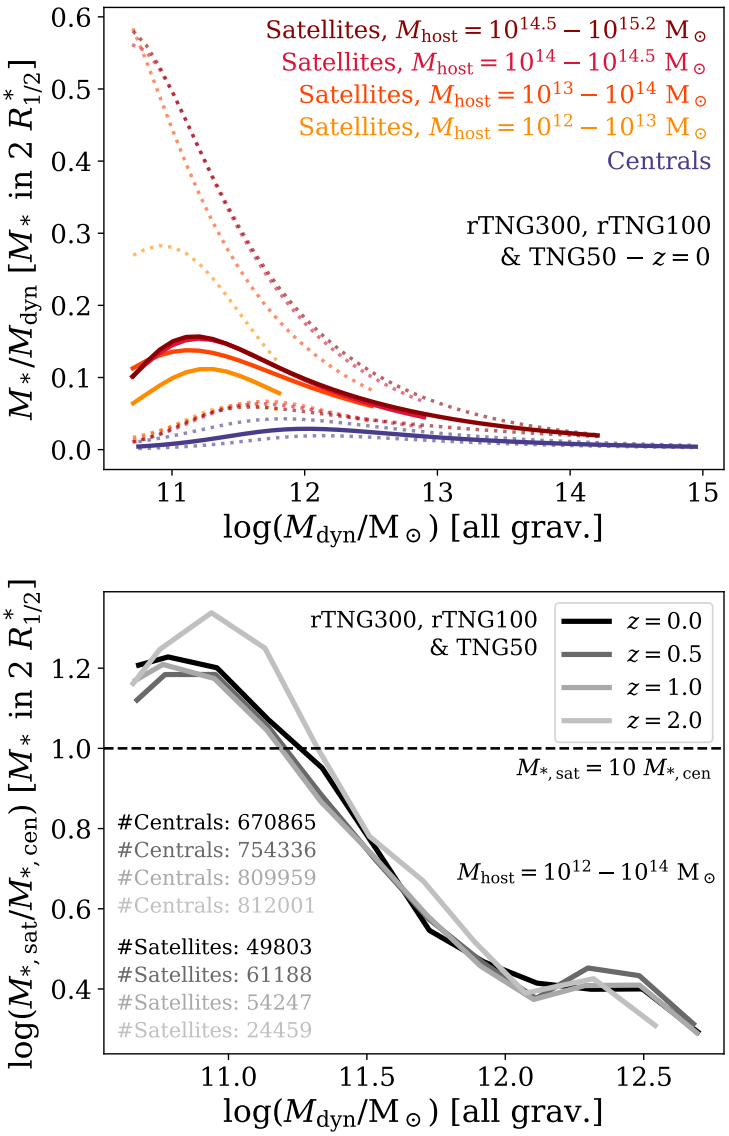

Figure 3.3: Stellar-to-halo mass relation for central and satellite galaxies with total dynamical masses of at least $10^{10.5}$ M$_\odot$ from rTNG300, rTNG100, and TNG50 as a function of host mass and redshift. *Top panel:* SHMR for centrals and subsamples of satellites within fiducial apertures at $z = 0$. Satellites are divided by host mass into bins of $10^{12} - 10^{13}$ M$_\odot$, $10^{13} - 10^{14}$ M$_\odot$, $10^{14} - 10^{14.5}$ M$_\odot$, and $10^{14.5} - 10^{15.2}$ M$_\odot$ (orange to dark red, solid curves). The most massive host mass bin includes only rTNG300 galaxies, while the others combine galaxies from rTNG300, rTNG100 and TNG50. Relations are shown as fits to the running medians of stellar mass fractions $M_*/M_{\rm dyn}$ within bins of 0.7 dex (solid curves). Dotted curves correspond to fits to their 16$^{\rm th}$ and 84$^{\rm th}$ percentiles. *Bottom panel:* Stellar mass ratios of satellite to central galaxies in rTNG300, rTNG100 and TNG50 as a function of dynamical mass at $z = 0.0$, 0.5, 1.0, 2.0 (black to light grey curves). I limit satellites to hosts of $10^{12} - 10^{14}$ M$_\odot$, since TNG50 does not include haloes with $> 10^{14}$ M$_\odot$ at earlier redshifts.

Sample	N	$M_1[\log \mathrm{M}_\odot]$	β	γ
Centrals	0.0258 ± 0.0003	11.70 ± 0.02	28.6 ± 0.8	10.4 ± 0.2
Sats., $M_{\mathrm{host}} = 10^{12-13}\,\mathrm{M}_\odot$	0.108 ± 0.003	11.12 ± 0.06	27.5 ± 2.9	15.6 ± 1.7
Sats., $M_{\mathrm{host}} = 10^{13-14}\,\mathrm{M}_\odot$	0.127 ± 0.008	10.85 ± 0.11	23.6 ± 6.1	10.1 ± 1.3
Sats., $M_{\mathrm{host}} = 10^{14-14.5}\,\mathrm{M}_\odot$	0.137 ± 0.004	10.93 ± 0.04	30.5 ± 3.6	10.9 ± 0.6
Sats., $M_{\mathrm{host}} = 10^{14.5-15.2}\,\mathrm{M}_\odot$	0.129 ± 0.006	10.85 ± 0.04	38.6 ± 7.2	9.5 ± 0.7

Table 3.3: Fit parameters for the median SHMRs of centrals and satellites as a function of host mass depicted in the top panel of Figure 3.3 using rTNG300, rTNG100, and TNG50. I follow the parametrization in Equation (3.1) (Moster et al. 2010; Moster et al. 2013): normalisation N, characteristic mass M_1, and the slopes at the low- and high-mass ends β and γ.

in hosts of $10^{14} - 10^{15.2}\,\mathrm{M}_\odot$ relies on only one massive cluster in TNG50 with a mass of $10^{14.3}\,\mathrm{M}_\odot$. Therefore, the SHMRs of satellites within hosts of this mass range may in reality be shifted to even larger stellar mass fractions.

In the bottom panel of Figure 3.3, I show the stellar mass ratio of satellites and centrals in rTNG300, rTNG100, and TNG50 as a function of total dynamical mass and its evolution with time. However, I only consider satellites in hosts of $10^{12} - 10^{14}\,\mathrm{M}_\odot$, since TNG50 does not include $10^{14}\,\mathrm{M}_\odot$ haloes at $z = 0.5$ and earlier redshifts. At all redshifts considered ($z = 0,\ 0.5,\ 1,\ 2$; black to light grey curves), the samples include tens of thousands of satellites and hundreds of thousands of centrals. At fixed dynamical mass, the stellar mass of satellites exhibits a significant difference to those of centrals – larger by a factor of at least 2.5 at $z = 0$. This increases substantially for subhaloes with $M_{\mathrm{dyn}} < 10^{12}\,\mathrm{M}_\odot$ – around which satellite subhaloes reach peak baryonic conversion efficiency – and reaches its maximum at the samples' dynamical mass limit of $10^{10.5}\,\mathrm{M}_\odot$. Here, satellites are more massive in stars than centrals by a factor of 16 at $z = 0$, $z = 0.5$, and $z = 1$, as well as a factor of 22 at $z = 2$. However, there is no statistically significant difference in the ratios of stellar mass between satellites and centrals from $z = 0$ to $z = 2$. Satellites already exhibit an offset in stellar mass at fixed dynamical mass as compared to those of centrals at early times: since the density profiles of both satellites and host environments stay on average similar between $z = 2$ and $z = 0$, tidal stripping in the host halo's gravitational potential operates – for satellites of a given dynamical mass – to the same degree at different redshifts.

3.2.3 Scatter in the stellar-to-halo mass relation

The environment affects the dark matter subhalo and the stellar body of a galaxy to a different degree, which results not only in an offset between centrals and satellites in groups and clusters in the SHMR but also in different scatter along the relation. In this section, I examine the scatter in stellar mass σ_* as a function of total dynamical mass and the ways in which the environment shapes it. I determine the stellar mass scatter by defining bins of fixed dynamical mass and by computing the

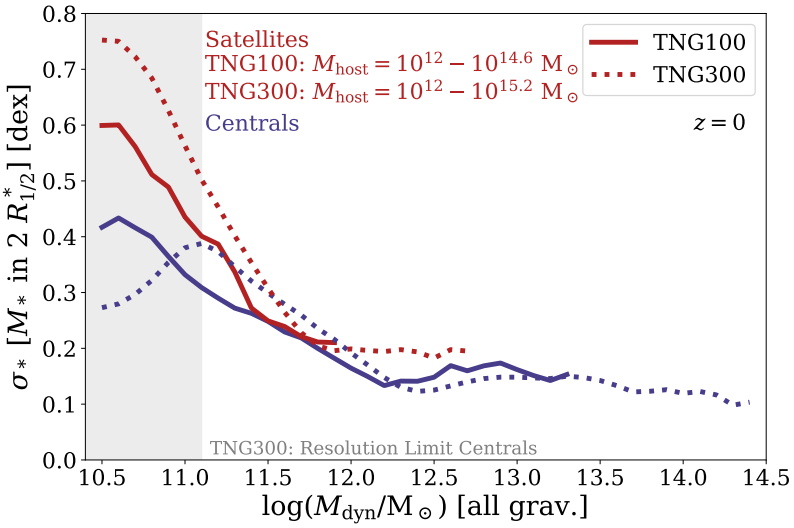

Figure 3.4: Scatter in (logarithmic) stellar mass σ_* as a function of total dynamical mass for centrals (blue curves) and satellites (red curves) in TNG100 (solid curves) and TNG300 (dotted curves). The grey area denotes the resolution limit in which the sample of centrals in TNG300 includes galaxies with only a single stellar particle and the distribution of stellar mass is no longer fully sampled.

standard deviation of the distribution of logarithmic stellar mass within. These distributions correspond approximately to Gaussians (for non-logarithmic masses this corresponds to a lognormal distribution, see also Anbajagane et al. 2020).

Figure 3.4 shows the scatter as a function of total dynamical mass for all centrals (blue curves) and satellites (red curves) in hosts of $10^{12} - 10^{14.6}$ M$_\odot$ in TNG100 (solid curves) as well as hosts of $10^{12} - 10^{15.2}$ M$_\odot$ in TNG300 (dotted curves). However, the low-mass end of TNG300 centrals reaches the resolution limit (grey area): here, the sample of centrals starts to include galaxies with only a single stellar particle and the SHMR's scatter is no longer fully sampled. Since the distribution of stellar mass within fixed dynamical mass bins is incomplete the scatter decreases. In both simulations, there is a significant offset between centrals and satellites in groups and clusters. The scatter of centrals and satellites increases towards lower dynamical masses to up to 0.43 dex for centrals and 0.60 dex for satellites in TNG100, as well as 0.38 dex for centrals and 0.77 dex for satellites in TNG300. Considered at the respective peak scatter of centrals, this results in an offset of 0.17 dex at $M_{\rm dyn} = 10^{10.6}$ M$_\odot$ for satellites in TNG100 and 0.12 dex at $M_{\rm dyn} = 10^{11.1}$ M$_\odot$ for satellites in TNG300. For TNG100, this dynamical mass yields an offset of only 0.1 dex.

As galaxies become less massive, the scatter increases for both centrals and satellites. While this effect is mainly driven by different assembly histories for centrals, it is even more pronounced for low-mass satellites as they become less resistant to their environment. For intermediate- to high-mass subhaloes ($M_{\rm dyn} \gtrsim 10^{12}$ M$_\odot$ for centrals, $M_{\rm dyn} \gtrsim 10^{11.5}$ M$_\odot$ for satellites) the scatter becomes constant around a value of $\sigma_* \sim 0.2$ dex for satellites and $\sigma_* \sim 0.15$ dex for centrals in both TNG100 and TNG300. For both centrals and satellites, constant scatter sets in for subhaloes that

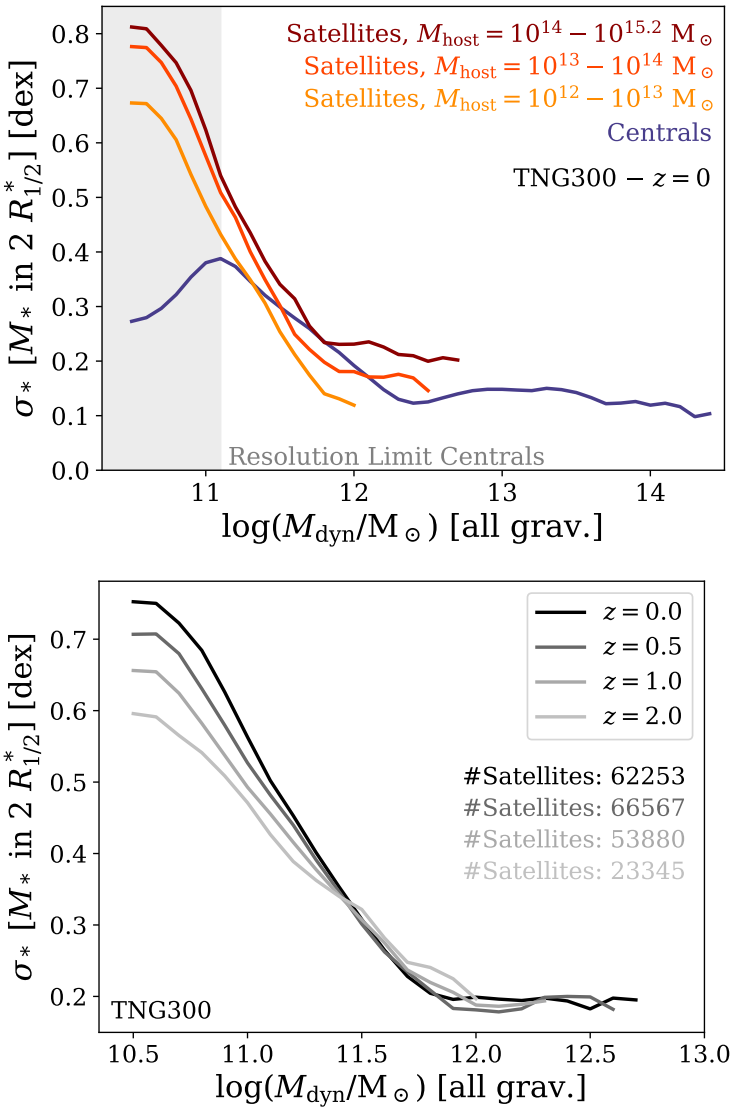

Figure 3.5: Scatter in stellar mass as a function of host mass and redshift. *Top panel:* Scatter in (logarithmic) stellar mass σ_* as a function of total dynamical mass in TNG300 for centrals (blue curve) and satellites in different bins of host mass (orange to red curves). *Bottom panel:* Stellar mass scatter σ_* of satellites in hosts of at least 10^{12} M$_\odot$ as a function of dynamical satellite mass at different redshifts: $z = 0.0,\ 0.5,\ 1.0,\ 2.0$ (black to light grey curves).

correspond to the SHMR's peak – subhaloes of peak star formation efficiency – and continues to their respective high mass ends.

Dependence of scatter on host mass and redshift

I examine the effects of group and cluster environments separately in the top panel of Figure 3.5 by splitting TNG300 satellite galaxies by their host mass. Over the whole range of dynamical mass, there is a continuous offset between satellites in different hosts. Satellites in hosts of $10^{14} - 10^{15.2}$ $M_\odot$ and $10^{13} - 10^{14}$ $M_\odot$ show the largest scatter of up to 0.8 dex while satellites in $10^{12} - 10^{13}$ $M_\odot$ hosts reach up to 0.7 dex. However, even satellites in less massive hosts already exhibit a significant difference to the centrals' relation. At a dynamical mass of $10^{11.1}$ $M_\odot$ – corresponding to the peak scatter of centrals – satellites show an offset of 0.15 dex, 0.12 dex, and 0.05 dex (in decreasing host mass bins) compared to centrals of the same mass. For all satellites, the scatter in stellar mass becomes constant around their respective subhalo mass of peak star formation efficiency. The offset between satellites in more and less massive hosts remains constant at the high subhalo mass end with satellites in $10^{12} - 10^{13}$ $M_\odot$ hosts settling around a scatter of 0.14 dex – similar to the scatter of centrals.

The bottom panel of Figure 3.5 shows the time evolution of the scatter σ_* for satellite galaxies in TNG300. This includes several tens of thousands of satellites each redshift considered ($z = 0,\ 0.5,\ 1,\ 2$). At all redshifts, the scatter of satellites at the massive dynamical mass end with $M_{\rm dyn} \gtrsim 10^{12}$ $M_\odot$ is roughly constant at $\sigma_* \sim 0.2$ dex. However, for lower-mass satellites, there is a slight, albeit clear trend of decreasing scatter with increasing redshift: while the scatter reaches up to 0.77 dex at $z = 0$, this peak value decreases continuously to 0.72 dex at $z = 0.5$, 0.67 dex at $z = 1$, and 0.61 dex at $z = 2$. Although my satellite sample shows no trend in its average SHMR at different times (see Figure 3.3), the scatter of stellar mass at fixed dynamical mass builds up over time. The scatter in the SHMR of centrals, on the other hand, only shows a slight increase in scatter with increasing redshift, consistent with the findings of Pillepich et al. (2018a).

3.2.4 Dependence on environment and accretion history

In this section, I investigate the connection of satellites and their environment more closely. Since host mass is not the only property that describes a galaxy's environment, I employ cluster-centric distance to account for the varying strength of cluster potentials, infall times to account for the period over which satellites have been exposed to environmental influence, and a local luminosity density to account for the immediate surroundings of satellites. Infall times correspond to the first time satellites crossed the virial radius of their present-day host halo's main progenitor (see Chapter 3.1.1 for details).

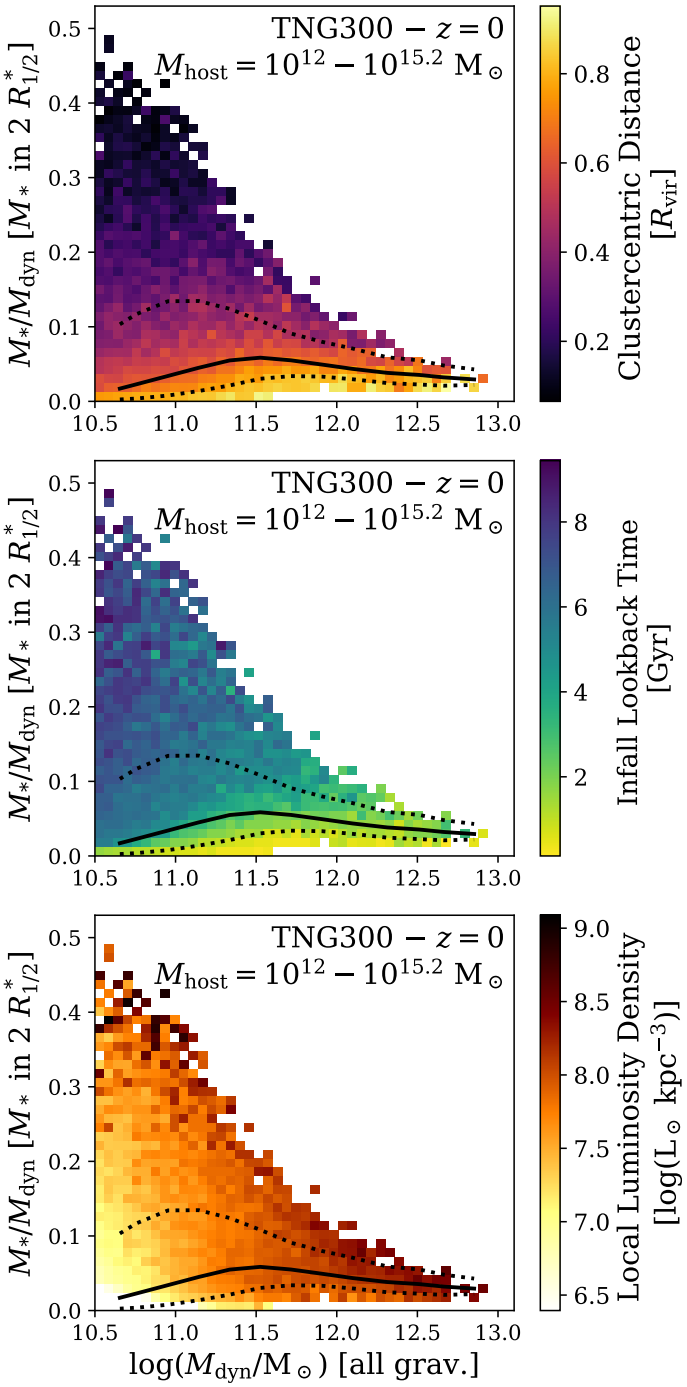

Figure 3.6: Satellite stellar-to-halo mass relation as a function of environment in TNG300. Satellite galaxies are located in hosts of at least 10^{12} $M_\odot$ at $z = 0$. I divide the SHMR into 2D bins and colour-code bins that contain at least five satellites by their median value of cluster-centric distance (top panel), lookback time to the first infall into the virial radius of the satellites' present-day host halo (middle panel), and local luminosity density for galaxies within 0.1 $R_{\rm vir}$ (bottom panel). Solid black curves show the medians in bins of total dynamical mass with width 0.5 dex, dotted curves correspond to 16$^{\rm th}$ and 84$^{\rm th}$ percentiles.

Figure 3.6 illustrates the SHMR of satellites in hosts of at least 10^{12} $M_\odot$ as a function of said environmental properties in TNG300. Bins including at least five satellites are colour-coded by their respective median values of cluster-centric distance (top panel), time of infall into their present-day host's virial radius (middle panel), and local luminosity density (bottom panel). I show results from TNG300 (without resolution correction) as I am focusing on qualitative effects.

At fixed dynamical mass, galaxies with larger stellar mass fractions reside on average closer to the cluster centre (where the host halo's gravitational potential is deeper), experienced an early infall into the virial radius of their present-day host, and are located in areas of higher local density. Lower stellar mass fraction satellites, on the other hand, reside at higher cluster-centric distances, fell later into their present-day environment, and inhabit regions of lower density. They have been exposed to weaker environmental effects for a shorter amount of time – and are closer to the distribution of central galaxies in the SHMR. However, there is an additional bias with dynamical mass for local luminosity density since more massive subhaloes host more luminous objects. At the high dynamical mass end, the correlation of stellar mass fractions with local density becomes less pronounced. Black curves correspond to the average SHMR (solid curves) as well as to the 16^{th} and 84^{th} percentiles (dotted curves) of the satellites. Only a small fraction of satellites contributes to the high stellar mass fraction tail, which can reach up to 50 per cent at the low dynamical mass end.

I quantify the differences between satellite subpopulations in Figure 3.7 and show the SHMR as a function of environment for TNG300 satellites at $z = 0$ in three bins of host mass: $10^{12} - 10^{13}$ $M_\odot$, $10^{13} - 10^{14}$ $M_\odot$, and $10^{14} - 10^{15.2}$ $M_\odot$ (from left to right columns). At a given dynamical mass, I divide the satellites into four quartiles with respect to each environmental quantity and fit the model in Equation (3.1) to the resulting SHMRs. Thus I am able to examine the relations of low and high cluster-centric distance populations (magenta/orange curves), early and late infallers (depending on host mass with respect to $2.5 - 4$ Gyr ago; blue/green curves), as well as satellites in low and high luminosity density environments separately (yellow/brown curves). Furthermore, I include the average SHMR of centrals (solid grey curves), as well as their 16^{th} and 84^{th} percentiles (dotted grey curves).

Clearly, the SHMR of satellite galaxies correlates with their environment, with the overall scatter and the offsets of the respective quartiles (low cluster-centric distance, early infall, high local luminosity density) increasing significantly with host mass. For all hosts and all environmental parameters, even the satellite subsamples that are subject to a weaker influence by their environment (i.e. high cluster-centric distance, late infall, low local density) already feature a significant offset from the centrals' SHMR. Peak stellar mass fractions range from 3 per cent for late-infall satellites in both $10^{14} - 10^{15.2}$ $M_\odot$ and $10^{12} - 10^{13}$ $M_\odot$ hosts to 4 per cent for satellites in low luminosity density areas of $10^{13} - 10^{14}$ $M_\odot$ hosts. On the other hand, satellites that have been subject to stronger environmental effects (i.e. low cluster-centric

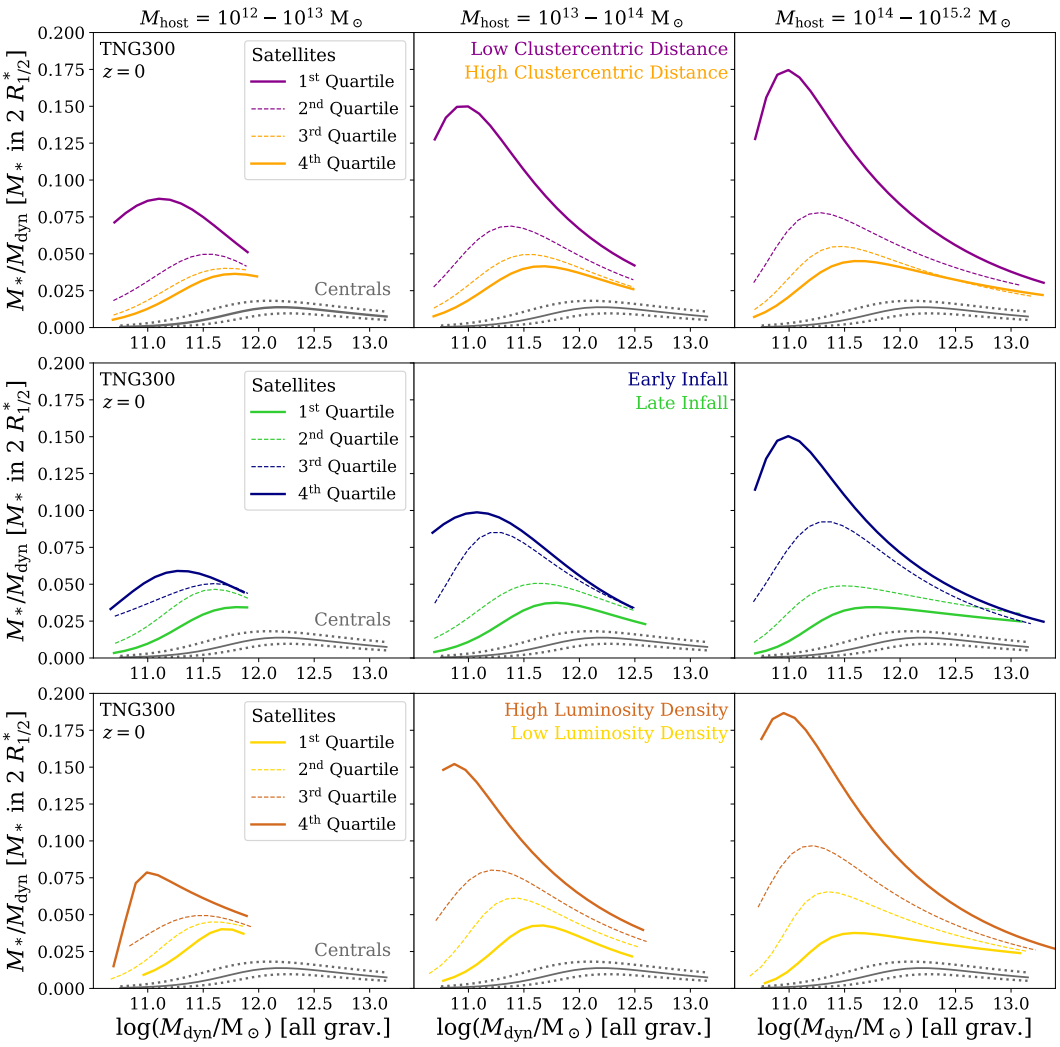

Figure 3.7: Stellar-to-halo mass relation as a function of environment and host mass in TNG300 at z = 0. Each row depicts a different environmental parameter: cluster-centric distance, infall time into the current host's virial radius, and local luminosity density (from top to bottom). Each column corresponds to a different host mass range: $10^{12} - 10^{13}$ M$_\odot$, $10^{13} - 10^{14}$ M$_\odot$, $10^{14} - 10^{15.2}$ M$_\odot$ (from left to right). Satellite galaxies are split into quartiles of low/high cluster-centric distance (purple/orange), early/late infall (blue/green), as well as low/high local luminosity density (yellow/brown) within bins of total dynamical mass with width 0.7 dex. Solid curves correspond to first and fourth quartiles, dashed curves to second and third quartiles. Grey lines depict the SHMR of central galaxies as fits to their running medians (solid curves) as well as 16$^{\rm th}$ and 84$^{\rm th}$ percentiles (dotted curves) to account for scatter in the relation.

distance, early infall, high local density) clearly exhibit even larger offsets from the SHMR of centrals, increasing with host mass. Their SHMRs reach peak stellar mass fractions ranging from 6 per cent for early infallers in $10^{12} - 10^{13}$ $M_\odot$ hosts to up to 18 per cent for satellites in high luminosity density regions of $10^{14} - 10^{15.2}$ $M_\odot$ hosts. While local luminosity density serves as a reasonable estimate of environmental impact in massive clusters of $10^{14} - 10^{15.2}$ $M_\odot$, these trends appear less regular in lower mass groups and more sparsely populated environments.

3.3 Interpretation, tools, and discussion

3.3.1 Transition of satellite galaxies: tidal mass loss vs. quenching

The offset between the SHMRs of centrals and satellites can be attributed – for the most part – to tidal stripping of satellites in interactions with the host halo's gravitational potential and the loss of their dark matter subhalo. Figure 3.8 illustrates the effects of environment on total dynamical mass as well as the stellar and dark matter components of TNG100 satellites over time. I show the ratio of their masses between $z = 0$ and their first infall into the virial radius of their present-day host's main progenitor for stellar (orange), dark matter (black), and total dynamical mass (grey) in my fiducial aperture choice (all gravitationally bound particles for $M_{\rm dyn}$ and $M_{\rm DM}$, all stellar particles within two stellar half-mass radii for M_*). Furthermore, satellites are divided by the mass of their host into bins of $10^{12} - 10^{13}$ $M_\odot$, $10^{13} - 10^{14}$ $M_\odot$, and $10^{14} - 10^{14.6}$ $M_\odot$ (increasing from left to right), as well as divided by their stellar mass in bins of $10^{9} - 10^{9.5}$ $M_\odot$, $10^{9.5} - 10^{10}$ $M_\odot$, $10^{10} - 10^{10.5}$ $M_\odot$, and $10^{10.5} - 10^{11}$ $M_\odot$ (from top to bottom). I show the mass ratios for two different samples of satellite galaxies: my fiducial satellite selection with present-day dynamical masses of $M_{\rm dyn,\ z=0} \geq 10^{10.5}$ $M_\odot$ (empty histograms), and satellites that reached a peak dynamical mass of $M_{\rm dyn,\ peak} \geq 10^{10.5}$ $M_\odot$ at some point throughout their lifetime (filled histograms). So the latter sample additionally includes satellite galaxies with present-day dynamical masses of less than $10^{10.5}$ $M_\odot$.

For the most part, the mass ratios of dark matter and total dynamical mass coincide with each other. Their distributions show almost exclusively mass ratios smaller than unity, corresponding to a net mass loss due to tidal stripping of the satellites' dark matter subhaloes – regardless of stellar mass or host mass bins. While it appears as if galaxies of larger stellar mass are subject to a stronger degree of tidal stripping of dark matter and total mass for my fiducial sample in the empty histograms, the higher mass loss tails are actually restricted by my initial subhalo selection of $M_{\rm dyn} \geq 10^{10.5}$ $M_\odot$. The tidal mass loss tails of my alternative sample in the filled histograms, which include less massive satellites, all have a similar extent irrespective of satellite stellar mass. For larger satellite stellar masses in the bottom panels, the distributions of dark matter and dynamical mass ratios of both satellite

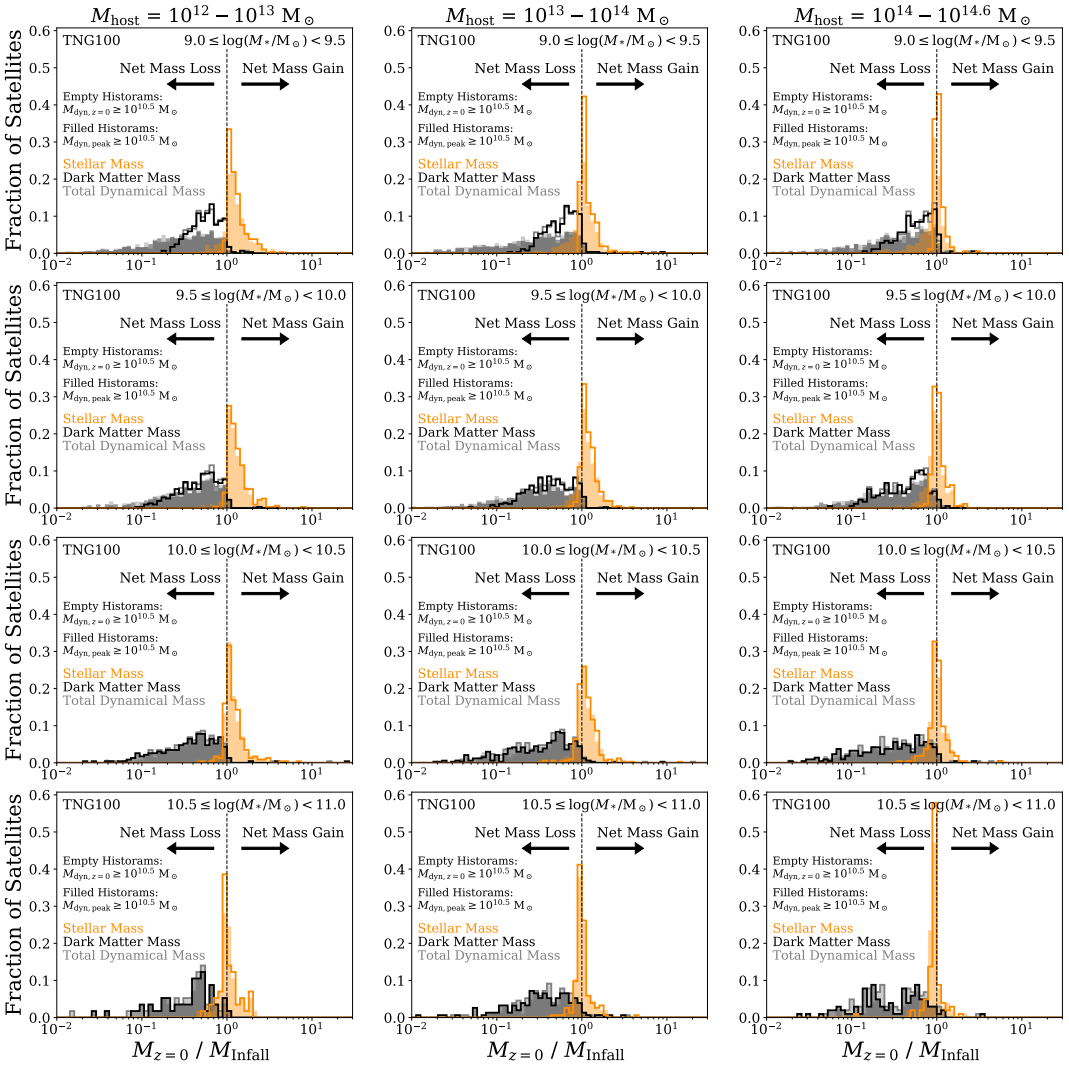

Figure 3.8: Ratios of satellite mass between z = 0 and first infall for satellite galaxies in TNG100. I define infall as the first time a satellite crosses the virial radius $R_{\rm 200c}$ of its present-day host. Mass ratios are shown for stellar (orange), dark matter (black) and total dynamical mass (grey) in my fiducial aperture choice: all gravitationally bound particles for total dynamical and dark matter mass as well as all stellar particles within two stellar half-mass radii for stellar mass. I show the distributions as a function of host mass across columns and satellite stellar mass across rows: $10^{12} - 10^{13}$ M$_\odot$, $10^{13} - 10^{14}$ M$_\odot$, and $10^{14} - 10^{14.6}$ M$_\odot$ in host mass (from left to right), as well as $10^{9} - 10^{9.5}$ M$_\odot$, $10^{9.5} - 10^{10}$ M$_\odot$, $10^{10} - 10^{10.5}$ M$_\odot$, and $10^{10.5} - 10^{11}$ M$_\odot$ in satellite stellar mass (from top to bottom). In addition to my fiducial satellite selection with present-day dynamical masses of $M_{\rm dyn,\,z=0} \geq 10^{10.5}$ M$_\odot$ (empty histograms), I show the mass ratios for all surviving satellites that reached a peak dynamical mass of $M_{\rm dyn,\,peak} \geq 10^{10.5}$ M$_\odot$ at some point in their lifetime (filled histograms).

samples coincide with each other. In these cases, tidal stripping did not put satellites in the original selection below my selection limit.

The evolution of the satellites' stellar mass component after infall is dominated by star formation. Most satellites show a net mass gain in stellar mass with mass ratios greater than unity. However, satellites in the most massive stellar mass bin exhibit peak ratios below unity. Black hole feedback might have already quenched these galaxies, thereby removing their ability to add new stars. Stellar mass loss can then occur either due to stellar evolution or tidal stripping. Furthermore, there is a clear shift with host mass: surviving satellites in more massive hosts are prone to lose parts of their stellar mass more easily. In cluster environments of $10^{14} - 10^{14.6}$ $M_\odot$ roughly 40 to 50 per cent of satellites show a net mass loss in their stellar mass components. However, since I only consider surviving satellites, those in less massive hosts that lost a larger fraction of their stellar mass since infall might simply have been disrupted. Satellites in more massive hosts, on the other hand, can be more massive themselves and can therefore lose a larger fraction of their stellar mass without falling beneath sample or resolution limits. Similar trends also hold for the alternative sample of surviving satellites that were selected using their peak dynamical mass.

This picture is consistent with results from literature: Smith et al. (2013) study the onset of stellar stripping. Using simulations of galaxies interacting with the gravitational potential of a Virgo-like cluster, they examine the remains of dark matter subhaloes at the point when 10 per cent of the satellites' stellar mass has been stripped. Comparing various galaxy models, the loss of stellar mass set in only after 15 to 20 per cent of the bound dark matter fraction was left.

Smith et al. (2016) follow these results up by investigating tidal stripping of dark matter and stellar mass of low-mass satellites in high-resolution cosmological hydrodynamical simulations. While losing 70 per cent of dark matter to interactions with the cluster potential, the stellar component remains unaffected. By the time the satellite has been stripped of 84 per cent of its dark matter, only 10 per cent of its stellar mass has been removed. As the dark matter subhalo has a larger extent compared to the galaxy itself, it is stripped first. Comparing stellar-to-halo size-ratios and mass loss for extended and concentrated galaxies, both Smith et al. (2016) and Chang et al. (2013) find concentrated galaxies to be less likely to be stripped by their environment. In these galaxies, the stellar mass resides deeper inside the subhalo, so a larger fraction of dark matter has to be removed for it to be affected. While Smith et al. (2016) find more massive galaxies to be more concentrated than low-mass galaxies – which should therefore be able to retain more of their stellar mass – galaxies in Figure 3.8 exhibit the opposite trend. Massive satellite galaxies in TNG100 are actually more likely to be stripped of their stellar component than low-mass satellites.

Furthermore, Bahé et al. (2019) find similar trends considering the mass loss of galaxies. They study the survival and disruption of satellite galaxies in groups and

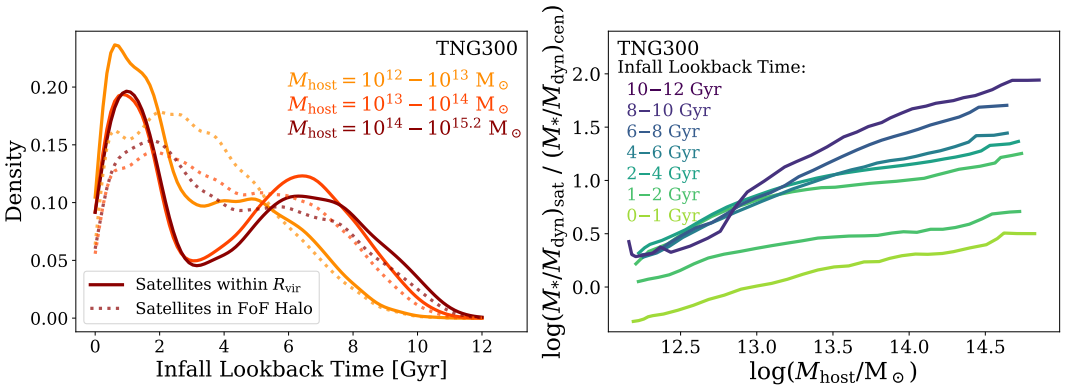

Figure 3.9: Distribution of satellite infall time & ratios of satellite vs. central stellar mass fractions. *Left panel:* Distribution of infall times for satellite galaxies in TNG300. I present their accretion history as a function of host mass in bins of $10^{12} - 10^{13}$ M$_\odot$, $10^{13} - 10^{14}$ M$_\odot$, and $10^{14} - 10^{15.2}$ M$_\odot$ (orange to dark red curves). Solid curves correspond to satellite galaxies within their host's virial radius, dotted curves to all satellites in the host's FoF halo, i.e. within *and* outside the virial radius. Infall distributions were smoothed using a Gaussian kernel with an average width of 0.3 Gyr. *Right panel:* Ratios of satellite and central stellar mass fractions $M_*/M_{\rm dyn}$ as a function of host mass in TNG300. I show the relation in different bins of infall lookback time: $0 - 1$ Gyr, $1 - 2$ Gyr, $2 - 4$ Gyr, $4 - 6$ Gyr, $6 - 8$ Gyr, $8 - 10$ Gyr, and $10 - 12$ Gyr ago (green to blue curves).

clusters using cosmological zoom-in simulations and find stellar mass to be stripped to a lesser degree than total subhalo mass. Satellites tend to either retain a significant fraction of their stellar mass or are disrupted completely (i.e. quickly).

3.3.2 Satellite SHMR shift as a function of host mass and infall times

In Figure 3.8, it does not appear as if there is a significant variation in the strength of tidal stripping with host mass: therefore, the cause for the shift in the SHMR in Figure 3.3 remains to be determined. If the distribution of satellite infall times changes with host mass, the dependence of the satellite SHMR shift with host mass may simply reflect an effect of different typical infall times. I examine this in the following section.

I present the infall distributions of TNG300 satellites – that survive to $z = 0$ with at least $10^{10.5}$ M$_\odot$ in dynamical mass and that are found within the virial radius of their host at $z = 0$ – in three bins of host mass ($10^{12} - 10^{13}$ M$_\odot$, $10^{13} - 10^{14}$ M$_\odot$, $10^{14} - 10^{15.2}$ M$_\odot$; orange to red, solid curves) in the left panel of Figure 3.9. The infall distributions are smoothed using a Gaussian kernel with an average width of 0.3 Gyr. Interestingly, the distribution of accretion times of surviving satellites is bimodal. This apparent bimodality of infall histories arises due to backsplash galaxies (Yun et al. 2019). After first pericentric passage, the orbits of satellites can still extend outside their host's virial radius. However, since I define satellites to be within the virial radius, these galaxies are not part of my sample while they would otherwise fill up the infall time distributions at intermediate times (dotted curves). Regardless, the accretion of satellites peaks over the last 2.5 Gyr with a smaller, secondary peak

$5-7$ Gyr ago. This secondary peak is shifted to earlier times for satellites in more massive hosts, however, it is less pronounced for satellites in less massive hosts of $10^{12}-10^{13}$ $M_\odot$. The infall times of satellites that survive through $z = 0$ and now reside in lower-mass hosts span an overall smaller range of time, which could be a reason why these satellite populations exhibit on average smaller deviations from the centrals' SHMR. Including satellites outside the virial radius would not change my results nor the trends with host mass for the SHMR or its scatter. In fact, they would reinforce the trends with host mass in the left panel of Figure 3.3 by expanding the SHMR shifts more significantly for satellites with larger dynamical mass.

The trends found above also hold when I consider an alternative sample by selecting satellites that survive through $z = 0$ by their peak instead of their present-day dynamical mass, as previously done in Chapter 3.3.1 and Figure 3.8. In this case, most satellites fall into their present-day host environment's progenitor earlier in time, with a broader early infall time peak ranging between lookback times of $6-10$ Gyr. Most early infallers in this alternative sample experience a strong degree of tidal stripping, which brings them below the dynamical mass limit imposed at present time for my fiducial satellite sample. However, the trends with host mass are still the same, with satellites in lower-mass hosts exhibiting later infall times. On the other hand, if I were to inspect the infall time distributions of all satellites ever accreted – so including not only the present-day, surviving satellite galaxies but all satellites with a peak dynamical mass of $M_{\rm dyn,\ peak} \geq 10^{10.5}$ $M_\odot$ that have ever been accreted – the infall times would appear somewhat differently. The infall distributions would cover the same range in time regardless of host mass, with low-mass hosts in fact peaking slightly earlier – rather than later – than more massive ones, consistent with the trends of halo formation time with halo mass. A significant fraction of satellites that fell in present-day groups and clusters early on, i.e. $8-12$ Gyr ago, have been disrupted in the meantime. Therefore, the infall time distribution of surviving satellites in Figure 3.9 is biased towards more recent cosmic epochs.

While there is a shift in the distribution of surviving satellite infall times with host mass, I still need to confirm whether this causes a shift in stellar mass fractions with host mass as in the top panel of Figure 3.3. Therefore, I further examine the combined dependence on host mass and infall times in the right panel of Figure 3.9. This panel depicts the ratio of stellar mass fractions $M_*/M_{\rm dyn}$ of satellites and centrals as a function of host mass in different bins of infall lookback time ($0-1$, $1-2$, $2-4$, $4-6$, $6-8$, $8-10$, $10-12$ Gyr ago; green to blue curves). Generally, even at fixed infall time, satellites exhibit a larger offset from the SHMR of centrals with increasing host mass – more massive clusters are in fact more efficient in driving satellites to larger stellar mass fractions. Furthermore, there is a clear trend with infall time: the earliest infallers ($10-12$ Gyr ago) in the most massive hosts can reach stellar mass fractions of up to a factor 100 larger than those of centrals. On the other hand, satellites in the most recent infall time bins ($0-1$ and $1-2$ Gyr ago) exhibit significantly lower ratios of stellar mass fractions than satellites of all other

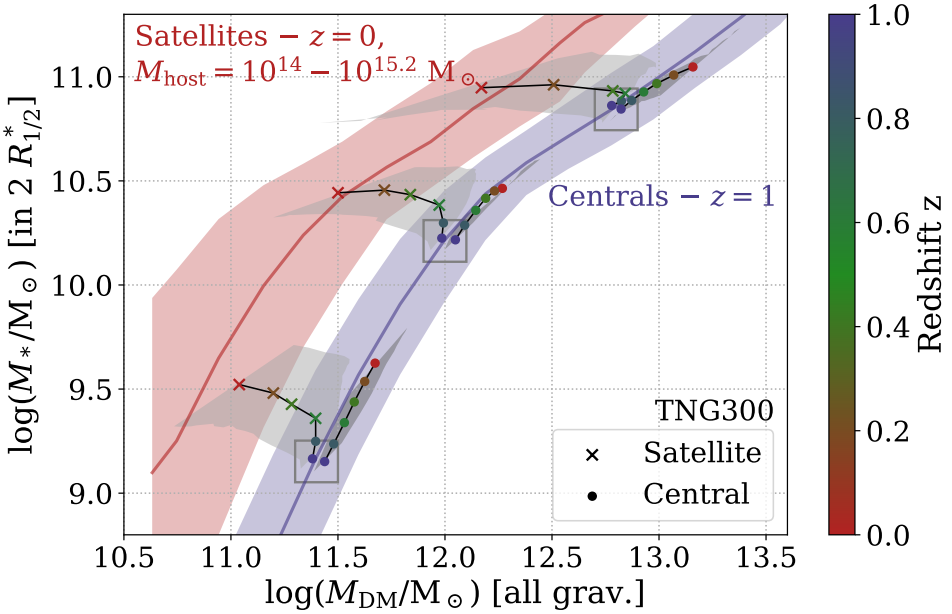

Figure 3.10: Evolution of stellar and dark matter mass in my fiducial aperture choice (all gravitationally bound dark matter particles) from z = 1 to z = 0 in TNG300. The blue curve corresponds to the SHMR for centrals at $z = 1$, the red curve to the SHMR of satellites in massive cluster hosts of $10^{14} - 10^{15.2}$ $M_\odot$ at $z = 0$. Shaded regions depict the scatter as 16th and 84th percentiles. I choose centrals at $z = 1$ within a parameter space of $M_{DM} = 10^{11.3} - 10^{11.5}$ $M_\odot$ and $M_* = 10^{9.05} - 10^{9.25}$ $M_\odot$, $M_{DM} = 10^{11.9} - 10^{12.1}$ $M_\odot$ and $M_* = 10^{10.11} - 10^{10.31}$ $M_\odot$, or $M_{DM} = 10^{12.7} - 10^{12.9}$ $M_\odot$ and $M_* = 10^{10.74} - 10^{10.94}$ $M_\odot$ (denoted by grey boxes), and follow their evolution to $z = 0$. Median evolutionary tracks are shown separately for galaxies that stay centrals or become satellites: centrals are denoted by dots, satellites by crosses. The markers are colour-coded by time, covering redshift $z = 1.0, 0.8, 0.6, 0.4, 0.2, 0.0$. Here, infall is defined as the first time the subhaloes are considered members of another FoF halo (*not* infall into its virial radius R_{200c} as for the rest of this chapter). Grey shaded areas correspond to the scatter of central and satellite evolutionary tracks as 16th and 84th percentiles.

infall times. These galaxies have not yet spent enough time inside their new host environment to have experienced extended stripping or even a pericentric passage.

3.3.3 Evolution of centrals and satellites in the stellar mass vs. halo mass plane

In order to illustrate the differences in the evolution of centrals and satellites, as well as the contributions of ongoing star formation and tidal stripping in the host potential, I present the SHMR of TNG300 as stellar mass versus dark matter mass and the evolution of galaxies between $z = 1$ and $z = 0$ in Figure 3.10. Here, I consider dark matter instead of dynamical mass in order to illustrate the impact of tidal stripping on haloes directly. While gas stripping does occur – especially for dwarf galaxies with larger gas fractions – it is negligible compared to the loss of dark matter. As seen in Figure 3.8, the distribution of dark matter mass loss traces the distribution of dynamical mass.

I consider the SHMR of centrals at $z = 1$ (blue curve) and compare it to the SHMR of satellites in massive clusters of $10^{14} - 10^{15.2}$ $M_\odot$ at $z = 0$. At $z = 1$, I define various parameter spaces in the SHMR (denoted by the grey boxes) and select two disjoint sets of galaxies in each bin – depending on whether they stay centrals or become satellites by $z = 0$. Their average evolutionary tracks are depicted at $z = 1.0,\ 0.8,\ 0.6,\ 0.4,\ 0.2,\ 0.0$ using median stellar and dark matter mass at the respective points in time. Markers show whether the galaxies are centrals (dots) or have become a satellite as member of another FoF halo (crosses).

Centrals remain undisturbed by the environment, grow more massive in both stellar and dark matter mass, and evolve more or less along the same $z = 1$ SHMR. The evolutionary tracks of satellites, however, present a different picture: in the low- and intermediate-mass bins, their dark matter growth is reduced and halted even while they are still considered centrals. Their relatively nearby, future host halo possibly already dominates the accretion of dark matter since mass accretion for clusters persists out to several virial radii (Behroozi et al. 2014). Star formation continues and they begin to move off their original SHMR in an almost vertical fashion.

In the massive bin, galaxies still evolve along the SHMR during this first phase: their star formation may be already quenched, in the TNG model via AGN feedback (e.g. Weinberger et al. 2017; Donnari et al. 2019; Terrazas et al. 2020; Donnari et al. 2021b), and they primarily grow due to mergers with other galaxies. However, as soon as galaxies become satellites of a more massive halo, tidal stripping by the potential of the new host removes the outer parts of the satellite galaxies' dark matter subhaloes and dominates the transition to the SHMR of satellites until $z = 0$ – irrespective of their dynamical or stellar mass. The star formation activity of galaxies in the low- and intermediate-mass bins decreases after infall. While the scatter for the evolutionary tracks (grey shaded areas) is fairly broad with up to $\sim 0.3 - 0.4$ dex at fixed dynamical mass, the tracks of the 16^{th} and 84^{th} percentile populations follow the same trends – shifted to lower or higher stellar masses, respectively. This scatter might be introduced by different orbital configurations or initial pericentric distances. However, I do not find significant stripping of stellar mass in the average satellite evolution tracks (as already evident from Figure 3.8).

Niemiec et al. (2019) found similar results in the Illustris simulation: after infall, satellite galaxies in massive clusters can be stripped of up to 80 per cent of their dark matter subhalo after spending $8 - 9$ Gyr in their host. Furthermore, these satellites continue to form stars until they experience their first pericentric passage. They interpret the shift in the SHMR of satellite galaxies to result from three different phases: (i) loss of dark matter by tidal stripping and increase in stellar mass by star formation, (ii) loss of dark matter and constant stellar mass after quenching, as well as (iii) combined loss of dark matter and stellar mass by tidal stripping. While I recover trends similar to the first two phases for the transition of satellite galaxies, I do not find a significant combined loss of dark matter and stellar mass for TNG galaxies. These differences might arise due to different galaxy formation models:

low-mass galaxies in Illustris have been found to be too large by a factor of $\sim 2-3$ in comparison to observations (Snyder et al. 2015) and IllustrisTNG (Pillepich et al. 2018b). Due to their increased extent, the stellar component of these galaxies may become subject to tidal stripping more easily.

3.3.4 Tools and fitting functions

I provide a family of fitting functions for the SHMR in IllustrisTNG. As for Figure 3.3, these functions are constructed using the combined sample of rTNG300, rTNG100, and TNG50. I adopt the parametrization from Moster et al. (2010) and Moster et al. (2013) as per Equation (3.1). I summarise the parameters for the best fitting models for dynamical and stellar masses in my fiducial aperture choice (all gravitationally bound particles for $M_{\rm dyn}$, stellar mass within two stellar half-mass radii for M_*) in Table 3.4. Since satellites in different environments form different SHMRs, Table 3.4 includes variations of host mass range and bin sizes. In Appendix B, I visualise how the fitting parameters vary with host halo mass.

3.3.5 Halo finder and resolution limitations

The results uncovered so far represent the outcome of the numerical galaxy formation model as implemented in IllustrisTNG. Other cosmological simulations in the future may return somewhat different quantitative (albeit not qualitative) solutions. In practice, even within the IllustrisTNG simulations, my quantitative results may depend to some extent on the underlying adopted identification tools as well as on the underlying numerical resolution.

In the following, I discuss the limitations and possible tensions for the measurement of dynamical masses accomplished with the SUBFIND algorithm (Springel et al. 2001; Dolag et al. 2009). By using all gravitationally bound particles for the subhalo masses, I rely on the way resolution elements (or particles) are assigned by the halo finder to subhaloes. There may be physical situations in which such assignments can be difficult or problematic. It should be noted that, although SUBFIND defines a subhalo as the collection of a certain minimum number of particles that survive the unbinding procedure, the choice of 20 as minimum number of resolution elements per subhalo adopted here cannot constitute an issue, as throughout the analysis I only consider galaxies with minimum dynamical masses of $10^{10.5}$ $M_\odot$ (i.e. at least many hundreds of particles for satellites even at the lowest resolution adopted in this chapter).

SUBFIND identifies substructure within a parent FoF halo as groups of particles that form gravitationally self-bound, locally overdense regions. Subhaloes in locations of generally higher density – such as areas close to the centres of host haloes – could be misidentified or have underestimated dynamical masses, with parts of their outskirts being ascribed to their centrals. I avoid these regions by imposing a minimum cluster-centric distance on my satellite sample: only satellites that are

M_{dyn} [all grav.], M_* [in 2 $R^*_{1/2}$]

Sample	Med. M_{host} [$\log M_\odot$]	N	M_1 [$\log M_\odot$]	β	γ
Centrals		0.0258 ± 0.0003	11.70 ± 0.02	28.6 ± 0.8	10.4 ± 0.2
Sats., $M_{host} = 10^{12-13}$ $M_\odot$	12.53	0.108 ± 0.003	11.12 ± 0.06	27.5 ± 2.9	15.6 ± 1.7
Sats., $M_{host} = 10^{13-14}$ $M_\odot$	13.52	0.127 ± 0.008	10.85 ± 0.11	23.6 ± 6.1	10.1 ± 1.3
Sats., $M_{host} = 10^{14-14.5}$ $M_\odot$	14.22	0.137 ± 0.004	10.93 ± 0.04	30.5 ± 3.6	10.9 ± 0.6
Sats., $M_{host} = 10^{14.5-15.2}$ $M_\odot$	14.67	0.129 ± 0.006	10.85 ± 0.04	38.6 ± 7.2	9.5 ± 0.7
Sats., $M_{host} = 10^{12-12.5}$ $M_\odot$	12.27	0.092 ± 0.010	11.17 ± 0.27	25.4 ± 8.8	16.4 ± 10.3
Sats., $M_{host} = 10^{12.5-13}$ $M_\odot$	12.75	0.123 ± 0.004	11.00 ± 0.05	33.6 ± 3.5	15.3 ± 1.4
Sats., $M_{host} = 10^{13-13.5}$ $M_\odot$	13.26	0.130 ± 0.003	11.12 ± 0.22	16.5 ± 5.8	13.2 ± 2.6
Sats,. $M_{host} = 10^{13.5-14}$ $M_\odot$	13.76	0.128 ± 0.009	10.76 ± 0.08	28.5 ± 7.8	9.3 ± 1.1
Sats., $M_{host} = 10^{12.5} - 10^{13.5}$ $M_\odot$	13.01	0.114 ± 0.005	10.88 ± 0.06	33.3 ± 5.4	10.5 ± 1.0
Sats., $M_{host} = 10^{13.5-14.5}$ $M_\odot$	13.94	0.133 ± 0.005	10.86 ± 0.05	28.00 ± 4.3	10.4 ± 0.7

Table 3.4: Fit parameters to the SHMR of centrals and satellites in various bins of host mass using rTNG300, rTNG100 and TNG50 galaxies and my fiducial aperture choice (all gravitationally bound mass for M_{dyn}, stellar mass within twice the stellar half-mass radius for M_*). I follow the parametrization in Equation (3.1), using normalisation N, characteristic mass M_1, and the slopes at the low- and high-mass ends β and γ.

located at least 0.05 R_{200c} from their host's centre are included. However, I have verified that not imposing this minimum cluster-centric distance does not change my results significantly.

Close objects might lead to discrepancies as well. If two galaxies are situated too near to one another – e.g. in a fly-by event – the algorithm might run into problems separating them since it only probes for local overdensities. However, considering the statistical size of my samples, I do not expect this to affect my findings.

Ayromlou et al. (2019) constructed an instantaneous technique to identify additional member particles of subhaloes in their local background environment. Using a Gaussian mixture method, they classify background particles into two components depending on whether particles share mean velocities and velocity dispersions similar to the original subhalo. These particles are then reassigned to the subhaloes in order to decontaminate the true background particles. This results in a noticeable effect on the satellite stellar mass function: masses of subhaloes can increase by factors of 2 or more. Mass changes are larger for more massive satellites and – at fixed subhalo mass – larger for satellites in lower-mass hosts.

Generally, these potential uncertainties could be alleviated at once by employing and comparing to another halo finder. 6D halo finders such as ROCKSTAR (Behroozi et al. 2013) or VELOCIRAPTOR (Elahi et al. 2019) additionally take velocity information into account to identify substructures, which could yield different dynamical masses for this chapter. However, I do not expect this to change the qualitative trends found in my results. While comparing the identification of environmental effects and tidal stripping of satellite galaxies between different halo finders might yield additional insights, it exceeds the scope of this chapter.

While my galaxy sample seems relatively safe regarding limitations in the identification of halo overdensities and substructures, satellites might become subject to artificial disruption because of the limited numerical resolution. When comparing my results across all the resolution levels of the IllustrisTNG suite, I find some dependence on numerical resolution, which is the reason why I present my results after applying a resolution correction that is gauged to reproduce quantitative results coherent with those from the highest-resolution realisation: TNG50 (see Appendix A).

However, by studying the evolution of satellite dark matter subhaloes in a series of idealized N-body simulations, van den Bosch and Ogiya (2018) find most tidal disruption events to be of numerical origin and that inadequate force softening (as that adopted in typical cosmological large-volume simulations like TNG100 or TNG300) can lead to overestimated mass loss. However, a number of caveats makes it difficult to extrapolate these findings to more realistic cosmological setups: their results are based on dark matter-only simulations (i.e. without contributions of baryonic effects), satellites are bound to purely circular, infinitely-long orbits, dynamical friction is not accounted for, and the host halo is represented by a static analytical potential. In fact, Bahé et al. (2019) relax some of these concerns by studying the survival rate of satellite galaxies in cosmological zoom-in simulations. According

to their findings, total disruption of satellites is negligible in massive clusters and predominantly occurs in lower-mass groups and during pre-processing. Furthermore, the disruption efficiency shows a strong correlation with redshift: the fraction of surviving satellites decreases towards earlier accretion times and is in any case physically negligible for accretion times of $z \gtrsim 4$. This is consistent with my findings in Figure 3.9. Furthermore, Bahé et al. (2019) find that while baryons contribute to the degree of mass loss satellite galaxies experience, they only have a small impact on their actual rate of survival. Whether subhaloes are artificially over-stripped or completely destroyed might correspond to different physical problems. While van den Bosch and Ogiya (2018) focus on the possibly artificial, *complete* disruption of subhaloes (i.e. overmerging), their results considering the actual amount of mass stripped are reassuring within the context of "low-resolution" cosmological simulations. According to their figure 10, the first 99 per cent of material stripped from a subhalo is perfectly well captured – also at the resolutions that are relevant here.

Chapter 4

The abundance of satellites around Milky Way- and M31-like galaxies with TNG50

In this chapter, I discuss the results of Engler et al. (2021a): *"The abundance of satellites around Milky Way- and M31-like galaxies with the TNG50 simulation: a matter of diversity"*. At a volume of $(50 \text{ comoving Mpc})^3$ and a baryonic mass resolution of 8×10^4 $M_\odot$, TNG50 bridges the gap between large-scale volumes and the regime of zoom-in simulations. Therefore, TNG50 includes a statistically significant sample of both MW/M31-like galaxies and their satellites. This enables me not only to reliably identify satellite galaxies down to stellar masses of $\sim 5 \times 10^6$ $M_\odot$ (approximately the stellar mass of Leo I), but also to study the evolution of satellite abundances throughout cosmic time, and to search for statistically significant correlations of satellite abundance with various host galaxy and halo properties.

This chapter is structured as follows: in Chapter 4.1, I introduce my selection of MW/M31-like hosts, satellite galaxies, and subhaloes. I present my results in Chapter 4.2: the satellite stellar mass function of TNG50 MW/M31-like hosts, comparisons with observational surveys and previous simulations, its evolution with redshift, differences between luminous satellite and dark subhalo populations, as well as baryonic vs. dark matter-only simulation results. Furthermore, I discuss dependencies of satellite abundances on the adopted selection of host galaxies, as well as various host properties. The results of this chapter are summarised in Chapter 6.2.

4.1 Methods

4.1.1 Selecting MW/M31-like galaxies in TNG50

The very choice of galaxies that can be considered as analogues of our Milky Way and Andromeda is essential in order to compare a simulated galaxy population to these observed systems (see Pillepich et al. in prep. for an extended discussion). The abundance of satellite galaxies – should it follow the abundance of subhaloes – is expected to depend on at least some properties of their hosts, particularly on host

total mass (Gao et al. 2004). Over the next sections, I quantify this in greater detail. Therefore, it is vital to adopt a clear definition of MW/M31-like hosts. Throughout this chapter, I refer to a fiducial sample of MW/M31-like TNG50 analogues as detailed below, as well as to two host samples based on the selection criteria of two observational surveys.

TNG50 MW/M31-like fiducial sample

Throughout this chapter, I define MW/M31-like galaxies in TNG50 based on their mass and morphology according to Pillepich et al. (in prep.). MW/M31-like galaxies are required to have a stellar mass of $M_* = 10^{10.5} - 10^{11.2}$ M$_\odot$ within an aperture of 30 kpc and to be disky in their stellar shape – either by having a minor-to-major axis ratio of their 3D stellar mass distribution of $s < 0.45$ (measured between one and two times the stellar half-mass radius) or by visual inspection of synthetic 3-band stellar-light images in face-on and edge-on projection. These visual inspections add 25 galaxies with $s > 0.45$ that display clear disk features or spiral arms to my sample of host galaxies. On the contrary, there are 18 hosts with $s < 0.45$ that display a disturbed morphology, weak or barely visible spiral arms, or a strong bar feature, which are still considered as MW/M31-like candidates. While other works in the literature employ kinematic decomposition as a morphology estimate, the minor-to-major axis ratio was chosen as an observationally motivated and a more readily available indicator. Furthermore, a minimum isolation criterion is imposed at $z = 0$. No other massive galaxies with $M_* > 10^{10.5}$ M$_\odot$ are allowed within a distance of 500 kpc of the MW/M31-like candidates and the mass of the candidates' host halo is limited to $M_{200c} < 10^{13}$ M$_\odot$. These host haloes are defined using a friends-of-friends (FoF) algorithm and their virial mass M_{200c} corresponds to the total mass of a sphere around the FoF halo centre with a mean density of 200 times the critical density of the Universe.

Galaxies that fulfill all of the aforementioned conditions – a stellar mass of $M_* = 10^{10.5} - 10^{11.2}$ M$_\odot$, a disky stellar morphology, and a relatively isolated environment – are considered to resemble the Milky Way and Andromeda to a reasonable degree, at least within the context of the general galaxy population. Note that this selection does *not* require TNG50 MW/M31-like galaxies to be the centrals of their host halo, i.e. they can be satellites of another galaxy. This allows my sample to include also galaxy pairs of Local Group-like systems, as it is not clear which of them – the MW-like or the M31-like galaxy – would be considered as the central galaxy of the system. In total, these criteria leave me with a sample of 198 MW/M31-like galaxies in TNG50, eight of which are satellite galaxies. I exclude these satellite hosts in later parts of the chapter where I specifically study the infall of satellite galaxy populations or host halo properties.

For the purposes of investigating differences between TNG50 and its dark matter-only (DM-only) analogue TNG50-Dark, I cross-match my sample of MW/M31-like hosts from the baryonic run to their DM-only counterparts (Rodriguez-Gomez et

al. 2015; Rodriguez-Gomez et al. 2017; Nelson et al. 2015) by maximising the number of common DM particles. Therefore, the DM-only host sample consists of 198 MW/M31-like haloes as well.

SAGA-like host selection

This host selection is based on the *K*-band luminosity and the local environment of host galaxies. I adopt the selection criteria from Geha et al. (2017) and Mao et al. (2021). Potential candidates are required to have a *K*-band luminosity in the range of $-23 > M_{\rm K} > -24.6$ and to have no bright galaxy within their virial radius (for which I adopt 300 kpc as the typical virial radius of a MW-like galaxy). Bright galaxies are defined by a magnitude of at least $K < K_{\rm host} - 1.6$. Furthermore, galaxies with a host halo mass of 10^{13} $M_\odot$ and above are excluded. Out of all TNG50 hosts that meet these criteria, I match the three most similar ones to each of the 36 observed SAGA hosts based on their *K*-band luminosity. This gives me a sample of 108 TNG50 SAGA-like hosts, which will be used in Figure 4.7. Note that this selection does *not* require the TNG50 SAGA-like galaxies to be the centrals of their host halo.

Local Volume (LV)-like host selection

This selection of hosts is based on observations of nearby host galaxies in the Local Volume (LV; Carlsten et al. 2021). As the observational selection is mainly based on luminosity and spatial proximity, I adopt a similar range in *K*-band luminosity of $-22.7 > M_{\rm K} > 24.5$. As there are no specific observational selection criteria regarding their environment and morphology, I choose my sample candidates to be the central galaxy of their respective dark matter halo and to have a disky stellar shape – either by having a minor-to-major axis ratio of their 3D stellar mass distribution of $s < 0.45$ (measured between one and two times the stellar half-mass radius) or by visual inspection of synthetic 3-band stellar-light images in face-on and edge-on projection. Out of all TNG50 hosts that meet these criteria, for each of the 6 observed LV hosts (not including the Galaxy and Andromeda), I choose the three TNG50 galaxies with the closest *K*-band luminosity. This gives me a sample of 18 TNG50 LV-like hosts, which will be used in Figure 4.8.

Basic properties of TNG50 MW/M31-like galaxies

I present my sample of MW/M31-like galaxies and some of their fundamental scaling relations in Figure 4.1. Its left panel shows the TNG50 stellar-to-halo mass relation (SHMR), as stellar mass M_* (within 30 physical kpc) as a function of total host halo mass $M_{\rm 200c}$. MW/M31-like galaxies are represented by blue circles and are shown in context of TNG50's general galaxy population, including both central and satellite galaxies (open circles). Vertical grey lines mark specific total host masses that my sample – which is selected based on stellar mass – covers. Dashed lines correspond to the $10^{\rm th}$ and $90^{\rm th}$ percentiles of my host mass range at $10^{11.9}$ $M_\odot$ and

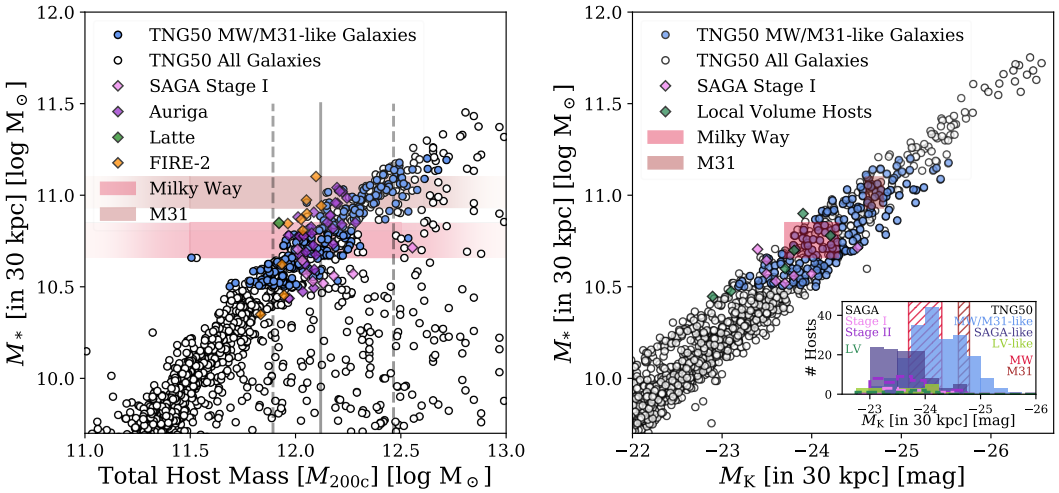

Figure 4.1: Properties and basic scaling relations for MW/M31-like hosts selected from the TNG50 simulation. Blue circles denote the MW/M31 analogues, while open circles indicate all galaxies in the simulation in the depicted parameter space. *Left panel:* stellar-to-halo mass relation, as stellar mass M_* (within 30 physical kpc) as a function of host halo mass M_{200c}: in my selection, MW/M31-like galaxies are not necessarily required to be centrals themselves. I compare my results from TNG50 to the first stage of the SAGA survey (pink diamonds, Geha et al. 2017), previous simulations – Auriga (purple diamonds, Grand et al. 2017), Latte (green diamond, Wetzel et al. 2016), and FIRE-2 (orange diamonds, Garrison-Kimmel et al. 2019) – as well as the MW (light red box, Licquia et al. 2015; Boardman et al. 2020) and M31 (light brown box, Sick et al. 2015). As the Latte and FIRE-2 simulations employ different definitions of host halo mass, I convert their masses to M_{200c} – note that their actual M_{200c} masses might be slightly different depending on their employed cosmology. The grey, vertical lines denote the median (solid line, $10^{12.1}$ M$_\odot$), as well as the 10$^{\text{th}}$ and 90$^{\text{th}}$ percentiles (dashed lines, $10^{11.9}$ M$_\odot$ and $10^{12.5}$ M$_\odot$, respectively) in total host mass for my sample of MW/M31-like galaxies, since my sample is primarily selected based on their stellar mass. *Right panel:* stellar mass as a function of absolute *K*-band luminosity M_K, both within 30 kpc. I compare the TNG50 galaxies to MW-like galaxies from the first stage of the SAGA survey (pink diamonds, Geha et al. 2017), hosts in the Local Volume (green diamonds, Carlsten et al., 2020a; Carlsten et al., 2021, as available, with additional data from Skrutskie et al. 2006; Lianou et al. 2019), as well as the MW (light red box, Drimmel and Spergel 2001) and M31 (light brown box, Hammer et al. 2007). *Right panel inset:* distributions of host *K*-band luminosity within 30 kpc. I compare my fiducial selection of TNG50 MW/M31-like galaxies (blue histogram) to the alternative TNG50 SAGA- and LV-like selections (dark purple and light green histograms, respectively), host galaxies from the SAGA survey's first and second stages (pink and purple histograms, respectively), LV hosts (dark green histogram), as well as the MW (red hatched area) and M31 (brown hatched area).

$10^{12.5}$ $M_\odot$, respectively. The solid, vertical line denotes the median host mass of my sample of MW/M31-like galaxies at $M_{200c} = 10^{12.1}$ $M_\odot$. Furthermore, I compare my sample of host galaxies to the first stage of the SAGA survey (pink diamonds, Geha et al. 2017) and previous hydrodynamical simulations of similar-mass hosts: Auriga (purple diamonds, Grand et al. 2017), Latte (green diamond, Wetzel et al. 2016), and FIRE-2 (orange diamonds, Garrison-Kimmel et al. 2019). As both Latte and FIRE-2 employ different measurements of host halo mass – M_{200m} (i.e. the total mass of a sphere around the FoF halo centre with a mean density of 200 times the mean density of the Universe) and M_{Δ_c} (i.e. the total mass of a sphere with a mean density of Δ_c times the critical density of the Universe, where Δ_c is derived from the collapse of a spherical top-hat perturbation), respectively – I convert their host masses into M_{200c} using the TNG50 relations of these different mass measurements.[1]

While both observations and simulations span a similar range in stellar mass, slightly shifted to less massive galaxies, the sample of TNG50 MW/M31-like galaxies is by design allowed to extend towards somewhat more massive host haloes. It is important to note the different approaches that are adopted across analyses in the definition of galaxies such as the MW and M31. While I adopt a host selection based on the host galaxies' stellar mass as an observable property, most previous hydrodynamical works employ a halo mass-based selection instead. Moreover, it is important to note that this is a volume-limited sample, with more numerous MW/M31-like galaxies towards the lower end of the mass range and fewer galaxies at the high-mass end, i.e. the mass distribution within the sample is not flat. This must be kept in mind when comparing medians and scatters across samples. I summarise the host selection criteria for host galaxies of all other simulations addressed in this chapter in Table 4.1 and discuss their impact on satellite populations in Chapter 4.2.4.

Finally, I compare to mass estimates of the MW (light red box) and M31 (light brown box). I show a stellar mass range of $M_* = 10^{10.66} - 10^{10.85}$ $M_\odot$ for the MW according to Licquia et al. (2015) and Boardman et al. (2020), as well as a stellar mass range of $M_* = 10^{10.9} - 10^{11.1}$ $M_\odot$ for M31 according to Sick et al. (2015). Within these shaded stellar mass bands, I indicate the currently available estimates on the host halo mass of the MW and M31 as darker regions: these lie in the range of $10^{11.5} - 10^{12.5}$ $M_\odot$ (see Callingham et al. 2019 for a compilation of estimates). As host halo mass is not an observable, I adopt the same estimate for both the MW and M31. Therefore, my fiducial selection of TNG50 MW/M31-like galaxies returns a range of host halo masses that is well consistent with current inferences for the Galaxy and Andromeda. In fact, the MW's mass estimates lie well in the centre of TNG50's

[1]The actual M_{200c} masses of simulations other than TNG50 might be slightly different depending on their adopted cosmology. I determine the TNG50 relations using least squares minimisation:

$$\log M_{200c} = 0.99 \times \log M_{200m} - 0.02 \quad (4.1)$$

$$\log M_{200c} = \log M_{\Delta_c} - 0.02 \quad (4.2)$$

sample of MW/M31-like galaxies. Based on the effective SHMR of TNG50, I would instead expect M31 to reside in a more massive halo than the MW.

The right panel of Figure 4.1 depicts the correlation of stellar mass M_* and absolute K-band luminosity M_K, both measured within an aperture of 30 kpc. Galaxy luminosities are constructed by assigning broad-band luminosities to each stellar particle using the stellar population synthesis model of Bruzual and Charlot (2003) according to each particle's age, mass, and metallicity. None of the luminosities include dust attenuation (see Vogelsberger et al. 2013 for details). As before, I contextualise my sample of MW/M31-like hosts (blue circles) with all galaxies in TNG50 in general (open circles). The two properties are tightly correlated (with a Pearson correlation coefficient of -0.85), depicting the K-band luminosity of galaxies as a clear proxy for their stellar mass. I compare the distribution of MW/M31-like hosts in TNG50 to observed systems from the first stage of the SAGA survey (pink diamonds, Geha et al. 2017), as well as hosts in the Local Volume (green diamonds, Carlsten et al. 2020a; Carlsten et al. 2021, as available, with additional data from Skrutskie et al. 2006; Lianou et al. 2019), all of which are consistent with the distribution of TNG50 hosts. Furthermore, I include estimates of the actual MW (red box) and M31 galaxies (brown box) using K-band luminosity measurements from Drimmel and Spergel (2001) for the MW and Hammer et al. (2007) for M31. Both galaxies' stellar mass and luminosity estimates agree remarkably well with the relation formed by MW/M31-like galaxies in TNG50.

More specifically, I compare the distributions of K-band luminosity (within 30 kpc) for various samples of host galaxies in the inset panel of the right panel of Figure 4.1. While my fiducial sample of TNG50 MW/M31-like hosts (blue filled histogram) peaks around the luminosity of the MW (red, dashed lines) and has a significant fraction of hosts at brighter luminosities to include analogues of Andromeda (brown, dashed lines), both the SAGA (pink and purple dashed histogram) and Local Volume hosts (dark green dashed histogram) are more concentrated at slightly fainter luminosities than the MW. By construction, the distributions of the observed hosts and of the analogue TNG50 SAGA- and LV-like selections (dark purple and light green histograms) display a good level of compatibility: this ensures an even-handed comparison of their satellite systems, which will follow below.

4.1.2 Selecting satellite galaxies

Throughout this chapter, I employ different definitions for satellite galaxies around MW/M31-like hosts. While satellites in IllustrisTNG are generally identified as subhaloes or local overdensities within larger FoF haloes using the SUBFIND algorithm (Springel et al. 2001; Dolag et al. 2009), I avoid to restrict my selection of satellites by FoF membership for the most part of this analysis. However, not all luminous subhaloes represent actual galaxies in TNG. Some correspond to fragmentations and clumps within other galaxies due to e.g. disk instabilities that SUBFIND identified as independent objects. I exclude these objects from my sample according to Nelson

Simulation	Reference	# of Hosts	Mass Selection	Other Selection Criteria
Aquarius (DMO)	Springel et al. (2008)	6 MW-like	$M_{200c} = 10^{11.9-12.3}$ M$_\odot$	no massive neighbour at $z = 0$, late-type galaxy via SAM
Via Lactea II (DMO)	Diemand et al. (2008)	1 MW-like	$M_{200m} = 10^{12.3}$ M$_\odot$, i.e. $M_{200c} = 10^{12.1}$ M$_\odot$	no recent major mergers
Phat ELVIS (DMO)	Kelley et al. (2019)	12 MW-like	$M_{\Delta_c} = 10^{11.8-12.3}$ M$_\odot$, i.e. $M_{200c} = 10^{11.6-12}$ M$_\odot$	isolated within 3 Mpc
APOSTLE (bary.)	Fattahi et al. (2016a)	12 LG-like	$M_{200c,\,LG} = 10^{12.2-12.6}$ M$_\odot$	pairs isolated within 2.5 Mpc, separation of $600 - 1000$ kpc
Latte (bary.)	Wetzel et al. (2016)	1 MW-like	$M_{200m} = 10^{12.1}$ M$_\odot$, i.e. $M_{200c} = 10^{12}$ M$_\odot$	slightly quiescent merger history
Auriga (bary.)	Grand et al. (2017)	30 MW-like	$M_{200c} = 10^{12.0-12.3}$ M$_\odot$	isolated, outside of $9 \times R_{200c}$ of any other halo
FIRE-2 (bary.)	Garrison-Kimmel et al. (2014, 2017, 2019)	2 LG-like	$M_{\Delta_c} = 10^{12.3-12.7}$ M$_\odot$, i.e. $M_{200c} = 10^{12.2-12.6}$ M$_\odot$	pairs isolated within 2.8 Mpc, no cluster within 7 Mpc, separation of ~ 800 kpc
FIRE-2 (bary.)	Garrison-Kimmel et al. (2014, 2017, 2019)	6 MW-like	$M_{200m} = 10^{12.0-12.3}$ M$_\odot$, i.e. $M_{200c} = 10^{11.9-12.2}$ M$_\odot$	isolated within 2.8 Mpc
ARTEMIS (bary.)	Font et al. (2021a)	45 MW-like	$M_{200c} = 10^{11.9-12.3}$ M$_\odot$	–
DC Justice League (bary.)	Applebaum et al. (2021)	2 MW-like	$M_{\Delta_c} = 10^{11.9-12.4}$ M$_\odot$, i.e. $M_{200c} = 10^{11.8-12.3}$ M$_\odot$	different merger histories
TNG50 (bary.)	Engler et al. (2021a)	198 MW/M31-like	$M_* = 10^{10.5} - 10^{11.2}$ M$_\odot$, i.e. $M_{200c} = 10^{11.9} - 10^{12.5}$ M$_\odot$	disky shape ($s < 0.45$), no massive galaxy within 500 kpc, host mass $M_{200c} < 10^{13}$ M$_\odot$

Table 4.1: List of simulations of MW/M31- and Local Group-like (LG) hosts referenced throughout this chapter, featuring studies of satellite abundances. This includes both dark matter-only (DMO, upper part) and baryonic simulations (lower section of the Table). I provide references and summarise both sample size and selection criteria of host galaxies and haloes. The latter include constraints on halo and stellar mass range, galaxy morphology, merger histories, and environment. Barring the mass constraints of the APOSTLE simulations, which apply to the total pair mass of their LG-like systems, all other mass selection criteria refer to individual MW/M31-like hosts. For TNG50, these can still include pairs of MW/M31-like hosts: in such cases, the quoted halo mass values refer to the host mass evaluated in a spherical-overdensity fashion starting from the halo center of the two galaxies. See Chapter 4.1.1 for further details on the host selection in TNG50. Different simulations adopt different measures of halo mass: M_{200c} (M_{200m}) corresponds to the total mass of a sphere around the FoF halo centre with a mean density of 200 times the critical (mean) density of the Universe, while M_{Δ_c} is the total mass of a sphere with a mean density of Δ_c times the critical density of the Universe. Δ_c is derived from the collapse of a spherical top-hat perturbation. I convert the host masses of simulations that use either M_{200m} or M_{Δ_c} into M_{200c} masses in order to put them directly into context with my sample of TNG50 MW/M31-like hosts. Note that the conversion between different cosmological mass measurements is based on the TNG50 relations of M_{200c} vs. M_{200m} (4.1) and M_{200c} vs. M_{Δ_c} (4.2). The actual M_{200c} values of other simulations might be slightly different depending on their adopted cosmology. The numbers in this table are relevant for the interpretation of e.g. Figure 4.9.

et al. (2019b), as these do not represent galaxies that formed by gas collapse at the centre of their DM haloes, which then fall into their $z = 0$ hosts.

Fiducial satellite selection. My fiducial satellite selection is based on the three-dimensional distance to their host MW/M31-like galaxy. I define satellites as galaxies within 300 physical kpc of their host – corresponding approximately to the virial radii of the MW and M31 – and require them to have a stellar mass of at least 5×10^6 $M_\odot$ (measured within twice the stellar half-mass radius $R^*_{1/2}$). This mass limit ensures an appropriately resolved identification with at least 63 stellar particles per galaxy and corresponds to the minimum stellar mass below which the TNG50 SHMR becomes incomplete due to its stellar mass resolution (see Appendix C for details on resolution effects). Furthermore, it corresponds to the mass of the MW's satellite galaxy Leo I. This selection leaves me with a total of 1237 satellite galaxies around 198 MW/M31-like hosts.

Observational satellite selections. I vary this selection in parts of Chapter 4.2.3 in order to match the selection criteria of observational surveys by employing no minimum stellar mass and varying the distance limit. For comparisons to the SAGA survey (Geha et al. 2017; Mao et al. 2021), I require satellite galaxies to lie within a two-dimensional, randomly projected aperture of 300 kpc from their host and to have a line-of-sight velocity within $\pm$250 km s^{-1}. For comparisons to Local Volume hosts from Carlsten et al. (2021), satellites are constrained to a two-dimensional, projected aperture of 150 kpc instead. Along the line of sight, satellites are restricted to distances of $\pm$500 kpc. While the line-of-sight distances of observed satellites in Carlsten et al. (2021) are estimated using either surface brightness fluctuations or the tip of their red giant branch, they also include a comparison to galaxies from TNG100, for which they adopt this physical distance requirement along the line of sight.

Alternative satellite selections. In Chapter 4.2.5, in order to compare the subhalo mass functions across numerical models, including DM-only simulations, I consider satellites as those within 300 physical kpc from their host centers and with a minimum dynamical mass – the sum of all gravitationally bound particles – of 5×10^7 $M_\odot$. According to the effective SHMR of TNG50, this value corresponds to the smallest total subhalo mass below which finite mass resolution makes the SHMR incomplete and artificially bends it – see bottom left panel of Figure C.2.

Finally, in cases where I compare all accreted satellites to their present-day population of survivors (Chapter 4.2.5), I do require them to be members of their host galaxy's FoF halo since their time of accretion is defined with respect to halo membership (Chua et al. 2017).

4.2 Results

4.2.1 Properties of satellite populations in TNG50

Before analysing the abundance of satellite galaxies around individual MW/M31-like hosts in TNG50, I investigate some of the properties and scaling relations of both satellites and subhaloes in Figures 4.2 and 4.3: their stellar-to-halo mass relation (SHMR) (Figure 4.2, left panel), the maximum of their circular velocity profile $V_{\rm max}$ as a function of stellar mass M_* (Figure 4.2, right panel), absolute r-band magnitude $M_{\rm r}$ as a function of stellar mass (Figure 4.3, top left panel), V-band half-light radius as a function of stellar mass (Figure 4.3, top right panel), and stellar 3D velocity dispersion σ_* as a function of stellar mass (Figure 4.3, bottom panel). In either figure, satellite galaxies with a stellar mass of $M_* \geq 5 \times 10^6$ M$_\odot$ are denoted as blue circles, satellites and subhaloes with smaller or no stellar mass whatsoever are marked as open circles. In order to illustrate the abundance of dark subhaloes, I assign random values to their stellar properties, detached from the main scaling relation: stellar masses of $10^2 - 10^3$ M$_\odot$, absolute r-band magnitudes of -2 to -4, and stellar 3D velocity dispersions of $0 - 10$ km s^{-1}. I mark the transition between luminous and dark regimes – the stellar mass resolution limit of TNG50 – as a dashed line in all panels. This corresponds to the minimum stellar mass that subhaloes contain, slightly lower than the target mass of a single stellar particle due to mass loss.

Satellite SHMR

Throughout this chapter, the satellites' stellar mass M_* is measured within twice the stellar half-mass radius, while their dynamical mass $M_{\rm dyn}$ corresponds to the sum of all gravitationally bound particles as defined by the SUBFIND algorithm (i.e. dark matter, stars, gas, and black holes).

The SHMR of satellites of MW/M31-like galaxies in TNG50 in the left panel of Figure 4.2 exhibits significant scatter. A large number of satellites show substantial offsets towards lower dynamical masses from their median SHMR (black curve) – predominantly due to tidal stripping of their dark matter haloes by their host's gravitational potential (see Chapters 3.3.1 and 3.3.3, as well as e.g. Joshi et al. 2019). Furthermore, I compare my sample to several SHMRs from simulations and semi-empirical models. The shaded grey region denotes the scatter of the SHMR for satellite galaxies in hosts of $10^{12} - 10^{13}$ M$_\odot$ in IllustrisTNG from Chapter 3.2.2 and Table 3.3. Although this range of host mass does not exactly match the selection of MW/M31-like hosts, the SHMRs are well in agreement, as to be expected modulo resolution effects. The purple and pink diamonds show the SHMR of satellites of MW analogues from other simulations – the DC Justice League (Applebaum et al. 2021) and NIHAO (Buck et al. 2019), respectively. The satellites of both simulations agree well with the overall SHMR in TNG50. The DC Justice League extends to particularly small stellar masses due to their high level of resolution.

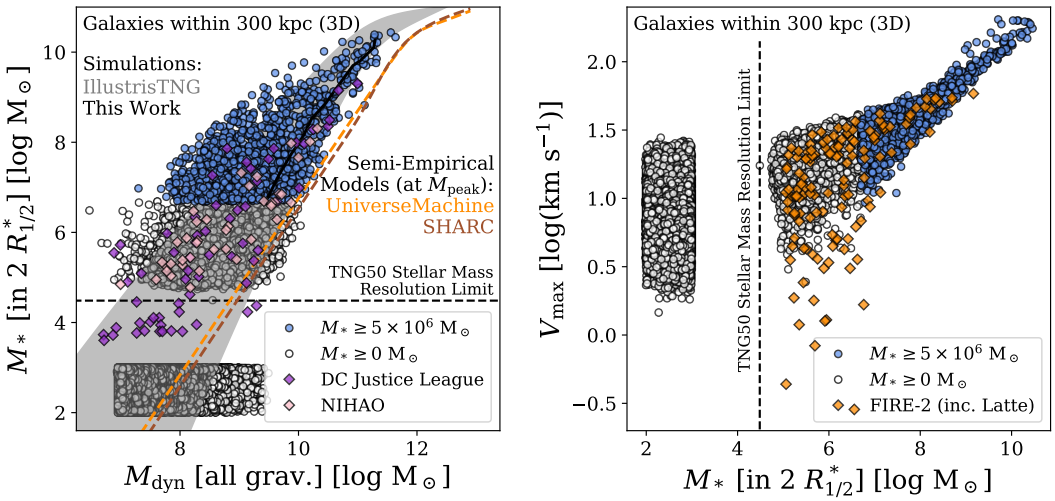

Figure 4.2: Properties and scaling relations of satellites and subhaloes around MW/M31-like galaxies in TNG50. In all panels, I require galaxies and subhaloes to be located within 300 kpc of their host. Blue circles correspond to satellite galaxies with a stellar mass of $M_* \geq 5 \times 10^6$ M$_\odot$, open circles show satellites and subhaloes with $M_* < 5 \times 10^6$ M$_\odot$, including dark subhaloes that do not host a stellar component. In this case, I assign random values to their stellar properties, disconnected from the main scaling relations. The dashed, black lines denote TNG50's stellar mass resolution limit at $10^{4.5}$ M$_\odot$, slightly below the mass of the target stellar particle after accounting for mass loss. *Left panel:* stellar-to-halo mass relation (SHMR), as stellar mass M_* (within twice the stellar half-mass radius) as a function of dynamical mass M_{dyn} (all gravitationally bound particles). For visualisation purposes, dark subhaloes are assigned a random stellar mass between 10^2 and 10^3 M$_\odot$. I compare the SHMR of my sample of satellite galaxies (solid, black curve) to results from simulations and semi-empirical models. The grey shaded area denotes the scatter for the SHMR of satellites in hosts of $10^{12} - 10^{13}$ M$_\odot$ from Chapter 3.2.2 and Table 3.3; the purple diamonds display satellite galaxies from the DC Justice League simulations of MW analogues (Applebaum et al. 2021), while the pink diamonds correspond to satellites of MW-like galaxies from NIHAO (Buck et al. 2019). The dashed curves display extrapolations for satellite galaxies from semi-empirical models: UniverseMachine (orange curve, Behroozi et al. 2019) and SHARC (brown curve, Rodríguez-Puebla et al. 2017). Note that both semi-empirical models define subhalo mass as peak mass, not as a dynamical mass at the present-day. *Right panel:* maximum circular velocity V_{max} as a function of stellar mass. Additionally, I compare to satellites of Local Group- and MW-like hosts from the FIRE-2 simulations (orange diamonds, Garrison-Kimmel et al. 2019); this includes satellites of the Latte simulation (Wetzel et al. 2016).

Finally, I compare to *extrapolations* for satellite galaxies of the semi-empirical models UNIVERSEMACHINE (dashed orange curve, Behroozi et al. 2019) and SHARC (dashed, brown curve Rodríguez-Puebla et al. 2017). Since both models consider satellite dynamical masses at their peak – as opposed to the present-day – the shift of the UNIVERSEMACHINE and SHARC SHMRs towards larger dynamical masses is expected (see Chapter 3.3.1 for a discussion). These differences between TNG50 and semi-empirical SHMRs hold regardless of whether I consider satellite populations of my full sample of TNG50 MW/M31-like hosts or simply the satellites of hosts that are centrals. Furthermore, it should be noted that both semi-empirical models were calibrated for more massive galaxies: Rodríguez-Puebla et al. (2017) even state that their SHMR should only be trusted down to (sub)halo masses of $10^{10.3}$ $M_\odot$. I merely report these extrapolations as references.

Relation of maximum circular velocity and stellar mass

The right panel of Figure 4.2 depicts the relation of the circular velocity profile's maximum $V_{\rm max}$ and stellar mass. $V_{\rm max}$ is defined as the maximum value of a subhalo's spherically-averaged circular velocity curve including all matter components: dark matter, stars, and gas. The satellites form a continuous relation in which their scatter increases substantially towards lower masses. Furthermore, I compare to satellite galaxies from the FIRE-2 simulations (orange diamonds, Garrison-Kimmel et al. 2019), which includes satellites of the Latte simulation (Wetzel et al. 2016). For the most part, their relation of maximum circular velocity and stellar mass is well in agreement with the satellite population of TNG50. At stellar masses below 10^7 $M_\odot$, their scatter surpasses TNG50's relation significantly, with FIRE-2 galaxies reaching smaller $V_{\rm max}$ values than any TNG50 galaxy at fixed satellite stellar mass.

Other observable dwarf properties

I illustrate the relation of absolute *r*-band magnitudes $M_{\rm r}$ and stellar mass in the top left panel of Figure 4.3. The TNG50 satellites exhibit a tight correlation, in agreement with satellite galaxies of the MW and M31. It should be noted that McConnachie (2012) and McConnachie et al. (2018) assume a *V*-band mass-to-light ratio of 1 for simplicity, so the MW and M31 satellites should in reality have slightly different stellar masses. However, these differences should not be significant. In this case, I convert absolute *V*-band luminosities from McConnachie (2012) and McConnachie et al. (2018) to the *r*-band using the luminosities' correlation in TNG50. This relation was determined using least squares minimisation:

$$M_{\rm r} = M_{\rm V} - 0.23\,\text{mag}. \tag{4.3}$$

The top right panel of Figure 4.3 depicts the size-mass relation using 2D stellar half-light radii (*V*-band) for TNG50 satellites with $M_* > 2 \times 10^6$ $M_\odot$, as well as for satellites of the MW (red diamonds), M31 (brown diamonds), and the DC Justice

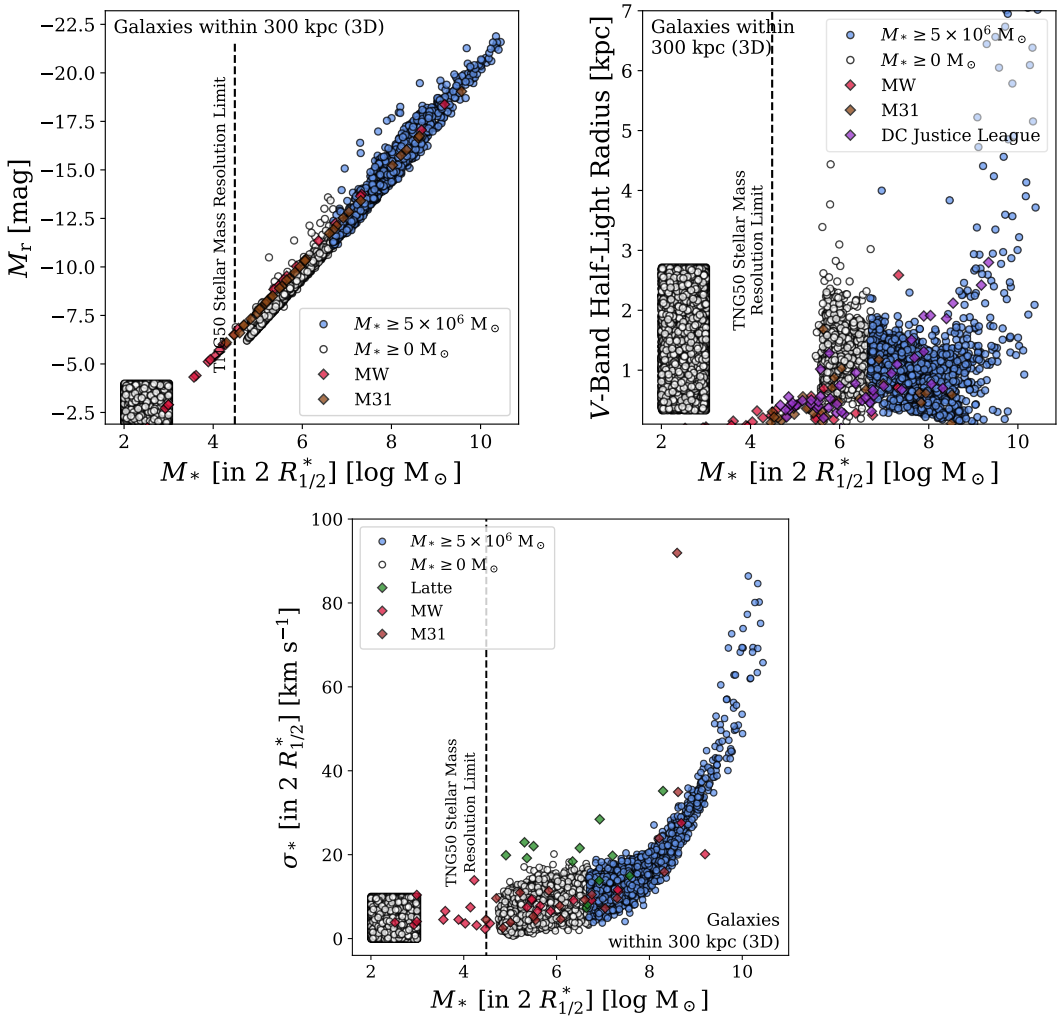

Figure 4.3: Further properties and scaling relations of satellites and subhaloes around MW/M31-like galaxies in TNG50. In all panels, I require galaxies and subhaloes to be located within 300 kpc of their host. Blue circles correspond to satellite galaxies with a stellar mass of $M_* \geq 5 \times 10^6$ M$_\odot$, open circles show satellites and subhaloes with $M_* < 5 \times 10^6$ M$_\odot$, including dark subhaloes that do not host a stellar component. In this case, I assign random values to their stellar properties, disconnected from the main scaling relations. The dashed, black lines denote TNG50's stellar mass resolution limit at $10^{4.5}$ M$_\odot$, slightly below the mass of the target stellar particle after accounting for mass loss. *Top left panel:* absolute r-band magnitude M_r as a function of stellar mass. Dark subhaloes are assigned absolute magnitudes ranging from -2 to -4. I compare to satellite galaxies from the MW (red diamonds, McConnachie 2012) and M31 (brown diamonds, McConnachie et al. 2018). *Top right panel:* size-mass relation using 2D stellar half-light radii (V-band) for TNG50 satellites and subhaloes. I compare to observed satellites of the MW and M31 (red and brown diamonds, respectively), as well as the DC Justice League simulations (purple diamonds). As TNG50, these works employ 2D stellar half-light radii (V-band). *Bottom panel:* stellar 3D velocity dispersion σ_* as a function of stellar mass. Dark subhaloes are assigned velocity dispersions of $\sigma_* = 0 - 10$ km s^{-1}. I compare to simulated satellite dwarf galaxies from the Latte simulation (green diamonds) and observed dwarfs from the MW and M31 (red and brown diamonds, McConnachie 2012; McConnachie et al. 2018, respectively).

League simulations (purple diamonds). There is a reasonable level of agreement between TNG50 and the satellites of both the Galaxy and Andromeda, as well as of the DC Justice League simulations, at the masses where a comparison is possible. In fact, here TNG50 sizes are 2D circularised radii from random projections and are not measured for galaxies with fewer than 10 stellar particles. More information on the size-mass relation in TNG50, outside of the context of MW/M31-like galaxies, can be found in Pillepich et al. (2019) and Zanisi et al. (2020).

Finally, I present the stellar 3D velocity dispersion σ_* as a function of stellar mass in the bottom panel of Figure 4.3. The stellar 3D velocity dispersion of simulated satellites is measured as the standard deviation of the velocities of all stellar particles within two times the stellar half-mass radius weighted by their respective stellar mass. The satellites form a continuous relation, in which the stellar 3D velocity dispersion increases significantly for more massive satellites. I include satellites from the Latte simulation (green diamonds, Wetzel et al. 2016), as well as from the MW and M31 as comparison (McConnachie 2012; McConnachie et al. 2018). While many of Latte's satellites exhibit slightly larger velocity dispersions than TNG50, most MW and M31 satellites agree reasonably well[2].

4.2.2 Satellite abundance of MW/M31-like galaxies in TNG50

I present the satellite abundance of all 198 MW/M31-like galaxies in TNG50 as cumulative stellar mass functions in the left panel of Figure 4.4. Satellites are defined as galaxies within a three-dimensional aperture of 300 kpc of their host and are required to have a stellar mass of at least 5×10^6 $M_\odot$. This minimum mass allows for an adequate level of resolution (see Appendix C for a detailed discussion) and approximately corresponds to the MW's own satellite galaxy Leo I.

Thin coloured curves in the background of Figure 4.4, left panel, correspond to the individual satellite stellar mass functions of all MW/M31-like hosts in TNG50, crosses denote systems with only a single satellite, while hosts with no satellites whatsoever are depicted as curves with $N_{\rm sat} < 1$: these are 6 of 198 hosts.

MW/M31-like galaxies in TNG50 exhibit a remarkable diversity with significant host-to-host scatter regarding their satellite populations, with total satellite counts ranging from 0 to 20. The thick, black curve displays the median satellite stellar mass function for MW/M31-like galaxies in TNG50, starting with the most massive satellite $M_* \sim 10^{8.5}$ $M_\odot$ and reaching a total number of five satellites down to $M_* \sim 10^{6.9}$ $M_\odot$. However, there is a significant amount of scatter, as shown by the grey shaded area denoting the $16^{\rm th}$ and $84^{\rm th}$ percentiles. The most massive satellite's stellar mass can vary by ± 1 dex, while the total number of satellites can range from 2 to 11 within the percentile range. This diversity between satellite systems persists

[2]There might be an apparent discrepancy between the stellar velocity dispersion and their maximum circular velocity in the right panel of Figure 4.2, as the Latte satellites are included in the FIRE-2 sample of Garrison-Kimmel et al. (2019). I speculate that this difference is due to different ways of measuring the velocity properties of satellites between the two studies.

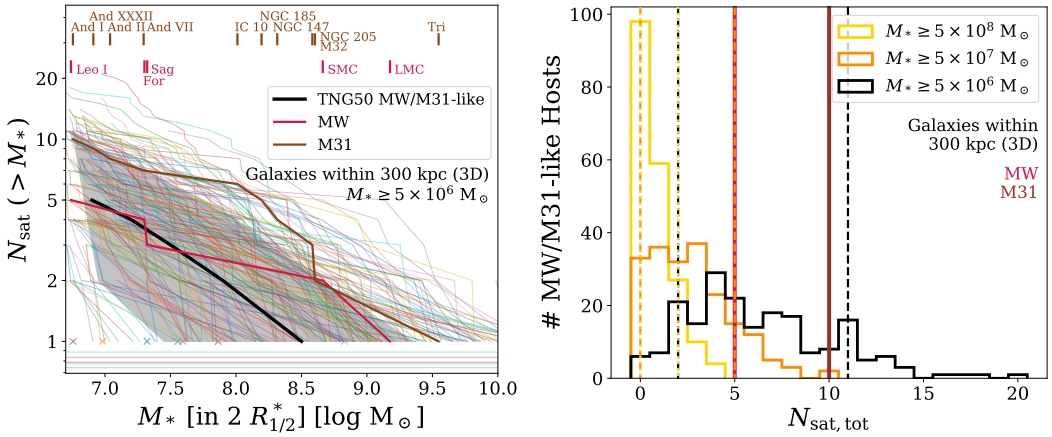

Figure 4.4: Satellite demographics around MW/M31-like galaxies in the TNG50 simulation at z = 0. *Left panel:* satellite abundance as cumulative stellar mass function for MW/M31-like hosts in TNG50. I define satellites as galaxies within 300 physical kpc (3D) of their host and with stellar masses of at least 5×10^6 M$_\odot$ (within twice the stellar half-mass radius $R^*_{1/2}$). The thin, coloured curves in the background illustrate the satellite systems of individual TNG50 hosts with crosses corresponding to systems with only a single satellite and horizontal lines with $N_{\rm sat} < 1$ denoting systems with no satellites meeting the selection: these are 6 among 198 systems. The thick, black curve and grey shaded area depict their median and scatter as 16$^{\rm th}$ and 84$^{\rm th}$ percentiles, computed in bins of satellite stellar mass and including galaxies with zero satellites in the calculations. Furthermore, I compare my findings in TNG50 to satellite abundances of the MW (red curve, McConnachie 2012) and M31 (brown curve, McConnachie et al. 2018). *Right panel:* distribution of total satellite abundance $N_{\rm sat,tot}$ around MW/M31-like hosts in TNG50 and its dependence on the imposed minimum stellar mass. I compare satellite systems with $M_* \geq 5 \times 10^8$ M$_\odot$ (yellow histogram), $M_* \geq 5 \times 10^7$ M$_\odot$ (orange histogram), and $M_* \geq 5 \times 10^6$ M$_\odot$ (black histogram; my fiducial selection). Dashed and dotted lines denote their scatter as 16$^{\rm th}$ and 84$^{\rm th}$ percentiles: 0 and 2 for satellites with $M_* \geq 5 \times 10^8$ M$_\odot$, 0 and 5 for $M_* \geq 5 \times 10^7$ M$_\odot$, as well as 2 and 11 for $M_* \geq 5 \times 10^6$ M$_\odot$. Furthermore, I include the total satellite abundances of the MW and M31 as solid, vertical lines (red and brown lines, respectively). Alternative versions of this figure, where satellite stellar masses are normalised to either host halo or host stellar masses, are given in Appendix D.

independent of host mass: in Appendix D and Figure D.1, I provide the same functions for satellite abundances normalised by host halo mass and host stellar mass.

I compare the findings of TNG50 to the local satellite systems of the MW and M31 (within 300 kpc), shown as thick, red and brown curves, respectively (McConnachie 2012; McConnachie et al. 2018). The MW's satellite stellar mass function falls well within TNG50's 1σ scatter. While its low-mass end coincides with the TNG50 median, its massive end reaches the upper limits of my scatter due to the presence of both the Small and Large Magellanic Cloud (SMC and LMC, respectively). M31, on the other hand, is slightly more satellite-rich than TNG50's 1σ scatter. However, it agrees well with many other, individual TNG50 MW/M31-like hosts of my sample. In fact, it should be noted that in my sample of TNG50 MW/M31-like hosts, which is intrinsically volume-limited, the stellar mass distribution is skewed towards masses more similar to the MW rather than the more massive M31 (see Figure 4.1): if instead I were to focus specifically on TNG50 M31 analogues in the left panel of Figure 4.4, the agreement between the TNG50 median and the observed M31's satellite mass

function would be notable. I explore the dependence of satellite abundance on both host selection and host properties further in Chapters 4.2.4 and 4.2.7.

I quantify the scatter in total satellite abundance, as well as the effects of my satellite selection and the imposed minimum stellar mass for satellite galaxies in the right panel of Figure 4.4. Here, I show the distribution of the total number of satellites $N_{\rm sat,tot}$ within 300 kpc (3D) of MW/M31-like hosts for three selections in stellar mass: $M_* \geq 5 \times 10^8$ M$_\odot$ (yellow histogram), $M_* \geq 5 \times 10^7$ M$_\odot$ (orange histogram), and $M_* \geq 5 \times 10^6$ M$_\odot$ (black histogram; my fiducial selection). The dotted and dashed vertical lines illustrate the scatter of the distribution of total satellite abundance as 16$^{\rm th}$ and 84$^{\rm th}$ percentiles. As it can be seen, the abundance of satellites with $M_* \geq 5 \times 10^6$ M$_\odot$ ranges from 6 MW/M31-like hosts with no satellites to one host with 20 satellites and peaks at a total of 4 satellites for 29 MW/M31-like hosts. For more massive satellites, e.g. $M_* \geq 5 \times 10^8$ M$_\odot$, the number of hosts with no satellites whatsoever increases to 98. In the right panels of Figure D.1 in Appendix D, I provide a similar quantification of the scatter in satellite abundances where the satellites are counted based on their mass normalised to their host's total or stellar mass: when the mass of satellites is normalised to their host's, the degree of diversity in total satellite abundance remains the same regardless of the adopted minimum satellite stellar mass, consistently with Poisson statistics (see also Chua et al. 2017, for a discussion on how the scatter can in fact become super-Poissonian at very low (subhalo) mass ratios).

Massive satellites around MW/M31-like hosts

The presence of massive satellites such as the LMC and SMC around the Galaxy, or Triangulum, M32, and NGC205 around Andromeda is an interesting feature that has been studied in previous theoretical works regarding their general abundance, orbital evolution, or correlations with the mass of their host (Tollerud et al. 2011; Busha et al. 2011a; Boylan-Kolchin et al. 2011; Patel et al. 2017; Shao et al. 2018). However, as previous works thus far have been based mostly on N-body only or DM-only calculations, it is useful to query the TNG50 systems as to the presence of massive satellites.

Interestingly, a significant fraction of TNG50 MW/M31-like galaxies include SMC and/or LMC-like satellites within 300 kpc. Assuming stellar masses of $10^{8.7\pm0.1}$ M$_\odot$ for SMC-like and $10^{9.2\pm0.1}$ M$_\odot$ for LMC-like satellites (McConnachie 2012), I find that 42 MW/M31-like galaxies host an SMC-like satellite (i.e. 21 per cent of hosts), 12 host an LMC-like galaxy as their most massive satellite (6 per cent of hosts), and 6 MW/M31-like hosts include both an SMC- and an LMC-like galaxy in their satellite population (with the LMC-like galaxy as their most massive satellite). This corresponds to 3 per cent of my MW/M31-like galaxies hosting both an SMC- and an LMC-like galaxy, and it is remarkably consistent with the results of Liu et al. (2011), which were based on SDSS data. However, it should be noted that these observations adopt different, luminosity-based selection criteria for both host and satellite

# MW/M31-like hosts with	±0.1 dex	±0.15 dex	±0.2 dex
SMC	42	62	77
LMC	12 (21)	20 (32)	27 (42)
LMC & SMC	6 (7)	10 (16)	18 (25)
M32/NGC205	48	63	75
Tri	7 (11)	14 (20)	21 (25)
Tri & M32/NGC205	2 (4)	4 (7)	11 (13)
Tri & M32 & NGC205	0 (0)	1 (1)	2 (3)
Med. $M_{\rm host}$ [log $\rm M_\odot$]			
SMC	12.2	12.3	12.3
LMC	12.3	12.3	12.2 (12.3)
LMC & SMC	12.2	12.3	12.3
M32/NGC205	12.3	12.2	12.3
Tri	12.3 (12.2)	12.3	12.3
Tri & M32/NGC205	12.4	12.4	12.4
Tri & M32 & NGC205	–	12.4	12.4

Table 4.2: Number of TNG50 MW/M31-like hosts in my fiducial sample with massive satellites such as the SMC and LMC, or M32, NGC205, and Triangulum (Tri). I adopt various mass bins for the reference mass of these massive satellites in order to reflect uncertainties in their measurements: ±0.1 dex, ±0.15 dex, and ±0.2 dex. LMC and Triangulum numbers without parentheses assume them to be the most massive satellite of their host, while the numbers inside parentheses allow for even more massive satellites in the same system. I adopt stellar mass estimates from McConnachie (2012) and McConnachie et al. (2018): 4.5×10^8 $\rm M_\odot$ for the SMC, 1.5×10^9 $\rm M_\odot$ for the LMC, 3.8×10^8 $\rm M_\odot$ for M32 and NGC205, as well as 3.5×10^9 $\rm M_\odot$ for Triangulum. Furthermore, I give the median host mass for all subsamples in the bottom part of the table. I add values in parentheses for systems with even more massive satellites than the LMC or Triangulum if their median host mass is different from the samples in which the LMC or Triangulum is the most massive satellite in the system.

galaxies, as well as spectroscopic distance cuts. As Busha et al. (2011a) show, such differences in sample selections can cause a difference of up to 10 per cent.

I summarise the abundance of SMC- and LMC-like satellites in Table 4.2, including adaptations of different mass bins for their selection. The subhalo IDs of the 6 MW/M31-like hosts with both an SMC- and an LMC-like satellite read: 416713, 430864, 497557, 503437, 511303, and 514829 with host halo masses of $\log M_{\rm 200c}/\rm M_\odot =$ 12.6, 12.3, 12.0, 12.2, 12.1, 12.1, respectively. These systems, as well as the infall history, spatial distribution, and star formation activity of their massive satellites will be addressed in future studies. However, as the data of TNG50 is publicly available, I provide these IDs for anyone who is interested in studying specifically these systems. In practice, the MW/M31-like hosts containing both an SMC- and an LMC-like satellite (assuming a mass bin of ±0.1 dex) cover a mass range of $M_{\rm 200c} = 10^{12} - 10^{12.6}$ $\rm M_\odot$ with a median host mass of $10^{12.2}$ $\rm M_\odot$, while the TNG50 MW/M31 analogues with an LMC-like galaxy as their most massive satellite have

a median host mass of $10^{12.3}$ $M_\odot$. Whereas both of these mass ranges include either a single or two hosts outside of the 10th and 90th percentiles of the host mass range of all TNG50 MW/M31-like galaxies, they fall well within the range of total halo mass estimates of either the Galaxy or Andromeda (see Figure 4.1). While both the median and the range of host masses for TNG50 MW/M31-like galaxies hosting massive, Magellanic Cloud-like satellites agree with previous host mass estimates from Busha et al. (2011b), Cautun et al. (2014b) predict less massive MW-like haloes. However, these are still consistent with some of the individual TNG50 MW/M31-like hosts with massive satellites. Furthermore, it should be noted that both of these works employ DM-only simulations as opposed to TNG50, which includes baryons. Their host mass estimates originate from measurements of maximum circular velocities of Magellanic Cloud-like subhaloes. I find the same host mass estimates when I increase the uncertainties for the stellar masses of SMC- and LMC-like satellites. With median host masses of $10^{12.3}$ $M_\odot$, these MW/M31-like systems lie between the median and the 90th percentile of my complete sample of TNG50 MW/M31-like analogues.

Table 4.2 shows also the number of TNG50 hosts around which satellites like M32 or NGC205 (with a stellar mass of 3.8×10^8 $M_\odot$), and/or like Triangulum orbit (with 3.5×10^9 $M_\odot$ in stars; McConnachie et al. 2018). However, the stellar mass functions of some of my TNG50 systems in Figure 4.4 extend even further beyond massive satellites such as the LMC or Triangulum. With stellar masses of more than 10^{10} $M_\odot$, they are almost as massive as the host galaxies themselves. These systems do not represent actual satellites but correspond to galaxies that are about to merge with the MW/M31-like host, representing imminent major mergers (yet, by selection, with $M_* < 10^{10.5}$ $M_\odot$ at $z = 0$).

TNG50 satellite systems most similar to the MW and M31

I conclude this overview of TNG50 MW/M31-like galaxies by visually contrasting MW- and M31-like satellite systems in TNG50 in Figures 4.5 and 4.6. Here, I show the projected stellar mass density of the 10 TNG50 galaxies that are most similar to either the MW or Andromeda, respectively. These hosts were selected by computing the residual sum of squares between the simulated and observed satellite mass functions above 5×10^6 $M_\odot$ over all satellite stellar mass bins and by identifying the systems with the lowest values. The subhalo IDs of MW analogues read: 555013, 517271, 536654, 513845, 574037, 482155, 515296, 526029, 499704, 504559. Those of M31 analogues read: 458470, 433289, 490814, 474008, 342447, 471248, 429471, 470345, 436932, 438148. Evidently, M31-like TNG50 systems are richer in more massive satellites than MW TNG50 analogues and exhibit more luminous, as well as extended stellar haloes. As I will explicitly demonstrate in Chapter 4.2.7, such a difference is to a first order related to Andromeda being a more massive galaxy than the MW, possibly also residing in a more massive host halo. As there are apparent qualitative similarities between my TNG50 M31 analogues and observations of M31 and its

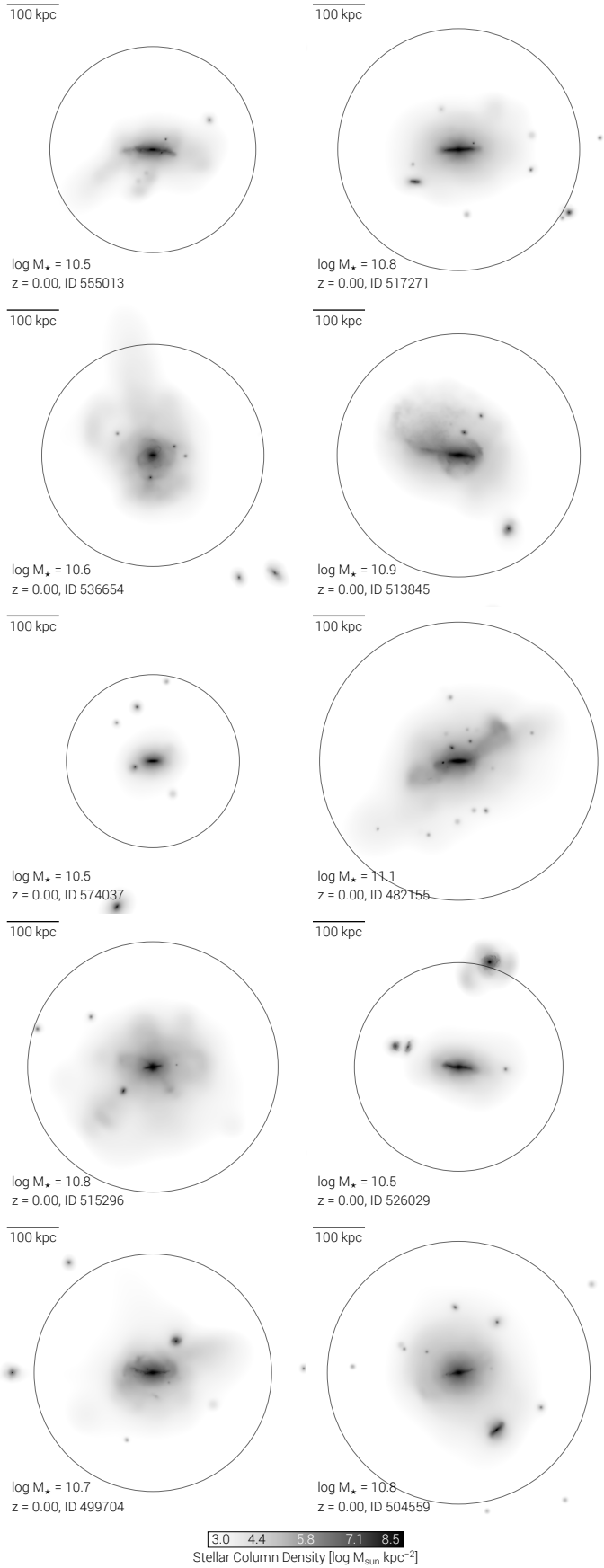

Figure 4.5: Stellar column density on 600 kpc per side of the ten TNG50 galaxies at $z = 0$ (edge-on projection) whose satellite stellar mass function is the most similar to that of the Galaxy. Circles denote the virial radius (R_{200c}) of the underlying DM host.

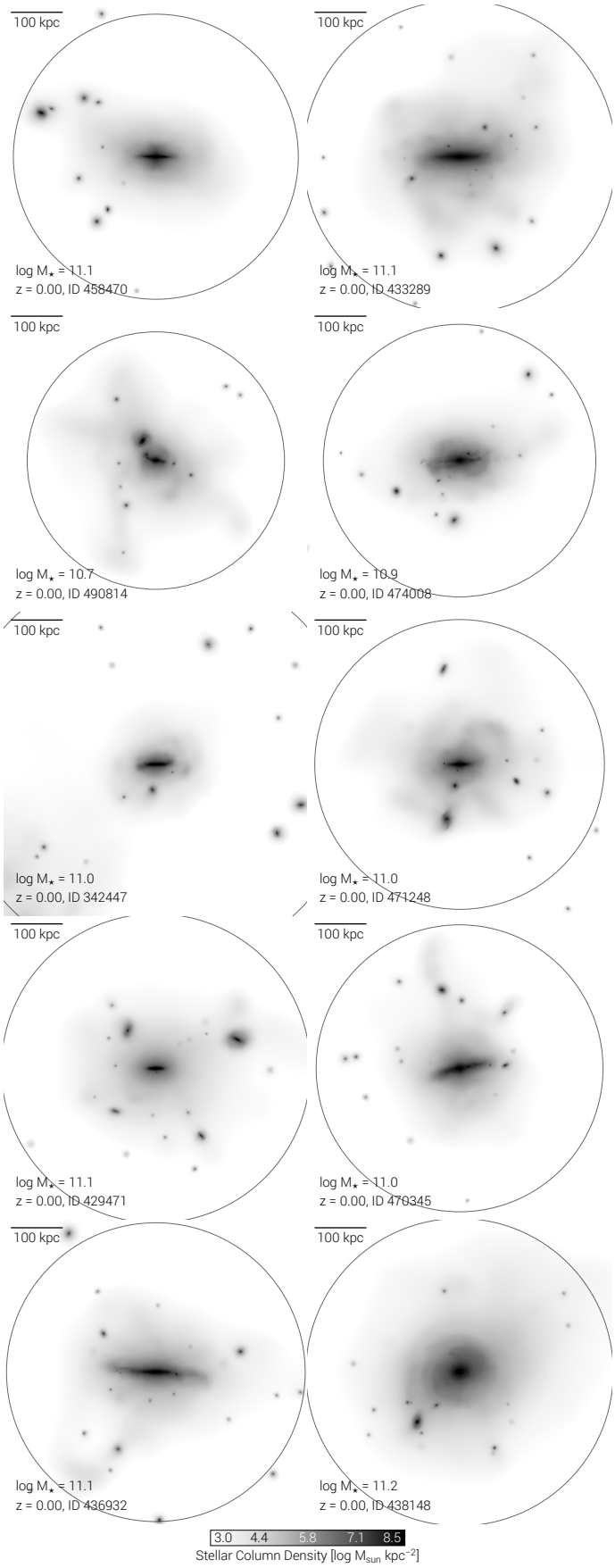

Figure 4.6: As in Fig. 4.5 but for the ten TNG50 galaxies at $z = 0$ whose satellite stellar mass function is the most similar to that of Andromeda. In TNG50, the latter are usually more massive and reside in more massive haloes (larger R_{200c}) than the satellite systems that are more similar to the Galaxy's.

satellite system from the Pan-Andromeda Archaeological Survey (PAndAS, Martin et al. 2013; Ibata et al. 2014), future quantitative comparisons might be warranted.

4.2.3 Comparisons to observations

Comparison to the SAGA survey

I compare the TNG50 results to findings from the SAGA survey (Geha et al. 2017; Mao et al. 2021) in Figure 4.7. In its top panel, I compare TNG50 and SAGA at face value, i.e. using my fiducial selection of TNG50 MW/M31-like hosts. In the bottom panel of Figure 4.7, instead, I compare the results of the SAGA survey to the satellite abundances of TNG50 hosts matched to replicate the SAGA host selection (see Chapter 4.1.1 for more details on host selections). In both cases, I characterise satellite abundances in terms of their *r*-band luminosity and include 34 MW-like hosts from the second stage of the SAGA survey (Mao et al. 2021). Their two remaining MW analogues host no satellites whatsoever and are not shown here. The SAGA galaxies are located at a distance of $20 - 40$ Mpc and were selected by assuming a MW-like halo mass of $0.6 - 2.7 \times 10^{12}$ $M_\odot$ and by using abundance matching to infer a *K*-band luminosity range of $-23 > M_K > -24.6$ as a proxy for stellar mass. Furthermore, SAGA hosts are required to be isolated in order to match the MW's large-scale environment. For these hosts, satellites are considered within a projected aperture of 300 kpc and a line-of-sight velocity of ± 250 km s^{-1} with an absolute *r*-band magnitude of $M_r < -12.3$, which are depicted as thick, coloured curves in the top panel of Figure 4.7. The redshifts of all SAGA satellites have been spectroscopically confirmed.

Similar to Figure 4.4, the satellite systems of individual TNG50 MW/M31-like hosts are shown in the background as thin, grey curves, while the thick, black curve corresponds to the median TNG50 satellite luminosity function and the grey shaded region denotes its scatter as 16$^{\text{th}}$ and 84$^{\text{th}}$ percentiles. For this comparison, I do not impose a minimum stellar mass to TNG50 satellites and rather match the satellite selection criteria of the SAGA survey (see Chapter 4.1.2). Furthermore, I include the satellite luminosity functions of both MW and M31 (within 300 kpc) as an additional comparison (red and brown curves, respectively), with M_r for MW/M31 satellites obtained from the M_V values of McConnachie (2012) and McConnachie et al. (2018) using the TNG50 M_r vs. M_V relation from Equation (4.3).

Overall, the top panel of Figure 4.7 displays a remarkable agreement between the *r*-band satellite abundances of TNG50, the SAGA galaxies, as well as the MW and M31. Whereas this level of agreement may be coincidental – as there the comparison is made at face value, i.e. without ensuring the compatibility of the hosts in the simulation and observed samples – this is in fact confirmed by the results in the bottom panel of Figure 4.7, where I employ a SAGA-like selection of TNG50 hosts (see Chapter 4.1.1 for details). The satellite systems of the SAGA-like TNG50 hosts are well in agreement with the MW and M31, as well as the actual MW-like galaxies

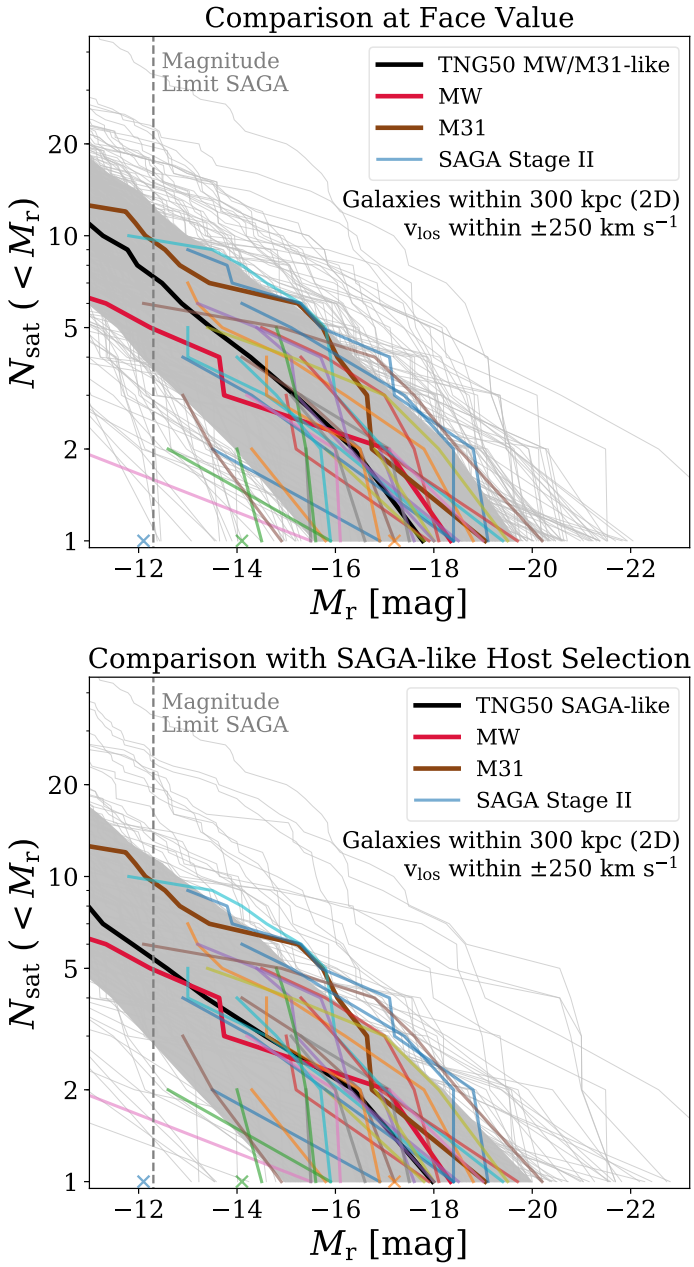

Figure 4.7: Satellite abundances in TNG50 and observations from the SAGA survey. I characterise satellite systems using satellite luminosity functions in the *r*-band for galaxies within a projected aperture of 300 kpc and line-of-sight velocities of ±250 km s^{-1} of their host galaxy (with no requirement on stellar mass). In both panels, the thin, grey curves in the background illustrate the satellite systems of individual TNG50 hosts, while the thick, black curves and grey shaded areas depict their median and scatter as 16th and 84th percentiles, computed in bins of satellite luminosity and including galaxies with zero satellites in the calculations. Thick, coloured curves correspond to the satellite systems of 34 observed MW-like galaxies from the SAGA survey's second stage (Mao et al. 2021, two more of their MW analogues host no satellites whatsoever and are thus not shown here), red and brown curves show the observed satellite systems of the MW and M31 (McConnachie 2012; McConnachie et al. 2018). *Top panel:* comparison at face value, i.e. I compare the satellite systems of observed hosts to those of my fiducial selection of TNG50 MW/M31-like hosts. *Bottom panel:* matched comparison, i.e. I select TNG50 hosts according to the selection criteria of the observations; furthermore, for each observed host, I choose and use only the three TNG50 hosts with closest *K*-band luminosity (see Chapter 4.1.1 for details).

of the SAGA survey. All satellite luminosity functions of observed galaxies lie either within the 1σ scatter of TNG50 or are consistent with the satellite abundances of individual TNG50 hosts. Compared to my fiducial selection of TNG50 MW/M31-like hosts, the SAGA-like selection is slightly less satellite rich. Furthermore, they exhibit a slightly larger scatter both in terms of their brightest satellite and their total satellite abundance.

Comparison to Local Volume hosts

In Figure 4.8, I quantify the comparison between TNG50 and the satellite systems of hosts in the Local Volume (i.e. within 12 Mpc), examined by Carlsten et al. (2021) using CFHT/MegaCam data. In the top panel, the comparison is "at face value", i.e. made in comparison to the TNG50 fiducial sample of MW/M31-like galaxies, whereas in the bottom panel I attempt to match the host selection of the Carlsten et al. (2021) sample. Namely, for each observed galaxy, I select three TNG50 central and disky galaxies with the closest K-band luminosity to the observed ones (see Chapter 4.1.1).

The hosts of Carlsten et al. (2021) span a halo mass range of $0.8 - 3 \times 10^{12}$ $M_{\odot}$, similar to the 10^{th} and 90^{th} percentiles of my TNG50 host halo mass range. In order to ensure completeness of the observed satellite systems down to $M_V \sim -9$, they exclusively consider satellites within the inner 150 kpc (3D) of their host galaxies. The satellite galaxies' line-of-sight distances are estimated using either surface brightness fluctuations (SBF) or the tip of the red giant branch (TRGB). As in the observations, I only count TNG50 galaxies within a projected aperture of 150 kpc of their host as satellites and do not require a minimum stellar mass. Furthermore, I limit satellite galaxies to line-of-sight distances of 500 kpc. Carlsten et al. (2021) include a comparison with satellite systems from TNG100 in their study and adopt this line-of-sight criterion as a compromise between SBF and TRGB distance estimates.

In Figure 4.8, the six satellite systems from Carlsten et al. (2021), as well as those of the MW and M31 are depicted as V-band luminosity functions by thick, coloured curves. The median and scatter of the TNG50 hosts are shown as thick, black curve and grey shaded area (thin, grey curves for individual TNG50 hosts). Both the top and bottom panel of Figure 4.8 show that, whereas most observed Local Volume systems overall fall within the satellite abundances from TNG50 and lie largely within the TNG50 1σ scatter, they are somewhat more concentrated on the satellite-richer side. Imposing an LV-like selection makes the TNG50 median and scatter to shift to slightly lower satellite abundances than those of the fiducial MW/M31-like selection (top vs. bottom panel).

Interestingly, the galaxies observed by Carlsten et al. (2021) exhibit a smaller host-to-host scatter for satellites in their host's inner regions, i.e. within 150 projected kpc, in comparison to satellite abundances measured across larger apertures: NGC4258, NGC4631, NGC4565, and M101, as well as the MW and M31, exhibit remarkably similar satellite abundances compared to their satellites counted across

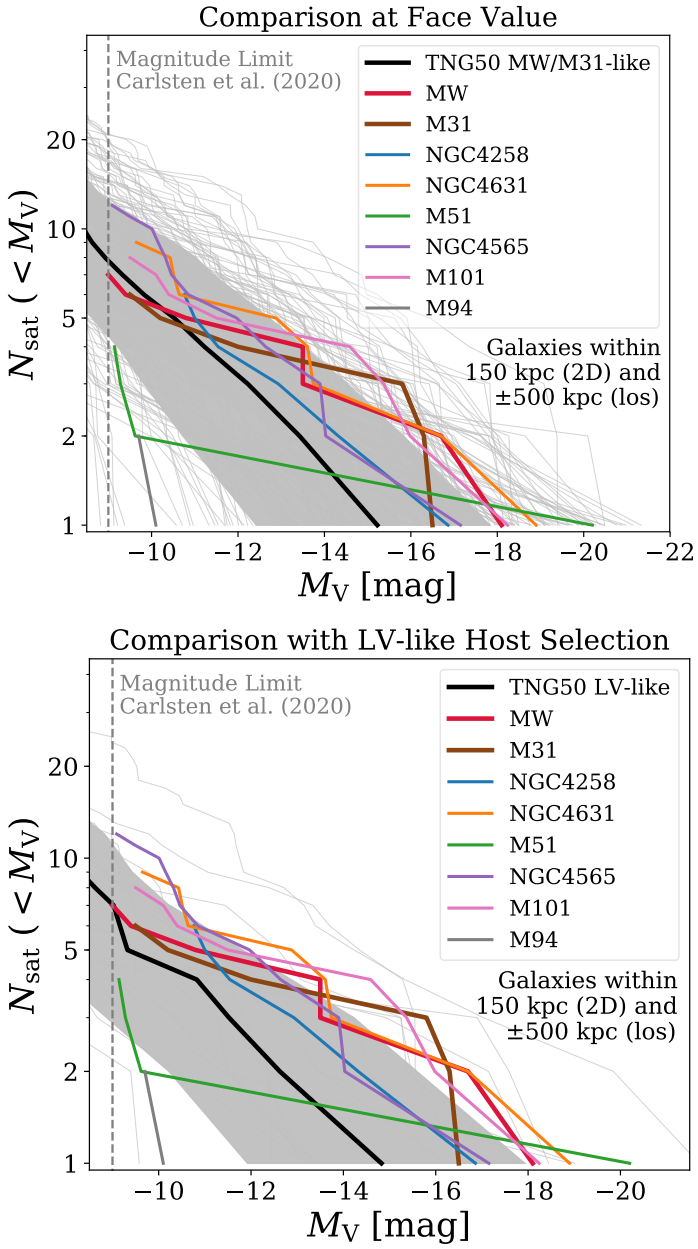

Figure 4.8: Satellite abundances in TNG50 and observed Local Volume galaxies. I characterise satellite systems using satellite luminosity function in the V-band comparing TNG50 to 8 hosts in the Local Volume from Carlsten et al. (2021) (including the MW and M31). Satellites are restricted to the inner (projected) 150 kpc of their host systems and to $\pm$500 kpc along the line of sight (los). In both panels, the thin, grey curves in the background illustrate the satellite systems of individual TNG50 hosts, while the thick, black curves and grey shaded areas depict their median and scatter as 16th and 84th percentiles, computed in bins of satellite luminosity and including galaxies with zero satellites in the calculations. Thick, coloured curves correspond to the satellite systems of the 8 Local Volume hosts. *Top panel:* comparison at face value, i.e. I compare the satellite systems of observed hosts to those of my fiducial selection of TNG50 MW/M31-like hosts. *Bottom panel:* matched comparison, i.e. I select TNG50 hosts according to the selection criteria of the observations; furthermore, for each observed host, I choose and use only the three TNG50 hosts with closest K-band luminosity (see Chapter 4.1.1 for details).

larger apertures (top panel of Figure 4.7 vs. top panel of Figure 4.8). While the scatter between individual TNG50 MW/M31-like hosts seems to be slightly smaller compared to my fiducial satellite selection in the left panel of Figure 4.4, further analysis of the spatial distribution of satellite galaxies – especially comparing the inner and outer regions of TNG50 hosts – will be addressed in future studies (Bose et al. in prep.).

4.2.4 Comparison to previous cosmological hydrodynamical simulations

I compare the satellite abundance of MW/M31-like galaxies in TNG50 to previous cosmological hydrodynamical galaxy simulations in Figure 4.9. Note that all of these simulations employ different definitions of MW- and/or M31-like galaxies with different host mass ranges on different mass types, as well as various other criteria on their morphology, environment, or merger history. Hence, as it is still useful to see all previous and current results in single plots, I consider such comparisons at face value. I summarise the host selection criteria of all simulations addressed in this chapter in Table 4.1. This means that although there is overlap between models with respect to their adopted mass range or some of their other criteria, all simulations study somewhat different kinds of host galaxies or samples with different distributions of galaxy or host mass. Therefore, some deviations concerning their individual or average satellite abundances are to be expected. Conversely, agreement across galaxy formation models cannot be over-interpreted as consistency, at least not before galaxy-to-galaxy variations and trends with host properties are accounted for.

The top panel of Figure 4.9 compares the satellite stellar mass functions of TNG50 – individual hosts as thin, grey curves in the background, as well as their median and scatter as thick, black curve and grey shaded area – to the TNG100 median (red curve), the Latte simulation (blue curve, Wetzel et al. 2016), FIRE-2 (brown curves, Garrison-Kimmel et al. 2019), as well as the scatter of Auriga (purple shaded area, Simpson et al. 2018) and APOSTLE (green shaded area, Sawala et al. 2016a). These comparisons are discussed here at face value, i.e. without adjusting for the different nominal selections of the underlying host properties – I expand on the effects of different host selections in Figure 4.10.

MW/M31-like systems in TNG100 contain systematically both a lower number of satellites and overall less massive satellites – an effect of decreased numerical resolution. I extensively discuss the impact of resolution on the abundance of both luminous satellite galaxies and dark subhaloes in more detail in Appendix C. The Latte simulation mostly exhibits a lower satellite abundance than the TNG50 median – albeit well within TNG50's 1σ scatter – but rises to meet the TNG50 median at the low-mass end. While their most massive satellite is $\sim$ 0.4 dex less massive than the TNG50 average, Latte only simulates a single MW-like galaxy. However, satellites as massive as the LMC tend to occur relatively rarely (e.g. Busha et al. 2011a; Liu et al. 2011; Tollerud et al. 2011; González et al. 2013) and it should be noted that Wetzel et al. (2016), in their figure 3, exclude the LMC for its mass and

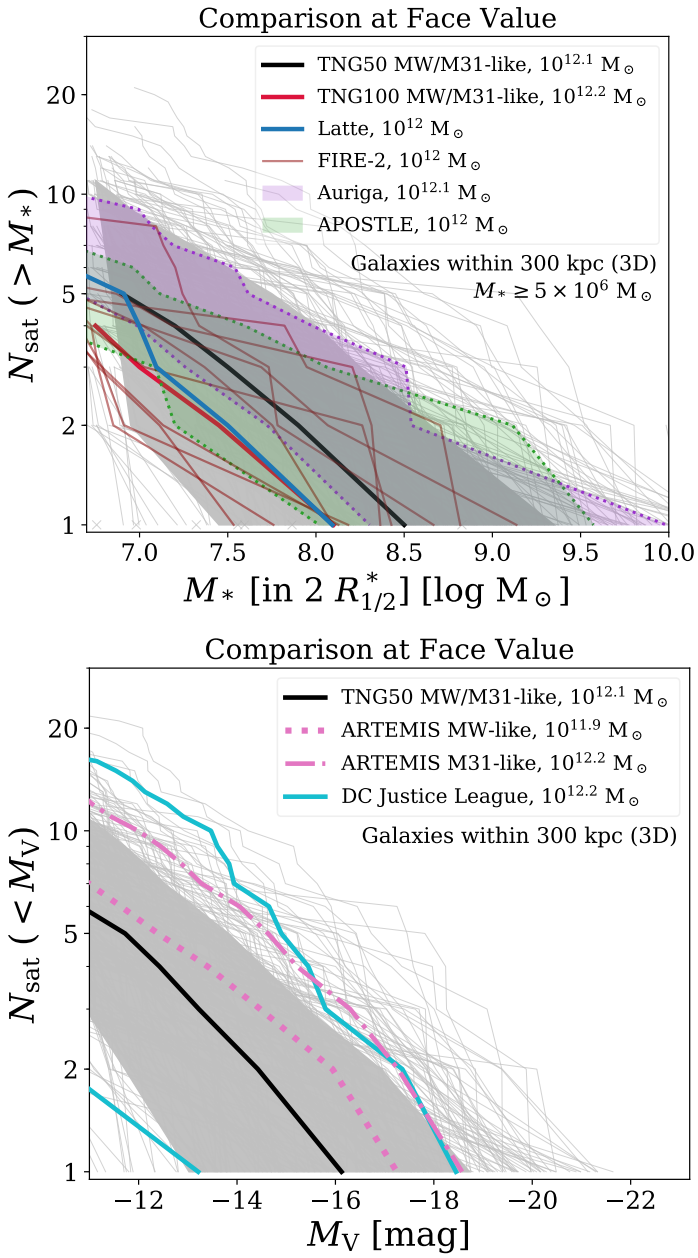

Figure 4.9: Satellite abundance in TNG50 and recent cosmological hydrodynamical simulations. The median host halo mass or host mass range (M_{200c}) of each simulation, i.e. curve, is given in the legend. Both panels depict comparisons at face value, i.e. I compare the satellite systems of previous simulations to those of my fiducial selection of TNG50 MW/M31-like hosts. The thin, grey curves in the background illustrate the satellite systems of individual TNG50 hosts, while the thick, black curves and grey shaded areas depict their median and scatter as 16$^{\rm th}$ and 84$^{\rm th}$ percentiles, computed in bins of satellite stellar mass and including galaxies with zero satellites in the calculations. *Top panel:* satellite stellar mass function comparing the satellite abundance of MW/M31-like galaxies in TNG50 to TNG100 (red curve), Latte (blue curve, Wetzel et al. 2016), FIRE-2 (brown curves, Garrison-Kimmel et al. 2019), Auriga (purple shaded area, Simpson et al. 2018), and APOSTLE (green shaded area, Sawala et al. 2016a). *Bottom panel:* satellite luminosity function in the V-band comparing TNG50 to the ARTEMIS (pink curves, Font et al. 2021a) and DC Justice League simulations (blue curves, Applebaum et al. 2021). The pink, dotted curve depicts the MW-like subsample of ARTEMIS, consisting of hosts with $M_{200c} < 10^{12}$ M$_\odot$, while the pink, dash-dotted curve shows their M31-like subsample with $M_{200c} > 1.2 \times 10^{12}$ M$_\odot$ (see Table 4.1 for their general selection criteria). I include the median host halo masses of all simulations in terms of M_{200c} in the legend.

Sagittarius due to its disruptive state from the reported MW satellite mass function in their comparison of Latte with the actual MW. While the two Local Group-like (LG) pairs and six isolated MW-like hosts of the FIRE-2 simulations exhibit significant scatter, their satellite abundance is overall consistent with MW/M31-like hosts in TNG50, well within TNG50's 1σ scatter. The overall abundances in Auriga extend to both larger numbers and more massive satellite galaxies than the TNG50 median – I expand on this comparison in the following section. The mass of their most massive satellites surpasses my 1σ scatter, however, it is still in agreement compared to individual TNG50 hosts. The LG-like hosts of APOSTLE exhibit similar trends and include a larger number of massive satellites. However, their satellite abundances are overall consistent with either TNG50's median and 1σ scatter or the individual TNG50 MW/M31-like hosts.

I show another set of V-band satellite luminosity functions in the bottom panel of Figure 4.10 and compare TNG50 to recent results from the ARTEMIS (pink curves, Font et al. 2021a) and DC Justice League simulations (blue curves, Applebaum et al. 2021). While ARTEMIS consists of a sample of 45 hosts, I show the average abundances of ARTEMIS subsamples that were specifically matched to either the MW (dotted curve, $M_{200c} < 10^{12}$ M$_\odot$) or M31 (dash-dotted curve, $M_{200c} > 1.2 \times 10^{12}$ M$_\odot$). Both their selections exhibit consistently larger satellite abundances than the TNG50 median, with their MW-like selection within and their M31-like selection outside of TNG50's scatter. However, M31-like hosts in ARTEMIS are still in agreement with the overall satellite abundance of individual TNG50 analogue hosts. The curves from the DC Justice League simulations illustrate the satellite abundances of two individual MW-like galaxies. Both of them lie outside of TNG50's 1σ scatter – one of them on the satellite-richer, the other on the satellite-poorer side – but are consistent with the satellite abundance of individual TNG50 MW/M31-like hosts. These deviations are expected considering the masses of the DC Justice League host haloes. With 0.75 and 2.4×10^{12} M$_\odot$, their halo masses are close to the 10^{th} and 90^{th} percentiles of the halo mass range of TNG50 MW/M31-like hosts.

Overall, I find an encouraging level of apparent agreement with other cosmological simulations. The number of satellites above a given stellar mass is consistently within a factor of 2 of TNG50's median from $M_* = 10^7 - 10^{8.5}$ M$_\odot$. The satellite abundance of MW-, M31-, or LG-like hosts holds across different definitions of host galaxies, different physical models, and various levels of numerical resolution – not just compared to TNG50 but among all simulations in general.

Dependence on host selection

While satellite abundances of different simulations are consistent when compared at face value, the effects of specific host galaxy and halo selections on their present-day satellites remain to be explored. I vary the criteria for the selection of MW/M31-like galaxies in Figure 4.10 and compare their satellite systems to my fiducial selection (black curve, see Chapter 4.1.1 for its specific criteria). For all TNG50 hosts, I define

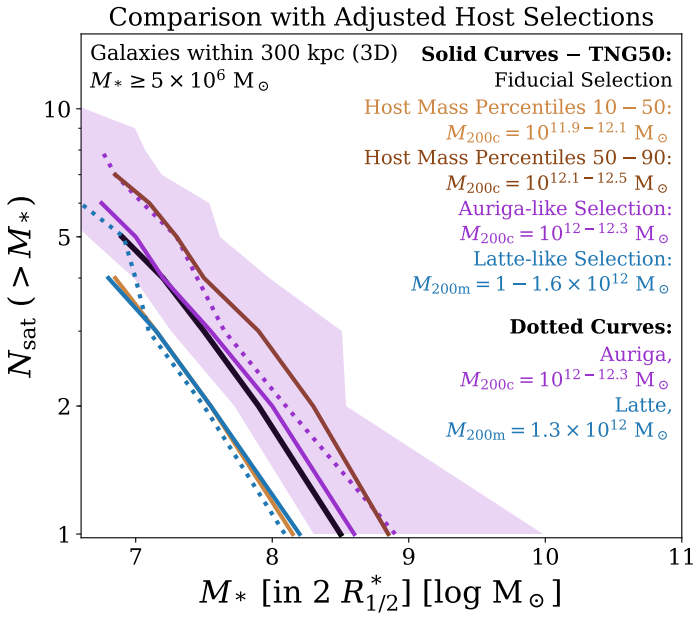

Figure 4.10: Satellite stellar mass functions for various definitions of MW/M31-like hosts. TNG50 satellites are required to be located within a 3D aperture of 300 kpc of their host and to have a stellar mass of $M_* \geq 5 \times 10^6$ M$_\odot$. I compare my fiducial selection of MW/M31-like galaxies (black curve, as in Figure 4.4) to several halo mass-based selections. The latter are limited to only central galaxies with no further requirements (e.g. on morphology or environment). Light and dark brown curves show satellite systems of lower- and higher-mass host haloes in TNG50. Their mass ranges correspond to the 10$^{\text{th}}$ to 50$^{\text{th}}$ percentiles, as well as the 50$^{\text{th}}$ to 90$^{\text{th}}$ percentiles of total halo mass covered by my fiducial host stellar mass range (see Figure 4.1). Furthermore, I match the host mass range of TNG50 hosts to those of the Auriga (purple curve) and Latte simulations (blue curve). For Latte, I assume a range of $\pm$0.1 dex in halo mass (see Table 4.1 for host selection criteria). The purple dotted curve and shaded region denote the median and scatter in satellite abundance of the actual Auriga simulations (Simpson et al. 2018, and private communication); the blue, dotted curve shows the satellite system of Latte (Wetzel et al. 2016).

satellites as galaxies with $M_* \geq 5 \times 10^6$ M$_\odot$ and within 300 kpc (3D) of their host galaxy. While I did also study a a subsample of my fiducial selection consisting of MW/M31-like hosts in the vicinity of a Virgo-like galaxy cluster (i.e. within 10 Mpc), I do not show their satellite abundances here. Their overall distributions lie well within the range of my entire fiducial sample with no distinct concentration on the satellite-richer or -poorer side and their median would coincide with the satellite stellar mass function of my fiducial sample.

For the remaining curves in Figure 4.10, I adopt alternative selections: namely, I consider TNG50 hosts with a certain total host halo mass, I exclusively consider centrals, and waive any further limitations on their morphology, merger history, or environment. I define low- and high-mass samples based on the halo masses that my fiducial stellar mass range covers in Figure 4.1: the low-mass sample covers the 10$^{\text{th}}$ to 50$^{\text{th}}$ percentile ($M_{200c} = 10^{11.9} - 10^{12.1}$ M$_\odot$, light brown curve), the high-mass sample corresponds to the 50$^{\text{th}}$ to 90$^{\text{th}}$ percentile of this range ($M_{200c} = 10^{12.1} - 10^{12.5}$ M$_\odot$, dark brown curve). Both curves display a distinct offset from my fiducial satellite stellar mass function: the low-mass sample hosts a smaller number of satellites,

which are less massive, while the high-mass sample extends to both larger satellite masses and higher total abundances.

Furthermore, I match the selection mass range to two previous cosmological simulations and show the corresponding TNG50 results: an Auriga-like selection (solid, purple curve) with $M_{200c} = 10^{12} - 10^{12.3}$ $M_\odot$ (Grand et al. 2017) and Latte (solid, blue curve). Since the Latte simulation consists of only a single MW-like galaxy with $M_{200m} = 1.3 \times 10^{12}$ $M_\odot$ (Wetzel et al. 2016), I simply assume a mass bin of ± 0.1 dex, resulting in a range of $M_{200m} = 1 - 1.6 \times 10^{12}$ $M_\odot$. M_{200m} corresponds to the total mass of a sphere around the FoF halo's centre with a mean density of 200 times the *mean* density of the Universe (as opposed to the Universe's *critical* density for M_{200c}). The satellite abundances of the actual Latte simulation (Wetzel et al. 2016) and the Auriga sample (Simpson et al. 2018) are given as a blue, dotted curve and purple, dotted curve and shaded area, respectively.

The TNG50 median satellite mass functions with the Auriga-like selection are very similar to the TNG50 median of my fiducial selection of MW/M31-like hosts, with a slight offset towards larger satellite abundances. Considering that the median host halo mass of my fiducial selection is at $M_{200c} = 10^{12.1}$ $M_\odot$, this result is reasonable. However, the median of the actual Auriga simulations displays slightly larger satellite abundances than my TNG50 Auriga-like selection and agrees more with my high-mass host sample. The Latte-like selection, on the other hand, returns TNG50 hosts whose satellite mass functions are in excellent agreement with that of the Latte simulation (blue solid vs. blue dotted curves), at least for satellite stellar masses above 10^7 $M_\odot$. Thus, when the host selection is properly matched, the TNG50 and Latte models (i.e. FIRE models since Latte employs physical models from FIRE) predict essentially identical MW-like satellite mass functions, despite starkly different numerical resolution and galaxy formation model assumptions.

4.2.5 Evolution of luminous and dark satellite populations through time

The satellites I observe today orbiting around galaxies like the MW and M31 do not represent the whole sample of galaxies that have ever been accreted. Most of the galaxies that enter the gravitational field of more massive haloes are destined to be destroyed and to ultimately form the diffuse stellar halo of their host galaxy (Purcell et al. 2007; Sales et al. 2007; Fattahi et al. 2020).

In this section, I compare present-day populations of satellite galaxies around MW/M31-like hosts in TNG50 to their abundance throughout cosmic time by taking all satellites ever accreted into account. This includes disrupted and merged satellites, backsplash galaxies, as well as present-day survivors.

I compare $z = 0$ and ever accreted median satellite stellar mass functions in Figure 4.11. TNG50 satellites are required to be located within 300 kpc (3D) of their host and to have a minimum stellar mass of 5×10^6 $M_\odot$. Note that, contrary to the rest of this chapter, the definition of satellite galaxies in this section is not solely based on the distance from their host but additionally requires them to be members

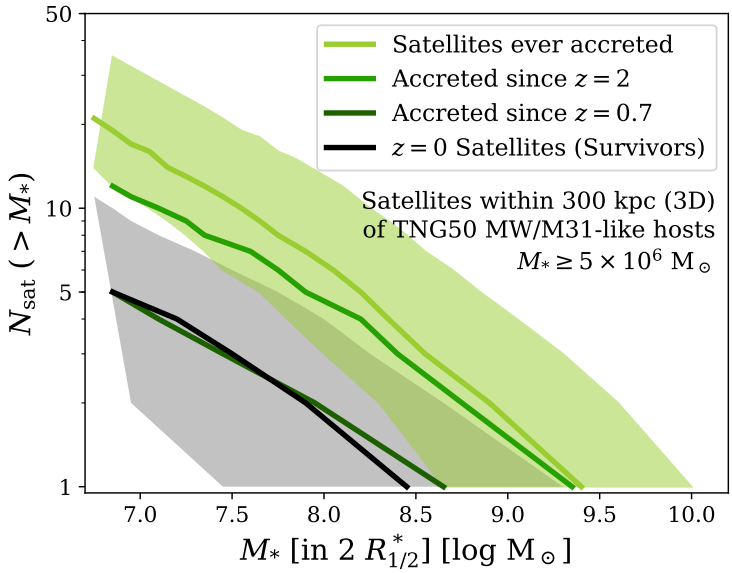

Figure 4.11: Satellite abundance of MW/M31-like hosts in TNG50 comparing past to present-day satellite populations. I illustrate this using the median satellite stellar mass function (within two stellar half-mass radii $R^*_{1/2}$) for satellite galaxies within 300 kpc (3D) of their MW/M31-like host and with a stellar mass of at least 5×10^6 M$_\odot$ for present-day satellites at $z = 0$ (black curve, as in Figure 4.4) and all satellites that have ever been accreted by their host (light green curve). Grey and green shaded areas denote their scatter as 16$^{\rm th}$ and 84$^{\rm th}$ percentiles. Furthermore, I limit satellites by their time of accretion to $z = 2$ (medium green curve) and $z = 0.7$ (dark green curve) to show the evolution of the median satellite population.

of the same FoF halo, since the identification of accreted satellites is based on their infall into a more massive host halo. Therefore, I limit my sample of MW/M31-like hosts to centrals, which leaves me with a sample of 190 hosts.

The black curve and grey scatter in Figure 4.11 show the median satellite stellar mass function and its scatter as 16$^{\rm th}$ and 84$^{\rm th}$ percentiles of present-day, surviving satellites – practically the median in the left panel of Figure 4.4 – while the light green curve and the corresponding shaded area display median and scatter of the stellar mass function of all satellites that have ever been accreted by these MW/M31-like hosts using the satellites' stellar mass at infall. Including all satellites ever accreted extends the stellar mass function both towards more massive satellites of $10^{9.4 \pm 0.5}$ M$_\odot$, as well as towards larger total satellite abundances of 21^{+13}_{-7}. At fixed minimum satellite stellar mass, the median abundance of all satellites ever accreted is larger than the median abundance of present-day survivors by a factor of $4 - 5$. This offset between surviving and accreted satellite populations is in qualitative agreement with previous DM-only and hydrodynamic simulations (Purcell et al. 2007; Sales et al. 2007). Fattahi et al. (2020) find a similar quantitative difference for satellites from the Auriga simulations.

Furthermore, I analyse the evolution of the satellite stellar mass function through time by limiting satellite galaxies according to their time of accretion either to satellites that have been accreted since $z = 2$ (medium green curve) or those that were

accreted onto their MW/M31-like host by $z = 0.7$ (dark green curve). Overall, the number of satellites that have been accreted since $z = 2$ decreases compared to all satellites ever accreted. While the massive end exhibits barely a difference, less massive satellites become increasingly affected since such galaxies are less resistant to environmental effects and are thus more prone to be disrupted. Shifting this limit on accretion time further towards the present day continues to decrease the number of satellites. In fact, the mass function of the present-day population of surviving satellite galaxies is similar to the one of satellites accreted since $z \sim 0.7$. So on average, present-day satellites of the MW and Andromeda fell into the gravitational potential of their host not earlier than $z \sim 0.7 - 1$.

4.2.6 Baryonic vs. DM-only simulation expectations

I examine differences between luminous satellite and dark subhalo populations in Figure 4.12. The top panel shows a subhalo mass function in terms of their total dynamical mass $M_{\rm dyn}$, i.e. all particles that are gravitationally bound to satellites, including dark matter, stars, gas, and black holes. Subhaloes are required to share the same FoF halo as their host, to be located within 300 kpc (3D) of their host galaxy, and to have a minimum dynamical mass of 5×10^7 $M_\odot$. This value corresponds to the smallest total subhalo mass below which the SHMR becomes incomplete and is artificially bent due to finite mass resolution (see Figure C.2, bottom left panel). Note that these subhaloes do not necessarily need to include a stellar component, meaning they can be either luminous or dark subhaloes. I compare the abundance of all subhaloes that have ever been accreted (blue curves) to the present-day population of surviving subhaloes at $z = 0$ (red curves), as well as surviving satellite galaxies at $z = 0$ with a stellar mass of $M_* \geq 5 \times 10^6$ $M_\odot$ (black curve). Furthermore, I illustrate differences between baryonic and DM-only simulations in Figure 4.12, by contrasting the subhalo samples from both TNG50 (solid curves), as well as its DM-only analogue simulation TNG50-Dark (dashed curves).

While the abundance of subhaloes at $z = 0$ is significantly larger than for luminous satellite galaxies, reaching 120 (200) in TNG50 (TNG50-Dark), surviving subhaloes and all subhaloes ever accreted exhibit a similar – albeit slightly smaller – difference as for satellite galaxies. At fixed dynamical mass, the number of surviving subhaloes at $z = 0$ is smaller than those that have ever been accreted onto MW/M31-like hosts by a factor of $3 - 5$. The abundance of subhaloes at $z = 0$ is always larger in TNG50-Dark than in the baryonic run by a factor of up to 2. However, this trend varies slightly when considering all subhaloes that have ever been accreted. Here, the abundance of massive subhaloes is the same in both TNG50 and TNG50-Dark. However, below dynamical masses of 10^{10} $M_\odot$, the number of subhaloes in TNG50-Dark becomes larger than the number of subhaloes in TNG50. The inclusion of baryonic processes affects the evolution of subhalo populations significantly both before and after accretion into their present-day host environment. Low-mass galaxies in baryonic simulations can experience substantial gas outflows

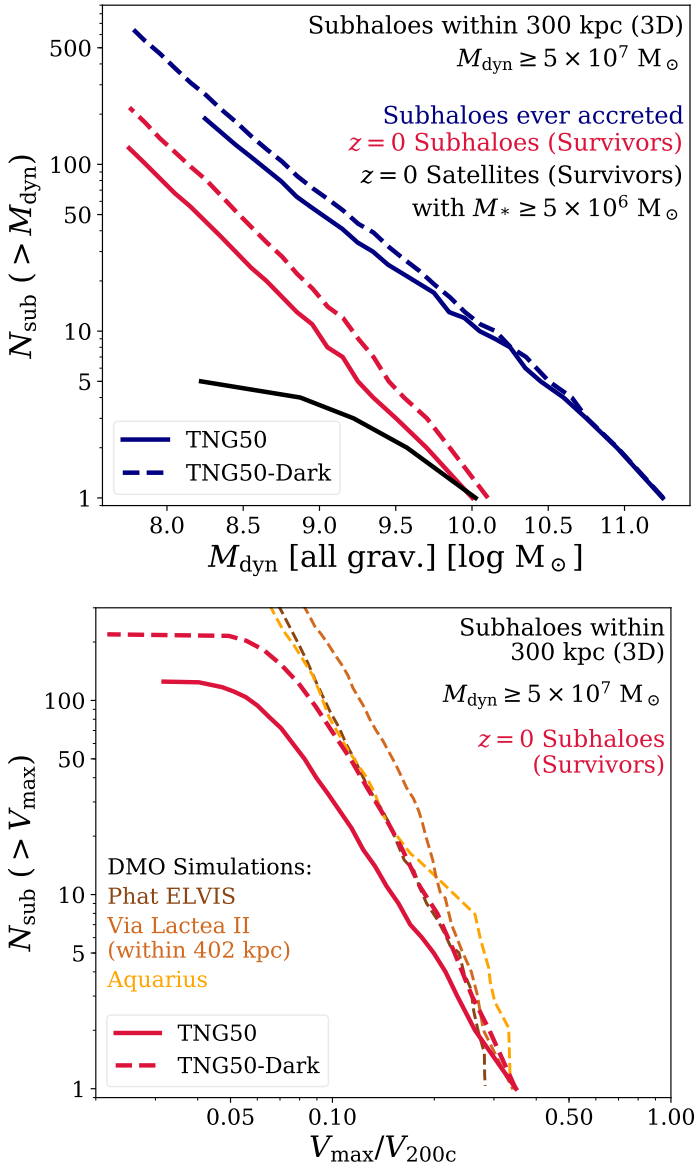

Figure 4.12: Subhalo abundance of MW/M31-like hosts in TNG50 comparing past to present-day satellite populations and baryonic to dark matter-only simulations. I illustrate this using the median subhalo abundance for subhaloes with dynamical mass $M_{\rm dyn} \geq 5 \times 10^7$ M$_\odot$ in terms of either total dynamical mass $M_{\rm dyn}$ (left panel) or normalised maximum circular velocity $V_{\rm max}/V_{\rm 200c}$ (right panel) using all gravitationally bound particles in both TNG50 (solid curves) and its dark matter-only analogue TNG50-Dark (dashed curves). Note that subhaloes are not required to include a luminous component. I compare all subhaloes that have ever been accreted by MW/M31-like hosts (blue curves), the surviving subhaloes at $z = 0$ (red curves), as well as subhaloes that host luminous satellite galaxies with stellar masses of at least 5×10^6 M$_\odot$. Furthermore, I include the subhalo abundance of several previous DM-only simulations in terms of their maximum circular velocity normalised by their host virial velocity $V_{\rm max}/V_{\rm 200c}$ in the right panel: Phat ELVIS (Kelley et al. 2019), Via Lactea II (Diemand et al. 2008), and Aquarius (Springel et al. 2008) (brown to orange, dashed curves). As the Phat ELVIS and Via Lactea II simulations employ different definitions of host virial properties, I convert their host velocities to $V_{\rm 200c}$ using the underlying relationships within TNG50 and neglect deviations due to the different adopted cosmological parameters. While Phat ELVIS and Aquarius require their subhaloes to be located within 300 kpc of their host as well, this distance limit is extended to 402 kpc for Via Lactea II subhaloes. I summarise their host selection criteria in Table 4.1.

due to galactic winds, leading to a redistribution of dark matter and lower masses compared to DM-only simulations. Intermediate-mass galaxies, on the other hand, have deeper potential wells and are therefore able to accrete more gas, resulting in larger masses in baryonic simulations (Chua et al. 2017). Furthermore, mass stripping and the survivability of subhaloes after infall correlates with the underlying structure of both subhalo and host. While a steeper matter density in subhaloes makes them more resistant to environmental effects, mass loss and total disruption, the same feature makes host haloes more efficient at tidal stripping, decreasing the survivability of subhaloes (Jiang and van den Bosch 2016). Introducing baryonic processes therefore changes both the overall mass range of subhaloes, as well as their survivability inside their host environment, resulting in different subhalo mass functions – both at accretion and at $z = 0$. Since DM-only simulations are missing complex and non-negligible physical processes, near-field cosmology as well as the analysis of MW/M31-like satellite systems and their evolution must rely on baryonic simulations.

I find similar trends for the abundance of subhaloes with $M_{\rm dyn} \geq 5 \times 10^7$ M$_\odot$ in terms of their maximum circular velocity $V_{\rm max}$ in the bottom panel of Figure 4.12. As the subhalo abundance in terms of $V_{\rm max}$ is expected to be essentially scale free when normalised to their host (Wang et al. 2012, however, see Chua et al. 2017 for the breaking of self-similarity in full-physics hydrodynamical simulations), I normalise the subhalo abundance by the virial velocity of their host halo $V_{\rm 200c}$. The number of surviving subhaloes at $z = 0$ (red curves) reaches 120 in TNG50 (solid curve) and 200 in TNG50-Dark (dashed curves) for $V_{\rm max}/V_{\rm 200c} \geq 0.02 - 0.07$, while their overall abundance is always larger in TNG50-Dark. Subhalo populations extend to normalised maximum circular velocities of ~ 0.35 in both TNG50 and TNG50-Dark. However, their distributions begin to flatten considerably towards the low-velocity end for subhaloes with $V_{\rm max}/V_{\rm 200c} < 0.07$.

Furthermore, I compare my findings from TNG50-Dark (red dashed curve) to other DM-only simulations: Phat ELVIS (Kelley et al. 2019), Via Lactea II (Diemand et al. 2008), and Aquarius (Springel et al. 2008) (brown to orange, dashed curves). All of the simulations employ different definitions of MW/M31-like haloes. I summarise their host selection criteria in Table 4.1. As both Phat ELVIS and Via Lactea II employ different measurements of their host haloes' virial properties – $V_{\Delta_{\rm c}}$ (i.e. the total velocity of a sphere with a mean density of $\Delta_{\rm c}$ times the critical density of the Universe, where $\Delta_{\rm c}$ is derived from the collapse of a spherical top-hat perturbation), and $V_{\rm 200m}$ (i.e. the velocity of a sphere around the FoF halo centre with a mean density of 200 times the mean density of the Universe), respectively –, I convert their host velocities into $V_{\rm 200c}$ using the TNG50 relations of these different velocity measurements. Note that the actual $V_{\rm 200c}$ velocities of these simulations might be slightly different depending on their adopted cosmology.

Both Phat ELVIS and Aquarius require satellites to be located within 300 kpc of their host galaxies, however, this aperture is extended in Via Lactea II to 402 kpc.

After normalising the subhaloes' maximum rotational velocities to their respective host velocity, all simulations exhibit overall consistent subhalo abundances. While the abundance of Via Lactea II is slightly larger than in TNG50-Dark, the abundances of Phat ELVIS and Aquarius coincide with TNG50-Dark at almost all velocities. Despite different definitions of MW/M31-like haloes – including limitations on mass ranges, morphologies, isolation criteria, and merger histories – I find a reasonable agreement and consistent subhalo abundances between TNG50-Dark and other, previous DM-only simulations.

4.2.7 Dependence on host properties

In this section, I investigate the correlations of satellite abundance with properties of their host and look for possible physical origins of the scatter in satellite abundance. The large number of MW/M31-like galaxies in TNG50 allows me to search for trends in a statistically significant manner and hence to provide the baryonic physics counterpart to previous results on subhaloes that were based on DM-only simulations (e.g. Gao et al. 2004, and subsequent similar analyses) or semi-analytic models (e.g. Sales et al. 2013; Starkenburg et al. 2013; Wang and White 2012). I characterise satellite systems using their stellar mass functions (limited to satellites within 300 kpc of their host and with $M_* \geq 5 \times 10^6$ $M_\odot$) in general, as well as in terms of the total number of satellites within 300 kpc.

Dependence on host galaxy properties

I illustrate dependencies of satellite abundances on host galaxy properties in Figure 4.13. Panels in the left column depict satellite stellar mass functions for subpopulations in various percentiles of the host property in question, with yellow to black curves. The specific colours of percentiles vary slightly depending on the distribution of the respective host property under consideration. The grey curves in the background show the individual stellar mass functions as reference. Right panels display the total number of satellites as a function of the respective host property for individual hosts and percentiles, as well as their running median and scatter (black curve and grey shaded area). These curves do not necessarily cover the entire range of the host property in question. Since the population of satellites might not be complete around the boundaries of the respective host property range, the running median and scatter could otherwise display misleading trends. Furthermore, I include either the 8 hosts of the SAGA survey's first stage (Geha et al. 2017) or the 36 hosts of its second stage (Mao et al. 2021) as comparison (green diamonds) and indicate the total abundance of MW and M31 satellites with $M_* \geq 5 \times 10^6$ $M_\odot$ (red and brown dashed lines, respectively). I characterise my hosts using stellar mass, star formation rate, K-band luminosity, and $g - r$ colour (from top to bottom). For stellar mass and K-band luminosity, I include estimates for the MW and M31 (red and brown shaded areas, respectively).

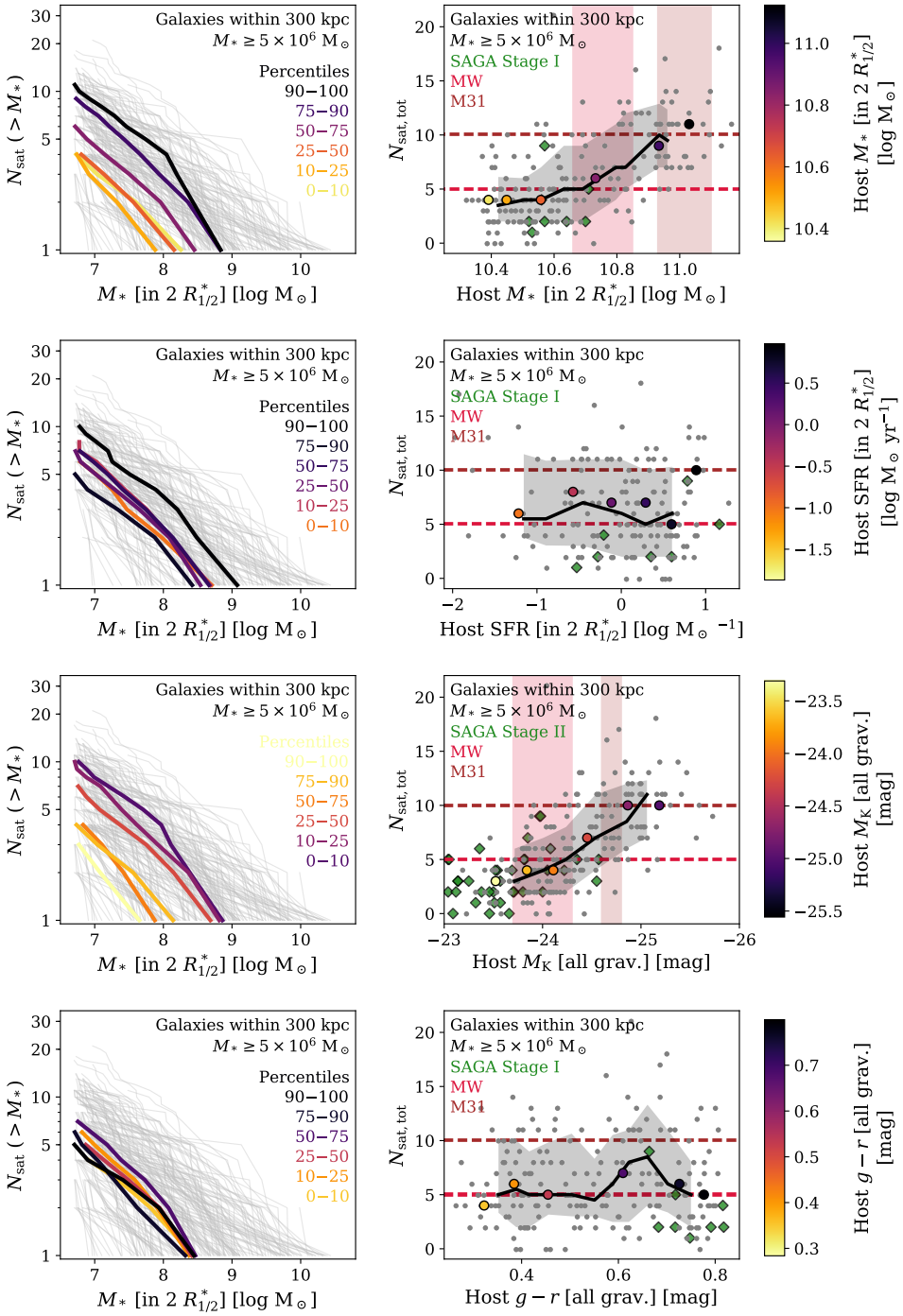

Figure 4.13: Dependence of satellite abundances on host galaxy properties for satellites within 300 kpc (3D) of their MW/M31-like host and with a stellar mass of at least 5×10^6 M$_\odot$. Each row investigates a different host property (from top to bottom): stellar mass M_*, star formation rate SFR (both within twice the stellar half-mass radius), K-band luminosity $M_{\rm K}$, and $g-r$ colour. *Left panels:* median satellite stellar mass functions in various percentiles of the host property in question (thick, yellow to black curves). The thin, grey curves in the background denote satellite stellar mass functions of individual TNG50 MW/M31-like hosts as a reference. *Right panels:* total number of satellites as a function host properties for the percentiles (yellow to black circles), all TNG50 MW/M31-like galaxies (grey circles), as well as their running median (black curves) and scatter (grey shaded area, 16$^{\rm th}$ and 84$^{\rm th}$ percentiles). Furthermore, I include MW-like hosts from the SAGA survey as a comparison (green diamonds): its first stage (Geha et al. 2017) consisting of 8 MW-like hosts for stellar mass, SFR and $g-r$ colour, as well as 36 hosts from its second stage (Mao et al. 2021) for K-band luminosity. The horizontal, dashed lines mark the total satellite abundance of the MW (red line) and M31 (brown line), while the vertical, shaded areas denote estimates of stellar mass (Licquia et al. 2015; Sick et al. 2015; Boardman et al. 2020) and K-band luminosity (Drimmel and Spergel 2001; Hammer et al. 2007).

In Figure 4.13, while there is overlap among the stellar mass functions of different percentiles and significant scatter in the total number of satellites as a function of host properties, I find the clearest trends with stellar mass and its observational counterpart, the *K*-band luminosity. Namely, more massive and brighter MW/M31-like galaxies do host a larger number of satellite galaxies. Furthermore, the strength of these correlations becomes more significant at higher masses and brighter luminosities. At fixed host stellar mass, there is a *normalised* 1σ scatter in total satellite abundance (calculated as $|N_{\mathrm{sat,\,tot}} - \langle N_{\mathrm{sat,\,tot}}\rangle| / \langle N_{\mathrm{sat,\,tot}}\rangle$) of up to ± 0.5 at $10^{10.5}$ $\mathrm{M}_{\odot}$ and ± 0.6 at $10^{10.8}$ $\mathrm{M}_{\odot}$; at fixed host *K*-band luminosity, there is a normalised scatter of up to ± 0.8 at -24 mag and ± 0.5 at -24.8 mag. While I did inspect correlations with the stellar mass function slope as well, I find either no or only very minor dependencies, e.g. the satellite stellar mass functions of more massive hosts tend to be slightly steeper. Considering the comparison to observations, I see that the TNG50 trends are well in agreement with those from the SAGA hosts – both exhibit a significant amount of scatter. Furthermore, Mao et al. (2021) recover the same significant correlation of satellite abundance and host *K*-band luminosity. Considering the MW and M31, I find their total satellite abundances to be consistent with the distributions of TNG50 MW/M31-like hosts given their estimates of stellar mass and *K*-band luminosity and amid a significant degree of scatter in both directions. Clearly, the observed satellite system of Andromeda is more compatible to those of TNG50 hosts with larger stellar masses and smaller K-band magnitudes, and it is in fact well reproduced by TNG50.

Dependence on host halo properties

I extend this investigation to host halo properties in Figure 4.14. As in Figure 4.13, I illustrate trends with percentile stellar mass functions (left panels) and the total number of satellites as a function of host halo properties (right panels). Once more, it should be noted that the specific colours of percentiles vary slightly depending on the distribution of the respective host property in question. Since I consider properties of the FoF halo, I limit my sample of MW/M31-like hosts to centrals, which leaves me with a sample of 190 hosts. Furthermore, I indicate the total satellite abundances of the MW and M31 with $M_{*} \geq 5 \times 10^{6}$ $\mathrm{M}_{\odot}$ (red and brown dashed lines, respectively).

I characterise the host halo by its total mass $M_{200\mathrm{c}}$, its assembly time, for which I employ z_{50} – the redshift at which 50 per cent of its present-day total mass had been assembled –, its concentration c_{-2}, and its shape s as its minor-to-major axis ratio (from top to bottom). I compute halo concentration by fitting an Einasto profile (Einasto 1965; Navarro et al. 2004) to the radial distribution of dark matter density $\rho_{\mathrm{DM}}(r)$ following Pillepich et al. (in prep.). The concentration parameter c_{-2} corresponds to the ratio of the virial radius and the radius at which the DM density profile's slope takes on an isothermal value. I measure DM halo shapes following Chua et al. (2019).

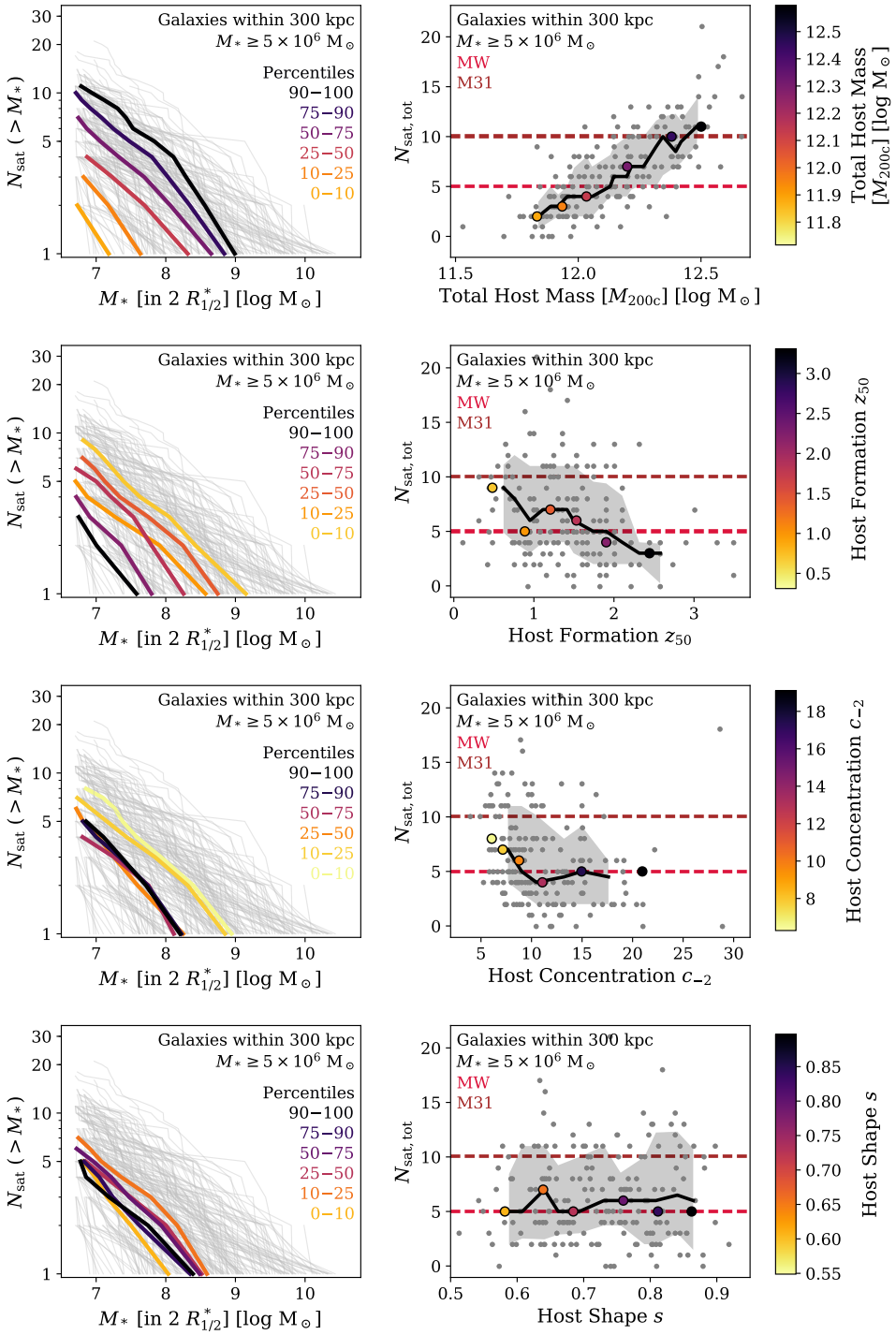

Figure 4.14: Dependence of satellite abundances on host halo properties (instead of host galaxy properties) for satellites within 300 kpc (3D) of their MW/M31-like host and with a stellar mass of at least 5×10^6 M$_\odot$. Each row investigates a different host property (from top to bottom): total mass M_{200c}, halo assembly time z_{50}, i.e. the redshift at which the MW/M31-like host had assembled 50 per cent of its mass, as well as halo concentration c_{-2} and halo shape as minor-to-major axis ratio s. *Left panels:* median satellite stellar mass functions in various percentiles of the host property in question (thick, yellow to black curves). The thin, grey curves in the background denote satellite stellar mass functions of individual TNG50 MW/M31-like hosts as a reference. *Right panels:* total number of satellites as a function host properties for the percentiles (yellow to black circles), all TNG50 MW/M31-like galaxies (grey circles), as well as their running median (black curves) and scatter (grey shaded area, 16$^{\rm th}$ and 84$^{\rm th}$ percentiles). The horizontal, dashed lines mark the total satellite abundance of the MW (red line) and M31 (brown line).

Overall, I find much stronger trends with halo mass and assembly than with host galaxy properties: more massive MW/M31-like haloes and those with a later assembly z_{50} host a larger number of surviving satellite galaxies by $z = 0$. At fixed total host mass, there is a *normalised* 1σ scatter in total satellite abundance (calculated as $|N_{\rm sat,\ tot} - \langle N_{\rm sat,\ tot}\rangle|/\langle N_{\rm sat,\ tot}\rangle$) of up to ± 0.8 at 10^{12} $M_\odot$ and ± 0.3 at $10^{12.4}$ $M_\odot$. However, the trend with host assembly evolves throughout time with different stages in halo formation: for earlier characterisations of the assembly times (z_{10}), the correlation with total satellite abundance is stronger than with later characterisations of halo assembly (z_{90}, see Appendix E and Figure E.1 for details). Host halo concentration has only a slight impact on the total abundance of present-day satellite galaxies: whereas less concentrated haloes host a larger number of $z = 0$ satellites, this trend flattens and disappears towards higher concentrations. Finally, there are no discernible trends with host halo shape.

As for Figure 4.13, I also inspected correlations with the stellar mass function slope, however, they are not shown since I find either no or only very minor dependencies, e.g. the satellite stellar mass functions of host haloes with a later assembly tend to be slightly less steep. I confirm the correlations described so far using Spearman correlation coefficients. While host K-band luminosity yields the best correlation coefficient of the host galaxy properties with -0.65, the trend with total host halo mass is even stronger with a Spearman correlation coefficient of 0.75. Therefore, total satellite abundances are more closely related to host halo than host galaxy properties. This is consistent with results from the APOSTLE and ARTEMIS simulations (Fattahi et al. 2016a; Font et al. 2021a).

The TNG-based findings uncovered in this chapter are qualitatively consistent with the trends between subhalo abundances and host halo properties in the Illustris simulation (Chua et al. 2017). But some differences do emerge: I expand on the host-dependent trends of subhalo, rather than satellite, abundances in TNG50 in Appendix F. As shown in Appendix F and Figure F.1, when considering subhalo abundance in the DM-only analogue simulation TNG50-Dark, the total abundance of subhaloes displays a strong dependence on host concentration. However, host haloes in TNG50-Dark are generally less concentrated than in TNG50: baryonic effects in TNG50 cause the host haloes to contract (see also Chua et al. 2017; Lovell et al. 2018 for Illustris and IllustrisTNG, as well as Duffy et al. 2010; Marinacci et al. 2014; Zhu et al. 2016; Fiacconi et al. 2016 for other previous cosmological and zoom-in simulations). This washes out the correlations between total satellite/subhalo abundance and host concentration that have been previously quantified with N-body only models.

To my knowledge, this is the first time that it has been possible to quantify the scatter and the dependence on host properties of the satellite abundance of MW/M31-like hosts with a full-physics, hydrodynamical galaxy-formation simulation that samples many tens, in fact a couple of hundred, MW/M31-like hosts. Both Figures 4.13 and 4.14 demonstrate that the observed satellite abundances of the MW

and M31 are well reproduced by TNG50 as they are in agreement with the distribution of TNG50 MW/M31-like hosts, even at fixed observed host properties. Whereas a significant degree of host-to-host variation remains also at fixed total satellite abundance, I find that, also according to TNG50, the larger number of satellites around Andromeda compared to those of the Galaxy suggest a higher total halo mass, more recent halo formation time, and lower halo concentration for the host halo of M31 in comparison to the MW's.

Chapter 5

Satellites of MW/M31-like galaxies with TNG50: gas content & star formation activity

This chapter presents the preliminary results of the upcoming publication Engler et al. (in prep.): *"Satellites of MW/M31-like galaxies with TNG50: gas content and star formation histories"*. As in Chapter 4, I focus on the TNG50 simulation for its large-scale, cosmological volume and its zoom-in-like resolution, as well as for its statistical sample of 198 MW/M31-like hosts. I study the evolution of the satellite populations within and outside the virial radius of these hosts with respect to their star formation activity and their gas content with a particular focus on atomic hydrogen HI as the fuel for star formation processes. While the working title of the paper that this chapter is based upon mentions star formation histories, it should be noted that these have not yet been constructed at the time of writing this thesis and are thus not included in the following discussion.

This chapter is structured as follows: in Chapter 5.1, I reintroduce my sample of TNG50 MW/M31-like hosts and briefly summarise their selection criteria again. Furthermore, I define several subsamples of specific Milky Way (MW), Andromeda (M31), as well as Local Group (LG) analogue hosts, and describe my satellite selection. I present my results in Chapter 5.2, including the phase-space distribution of satellites, their quenched fractions as a function of satellite stellar mass, as well as their gas content as a function of distance to their host galaxy, phase-space position, and time of infall. Furthermore, I analyse the co-evolution of satellite mass components after infall. The results of this chapter are summarised in Chapter 6.3.

5.1 Methods

5.1.1 Host selection

In this chapter, I examine the satellite populations of TNG50 MW/M31-like hosts used throughout Chapter 4. As discussed in Chapter 4.1.1, the chosen selection criteria that define these galaxies are essential to ensure a realistic sample of hosts, as

well as realistic environments for the satellite populations I will investigate below. The adopted criteria for my fiducial sample of MW/M31-like hosts, as well as several alternative and more specific subselections of hosts that are used throughout this chapter, are summarised below.

Fiducial sample of TNG50 MW/M31-like hosts

I define MW/M31-like galaxies according to Pillepich et al. (in prep.) based on their mass, morphology, and their environment at redshift $z = 0$. A detailed description of these selection criteria can be found in Chapter 4.1.1. Briefly summarised again, these read:

- *Stellar mass:* MW/M31-like candidates are required to have a stellar mass in the range of $M_* = 10^{10.5} - 10^{11.2}$ $M_\odot$ within an aperture of 30 kpc.
- *Morphology:* TNG50 MW/M31-like candidates need to exhibit a disky stellar morphology. Their shape is determined based on either the minor-to-major axis ratio of their 3D stellar mass distribution ($s < 0.45$) or by visual inspection of synthetic 3-band stellar light images in face-on and edge-on projection.
- *Environment:* a minimum isolation criterion is imposed at $z = 0$. No other massive galaxies with $M_* > 10^{10.5}$ $M_\odot$ is allowed to be located within 500 kpc of the MW/M31-like candidate. Furthermore, their host halo mass is limited to $M_{200c} < 10^{13}$ $M_\odot$.

Host haloes are defined using a friends-of-friends (FoF) algorithm. Their virial mass M_{200c} denotes the total mass of a sphere around the FoF halo centre with a mean density of 200 times the critical density of the Universe. These requirements result in a sample of 198 MW/M31-like hosts in TNG50, eight of which are satellite galaxies.

Specific TNG50 MW and M31 analogues

I further restrict my sample of 198 MW/M31-like hosts to specific analogues of the MW and M31 systems based on the findings of Chapter 4.2.2. It is important to note that these TNG50 hosts are analogues to the observed MW and M31 solely based on their satellite populations with no regards to further internal properties of the host galaxies themselves. These samples consist of the systems depicted in Figures 4.5 and 4.6. They are selected by computing the residual sum of squares between the simulated and observed satellite mass functions above 5×10^6 $M_\odot$ over all satellite stellar mass bins and by identifying the systems with the lowest values. Furthermore, the systems with particularly massive satellites summarised in Table 4.2 are included. Hosts that include both an LMC- and SMC-like satellite are added to the sample of MW-like analogues whereas systems with both a Triangulum- and an M32/NGC205-like satellite are added to the sample of M31 analogues (assuming satellite masses within ± 0.1 dex of their observed counterparts). This results in

16 TNG50 MW analogues and 11 TNG50 M31 analogues. I compare the phase-space distribution of their satellite populations to those of the observed MW and M31 systems in Chapter 5.2.1.

TNG50 Local Group-like systems

Furthermore, I divide the host sample into isolated TNG50 MW/M31-like and Local Group-like (LG) hosts. In order to determine which hosts may be part of an LG-like system, I examine their environment for the presence of another MW-mass galaxy: LG-like candidates are required to have one other galaxy of similar mass, i.e. in the range of $10^{10.5} - 10^{11.2}$ $M_\odot$, within a distance of $500 - 1000$ kpc. This nearby galaxy needs to exhibit a negative radial velocity with respect to the original MW/M31-like host. Hosts that meet these requirements are considered to be part of an LG-like system. This yields a sample of 10 TNG50 LG-like hosts and 185 isolated MW/M31-like hosts. Another three TNG50 hosts actually have two similar-mass galaxies with approaching radial velocities within $500 - 1000$ kpc. I will examine the differences between star formation activities of satellite populations around isolated MW/M31-like and LG-like hosts in Chapter 5.2.3.

SAGA-like host selection

Finally, I employ the 108 TNG50 SAGA-like hosts again in this chapter. For this, I adopt the selection criteria from Geha et al. (2017) and Mao et al. (2021) (K-band luminosity within $-23 > M_K > -24.6$, as well as isolation criteria) and match the three most similar TNG50 hosts to each of the 36 SAGA MW-like galaxies based on their K-band luminosities. For more details on this selection, see Chapter 4.1.1.

5.1.2 Satellite selection

In the following sections of this chapter, I employ similar samples of satellite galaxies around TNG50 MW/M31-like hosts as throughout Chapter 4. As above, satellites and subhaloes in IllustrisTNG are identified as local overdensities within larger FoF haloes using the SUBFIND algorithm (Springel et al. 2001; Dolag et al. 2009). Since not all luminous subhaloes correspond to actual galaxies, I remove these clumps and fragmentations within other TNG galaxies according to Nelson et al. (2019a).

Throughout the following analysis, the satellite selection varies from being determined by FoF membership (to find satellites out to $\gtrsim 1$ Mpc, as well as to define their respective time of infall) to being located within various physical apertures (e.g. within 300 kpc or 600 kpc). As these satellite samples overlap for the most part, there is no qualitative difference in my results between employing one or the other satellite definition. As in Chapter 4, I require them to have a stellar mass within two stellar half-mass radii $R^*_{1/2}$ of at least 5×10^6 $M_\odot$. This corresponds to the mass of the MW's own satellite galaxy Leo I and ensures an appropriate level of numerical resolution with at least 63 stellar particles.

Furthermore, I employ an observational satellite selection according to the SAGA survey (Geha et al. 2017; Mao et al. 2021) in Chapter 5.2.2. As previously described in Chapter 4.1.2, this selection requires satellite galaxies to lie within a two-dimensional, randomly projected aperture of 300 kpc from their host and to have a line-of-sight velocity of $\pm$250 km s^{-1}.

5.2 Results

5.2.1 Satellites of MW/M31-like hosts in phase-space

Before analysing the gas content and star formation activity of the satellite populations of my full sample of TNG50 MW/M31-like hosts, I focus on the specific MW and M31 analogues obtained in Chapter 4.2.2 and examine their satellite distributions in phase-space. The top panels of Figure 5.1 depict the 3D phase-space of satellite galaxies with $M_* \geq 5 \times 10^6$ M$_\odot$ within 600 kpc of the 16 MW (left panel) and 11 M31 (right panel) analogues. TNG50 satellites are shown as filled circles – with each colour corresponding to a different host – while the red and brown, empty diamonds display the satellites of the actual MW and M31 galaxies (McConnachie 2012). Furthermore, I highlight massive satellites with $M_* \geq 10^{8.5}$ M$_\odot$ – i.e. analogues to the Magellanic Clouds or M32, NGC205, and Triangulum – by assigning them larger symbols. The dotted curves depict the escape velocity from the host, assuming a median host halo mass of $10^{12.1}$ M$_\odot$ for TNG50 analogues of the MW, as well as $10^{12.4}$ M$_\odot$ for TNG50 analogues of Andromeda.

Overall, I find consistent phase-space distributions of TNG50 satellites with both observed satellite systems. While the massive satellites of the MW and M31 mostly reside relatively close to their respective host galaxy, massive satellites around TNG50 MW and M31 analogues are distributed across all distances – usually with relative velocities close to escape velocity. Still, there are massive TNG50 satellites that inhabit the same phase-space regions as the SMC and LMC. The area around M32 and NGC205 in the right panel of Figure 5.1, on the other hand, appears to be devoid of TNG50 satellites. However, it should be kept in mind that these phase-space distributions depict but an instant in time. There are several massive satellites around TNG50 M31 analogues at low distances and negative absolute velocities that might occupy these regions soon thereafter. Furthermore, these massive satellites can fall into their present-day host environment together with several less massive and/or other massive satellites as members of a group, as is illustrated by the infalling group of satellites into a TNG50 M31 analogue host (blue dots in the lower right corner).

I expand the comparison of satellite phase-space distributions using the 36 observed MW-like hosts from the second stage of the SAGA survey (Mao et al. 2021) and employ the TNG50 SAGA-like host sample from Chapters 4.1.1 and 4.2.3 consisting of 108 matched, simulated hosts. The bottom panel of Figure 5.1 depicts the phase-space distributions of TNG50 satellites with absolute r-band luminosities of

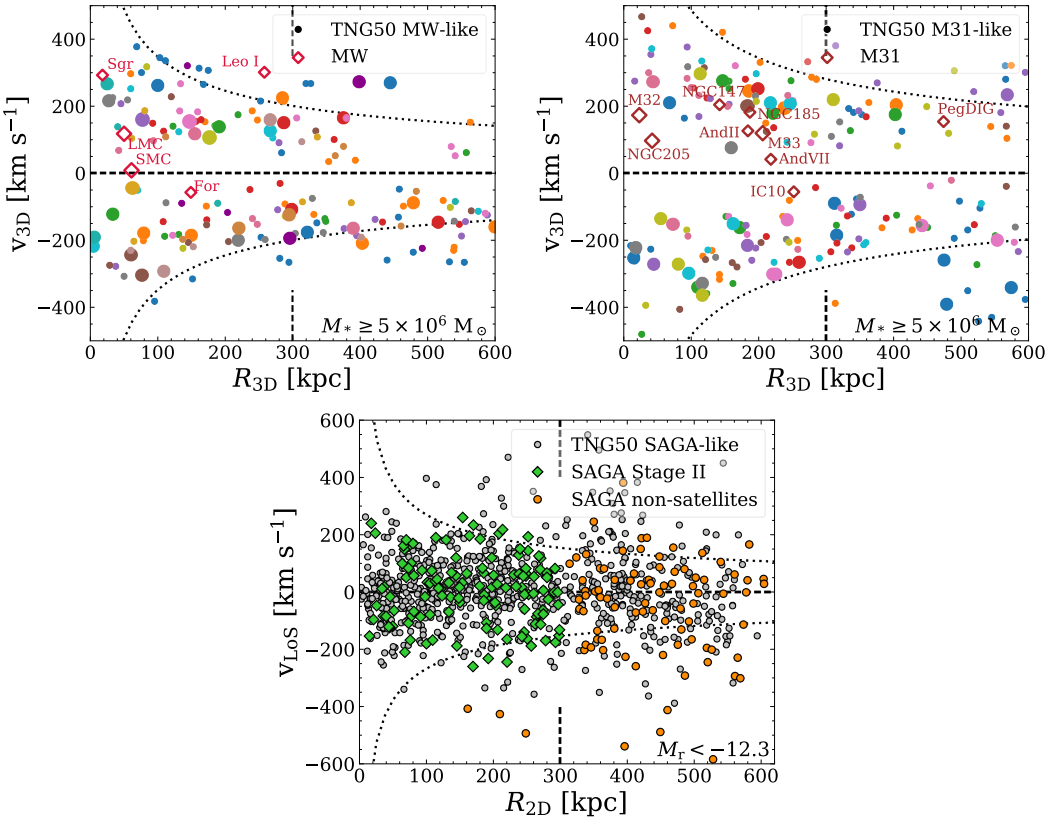

Figure 5.1: Phase-space distributions of satellite galaxies comparing TNG50 to the MW, M31, and the SAGA survey. *Top panels:* 3D phase-space of satellite galaxies with $M_* \geq 5 \times 10^6$ M$_\odot$ within 600 kpc of the 16 TNG50 MW analogues (left panel) and the 11 TNG50 M31 analogues (right panel) from Chapter 4.2.2 (filled circles). Each colour corresponds to the satellites of a different host galaxy. The empty red and brown diamonds correspond to the satellite galaxies of the MW and M31, respectively (McConnachie 2012). The dashed vertical lines denote 300 kpc as the typical virial radius of a MW/M31-like host, while the dotted curves illustrate the escape velocity assuming a host halo mass of $10^{12.1}$ M$_\odot$ for the MW and $10^{12.4}$ M$_\odot$ for M31. These masses correspond to the median host masses of my MW and M31 analogue samples. *Bottom panel:* 2D phase-space distribution of satellite galaxies with $M_r < -12.3$ within 600 kpc of the 108 TNG50 SAGA-like hosts (grey circles). The dashed vertical lines are identical to the top panels, whereas the dotted curves now mark the escape velocity for a median host halo of mass of $10^{11.9}$ M$_\odot$. I compare to observations from the SAGA survey (Mao et al. 2021): green diamonds denote the satellites of their 36 MW-like hosts, while the orange dots correspond to non-satellites outside their distance and velocity boundaries.

$M_r > -12.3$ (grey dots), as well as SAGA stage II satellites (green diamonds) and non-satellites (orange squares). Overall, I find consistent phase-space distributions between TNG50 and the SAGA survey, both within and outside of the host galaxy's virial radius of 300 kpc.

5.2.2 Satellite quenched fractions

I study the star formation activity of satellite galaxies around MW/M31-like hosts in TNG50, i.e. their quenched fractions as a function of satellite stellar mass M_*, in Figure 5.2. Satellites are defined to be quenched based on their star formation rate (SFR) and their distance to the star forming main sequence of $\Delta \log(\mathrm{SFR}) \leq -1$. I compare various samples of satellite galaxies in physical apertures from their host. This includes physical 3D distances – galaxies within 300 kpc, i.e. the typical virial radius of a MW/M31-like galaxy (red curve), or within $300 - 600$ kpc (blue curve) – and an observational selection of TNG50 satellites that adopts the selection criteria of the SAGA survey (pink curve). Here, satellites are defined as galaxies within a projected 2D aperture of 300 kpc of their host with line-of-sight velocities of ± 250 km s^{-1}. Furthermore, I compare my TNG50 satellites to observed satellites of the MW and M31 (red dots, Wetzel et al. 2015), as well as satellites around MW-like hosts from the second stage of the SAGA survey (pink dots, Mao et al. 2021). Note that these comparisons are made *at face value*, i.e. without adjusting for their respective quenched definitions. Wetzel et al. (2015) consider satellites with a gas fraction of $M_{\mathrm{gas}}/M_* < 0.1$ to be quenched, whereas the definition of Mao et al. (2021) is based on Hα equivalent widths $\mathrm{EW}(\mathrm{H}\alpha) < 2$ Å. A more detailed comparison to the observations of Wetzel et al. (2015) will follow below and in Figure 5.3.

Overall, satellite galaxies in Figure 5.2 all display the same qualitative trend, regardless of their selection and the distance to their host galaxy: less massive satellites exhibit larger quenched fractions. As less massive galaxies have shallower gravitational potentials of their own, they are more prone to be affected by environmental effects and to be stripped of their gas – and subsequently quenched – in the halo of their host galaxy. Quantitatively, I find the highest quenched fractions for satellites within 300 kpc of their host, ranging from 98 per cent at the low-mass end to 6 per cent for massive satellites with 10^{10} M$_\odot$. Satellites outside of their host's virial radius at $300 - 600$ kpc, on the other hand, show consistently lower quenched fractions of 90 to 0 per cent. Environmental effects become more effective towards the inner regions of host haloes. The observational SAGA-like selection of TNG50 satellites within 300 kpc (2D) exhibits lower quenched fractions compared to the three-dimensional selection at almost all stellar masses. This discrepancy is driven by star-forming field galaxies in the fore- and background of MW/M31-like hosts contaminating the satellite sample.

Compared to observations, I find a reasonable level of agreement between TNG50 and satellites within 300 kpc of the MW and M31 across the whole range of stellar

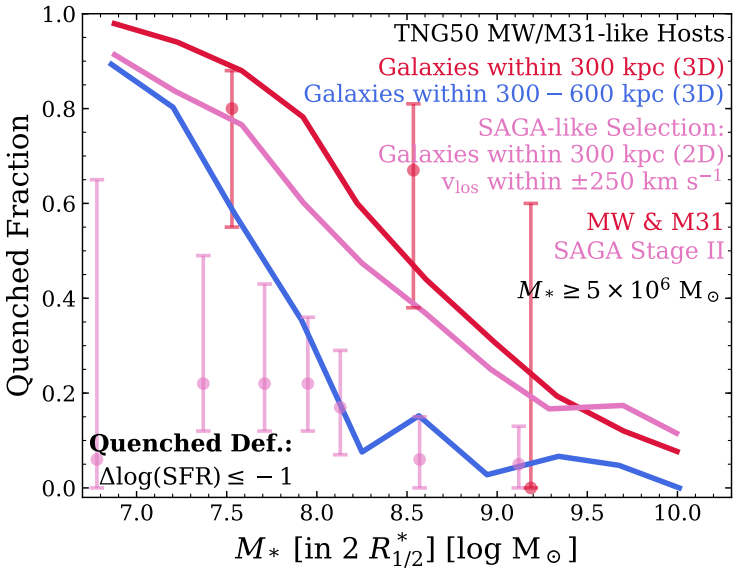

Figure 5.2: Quenched fractions of satellite galaxies around MW/M31-like hosts in TNG50, observed MW-like galaxies from the SAGA survey, as well as the observed MW and M31 galaxies. I compare the quenched fractions of TNG50 satellites within 300 kpc of their host (3D, red curve) to those at distances of 300 − 600 kpc (3D, blue curve), as well as to an alternative selection of satellites that adopts the selection criteria of the SAGA survey, i.e. within 300 kpc (2D) and with line-of-sight velocities of ±250 km s^{-1} (pink curve). Furthermore, the TNG50 results are compared to observed satellites of the MW and M31 (red dots, Wetzel et al. 2015) and from the SAGA survey (pink dots, Mao et al. 2021). The comparisons to observations are made at face value as they adopt different definitions of quenched states: while I define galaxies to be quenched based on their distance to the star forming main sequence (SFMS), Wetzel et al. (2015) employ a gas fraction criterion for MW and M31 satellites and the quenched fractions of Mao et al. (2021) are based on Hα equivalent widths.

mass. Satellites from the second stage of the SAGA survey, however, exhibit significantly lower quenched fractions than any TNG50 satellite sample or satellites of the MW and M31, reaching quenched fractions of only up to 65 per cent according to their scatter at the low-mass end. While their sample should include some interloper field galaxies, such a discrepancy cannot merely be attributed to contamination of the satellite sample by foreground and background galaxies. However, I should note again that both Wetzel et al. (2015) and Mao et al. (2021) adopt different quenched definitions for their satellite samples. As the SAGA survey employs a quenched definition based on the Hα equivalent width, radiative transfer models are required to perform a mock spectroscopy on TNG50 satellites in order to achieve a proper, matched comparison. Alternatively, the TNG models might not be able to correctly capture some processes in place. While such a matched comparison with the SAGA survey has not yet been made at the time of writing this thesis, I plan to further address this in the future.

Recently, Font et al. (2021b) were able to attribute the low quenched fractions of the SAGA satellites to the survey's surface brightness limit based on the results of the ARTEMIS simulations. Due to this limitation, the SAGA satellites are biased to more actively star-forming populations (see their figure 2). I aim to confirm this with

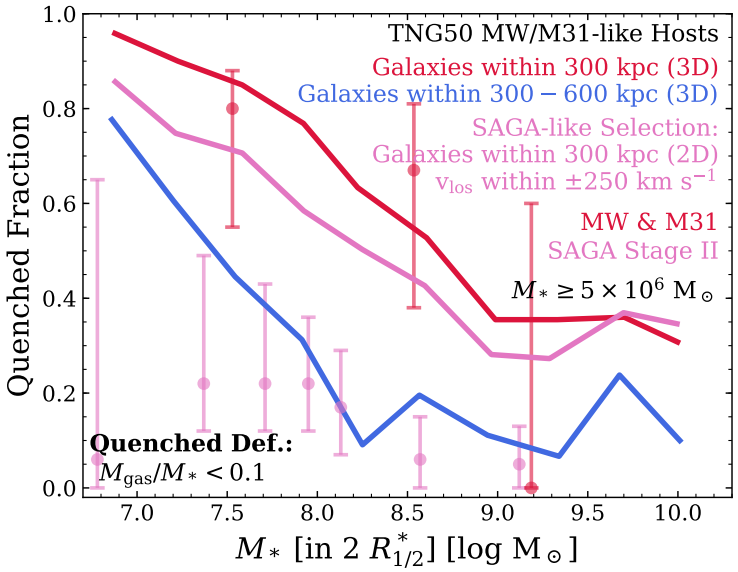

Figure 5.3: Same as Figure 5.2, however, the quenched definition is now based on the gas fraction criterion of $M_{gas}/M_* < 0.1$ from Wetzel et al. (2015). I illustrate quenched fractions as a function of stellar mass for satellite galaxies around MW/M31-like hosts in TNG50 within 300 kpc of their host (3D, red curve), at distances of 300 − 600 kpc (3D, blue curve), as well as using an alternative selection of satellites that adopts the selection criteria of the SAGA survey, i.e. within 300 kpc (2D) and with line-of-sight velocities of ±250 km s^{-1} (pink curve). Furthermore, I compare the TNG50 results to observed satellites of the MW and M31 (red dots, Wetzel et al. 2015) and the SAGA survey (pink dots, Mao et al. 2021). It should be noted that the comparison to observations of the SAGA survey is made at face value as their quenched definition is based on Hα equivalent widths.

TNG50 in the future.

Comparison to MW & M31 satellites: gas fraction-based quenched definition

In Figure 5.3, I change the adopted quenched definition from star formation rate-based to gas fraction-based according to Wetzel et al. (2015) for a matched comparison to the observed quenched fractions of MW and M31 satellites. Satellites with gas fractions of $M_{gas}/M_* < 0.1$ are considered to be quenched. I discuss the differences and the overlap between star-forming and quenched satellite subsamples from star formation rate-based and gas fraction-based quenched definitions in Appendix G.

Overall, Figure 5.3 depicts quenched fractions of the same satellite samples as Figure 5.2. This includes TNG50 satellites of MW/M31-like hosts within 300 kpc (3D, red curve), within 300 − 600 kpc (3D, blue curve), as well as for the SAGA-like satellite selection within projected 300 kpc and line-of-sight velocities of ±250 km s^{-1} (pink curve). Furthermore, the quenched fractions of MW and M31 satellites, as well as satellites from the SAGA survey's second stage (both within 300 kpc) depicted as red and pink dots, respectively. Note that for the SAGA survey, this still corresponds to a comparison at face value as they employ a quenched definition based on Hα equivalent widths.

Qualitatively, TNG50 satellites still exhibit the same trend as in Figure 5.2: the quenched fractions increase significantly towards lower satellite masses, i.e. most less massive satellite galaxies do not actively form stars. Quantitatively, however, defining the quenched state based on gas fractions slightly decreases the quenched fractions at the low-mass end ($M_* \lesssim 10^7$ M$_\odot$) to 78 per cent for TNG50 satellites at distances of $300 - 600$ kpc to their host and to 86 per cent for the SAGA-like selection of satellites (compared to previously $\sim$ 90 per cent for either in Figure 5.2). Satellites within 300 kpc of their host remain relatively unaffected with 96 per cent of them quenched. Therefore, some low-mass satellite galaxies with small gas fractions might still be actively forming stars in TNG50. At the high-mass end, on the other hand, employing a gas fraction-based quenched definition for TNG50 satellites results in the opposite trend. For satellites with $\sim 10^{10}$ M$_\odot$, the quenched fractions increase significantly compared to the star formation rate-based ones to 10 per cent for satellites at distances of $300 - 600$ kpc, 35 per cent for satellites according to the SAGA-like selection, and 30 per cent for satellites within 300 kpc of their MW/M31-like host (previously 0, 6, and 10 per cent, respectively). Massive satellites with small gas fractions may still be actively forming stars. Overall, matching the quenched definition to those of observed MW and M31 satellites within 300 kpc still results in a very good level of agreement between the observations of Wetzel et al. (2015) and the TNG50 simulations. For the SAGA survey, however, the previous discrepancies still hold due to their particularly small quenched fractions.

5.2.3 Dependence of satellite quenched fractions on host properties

With a statistical host sample of 198 MW/M31-like galaxies, the influence of host properties on the star formation activity of their satellites can be studied as well. In Figure 5.4, I examine the quenched fractions of various subpopulations of satellites split according to their total host mass M_{200c} (top left panel), host formation time z_{50}, i.e. the redshift at which the host halo had formed 50 per cent of its present-day total mass (top right panel), the average accretion time of each host's satellite population $t_{\mathrm{acc,\ avg}}$ (bottom left panel), as well as whether their host is isolated or part of a Local Group-like system (bottom right, see Chapter 5.1.1 for their selection criteria). In all panels, I employ the fiducial quenched definition based on the distance to the star forming main sequence (SFMS).

The quenched fraction of satellites of massive hosts of $M_{200c} = 10^{12.1} - 10^{12.8}$ M$_\odot$ (red curve) and less massive hosts $10^{11.5} - 10^{12.1}$ M$_\odot$ (blue curve) in the top left panel of Figure 5.4 exhibit the clearest difference. Across all stellar masses, satellites in more massive hosts display larger quenched fractions. While satellite galaxies with $M_* \gtrsim 10^{9.4}$ M$_\odot$ in lower mass hosts remain star-forming, 10 per cent of even the most massive satellites with $M_* \sim 10^{10}$ M$_\odot$ in more massive MW/M31-like hosts are quenched. Due to the higher satellite-to-host mass ratio, environmental effects can affect them more easily (e.g. De Lucia et al. 2012; Wetzel et al. 2012; Bahé et al. 2017; Davies et al. 2019, and see Chapter 1.2.1 and 1.2.2).

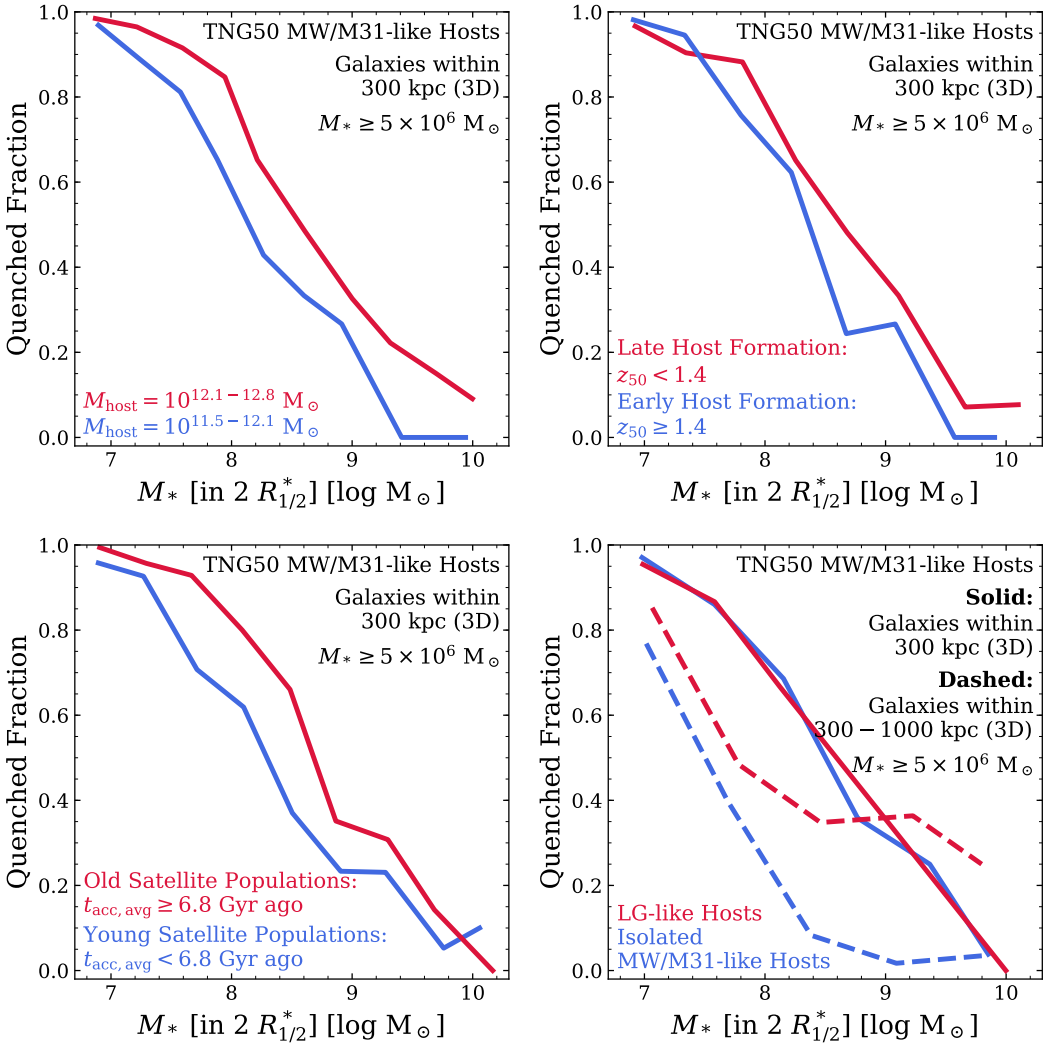

Figure 5.4: Dependence of satellite quenched fractions on host properties. Trends are depicted as medians for two subpopulations of all galaxies with $M_* \geq 5 \times 10^6$ M$_\odot$ within 300 kpc of TNG50 MW/M31-like hosts, depending on the host property in question (red and blue curves). I define galaxies to be quenched based on their distance to the SFMS. *Top left panel:* host halo mass as M_{200c} for less massive hosts of $10^{11.5} - 10^{12.1}$ M$_\odot$ and more massive hosts of $10^{12.1} - 10^{12.8}$ M$_\odot$. *Top right panel:* host halo formation time for hosts with late ($z_{50} < 1.4$) and early assembly ($z_{50} \geq 1.4$). Here, z_{50} corresponds to the redshift at which the host halo formed 50 per cent of its present-day total mass. *Bottom left panel:* average satellite infall age for systems with older satellites with average accretion times of $t_{\rm acc,\,avg} \geq$ 6.8 Gyr ago and younger satellite populations with $t_{\rm acc,\,avg} <$ 6.8 Gyr ago. *Bottom right panel:* for isolated MW/M31-like and LG-like hosts (see Chapter 5.1.1 for details). In addition to the quenched fractions of galaxies within 300 kpc (solid curves), I illustrate the quenched fractions of galaxies at larger distances of 300 − 1000 kpc to their host galaxy (dashed curves) as the satellites around LG-like hosts may become subject to further environmental effects in the intragroup medium.

Satellites of hosts with a later formation time of $z_{50} < 1.4$ (red curve) an earlier formation time of $z_{50} \geq 1.4$ (blue curve) in the top right panel are less clearly separated regarding their quenched fractions. There is a slight trend for satellites in hosts that assembled at a later time to be more quenched, however, this might stem from the correlation with total host mass. As briefly discussed in Appendix E of this thesis, host formation time – particularly in its early to intermediate stages – is slightly correlated with the present-day total mass of less massive host haloes.

The overall age of a host's satellite population – characterised by its average accretion time in the bottom left panel of Figure 5.4 – depicts a slightly clearer trend for quenched fractions across most of the satellite stellar mass range considered. Older satellite populations that were accreted on average ≥ 6.8 Gyr ago (red curve) exhibit higher quenched fractions than younger populations (blue curve) as older satellite populations have been subject to environmental effects and quenching mechanisms of their host for longer.

Comparing the quenched fractions of satellites within 300 kpc of the 10 LG-like hosts in TNG50 (red, solid curve) to isolated MW/M31-like hosts (blue, solid curve) in the bottom right panel of Figure 5.4 reveals almost no difference whatsoever. The environment within the virial radius of the main galaxy of an LG-like system has the same impact on its satellite population as in isolated MW/M31-like hosts. However, there is a significant difference for satellites at larger distances of $300 - 1000$ kpc (dashed curves). While these satellites generally exhibit lower quenched fractions than their counterparts in their hosts' inner regions – at the low-mass end up to 85 per cent for satellites of LG-like systems and up to 77 per cent for satellites of isolated MW/M31-like hosts – the quenched fractions of satellites in the outskirts of LG-like systems are consistently higher than those of isolated hosts, particularly at intermediate satellite stellar masses of $M_* \gtrsim 10^8$ $M_\odot$. Both the host's companion galaxy as well as the intragroup medium between them are able to affect satellites at larger distances more significantly – and subsequently quench their star formation activities.

5.2.4 Gas content of satellites around TNG50 MW/M31-like hosts

As seen in the previous sections of this chapter, satellite galaxies around MW/M31-like hosts – particularly within their virial radius – have mostly ceased to form stars. In the following, I examine how these satellite galaxies quench after infall with respect to their gas content as fuel for star formation processes and with a special emphasis on their hydrogen content. The molecular clouds in which star formation takes place are usually embedded in regions of cold atomic hydrogen (HI, e.g. Taylor et al. 1994; Hernquist et al. 1996; Pisano and Wilcots 1999).

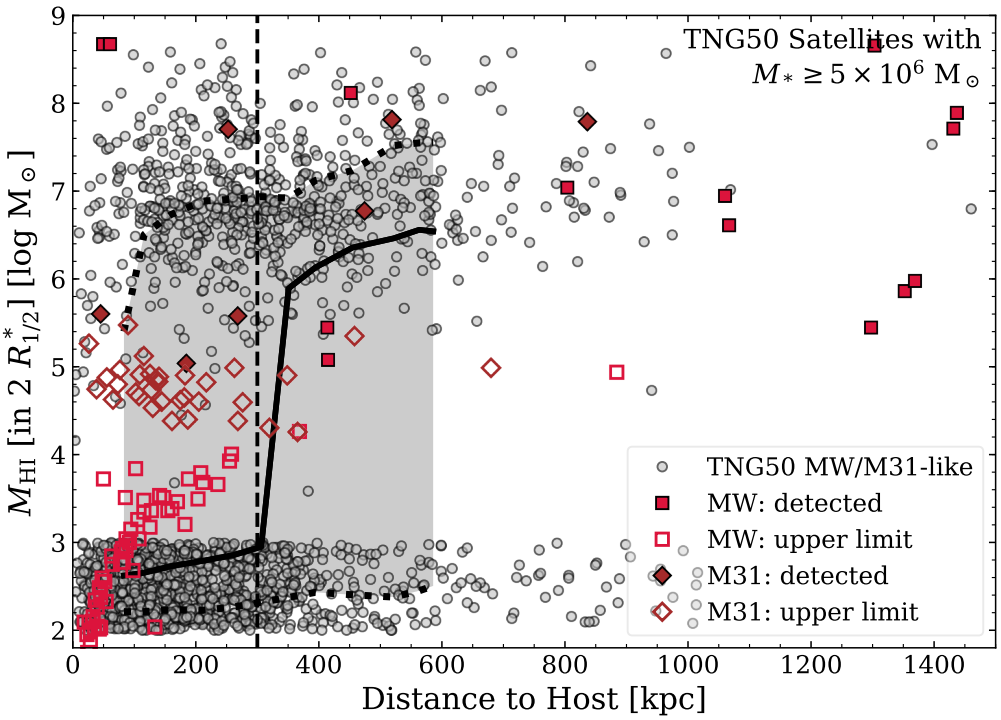

Figure 5.5: HI gas mass as a function of distance to their host galaxy (3D) for TNG50 satellites with a stellar mass of at least $M_* \geq 5 \times 10^6$ M$_\odot$ around MW/M31-like hosts (grey dots). I assign random HI masses of 10^2 to 10^3 M$_\odot$ for satellites containing no gas whatsoever due to resolution limitations. The solid, black curve corresponds to the TNG50 median, while the dotted, black curves and grey, shaded area denote their scatter as 16$^{\rm th}$ and 84$^{\rm th}$ percentiles. I compare the TNG50 satellites to the observed satellites of the MW and M31 (red squares and brown diamonds, respectively, Putman et al. 2021). While the filled squares and diamonds show detected HI mass measurements, the open symbols correspond to non-detections and simply denote upper limits. Note that there is no minimum stellar mass for MW and M31 satellites, i.e. their samples include even ultra-faint satellite galaxies.

HI mass vs. distance to host

I study the HI gas mass within two stellar half-mass radii $R^*_{1/2}$ of all satellites of TNG50 MW/M31-like galaxies as a function of the 3D distance to their host in Figure 5.5. The HI masses are based on the work of Popping et al. (2019) who calculated the total and molecular hydrogen content of TNG50 gas cells based on various theoretical recipes. Here, I employ HI masses obtained using the metallicity-based approach of Gnedin and Kravtsov (2011). As these HI masses cannot be computed for TNG50 satellites that contain no gas whatsoever due to limitations in numerical resolution, I simply assign them a random mass of $M_{\rm HI} = 10^2 - 10^3$ M$_\odot$, detached from the main relation. The grey circles in Figure 5.5 denote individual TNG50 satellites while the solid, black curve illustrates their median. The grey, shaded area and dotted, black curves correspond to their scatter as 16$^{\rm th}$ and 84$^{\rm th}$ percentiles. I compare the HI masses of TNG50 satellites to those of the observed satellite dwarf galaxies around the MW and M31 (red squares and brown diamonds, respectively, Putman et al. 2021). Filled symbols correspond to detected HI measurements while the open

squares and diamonds have no detected HI content and merely represent upper limits according to the GALFA-HI (Peek et al. 2011; Peek et al. 2018) and HI4PI (HI4PI Collaboration et al. 2016) surveys employed by Putman et al. (2021). It should be noted that while the TNG50 satellites in Figure 5.5 are restricted to $M_* \geq 5 \times 10^6$ M$_\odot$, there is no stellar mass limitation on the observed satellite galaxies of the MW and M31. Their satellite samples include even ultra-faint dwarf galaxies.

While there are TNG50 satellites with and without significant HI content both within 300 kpc of their host (dashed, vertical line) and at larger distances out to $\gtrsim$ 1000 kpc, there is a very steep transition between these gas-rich and gas-poor populations. Outside of $300 - 350$ kpc most satellite galaxies contain a significant amount of HI with $M_{\rm HI} \sim 10^6 - 10^7$ M$_\odot$. However, these gas masses drop dramatically and very rapidly for satellites in the inner regions of TNG50 MW/M31-like hosts. Here, most satellite galaxies contain no resolved HI whatsoever. With their fuel for star formation gone, these satellites become quenched.

This behaviour is consistent with that of the observed dwarf satellites around the MW and M31 from Putman et al. (2021). Most satellites with detected HI content are located outside of the virial radius of their host. Within $300 - 350$ kpc, the observed satellite galaxies become dominated by non-detections. The closer they are to their host galaxy, the smaller their upper HI limits become. One notable exception from this are the two red squares in the upper left corner of Figure 5.5 with $M_{\rm HI} \sim 10^{8.7}$ M$_\odot$ at a distance of $\sim$ 50 kpc. These points correspond to the LMC and SMC and exhibit larger HI masses than any of the TNG50 satellites that are located this close to their host galaxy. As the LMC and SMC are the most massive satellite galaxies of the MW and are most likely still on their first infall (Besla et al. 2007; Besla et al. 2010; Boylan-Kolchin et al. 2011; Kallivayalil et al. 2013), they are more resistant to environmental effects and are able to retain their gas more efficiently.

Satellite gas fractions in phase-space

I extend the study of the gas content of satellite galaxies around TNG50 MW/M31-like hosts to the phase-space in Figure 5.6. Thus, not only their host-centric distance but also their relative velocity are taken into account. In order to show their evolution from gas-rich to gas-poor, all galaxies within 600 kpc of their MW/M31-like hosts are included in the sample and are subsequently divided into 2D bins. Bins containing at least five satellite galaxies are colour-coded by their median gas fraction (blue to red from gas-rich to gas-poor). I consider both all gas (left panels) and specifically HI (right panels) within two stellar half-mass radii (i.e. within the main body of the galaxy). For TNG50 satellites that contain no gas whatsoever due to numerical resolution limitations , I assign a random gas mass of $10^2 - 10^3$ M$_\odot$ for either all gas or HI. The top panels depict the phase-space distribution of satellites in a random projection using their 2D distance to their host galaxy and their corresponding relative line-of-sight velocity – similar to how they might arise from observations. In the bottom panels, I employ 3D distance and velocities instead.

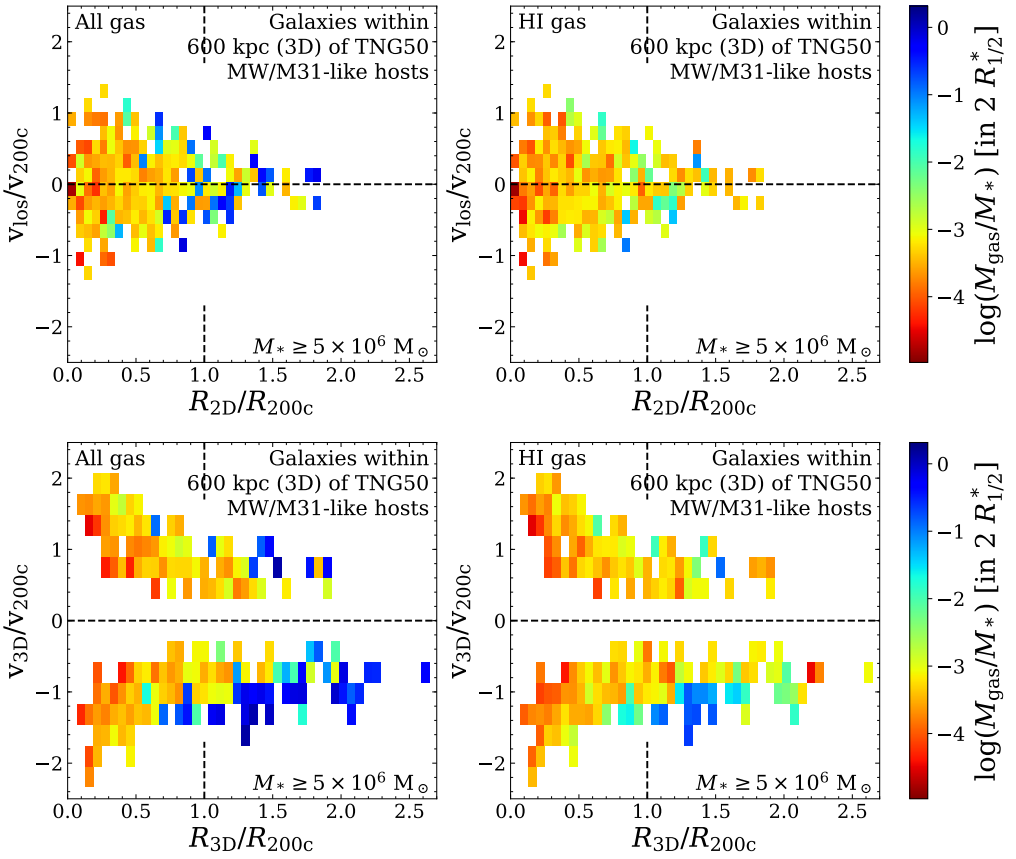

Figure 5.6: Phase-space distributions of satellites around TNG50 MW/M31-like hosts colour-coded by their gas fractions. I extend the sample beyond the virial radius (dashed, vertical lines) and include all galaxies with $M_* \geq 5 \times 10^6$ M$_\odot$ within 600 kpc of their host in the sample. Each bin contains a minimum of 5 satellites. The top panels show the phase-space distribution in a random projection using a 2D distance to their host and the corresponding line-of-sight velocity, while the bottom panels depict the 3D phase-space distribution. The left panels take all gas into account; the right panels are focused exclusively on HI gas. TNG50 satellites that do not contain any gas are assigned a random gas mass of $10^2 - 10^3$ M$_\odot$ (for either all gas or HI). It should be noted that while there is a visible gradient, most satellites (particularly within 300 kpc) barely contain gas with gas fractions of < 10 per cent.

Overall, the same trend is clearly visible in all panels of Figure 5.6: gas-rich satellites are predominantly found in the outer parts of the phase-space distribution whereas the closer satellites are located towards the central regions of phase-space, the smaller their average gas fractions are. However, it is important to note that while there is a visible gradient from gas-rich to gas-poor, most satellites – particularly within 300 kpc – barely contain gas, with gas fractions of < 10 per cent. Even the galaxies in the other regions of the phase-space at larger distances to their host with larger gas fractions (for all gas) are on average already gas-poor in HI. Considering the projected phase-space, no satellite bin contains HI gas fractions of more than 10 per cent. In 3D phase-space, on the other hand, such satellites are visible among infalling populations (i.e. at negative velocities) outside the virial radius. While projection effects can wash out some details of this trend, they still display the

same development.

However, the evolution of the gas content of satellites is best visualised in the bottom left panel of Figure 5.6. Here, satellite all-gas fractions are depicted in 3D phase-space. Gas-rich satellites are predominantly found at larger distances beyond the virial radius at infalling, negative velocities and – to a lesser degree – at outgoing, positive relative velocities. These backsplash galaxies may have retained more of their gas due to their own mass or possibly a favourable orbital configuration. Following their trajectory through phase-space, satellites continue to lose gas to their host environment: the closer they travel to its central regions towards smaller distances and relative velocities, the gas-poorer they become. I will examine link of phase-space trajectory and the satellites' time of infall in the next section.

Correlation of gas content and infall time

The trajectory of satellites across phase-space from its outer regions as an infalling galaxy to its centre close to its host takes place over several Gyr. I illustrate this in the left panel of Figure 5.7 by depicting the 3D phase-space distribution of satellite galaxies with $M_* \geq 5 \times 10^6$ $M_\odot$ within the FoF haloes of TNG50 MW/M31-like hosts as a function of their time since infall (with early to late infallers from red to blue). As in Figure 5.6, their distribution is divided into 2D bins. Bins containing at least three satellites are colour-coded accordingly. The resulting phase-space distribution displays a clear correlation with infall time: satellites that experienced their first infall only recently are found in the outskirts of phase-space at large distances and predominantly infalling, negative velocities. Their average time of infall continuously shifts to earlier times towards the central regions of phase-space with the most ancient infallers closest to their host and with the smallest relative velocities. This phase-space distribution and its correlation with infall time are well in agreement with previous studies regarding the satellite populations of galaxy clusters in simulations and observations (Rhee et al. 2017; Pasquali et al. 2019; Smith et al. 2019a). However, – to my knowledge – this is the first project to show that this trend holds for less massive hosts as well with a statistically significant sample of both satellite galaxies and MW/M31-like hosts.

As satellite gas fractions and their time since infall exhibit very similar trends in phase-space, I examine their correlation with each other in the right panel of Figure 5.7 with respect to both their HI and H_2 content. For satellites that originally contain no gas whatsoever due to the limitations of numerical resolution, I simply assign a random gas fraction of $10^{-5} - 10^{-6}$, detached from the main relation. The brown dots illustrate the HI content of satellite galaxies while the brown, solid curve and shaded area denote their median and scatter (16^{th} to 84^{th} percentiles) as a function of their time since infall. The red, dashed curve and the red, dotted curves correspond to the median and scatter of their H_2 gas fractions.

While recent infallers exhibit a larger fraction of H_2 than HI within two stellar half-mass radii (albeit I do not show it here, this trend is reversed when considering

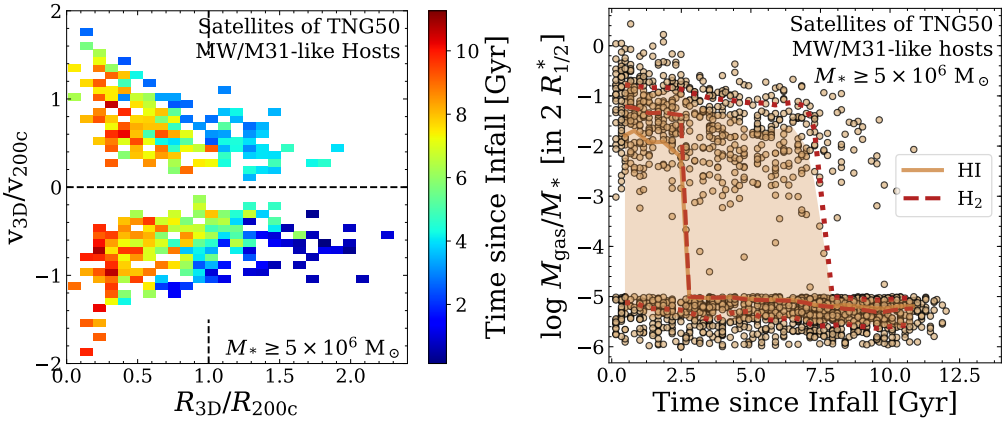

Figure 5.7: Correlation of satellite infall time with their distribution in phase-space and their gas content. *Left panel:* phase-space distribution of satellite galaxies with $M_* \geq 5 \times 10^6$ M$_\odot$ around TNG50 MW/M31-like hosts, colour-coded by time since infall (red to blue for ancient to recent infall times). Each bin contains a minimum of 3 satellites. *Right panel:* satellite gas fractions within two stellar half-mass radii $R^*_{1/2}$ (i.e. within the galaxy's main body) as a function of time since infall. Brown circles denote HI fractions; the brown, solid and red, dashed curves illustrate the running medians of HI and H_2 fractions, respectively. The scatter of HI and H_2 gas fractions as 16th and 84th percentiles are illustrated as brown, shaded areas and red, dotted curves.

all gravitationally bound gas due to the larger abundance of atomic hydrogen in their gaseous haloes), both exhibit the same correlation with intermediate and later times of infall. The longer a galaxy has spent as a satellite, the smaller are their gas fractions in terms of HI and H_2. For satellites that have been accreted more than 2.5 Gyr ago, gas fractions drop dramatically and the satellite populations of TNG50 MW/M31-like host become dominated by satellites containing amounts of gas that are too small to resolve numerically – the equivalent of observational non-detections. This evolution after infall is consistent with a ram pressure stripping scenario in TNG50. As galaxies become satellites of a new host and enter its gaseous halo, ram pressure drives gas from both their own halo as well as their galaxies. With most of their gas reservoirs lost over the course of a few Gyr, the satellites cease to form stars and become passive (Yun et al. 2019; Donnari et al. 2021b), resulting in the quenched fractions seen in Figure 5.2.

5.2.5 Evolution of satellite mass components after infall

In the following, I summarise the evolution of galaxies after they become satellites of a new host environment as well as the scope of environmental effects that act on them and their mass components. Figure 5.8 depicts the evolution of mass as a function of time since infall for satellite galaxies around present-day MW/M31-like hosts in TNG50; this includes all gravitationally bound dark matter (black curves), all gravitationally bound gas (purple curves) and gas within two stellar half-mass radii $R^*_{1/2}$ (i.e. within the main body of the galaxy, green curve), as well as stellar

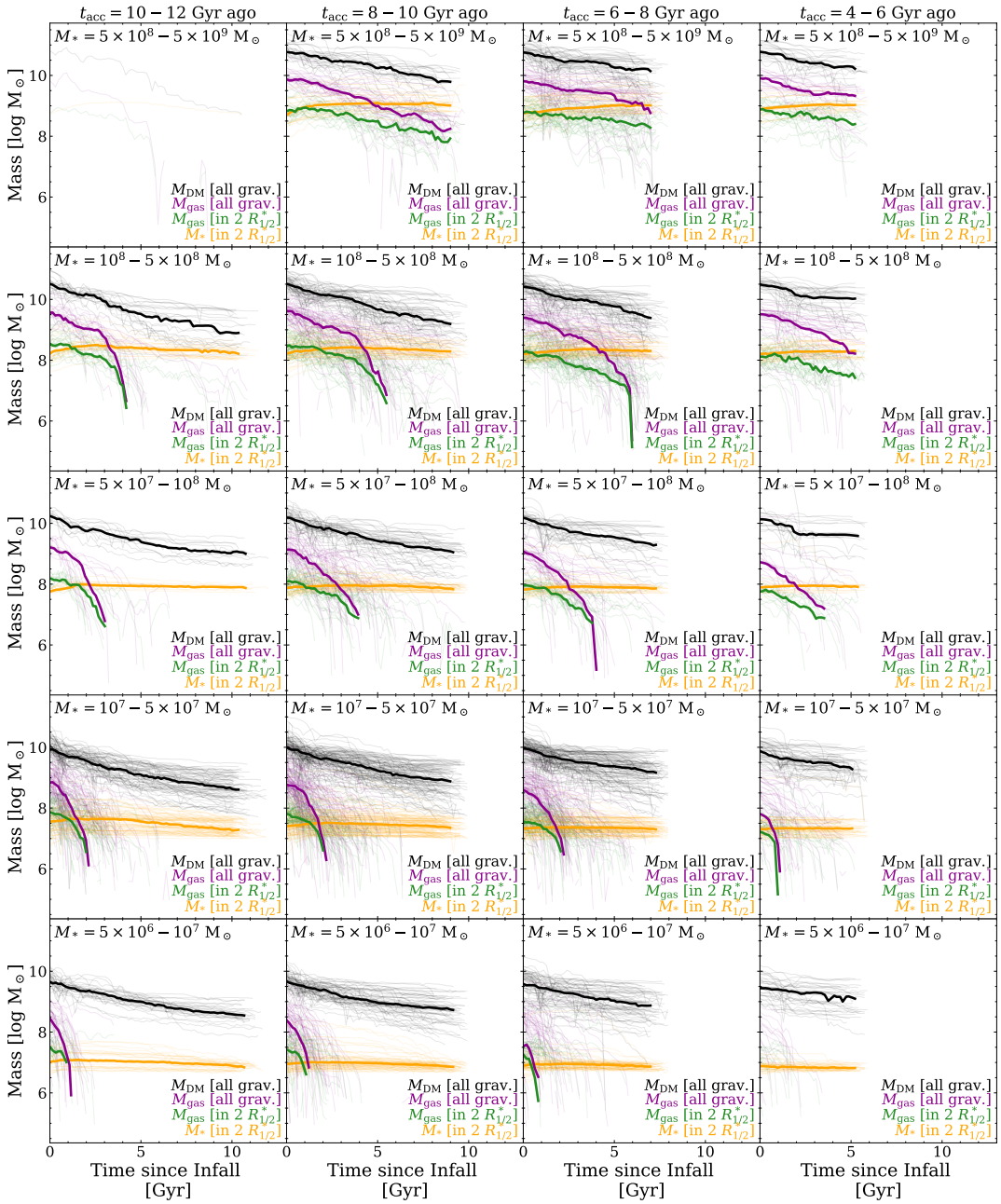

Figure 5.8: Evolution of mass components after infall for present-day satellite galaxies around TNG50 MW/M31-like hosts. I divide satellite populations by their stellar mass and their time of first infall into any host (i.e. not necessarily their present-day MW/M31-like host). Each column corresponds to a different infall time period (with early to late infall from left to right), each row denotes a different satellite stellar mass range (decreasing from top to bottom). Each panel illustrates the evolution of all gravitationally bound dark matter (black curves), all gravitationally bound gas (purple curve), gas within $2R^*_{1/2}$ (i.e. within the main body of the galaxy, green curve), and stellar mass within $2R^*_{1/2}$ (orange curve). Thin curves in the background correspond to the mass evolution of individual satellite galaxies whereas the thick curves depict their median.

mass within $2R^*_{1/2}$ (orange curves). The thick curves illustrate the median mass evolution of TNG50 satellites regarding these mass components. However, as the medians of evolutionary tracks may be hard to interpret, I show the tracks of individual satellites in the background as thin curves. Furthermore, I examine their evolution as a function of satellite stellar mass – as their own mass increases their resistance to environmental effects – and infall time – since the resulting impact on satellite galaxies become more significant over time. Each row corresponds to a different range in satellite stellar mass (decreasing from top to bottom) while each column denotes a different period of accretion time $t_{\rm acc}$ with early infallers in the left and recent infallers in the right column. As the subsample of the most massive satellites with $5 \times 10^8 - 5 \times 10^9$ M$_\odot$ that experienced their first infall $10 - 12$ Gyr ago in the top left panel only contains a single galaxy, I only show its individual evolutionary tracks without a median. Furthermore, this mass bin spans a larger range than all others to account for the smaller abundance of massive satellites around MW/M31-like hosts.

Qualitatively, satellite mass components exhibit the same evolution regardless of their stellar mass or their time of accretion. Dark matter mass decreases with time due to tidal stripping inside the gravitational potential of their new host. However, dark matter remains the dominant mass component for all satellite galaxies at present-day times – even after $10 - 12$ Gyr of active tidal stripping (see left panels of Figure 5.8). The gas content of both their haloes as well as within the satellite galaxies themselves is removed simultaneously and quickly over the course of a few Gyr after accretion, as the satellites become subject to ram pressure stripping (as tidal stripping would only remove the outer gas at first). The period over which satellite galaxies lose their gas is a function of their own stellar mass: more massive satellite galaxies are able to retain their gas for longer as they are more resistant to environmental effects due to their deeper gravitational potential wells. This period ranges from $1 - 2$ Gyr for satellites with $M_* \sim 5 \times 10^6 - 10^7$ M$_\odot$ to $4 - 6$ Gyr for more massive satellites with $10^8 - 5 \times 10^8$ M$_\odot$ (bottom to top panels). On average, most satellites around TNG50 MW/M31-like hosts do not contain gas anymore (i.e. too little gas to resolve numerically). Only the most massive satellites with $5 \times 10^8 - 5 \times 10^9$ M$_\odot$, as well as those with $10^8 - 5 \times 10^8$ M$_\odot$ that experienced their infall $4 - 6$ Gyr ago manage to retain gas until the present day. The least massive galaxies with $5 \times 10^6 - 10^7$ M$_\odot$, on the other hand, that became satellites $4 - 6$ Gyr ago – on average – did not even contain any gas at their time of accretion. The overall gas mass of satellites is actually somewhat correlated with their time of accretion: early infallers with $t_{\rm acc} = 10 - 12$ Gyr ago had slightly larger gas masses at their time of infall than satellites with $t_{\rm acc} = 4 - 6$ Gyr as these more recent infallers had more time to transform their gas into stars before encountering the environment of a more massive host galaxy.

Finally, the stellar mass component of satellites evolves relatively flat after accretion. While there might still be a slight increase in stellar mass during the first

$1-2$ Gyr as a satellite (particularly for more massive satellites), active star formation ultimately ceases and the satellite galaxies become quenched as they lose their gas reservoirs to the gaseous halo of their host due to ram pressure stripping. For the earliest infallers with $t_{\rm acc} = 10-12$ Gyr ago, there is a slight decrease in stellar mass at more recent times, particularly in the $10^7 - 5 \times 10^7$ $M_\odot$ bin. These satellites have lost enough of their dark matter halo to tidal stripping in the gravitational of their host that it has begun to affect the main body of the satellite galaxy itself. If we were to look at all gravitationally bound stellar mass instead, there would be a slight decrease in stellar mass towards present-day times. However, most satellites in my sample that have been accreted more recently, have not been significantly affected by tidal stripping of their stars, yet. This is consistent with the results of Chapter 3: even at the scale of the MW, the resulting shift of the satellites' SHMR is the same as their stellar mass remains largely unaffected by tidal stripping (see Figure 3.8 and Chapter 3.3.1 for a discussion). It should be noted, however, that this is a somewhat biased view as I only consider the present-day, surviving satellite populations of TNG50 MW/M31-like hosts. As seen in Chapter 4.2.5, the number of all satellites ever accreted is significantly larger. Most satellites that would exhibit a significant amount of stellar mass loss within the main body of their respective galaxy, would be quickly disrupted at this point (Bahé et al. 2019) and would thus not be included in the satellite sample depicted in Figure 5.8.

Chapter 6

Conclusions & outlook

Over the last chapters, I introduced the ΛCDM model of cosmological structure formation, halo environments across a range of several orders of magnitudes in mass, and the effects they assert on satellite galaxy populations. I established the fundamentals of cosmological simulations of galaxy formation, the physical processes their models describe, and presented the IllustrisTNG suite of cosmological magneto-hydrodynamical simulations. I analysed environmental effects on satellite galaxy populations in an unprecedented combination of statistical sample size and numerical resolution across simulation volumes, resolution levels, as well as baryonic and dark matter-only implementations. This has resulted in mass ranges covering multiple orders of magnitude for both host and satellite samples, ranging from massive galaxy clusters similar to the observed Coma, Perseus, or Virgo clusters to Local Group-like environments and more isolated Milky Way- (MW) and Andromeda-like (M31) systems for host environments. Satellite galaxies range from classical dwarf galaxies like Leo I to Magellanic Cloud-like, or even MW-like and more massive satellites around cluster hosts.

Thus, I have been able to investigate the galaxy-halo connection of satellite and central galaxies in the stellar-to-halo mass relation as the most fundamental scaling relation in a ΛCDM framework, to study its differences for satellite galaxies in group and cluster environments, as well as to identify the processes responsible for driving the resulting disparities (see Chapter 3). I have put the present-day, observed satellite populations of the Milky Way and Andromeda galaxies in a cosmological context, studied the abundance of satellite and subhalo populations in comparison to both observational surveys and previous simulations, and was able to reconcile the missing satellites problem as one of the remaining challenges to the ΛCDM model (see Chapter 4). Finally, I have analysed the star formation activity of satellite populations around MW/M31-like hosts, investigated how they lose their gas reservoirs and quench within the virial radius of their host halo, and summarised the interconnected co-evolution of their mass components – dark matter, gas, and stars – after infall to identify the environmental processes acting on them (see Chapter 5).

In the following, I summarise the results of Chapters 3, 4, and 5 before putting their findings into a greater context and concluding my thesis in Chapter 6.4.

6.1 Summary of Chapter 3: the distinct SHMRs of satellite and central galaxies

I have analysed the stellar-to-halo mass relation (SHMR) in the suite of cosmological magneto-hydrodynamical simulations IllustrisTNG, using all three flagship runs TNG50, TNG100, and TNG300. I distinguished between centrals and satellites with total dynamical masses of $M_{\rm dyn} \geq 10^{10.5}$ M$_\odot$ and considered exclusively satellites in group- and cluster-like hosts with $M_{\rm host} = 10^{12} - 10^{15.2}$ M$_\odot$. I have characterised the effects of such environments on the evolution of galaxies, their surrounding dark matter subhaloes, and the SHMR scatter as a function of total dynamical mass. I have combined the results of all three IllustrisTNG simulations to maximise the dynamic range and have devised a resolution correction of the galaxy stellar masses that extrapolates the TNG100 and TNG300 results to TNG50 resolution, resulting in three sets of output with the same effective numerical mass resolution.

The results of Chapter 3 are summarised as follows.

- The SHMR of satellite galaxies in groups and clusters of with $M_{\rm host} \geq 10^{12}$ M$_\odot$ exhibits a significant offset from the SHMR of centrals (Figure 3.1). At fixed $z = 0$ dynamical mass, satellites have larger stellar masses and larger stellar mass fractions. This shift and the scatter of the relation correlates with the mass of their host: for example, satellites in hosts of $10^{14} - 10^{15.2}$ M$_\odot$ at $z = 0$ reach median stellar mass fractions of up to 15 per cent at the SHMR's peak, while satellites in less massive hosts of $10^{12} - 10^{13}$ M$_\odot$ reach only 10 per cent (Figure 3.3, top panel). This is a significant difference compared to centrals, which display a peak stellar mass fraction of about $2 - 4$ per cent.

- This offset between the SHMRs of central and satellite galaxies is the result of environmental effects that act in an outside-in fashion. Since the inner galaxy regions remain largely unaffected by their environment, the offset between the SHMRs of centrals and satellites disappears if I measure masses within sufficiently small physical apertures (Figure 3.2).

- The ratio of stellar mass between satellites and centrals as a function of total dynamical mass for satellites within their host's virial radius $R_{\rm 200c}$ increases towards lower dynamical mass (up to a factor of 16 at $z = 0$) and shows no significant evolution with time in the range $z = 0 - 2$ (Figure 3.3, bottom panel). The tidal forces within the host halo's gravitational potential strip a significant fraction of satellite subhaloes over relatively short time scales.

- While the scatter σ_* in (logarithmic) stellar mass as a function of dynamical mass of both centrals and satellites follows the same shape – roughly constant at $0.1 - 0.2$ dex for dynamical masses above the respective SHMR peak, and increasing towards the lower mass end – satellites exhibit a higher scatter over the whole range of dynamical mass (Figure 3.4). However, the rise in scatter at

low subhalo masses is steeper for satellites than for centrals since these dwarf-like satellites are more susceptible to the impact of group and cluster environments. Here, σ_* reaches up to $0.6 - 0.8$ dex for the least massive galaxies considered. The SHMR scatter of the mass-limited sample of satellites increases continuously with increasing host mass (Figure 3.5, top panel). Satellites with $M_{\rm dyn} \gtrsim 10^{12}$ M$_\odot$ show no evolution with redshift. For satellites of lower dynamical mass, however, the scatter decreases systematically with increasing redshift – albeit only weakly (Figure 3.5, bottom panel).

- At fixed $z = 0$ dynamical masses, satellites with higher apparent stellar mass fractions tend to reside closer to the group or cluster centre, experienced an earlier infall (both into the virial radius of their present-day host as well as into another halo in general), and inhabit higher local luminosity density regions than analogue satellites with lower stellar mass fractions (Figures 3.6 and 3.7).

- Infall into a more massive environment affects the dark matter and stellar components of satellite galaxies in different ways (Figure 3.8). While dark matter mass is dominated by tidal stripping and overall mass loss – regardless of host mass or the satellites' stellar mass – there is a significant net increase for stellar mass and still ongoing star formation post-infall. However, the stellar mass distribution shifts towards net mass loss with both increasing host mass and galaxy stellar mass. Tidal stripping of stars becomes more efficient within the deeper potentials of massive galaxy clusters. Since more massive galaxies might already be quenched pre-infall, they show a less distinct net mass gain.

- More massive clusters are more efficient in driving satellites to larger stellar mass fractions (Figure 3.9). Satellites that survive through $z = 0$ in lower-mass hosts cover a smaller range of infall times compared to satellite populations in more massive hosts – and are therefore exposed to their host environment for a shorter time. Furthermore, as noted above, satellites with earlier infall time have been exposed to the cluster/group potential for a longer time and generally exhibit larger SHMR offsets from central galaxies. Yet, even at fixed infall time, the stellar mass fractions of satellites exhibit an increasing offset with host mass compared to the SHMR of centrals.

- Considering the evolution of centrals into satellites in the SHMR plane between $z = 1$ and $z = 0$ (Figure 3.10), I find the transition to be dominated by dark matter loss and tidal stripping after star formation has been quenched by the infall into a more massive host. However, even before the galaxies have become satellites they start to move off the centrals' SHMR due to a decreasing growth in dark matter and continued star formation. Galaxies that stay centrals, on the other hand, simply evolve along the SHMR (which evolves only weakly at $z < 1$) and increase in both stellar and dark matter mass.

In conclusion, I have highlighted the influence of group and cluster environments on the stellar and dynamical mass components of satellite galaxies. Satellite galaxies selected at a given time with a certain minimum dynamical or total mass do not simply contribute to the scatter in the SHMR of central galaxies but form their own distinct and separate relation. Whether they become satellites of a low-mass group or of a massive galaxy cluster, their SHMR shifts and their scatter increases with respect to the SHMR of centrals. While satellites might appear to be more efficient at forming stars when compared to centrals at fixed total dynamical mass, this difference is predominantly caused by tidal stripping of their dark subhaloes by the gravitational potential of a more massive host halo.

6.2 Summary of Chapter 4: satellite abundance of MW/M31-like galaxies with TNG50

I have analysed the abundance of satellite galaxies at $z = 0$ around 198 MW- and M31-like galaxies in TNG50, the final instalment in the IllustrisTNG suite of cosmological magneto-hydrodynamical simulations. Thanks to the available volume and the zoom-in-like resolution of TNG50, I have obtained a statistically-significant sample of both MW/M31-like galaxies as well as their satellite populations within 300 kpc (3D) and were able to reliably resolve satellites down to stellar masses of 5×10^6 $M_\odot$. From TNG50, I have selected MW/M31 analogues as disky galaxies with a stellar mass of $M_* = 10^{10.5-11.2}$ $M_\odot$ in relative isolation at $z = 0$ (Figure 4.1). I have compared my findings to both recent observational surveys and previous cosmological zoom-in and large-scale simulations by carefully matching both selection criteria and mass or magnitude distributions of the hosts. I have put the population of present-day survivors in contrast to the abundance of all satellites that have ever been accreted by MW- and M31-like hosts for luminous satellite galaxies in TNG50 as well as subhaloes in both TNG50 and its dark matter-only analogue TNG50-Dark. Furthermore, I have compared the results for TNG50-Dark to subhalo abundances of other, previous DM-only simulations. Finally, I quantified the correlations of satellite abundance with various host galaxy and host halo properties.

The results of this Chapter 4 are summarised as follows.

- Satellite galaxies around TNG50 MW/M31-like hosts follow basic scaling relations that are in reasonable agreement with satellite populations from previous zoom-in simulations, semi-empirical models, and observed Local Volume dwarfs (Figures 4.2 and 4.3).

- The abundance of satellite galaxies around MW- and M31-like hosts in TNG50 is remarkably diverse and exhibits a significant host-to-host scatter (Figure 4.4, left panel). The total number of satellites with $M_* \geq 5 \times 10^6$ $M_\odot$ around TNG50 hosts ranges from 0 to 20 (i.e. between 2 and 11 within $16^{\text{th}} - 84^{\text{th}}$ percentiles). This degree of scatter persists even at fixed host halo mass: the total

number of satellites in 10^{12} $M_\odot$ hosts range from 0 to 11 (Figure 4.14). However, the median TNG50 MW/M31-like galaxy has a total of 5 satellites down to $M_* \sim 5 \times 10^6$ $M_\odot$, the most massive of which reaches a stellar mass of $M_* \sim 10^{8.5}$ $M_\odot$.

- While the distribution of total satellite abundance appears to be skewed to lower numbers when increasing the minimum satellite stellar mass, this is merely an effect of Poisson statistics (Figure 4.4, right panel). In fact, their normalised distributions show that the diversity, i.e. scatter, of satellite systems remains the same regardless of the employed minimum stellar mass (Figure D.1, right panels).

- Considering not only the present-day, surviving satellite population at $z = 0$ but all satellites that have ever been accreted by MW/M31-like hosts, I show that at a fixed minimum stellar mass, the number of ever accreted satellites is larger by a factor of $4 - 5$ than those that survive through $z = 0$ (Figure 4.11). According to TNG50, on average, present-day satellites of the MW and Andromeda have been accreted more recently than $z \sim 0.7 - 1$.

- While there can be up to 120 surviving subhaloes in TNG50 MW/M31-like galaxies with $M_{\rm dyn} \geq 5 \times 10^7$ $M_\odot$ and $V_{\rm max}/V_{\rm 200c} \sim 0.02$, their number is vastly reduced (by more than a factor of 10) when I additionally require them to host a luminous galaxy, e.g. with $M_* \geq 5 \times 10^6$ $M_\odot$ (Figure 4.12). Moreover, the TNG model returns a suppressed cumulative subhalo mass function in comparison to DM-only predictions.

- Using the baryonic simulation, I show that the abundance of satellites depends on host properties. More massive and K-band brighter galaxies host more satellites at $z = 0$ (Figure 4.13). Furthermore, more massive haloes, haloes that assembled later in time, and those that are less concentrated host a larger number of satellites at present-day times (Figure 4.14), with the latter correlation being weaker than those with mass and assembly time. Overall, the abundance of satellite galaxies around MW/M31-like galaxies in TNG50 correlates more strongly with host *halo* than host *galaxy*: total satellite abundance exhibits the most significant correlation with host halo mass.

- Whereas Andromeda holds a richer system of satellites than the 1σ scatter of the TNG50 MW/M31-like galaxies, this is reasonable since the mass of Andromeda lies at the high-mass end of the TNG50 galaxies selected for the comparison (see Figures 4.13 and 4.14). Moreover, while both the Galaxy and Andromeda host a few more massive satellites than the TNG50's average, hosts similar to these do exist in TNG50 (Figures 4.5 and 4.6). In fact, there are 6 MW/M31-like galaxies (i.e. 3 per cent of MW/M31-like hosts) in TNG50 that host both a Large and a Small Magellanic Cloud-like satellite (with the LMC-like galaxy as their most massive satellite).

- Comparing the satellite abundances in TNG50 with observed hosts – e.g. MW-like galaxies from the SAGA survey (Geha et al. 2017; Mao et al. 2021) and hosts in the Local Volume (Carlsten et al. 2021) – yields consistent results (Figures 4.7 and 4.8, respectively). In both the comparison at face value with my fiducial TNG50 sample of MW/M31-like hosts and the comparison with the matched selections of my SAGA- and LV-like host samples, TNG50's median and scatter agree well with the observational results from SAGA, but less so from Carlsten et al. (2021).

- TNG50 MW/M31-like hosts exhibit satellite mass functions that are in good overall agreement compared to previous cosmological hydrodynamical simulations of MW-like hosts, even those with better numerical resolution (Figure 4.9). When compared at face value, there is a significant scatter not only between simulations but also between hosts of the same models. However, these deviations are expected given the large intrinsic galaxy-to-galaxy variations and the host-dependent trends of the satellite abundances, especially with host mass. In fact, when I compare TNG50 results by replicating the host mass selection of the Auriga and Latte simulations, I obtain remarkably consistent results (Figure 4.10).

In conclusion, thanks to the TNG50 simulation I have highlighted and quantified the diversity of satellite populations around MW- and M31-like galaxies, utilising a statistical sample of 198 hosts. The reasons for this diversity in present-day, surviving satellites depend on properties of the host itself and on environmental effects. More massive hosts and hosts with a later halo assembly are richer in surviving satellite galaxies at $z = 0$, as accreted satellites can be disrupted or merge inside their host halo. Overall, however, amid such galaxy-to-galaxy diversity and different galaxy formation models, the satellite abundances predicted by TNG50 are consistent with observed galaxies within the Local Volume and beyond, as well as several previously simulated MW- and M31-like galaxies. However, whereas the scientific conclusions from previous comparisons had been de facto impaired by limited host number statistics and by host selections and mass ranges that were not necessarily compatible, I am now able to assess the bounty of the theoretical model while controlling for selection effects. Twenty years after the original formulation of the missing satellites problem, we can confidently put it to rest.

6.3 Summary of Chapter 5: gas content & SF activity of TNG50 MW/M31-like satellites

In Chapter 5, I have analysed the star formation activity of present-day satellite galaxies around 198 MW/M31-like hosts in TNG50. The combination of cosmological volume and zoom-in-like resolution allows me to study statistical samples of both hosts and satellites, and to reliably identify satellite galaxies down to stellar

masses of $M_* = 5 \times 10^6$ M$_\odot$. I have examined the spatial distribution of satellite populations around their host galaxy and compared them to observed systems. I have studied the star formation activity of satellites in various distance apertures around their hosts to investigate the impact of environmental effects on different subpopulations of satellites. Furthermore, my statistical host sample allows to search for correlations between satellite quenched fractions and host properties. In order to determine how satellite galaxies have become quenched, I have explored their gas content with a specific focus on atomic hydrogen as the fuel for star formation processes, and have related their lack of gas to their location within the host system as well as their time of infall. Finally, I have analysed the effects of environment on the evolution of satellite galaxies and their specific mass components as a function of both their own stellar mass and their time of infall.

The results of Chapter 5 are summarised as follows.

- Satellites around TNG50 MW/M31-like hosts exhibit a realistic phase-space distribution compared to observed satellite galaxies around the MW and M31, as well as MW-like systems from the SAGA survey (Mao et al. 2021). Whereas massive TNG50 satellites similar to the LMC, SMC, Triangulum, M32, and NGC205 are located across all distances to their respective hosts, some inhabit regions as close to their host galaxy as their observed counterparts (Figure 5.1).

- The quenched fractions of satellites around MW/M31-like hosts in TNG50 is a strong function of their own stellar mass: most low-mass satellite galaxies have ceased to form stars. Below stellar masses of 10^7 M$_\odot$, this reaches up to 98 per cent for satellite galaxies within 300 kpc of their host and 90 per cent for satellites outside the virial radius at distances of $300 - 600$ kpc (Figure 5.2). For the latter population, quenched fractions are consistently lower across the range of satellite stellar masses.

- The quenched fractions of TNG50 satellites are in agreement with the observed satellites around the MW and M31 (Figures 5.2 and 5.3). This holds for both a comparison at face value using the fiducial, SFR-based quenched definition for TNG50, as well as with the gas fraction-based quenched definition the observations employ (Wetzel et al. 2015). However, the quenched fractions of satellites around TNG50 MW/M31-like hosts are in stark contrast to those of the SAGA survey (Mao et al. 2021). The satellites of the observed SAGA hosts exhibit consistently lower quenched fractions than TNG50 satellites across all stellar masses, reaching only up to 65 per cent at the low-mass end. This discrepancy may be caused by the SAGA survey's surface brightness limit (see figure 2 of Font et al. 2021b) or by an inaccurate comparison at face value. As the SAGA survey employs a quenched definition based on the Hα equivalent width, radiative transfer models are required in order to perform a proper comparison by creating mock spectroscopy of TNG50 satellites. I will address this in the future.

- Satellite quenched fractions are further correlated with host properties (Figure 5.4). More massive hosts that assembled later in time, as well as those harbouring an older satellite population with an earlier average accretion time exhibit systematically larger satellite quenched fractions. Whereas there is no difference between the quenched fractions of satellites within 300 kpc of either isolated MW/M31-like or LG-like hosts in TNG50, satellites outside the virial radius of LG-like hosts at distances of $300 - 1000$ kpc exhibit significantly larger quenched fractions than those of isolated MW/M31-like hosts.

- The gas content and HI masses of TNG50 satellites around MW/M31-like systems is a strong function of host-centric distance, decreasing the closer they get to their host (Figure 5.5). While most satellites outside the virial radius of their host still contain atomic hydrogen, their HI content drops drastically around distances of $300 - 350$ kpc. Within 300 kpc, most TNG50 satellites contain no gas whatsoever (i.e. too little gas to resolve numerically). This trend is consistent with the behaviour of observed satellites around the actual MW and M31 galaxies (Putman et al. 2021).

- Satellite gas content is further correlated with their position in phase-space. Satellites in the outer regions of phase-space, i.e. at larger distances to their host and with infalling relative velocities (and to a lesser degree for outgoing velocities) tend to be on average gas-richer than those in the inner regions of phase-space. At small host-centric distances and relative velocities close to 0 km s^{-1}, satellites exhibit the smallest gas fractions (Figure 5.6). On average, the gas fractions of those within the virial radius lie below 10 per cent. This holds for all gas in general, as well as HI specifically, in both projected and three-dimensional phase-space.

- The satellite galaxies' times of first infall are well correlated with their their phase-space position and, therefore, with their gas fractions (Figure 5.7). Whereas satellites with recent infall times ($0 - 4$ Gyr ago) are on average located in the outer regions of phase-space, ancient infallers ($8 - 12$ Gyr ago) inhabit its central regions. This clear trajectory throughout phase-space is consistent with the findings of previous studies of satellite populations in galaxy clusters (Rhee et al. 2017; Pasquali et al. 2019; Smith et al. 2019c). Furthermore, satellite gas fractions in terms of atomic and molecular hydrogen are correlated with infall time and depict a bimodal distribution. While recent infallers still contain significant amounts of gas, gas fractions drop notably and rapidly for satellites whose first infall occurred more than 2.5 Gyr ago. These TNG50 satellites mostly contain no gas at all (i.e. too little gas to resolve numerically).

- MW/M31-like hosts in TNG50 exert distinct environmental effects on the evolution of their satellites' mass components after infall (Figure 5.8). While dark

matter remains the dominant mass component throughout their lifetime, it decreases continuously as the satellites' dark matter haloes are removed by tidal stripping in the gravitational potential of their host. After infall, the satellites start to lose gas from both their halo as well as the main body of the galaxy simultaneously as they become subject to ram pressure stripping in the gaseous halo of their host. Although more massive satellites are deprived of their gas more slowly than their less massive counterparts, most satellites do not contain any detectable gas by $z = 0$. On average, only the most massive satellites with stellar masses of $5 \times 10^8 - 5 \times 10^9$ $M_\odot$ manage to retain their gas until the present day. With their gas reservoirs gone, satellite galaxies cease to form stars soon after their infall. Although there is still a slight increase in stellar mass after infall, it remains mostly constant throughout time. Once enough of the satellite dark matter halo has been removed, the stars in their halo and in their galaxy's main body start to be affected by tidal stripping as well.

In conclusion, I have highlighted and investigated the star formation activity and gas content of satellite galaxies around MW/M31-like hosts in TNG50 along with their evolution after infall. Within the virial radius of their host, satellites experience ram pressure stripping, rapidly lose their gas reservoirs over the course of a few Gyr, and subsequently cease to form stars and become quenched. This process is particularly effective for low-mass satellites. Since more massive satellites are more resistant to their environment, they manage to retain their gas for longer and may continue to form stars even up to the present day. MW/M31-like hosts in TNG50 assert environmental effects on their satellites to a similar degree as the observed MW and M31 systems, with a sharp drop in satellite gas content for populations within the virial radius – for all gas in general, as well as HI and H_2 specifically. Thus, the TNG50 model produces a realistic population of satellite galaxies in MW/M31-like systems with respect to their distribution, gas content, and star formation activity, and illustrates the interconnected co-evolution of their mass components under the influence of their environment after infall.

6.4 Final discussion

6.4.1 On IllustrisTNG and the choice of simulations

This thesis has given an insight into the evolution of satellite galaxy populations under the influence of clusters, groups, and MW/M31-like hosts according to the IllustrisTNG models within the ΛCDM framework of structure formation. Thus, I have investigated the impact of infall into a new and more massive environment on the dark matter haloes of satellites, their gas content, their star formation activity, and their overall survivability in their abundance at the present day, and have identified the responsible processes. I utilised the full range of the IllustrisTNG suite of

cosmological magneto- hydrodynamical simulations from TNG300 – the largest volume with a lower level of resolution – to TNG50 – the smallest cosmological volume with the highest resolution on a zoom-in-like level (see Chapter 2.3 and Table 2.1) – across various resolution runs (see Chapter 3.2.1, as well as Appendix A and C) and baryonic vs. N-body, dark matter-only implementations (see Chapter 4.2.6 and Appendix F). As the whole IllustrisTNG suite employs the same, consistent physical models across all volumes and resolutions, it has enabled me to study properties of satellite galaxies on a population basis in an unprecedented combination of statistical sample size and available mass range with reliably resolved satellites down to stellar masses of 5×10^6 $M_\odot$ in TNG50. This has resulted in host halo samples in the range of tens to several ten thousand in various host mass ranges between $10^{12} - 10^{15.2}$ $M_\odot$ and satellite populations in groups and clusters from thousands to tens of thousand across the mass spectrum when combining TNG300, TNG100, and TNG50 at $z = 0$ (see Tables 3.1 and 3.2). Moreover, TNG50 contains the first statistical sample of 198 high-resolution MW/M31-like galaxies hosting more than 1200 satellite galaxies with stellar masses of $M_* \geq 5 \times 10^6$ $M_\odot$ within 300 kpc (see Chapters 4.1.1 and 4.1.2).

IllustrisTNG vs. previous simulations

In previous large-scale simulations such as the original Illustris, EAGLE, or Horizon-AGN, which all employ a cubic volume with a side-length about 100 Mpc, the host mass range would be more limited for massive galaxy clusters with total masses on the order of 10^{15} $M_\odot$. Illustris (and TNG100), for example, only include 14 Virgo-like galaxy clusters with more than 10^{14} $M_\odot$. Thus, larger volumes such as the one of TNG300 are required to increase the statistics for massive hosts like the Coma and Perseus clusters and to study the effects of such environments on their satellite populations. While these intermediate volumes yield significantly larger, statistical samples of several thousand MW/M31-like hosts (see e.g. figure 1 of Nelson et al. 2015 for Illustris) compared to 198 in TNG50, their baryonic particle masses of $10^6 - 10^7$ $M_\odot$ severely reduce the satellite mass range that can be resolved reliably. Thus, the analysis of their abundance and star formation activities would be practically limited to Magellanic Cloud-like satellites.

These issues could be circumvented by employing zoom-in simulation suites of LG- and MW/M31-like hosts such as APOSTLE (Fattahi et al. 2016a) and Auriga (Grand et al. 2017). With mass resolutions on the order of 10^4 $M_\odot$, these simulations have been able to resolve satellite galaxies to lower masses than TNG50. However, host sample size is essential in order to put the observed satellite systems of the MW and M31 into a cosmological context. Although the sample sizes of such zoom-in simulations have increased in recent years from 12 LG-like systems in APOSTLE to 30 isolated MW-like hosts in Auriga and even 45 MW- and M31-like hosts in the ARTEMIS simulations (Font et al. 2021a), none of them reach the statistical host sample size of TNG50 with 198 MW/M31-like hosts (see Chapter 4.2.4 and Table 4.1

for a comparison). Furthermore, the TNG50 hosts not only employ a similar level of resolution but were simulated in a full cosmological context within a volume of $(50\ \mathrm{Mpc})^3$.

Limitations

However, it should be noted that the mass range of satellites around MW/M31-like hosts that I investigate throughout Chapters 4 and 5 (i.e. $M_* \geq 5 \times 10^6\ \mathrm{M}_\odot$) only reaches down to the Leo I dwarf galaxy of the MW. Thus, I was merely able to probe the more massive half of the MW's regime of bright, classical satellites. While the number of known classical satellites within the virial radius of the MW has stayed almost constant over the last two decades, most newly detected satellites were found in the ultra-faint regime with stellar masses of $\lesssim 10^5\ \mathrm{M}_\odot$ (see Chapter 1.3). As this is only slightly above the mass of a single stellar particle in TNG50, even higher levels of numerical resolution are required to characterise the full regime of bright, classical satellites and to probe into the ultra-faint regime within a cosmological context. From a zoom-in perspective, the DC Justice League project has recently managed to resolve ultra-faint satellite galaxies around four simulated MW-mass hosts with a particularly high resolution of $\sim 10^3\ \mathrm{M}_\odot$ (Applebaum et al. 2021).

6.4.2 On environmental effects

Nevertheless, this thesis has shown that less massive environments like the Local Group or individual MW/M31-like hosts exert distinct influences on their satellite galaxy populations: from the degree of tidal stripping that their dark matter haloes experience (Figures 3.3 and 3.8) and their overall survivability compared to past populations (Figure 4.11) to the loss of their gas reservoirs due to ram pressure stripping (Figures 5.5 and 5.6) and the subsequent quenching of star formation processes (Figure 5.2). The mass components of satellite galaxies in TNG50 exhibit a continuously intertwined co-evolution after infall that not only depends on their own mass to make them more resistant to environmental effects but also on their time of infall, i.e. the period over which they have been subject to the gravitational potential of their host (Figure 5.8). They even exhibit a distinct distribution of infall times compared to satellite populations in more massive group and cluster hosts (Figure 3.9).

While the observed satellite populations of the MW and M31 contain little to no detected gas – consistent with my findings in TNG50 – there are no active signs of gas loss at the present day similar to jellyfish galaxies in cluster hosts, which form gaseous tails as they become subject to ram pressure stripping (e.g. Yun et al. 2019 and see Chapter 1.2). The mere lack of present-day jellyfish around the MW and M31, however, does not constitute a statement about their circumgalactic media or their gaseous haloes. As seen in Figure 5.7, satellites around MW/M31-like hosts are swiftly deprived of their gas after infall according to TNG50. Therefore, observing the gas content and spatial distribution of these satellites at the right point in time is

imperative when searching for jellyfish signatures. As the TNG simulations allow to follow satellite populations throughout cosmic time, this will be further addressed in the future. Extending the search for jellyfish galaxies down to less massive hosts is of interest for observational surveys as well: the LOFAR Two-metre Sky Survey (LoTSS, Shimwell et al. 2017; Shimwell et al. 2019) has announced to expand its study of jellyfish to galaxy groups in the future in order to utilise their larger abundance (Roberts et al. 2021).

Since the star formation activity of these satellites subsequently decreases and comes to a halt, their build-up in stellar mass is distinct from similar-mass field galaxies. While Joshi et al. (2021) have analysed the star formation histories of TNG50 satellite galaxies over a range of group and cluster environments and uncovered a large diversity, the star formation histories of satellites within MW/M31-like systems specifically remains to be explored. Based on my contributions to the study of Jackson et al. (2020), in which we examined the stellar mass build-up of observed SDSS and simulated TNG300 central galaxies, I aim to construct the star formation histories of satellite galaxies around TNG50 MW/M31-like hosts and will analyse them in a publication on the results of Chapter 5.

6.4.3 On the importance of matched comparisons

Chapters 4 and 5 have highlighted the importance of carefully matched comparisons – both between simulations with different physical models, as well as between observations and simulations. This includes the definition of reasonable selection criteria for my fiducial sample of TNG50 MW/M31-like hosts (see Chapter 4.1.1 and Pillepich et al. in prep.), finding appropriate analogues to the SAGA survey (Figure 4.7) and Local Volume hosts (Figure 4.8), as well as matching the host halo mass ranges of previous simulations correctly (Figure 4.10; see Table 4.1 for a summary). Observational selections of satellite galaxies need to be taken into account as well: while three-dimensional distances and apertures may be available in simulations and observations of nearby satellite galaxies (e.g. McConnachie 2012; McConnachie et al. 2018), observations of objects at larger distances are limited to projections and need to rely on additional line-of-sight distance criteria (see Chapter 4.1.2). Furthermore, they may be subject to luminosity and surface brightness limitations (Geha et al. 2017; Carlsten et al. 2021; Mao et al. 2021). Thus, samples can be contaminated by foreground and background galaxies. Although comparisons between simulations at face value can already yield some insights, it is essential to take these aspects into account in order to perform a proper quantitative comparison.

As shown by my study of the quenched fractions of satellites around TNG50 MW/M31-like hosts in Chapter 5.2.2, this is not only limited to the satellite selections themselves but also includes the employed quenched definition. The fiducial TNG characterisation of star formation activity is based on the satellites' distance to the star forming main sequence (Pillepich et al. 2019). Galaxy star formation rates, however, are not directly observable. Therefore, observational definitions of

star formation activity are based on satellite gas fractions (Wetzel et al. 2015) or the Hα equivalent widths (Mao et al. 2021) instead. While I did perform comparisons employing gas fraction-based quenched definitions (Figure 5.2 vs. 5.3; see also Appendix G and Figure G.1), this thesis does not include a matched comparison with the SAGA survey based on Hα equivalent widths. Thus, the discrepancy between the quenched fractions of satellites around TNG50 MW/M31-like hosts and SAGA MW-like hosts (as well as observed MW and M31 satellites vs. SAGA satellites) remains to be explored. In principle, this may be achieved by performing mock spectroscopy on TNG50 satellites using radiative transfer codes such as SKIRT (Baes et al. 2011; Camps and Baes 2015). In the past, Schulz et al. (2020) and Popping et al. (2021) have successfully applied SKIRT to TNG50 galaxies in order to investigate the relation of the UV-slope and the ratio between infrared- and UV-luminosities for galaxies on the SFMS, as well as to study their dust-continuum size at $z = 1 - 5$.

It should be noted, however, that Font et al. (2021b) were recently able to attribute the low quenched fractions of the SAGA satellites to the survey's surface brightness limit based on results of the ARTEMIS simulations. Due to this limitation, the SAGA satellites are biased towards more actively star-forming populations. I aim to confirm this with TNG50 in the future.

6.4.4 On the ΛCDM model

It should once more be noted that the IllustrisTNG simulations – and thus the results presented in this thesis – are based on the ΛCDM model of cosmological structure formation (see Chapter 1.1). I have reproduced the stellar-to-halo mass relation (SHMR) as the most fundamental scaling relation of galaxy evolution in this context (see Chapter 3, as well as Pillepich et al. 2018a for other reference SHMRs) and have found that it is not a single, universal relation for all galaxy populations. Depending on their status as centrals or satellites, as well as the masses of the satellites' host haloes, there is a systematic shift to smaller dynamical masses due to the influence of their host environment and the strength of its gravitational potential. While it would otherwise seem as if satellite galaxies merely contribute to the scatter of the SHMR of centrals in a situation where centrals and satellites cannot be distinguished, they actually form their own, distinct SHMR.

Furthermore, I have managed to address and overcome one of the most significant remaining challenges to ΛCDM, the missing satellites problem (Klypin et al. 1999; Moore et al. 1999a), as part of Chapter 4. Dark matter-only simulations have repeatedly resulted in much larger abundances of low-mass subhaloes than there are luminous dwarf galaxies around the MW and M31, even after their observations extended into the ultra-faint regime in recent years. This apparent overabundance of small-scale structure in cold dark matter-based simulations has been a significant factor for examining warm dark matter models instead. In this case, haloes of dwarf galaxies are the smallest structures to form (see Chapter 1.1 and e.g. Lovell et al. 2016). While previous baryonic zoom-in simulations of MW-like systems with

smaller host samples such as Latte (Wetzel et al. 2016), APOSTLE (Sawala et al. 2016a), or Auriga (Simpson et al. 2018) have shown significant differences between their abundance of subhaloes (which may be either dark or luminous) and actual luminous satellite galaxies, I recover this trend in TNG50 with a statistical sample of 198 MW/M31-like hosts that have been simulated at a zoom-in-like resolution and in a full cosmological context instead of individually. Thus, the missing satellites problem in ΛCDM has finally been overcome: from a satellite abundance perspective, there is no need for warm dark matter. Other cosmological issues, however, such as the internal distribution of dark matter in dwarf galaxies and whether they result in cusp or core density profiles in their central regions still persist (Flores and Primack 1994; Moore 1994, as well as Pontzen and Governato 2014 for a review). This will be further addressed in the future and will further determine the properties of dark matter, as well as the particles it consists of.

6.4.5 In conclusion

Throughout this thesis, I have analysed the abundance and evolution of satellite galaxy populations with IllustrisTNG. While I have focused on the impact of environmental effects on satellite mass components, these processes are actually non-linearly coupled with secular feedback and other internal processes, such as AGN feedback or galactic winds caused by supernova feedback. Nevertheless, within the potentials of MW/M31-like hosts to cluster haloes and with a sufficiently large host-to-satellite mass ratio, environmental effects dominate the evolution of their satellites. Across host mass ranges, they cause the mass components of satellite galaxies to rearrange.

The IllustrisTNG simulation suite is the most well-suited tool to study the aspects of galaxy evolution I addressed in the previous chapters: the evolution of satellites and host galaxies, as well as their respective dark matter haloes are simulated within a large-scale environment in a full cosmological context, following their mass components individually throughout cosmic time. Furthermore, the range of simulations and resolution levels available allows to study satellite galaxies not only on a population basis, but also down to stellar masses otherwise only accessible through dedicated zoom-in simulations. TNG50 provides realistic environmental effects and stripping processes even for satellites as small as the Leo I dwarf galaxy. While I have focused on satellites around MW/M31-like hosts in TNG50 here, the resolution convergence of stripping processes in IllustrisTNG will be analysed in Lovell et al. (in prep.), to which I have contributed satellite and subhalo mass functions characterised by their dynamical and stellar mass, across host masses, simulation volumes, and resolution levels.

In conclusion, I have examined the SHMR as the most fundamental scaling relation in a ΛCDM framework across galaxy and host populations and explored the

resulting discrepancies. I have analysed the diversity in satellite and subhalo populations around analogue hosts to the MW and M31 galaxies, highlighted the importance of carefully matching comparisons with both observational surveys and previous simulations, and have overcome one of the central challenges for the ΛCDM model of cosmological structure formation. Finally, I have investigated the star formation activity, the gas content, as well as the intertwined co-evolution of satellite mass components after infall for various subpopulations around MW/M31-like systems. Thus, this thesis has portrayed a realistic evolution for galaxies after they become satellites of a new host environment according to the IllustrisTNG simulations, ranging from their galaxy-halo connection to the relationship between their gas content and star formation activity; from past to present-day satellite populations; and from massive galaxy clusters to the Local Group.

Appendix A

Rescaling stellar mass

In order to combine the statistics available in TNG300 with the improved resolution of TNG100 and TNG50, I rescale stellar masses as a function of dynamical mass by utilising the differences between simulation volumes and resolution levels. For similar approaches and motivations I refer the reader to Pillepich et al. (2018a), as well as Vogelsberger et al. (2018) and Vogelsberger et al. (2020b).

While TNG100 (aka TNG100-1) was run at a baryonic mass resolution of 1.4×10^6 $M_\odot$, both TNG100-2 (the lower resolution version of TNG100) and TNG300 employ a mass resolution lower by a factor of 8 at 1.1×10^7 $M_\odot$. TNG50 reaches a mass resolution of 8.5×10^4 $M_\odot$ – higher than TNG100-1 by a factor of 16 (see also Table 2.1 for more details on differences between simulation runs).

Figure A.1 illustrates the resolution effects on the SHMR as stellar mass fractions as a function of dynamical mass for centrals (upper left panel), as well as satellites in hosts of $10^{12} - 10^{13}$ $M_\odot$ (top right), $10^{13} - 10^{14}$ $M_\odot$ (bottom left), and $10^{14} - 10^{15.2}$ $M_\odot$ (bottom right). Solid curves correspond to the original SHMRs of different simulation runs: TNG300 (orange curve), TNG100-1 and TNG100-2 (thick and thin blue curves), as well as TNG50 (green curve). It is reassuring that, despite the different volume realisations and sizes, the outputs of TNG100-2 and TNG300 are perfectly consistent.

Now, dotted curves depict the *rescaled* SHMRs for rTNG300 (orange) and rTNG100 (blue), namely the resolution-corrected values with the same effective numerical mass resolution as in TNG50. In the following, I give more details on the procedure I adopt to obtain them.

Overall, I follow the approach in Pillepich et al. (2018a). However, differently from there, since centrals and satellites in different hosts form distinct SHMRs, I rescale them separately according to their environment. However, due to the statistics available, I only rescale stellar masses to TNG50 at low to intermediate dynamical masses. At higher dynamical mass, I switch to TNG100 as a reference, by in practice following a two-step procedure. Firstly, for rTNG300, I utilise the offset between TNG100-1 and TNG100-2 to rescale the stellar masses in TNG300 to the resolution of TNG100:

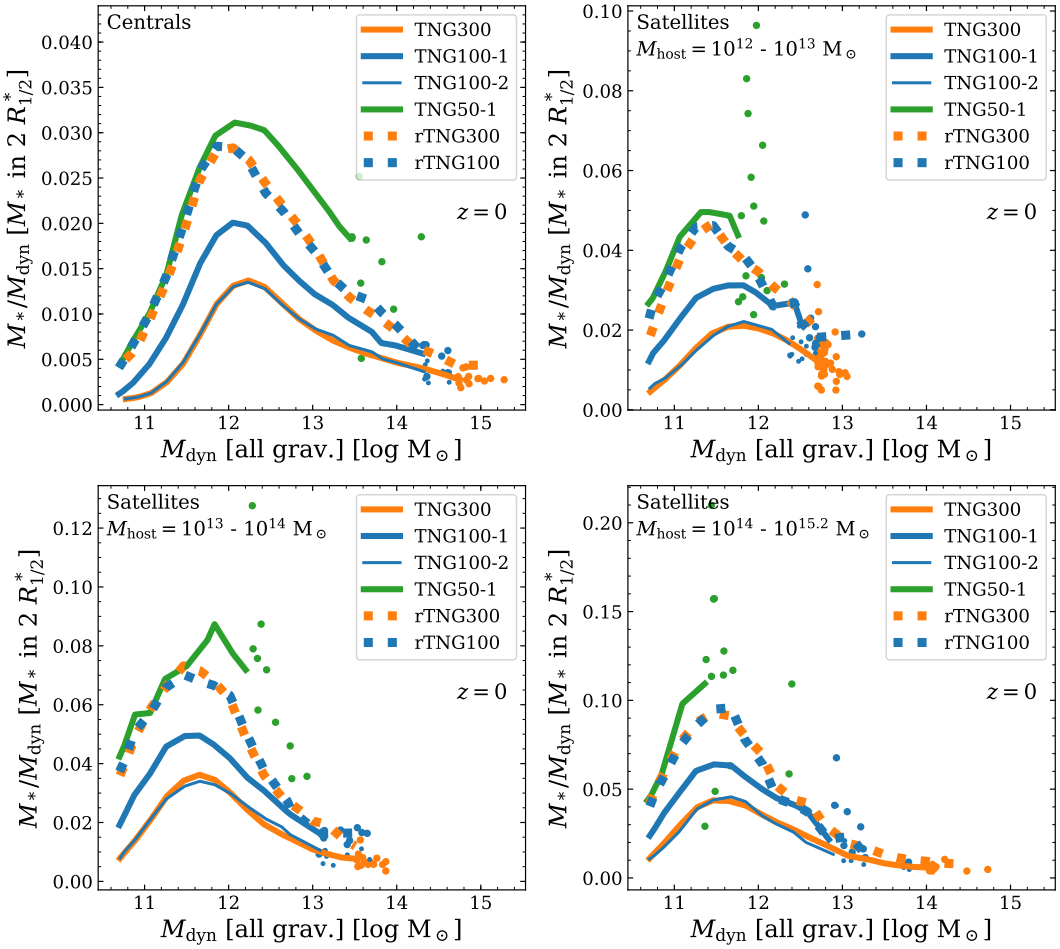

Figure A.1: Stellar-to-halo mass relations at z = 0 within fiducial apertures, illustrating the deviations between simulation volumes and resolution levels (TNG300 in orange, TNG100 and TNG100-2 in blue, TNG50 in green). I rescale stellar masses in TNG300 and TNG100 with respect to their host halo – i.e. separately for centrals (top left) and satellites in hosts of $10^{12} - 10^{13}$ M$_\odot$ (top right), $10^{13} - 10^{14}$ M$_\odot$ hosts (bottom left), and $10^{14} - 10^{15.2}$ M$_\odot$ (bottom right). Dotted orange and blue curves depict rescaled stellar masses for rTNG300 and rTNG100, i.e. resolution-correct values (see text for details).

$$M_*(M_{\rm dyn};\ {\rm (r)TNG300}) = M_*(M_{\rm dyn};\ {\rm TNG300}) \times \frac{M_*(M_{\rm dyn};\ {\rm TNG100\text{-}1})}{M_*(M_{\rm dyn};\ {\rm TNG100\text{-}2})}. \quad \text{(A.1)}$$

Here, $M_*(M_{\rm dyn};\ {\rm TNG100\text{-}1})$ and $M_*(M_{\rm dyn};\ {\rm TNG100\text{-}2})$ correspond to the average stellar mass at the respective dynamical mass and resolution level. I apply this scaling in bins of total dynamical mass to an upper limit. For centrals, this corresponds to $M_{\rm dyn} = 10^{14}$ M$_\odot$; for more massive centrals, the fraction in Equation (A.1) is averaged for all centrals with $M_{\rm dyn} = 10^{13} - 10^{14}$ M$_\odot$. I proceed similarly with satellites: satellites in $10^{12} - 10^{13}$ M$_\odot$ hosts are rescaled according to Equation (A.1) up to $M_{\rm dyn} = 10^{12}$ M$_\odot$, for more massive satellites the rescaling factor is averaged over all satellites with $M_{\rm dyn} \geq 10^{12.5}$ M$_\odot$. For satellites in $10^{13} - 10^{14}$ M$_\odot$ and $10^{14} - 10^{15.2}$ M$_\odot$ hosts, I apply an upper limit of $10^{13.5}$ M$_\odot$ and 10^{13} M$_\odot$. In order to rescale the massive end, I use the average rescaling factor for satellites with $M_{\rm dyn} \geq 10^{12.5}$ M$_\odot$ in both host mass bins.

Finally, I rescale stellar masses for galaxies at lower and intermediate dynamical masses of both TNG300 and TNG100-1 to TNG50, according to the offset between TNG50 and TNG100-1:

$$M_*(M_{\rm dyn};\ {\rm rTNG300}) = M_*(M_{\rm dyn};\ {\rm (r)TNG300}) \times \frac{M_*(M_{\rm dyn};\ {\rm TNG50})}{M_*(M_{\rm dyn};\ {\rm TNG100\text{-}1})}, \quad \text{(A.2)}$$

$$M_*(M_{\rm dyn};\ {\rm rTNG100}) = M_*(M_{\rm dyn};\ {\rm TNG100}) \times \frac{M_*(M_{\rm dyn};\ {\rm TNG50})}{M_*(M_{\rm dyn};\ {\rm TNG100\text{-}1})}. \quad \text{(A.3)}$$

As in Equation (A.1) both $M_*(M_{\rm dyn};\ {\rm TNG50})$ and $M_*(M_{\rm dyn};\ {\rm TNG100\text{-}1})$ represent the average stellar mass at the dynamical mass considered. I follow Equations (A.2) and (A.3) up to dynamical masses of $10^{12.2}$ M$_\odot$ for centrals, $10^{11.9}$ M$_\odot$ for satellites in hosts of $10^{12} - 10^{13}$ M$_\odot$, and $10^{11.6}$ M$_\odot$ for satellites in hosts of both $10^{13} - 10^{14}$ M$_\odot$ and $10^{14} - 10^{15.2}$ M$_\odot$. At larger dynamical mass, statistics in TNG50 become insufficient to continue the rescaling process in the same way. In order to avoid a sharp drop in stellar mass to the level of TNG100-1, I still include TNG50 galaxies at higher dynamical masses. However, since galaxies in this mass range are subject to sample variance, I only use the median stellar mass of all galaxies within a larger dynamical mass bin of 0.7 dex to a power of 0.5.

Appendix B

Fitting the satellite stellar-to-halo mass relation as a function of host mass

In Section 3.3.4 and Table 3.4, I provide fitting formulae for the SHMR of centrals and satellites considering various bins of host mass. The dependence of the four fitting parameters – normalisation N, characteristic mass M_1, and the slopes at the low- and high-mass ends β and γ – on host mass is illustrated in Figure B.1. Masses used in the SHMR are measured in my fiducial aperture choice: all gravitationally bound particles for $M_{\rm dyn}$, and stellar mass with twice the stellar half-mass radius for M_*.

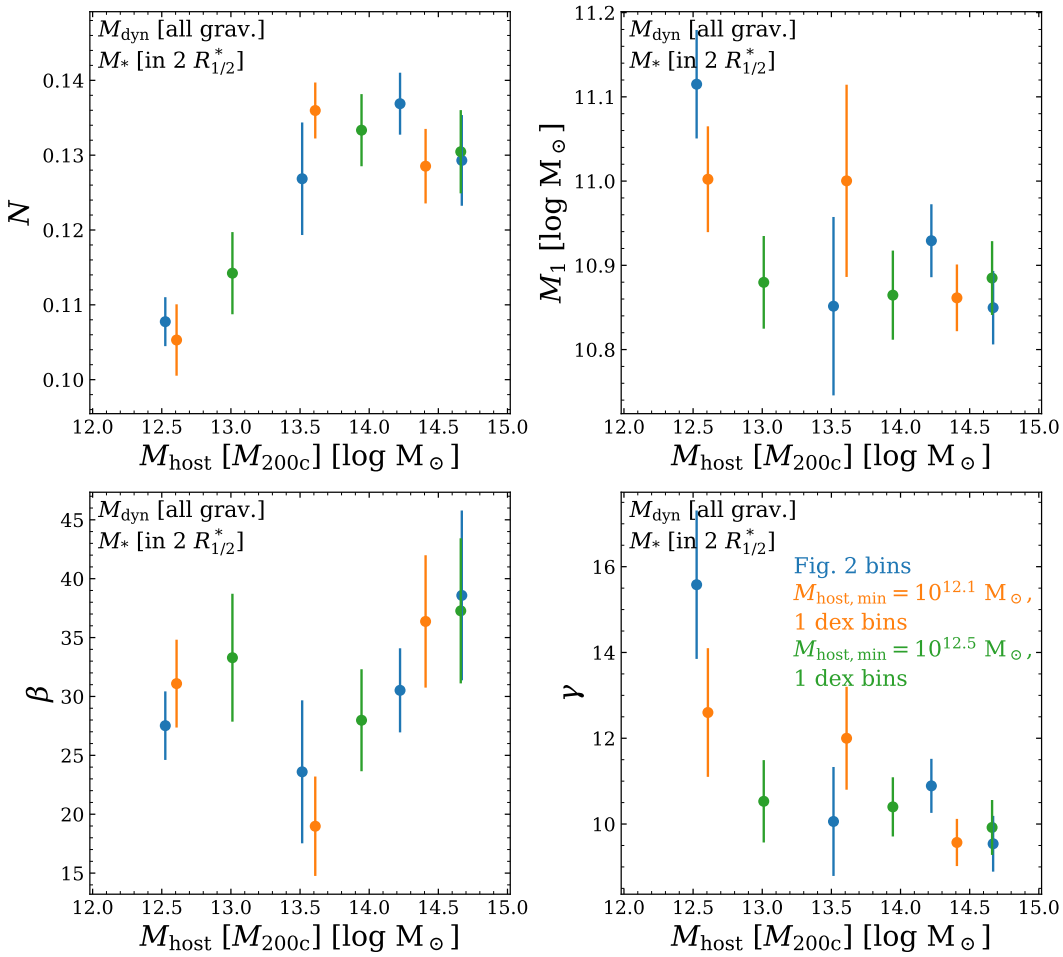

Figure B.1: Fit parameters for the satellite SHMR as a function of median host mass. I use Equation (3.1) to fit the SHMR. This includes the normalisation N (upper left panel), characteristic mass M_1 (upper right panel), and the slopes at the low- and high-mass ends β and γ (lower left and right panel, respectively). In order to illustrate their dependence on host mass, I show the fit parameters for satellites in different bins of host mass. Errorbars correspond to the respective fitting errors.

Appendix C

Subhalo & satellite abundance: resolution effects

Throughout Chapter 4, I focus on the highest resolution run of the TNG50 simulation series, TNG50-1 aka simply TNG50, and its DM-only analogue TNG50-1-Dark (aka TNG50-Dark). However, as is evident in the top panel of Figure 4.9 when comparing satellite abundances in TNG50 and TNG100, a lower numerical resolution decreases the number of surviving satellite galaxies at $z = 0$ significantly – either through a lower build-up of stellar mass or more effective artificial disruption.

I examine the impact of different resolution levels on present-day satellite and subhalo populations in this section. I start in Figure C.1 by presenting the subhalo abundance around MW- and M31-like hosts for TNG50-Dark (left panels) and TNG50 (right panels), both in terms of the subhaloes' maximum circular velocity $V_{\rm max}$ (top panels) and their dynamical mass $M_{\rm dyn}$ (bottom panels). These are global subhalo properties, independent of their stellar mass content. Furthermore, I count all subhaloes, both luminous and dark. In all cases, I show subhalo abundances of different resolution runs: TNG50-1-, -2-, -3- and -4-Dark, as well as TNG50-1, -2, -3, and -4 (blue, orange, green, and red curves, respectively), with progressively poorer spatial and mass resolutions (see Pillepich et al. 2019; Nelson et al. 2019a for details). In order to compare TNG50 and its DM-only analogue across resolution levels, I simplify my selection of MW/M31-like hosts: I exclusively consider centrals and base my selection on a range in total host halo mass of $M_{\rm 200c} = 10^{11.9} - 10^{12.5}$ M$_\odot$. This corresponds to the $10^{\rm th}$ and $90^{\rm th}$ percentiles of the halo mass range covered by my fiducial sample (see Figure 4.1 and Section 4.1.1).

Overall, the subhalo abundance is very similar across different resolution runs at larger velocities and dynamical masses, reaching up to $V_{\rm max} \sim 60 - 70$ km s^{-1} and $M_{\rm dyn} \sim 10^{10.2}$ M$_\odot$ in both TNG50-Dark and TNG50. At the low-velocity end, however, the subhalo distribution becomes flat: the numerical resolution is not sufficient to resolve these subhaloes anymore and they are artificially disrupted. This occurs at maximum circular velocities of $5 - 7$ km s^{-1} ($10 - 12$ km s^{-1}, $20 - 22$ km s^{-1}) in both the DM-only and the baryonic version of TNG50-1 (-2, -3).

Although the subhalo distributions flatten not as clearly when viewed in terms of dynamical mass for TNG50-Dark, I can clearly see down to what subhalo masses the

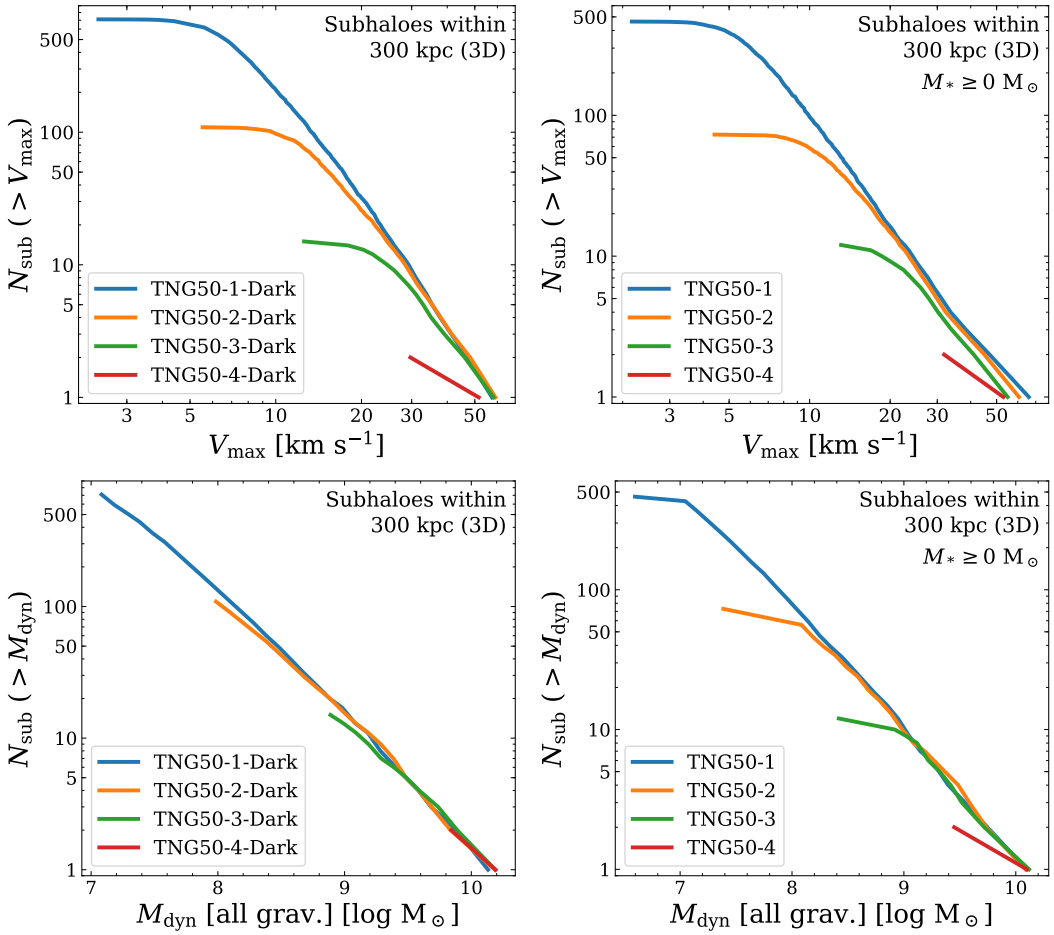

Figure C.1: Impact of numerical resolution on the abundance of dark and luminous subhaloes within 300 kpc of MW/M31-like hosts. I illustrate trends from DM-only analogues (left panels) and baryonic runs (right panels) at different resolution levels: TNG50-1 and TNG50-1-Dark (blue curves), TNG50-2 and TNG50-2-Dark (orange curves), TNG50-3 and TNG50-3-Dark (green curves), as well as TNG50-4 and TNG50-4-Dark (red curves). *Top panels:* subhalo abundance in terms of their maximum circular velocity $V_{\rm max}$. *Bottom panels:* subhalo abundance in terms of their dynamical mass $M_{\rm dyn}$.

subhalo abundances are well converged in the baryonic runs. By comparing across the different resolution levels, I can confidently say that TNG50 satellite abundance results are well converged, i.e. they rise monotonically without being incomplete due to numerical resolution limits, for $V_{\rm max} \gtrsim 5{\rm km\ s^{-1}}$ and $M_{\rm dyn} \gtrsim 10^7\ {\rm M_\odot}$.

For the abundance of *luminous* satellite galaxies, the resolution trends are qualitatively similar as those seen thus far, as is shown in Figure C.2. The top panels show the distribution of satellites with a luminous component down to $M_* = 5.5 \times 10^4\ {\rm M_\odot}$ ($6 \times 10^5\ {\rm M_\odot}$, $6 \times 10^6\ {\rm M_\odot}$) in TNG50-1 (-2, -3) (blue, orange, and green curves) in terms of maximum circular velocity $V_{\rm max}$ (top left panel) and dynamical mass $M_{\rm dyn}$ (top right panel). Satellite distributions flatten and become incomplete below $V_{\rm max} \sim 18\ {\rm km\ s^{-1}}$ ($25\ {\rm km\ s^{-1}}$) and $M_{\rm dyn} \sim 10^{8.5}\ {\rm M_\odot}$ ($10^{9.3}\ {\rm M_\odot}$) in TNG50-1 (-2). So, when subhaloes and satellites are characterised by properties that relate to their total mass (i.e. $V_{\rm max}$ or $M_{\rm dyn}$), the resolution convergence of the subhalo/satellite abundance in baryonic simulations behaves very similar to that in DM-only models, with resolution effects progressively creeping in from the low-mass end.

The resolution convergence becomes more complex when satellite galaxies are counted based on properties related to their stellar mass. The bottom left panel connects the stellar mass and dynamical mass of satellites in their stellar-to-halo mass relation (SHMR). At fixed dynamical mass, higher levels of resolution imply larger stellar masses – as is evident at the SHMR's massive end (see also Appendix A and Pillepich et al. 2018a). At lower dynamical masses, however, the SHMR begins to flatten (at $10^{8.7}\ {\rm M_\odot}$ for TNG50-1, $10^{9.5}\ {\rm M_\odot}$ for TNG50-2, and $10^{10}\ {\rm M_\odot}$ for TNG50-3). This is not a physical part of the relation but a limitation due to the finite stellar mass particle resolution. While the underlying galaxy formation model would entail a certain average SHMR with a related scatter, only satellites with at least one stellar particle can be accounted for: subhaloes that remain dark due the limitations of stellar mass resolution are not included in the average SHMR curves and would otherwise populate the bottom part of the plot. The relations flatten at these dynamical masses since they are "incomplete". The shape of the SHMR curves indicate the minimum stellar mass to which I can reliably count satellites in each simulation: for TNG50, this limit emerges at $M_* \gtrsim 10^6\ {\rm M_\odot}$. Therefore, I choose $M_* \geq 5 \times 10^6\ {\rm M_\odot}$ as my fiducial minimum satellite stellar mass in TNG50.

Finally, the bottom right panel of Figure C.2 shows the median satellite stellar mass function for my fiducial selection, i.e. satellites with a stellar mass of $M_* \geq 5 \times 10^6\ {\rm M_\odot}$, across TNG50 resolution levels. While the satellite stellar mass functions are converg*ing*, poorer resolution implies artificially suppressed satellite mass functions. However, this mostly seems to relate to the reduced stellar masses in subhaloes of a given dynamical mass instead of the enhanced disruption of subhaloes or satellites at progressively poorer resolution. I confirm this by showing the satellite stellar mass function of an additional sample of repopulated TNG50-2 subhaloes (rTNG50-2, pink curve). Here, each TNG50-2 subhalo that survives through $z = 0$ in the selected MW/M31-like hosts has not been assigned its simulated TNG50-2 stellar

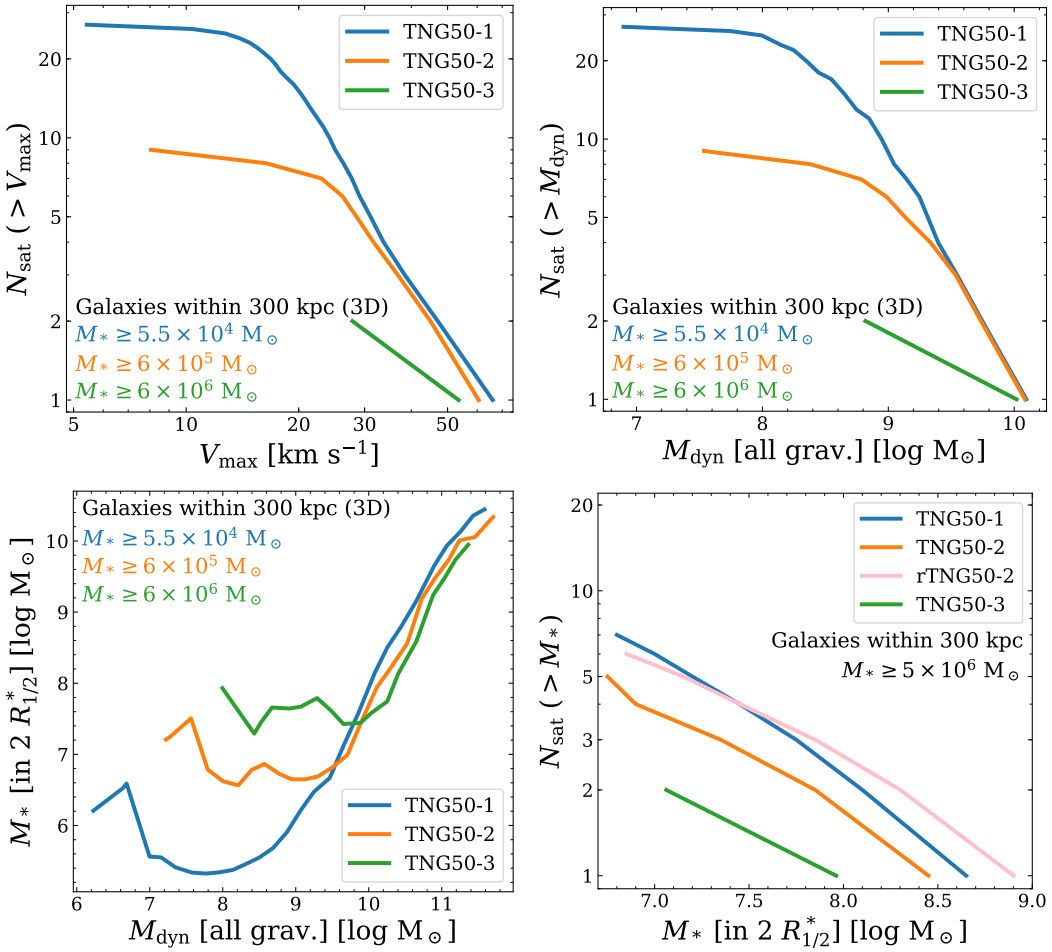

Figure C.2: Resolution effects on luminous satellite galaxies within 300 kpc of MW/M31-like hosts in TNG50. In all panels, I compare TNG50-1 (blue curve), TNG50-2 (orange curve), and TNG50-3 (green curve). *Top panels:* satellite abundance in terms of maximum circular velocity $V_{\rm max}$ (top left) and dynamical mass $M_{\rm dyn}$ (top right), down to the least massive satellite available: $M_* \geq 5.5 \times 10^4$ M$_\odot$ in TNG50-1, $M_* \geq 6 \times 10^5$ M$_\odot$ in TNG50-2, and $M_* \geq 6 \times 10^6$ M$_\odot$ in TNG50-3. *Bottom left panel:* average stellar-to-halo mass relation for all luminous satellites of MW/M31-like galaxies in TNG50-1, -2, and -3. *Bottom right panel:* satellite stellar mass function using stellar mass within twice the stellar half-mass radius for satellite galaxies according to my fiducial satellite selection of $M_* \geq 5 \times 10^6$ M$_\odot$. Additionally, I include a sample of TNG50-2 subhaloes that have been repopulated with galaxy stellar masses according to the most similar subhalo in TNG50-1 (rTNG50-2, pink curve).

mass, but the stellar mass of the TNG50-1 subhalo that is most similar in dynamical mass. This not only increases the stellar mass of luminous TNG50-2 satellites in general; it also populates some of its dark subhaloes – which are otherwise not able to form a galaxy due to the stellar particle mass resolution limitations – with a luminous component. The stellar mass function of rTNG50-2 satellite galaxies essentially coincides with the satellite abundance of TNG50-1. Therefore, the differences between TNG50 resolution levels (or at least between TNG50-1 and TNG50-2) are almost entirely driven by the lower build-up of stellar mass in the lower-resolution runs. Artificial disruption of subhaloes (van den Bosch and Ogiya 2018), on the other hand, has little to no effect on the differences of satellite abundance between resolution levels in the considered regimes.

Appendix D

Normalised satellite abundance

While the total number of satellites grows on average with the mass of their host, a significant degree of scatter remains even at fixed host stellar and total masses (top right panels of Figures 4.13 and 4.14, respectively). I verify my results from Section 4.2.2 regarding the diversity in satellite abundance around MW/M31-like hosts in Figure D.1 by normalising satellite stellar masses by either total host halo mass (top left panel) or host stellar mass (bottom left panel).

As in the left panel of Figure 4.4, the thin, coloured curves in the background correspond to the individual satellite stellar mass functions of all MW/M31-like hosts in TNG50, while crosses denote systems with only a single satellite and hosts with no satellites whatsoever are depicted as curves with $N_{\rm sat} < 1$ (6 out of 198 hosts). For both the normalisation by total host halo mass and by host stellar mass, the diversity persists: the total satellite counts still range between 0 and 20, while their $16^{\rm th}$ and $84^{\rm th}$ percentiles range from 2 to 11 satellites.

Furthermore, I present analogues to the right panel of Figure 4.4 as distributions of total satellite abundance normalised by their median in the right panels of Figure D.1. I consider satellites as all galaxies within 300 kpc of MW/M31-like hosts with a stellar mass of at least 5×10^6 $\mathrm{M}_\odot$ and show their distributions for three selections in normalised stellar mass (by host total mass in the top right panel and by host stellar mass in the bottom right panel). Assuming an average total host halo mass of $M_{\rm 200c} = 10^{12.1}$ $\mathrm{M}_\odot$ and an average host stellar mass of $M_* = 10^{10.8}$ $\mathrm{M}_\odot$, the bins of normalised satellite stellar mass in the right panels of Figure D.1 correspond to the same typical stellar masses as in Figure 4.4: 5×10^8 $\mathrm{M}_\odot$ (yellow histogram), 5×10^7 $M_\odot$ (orange histogram), and 5×10^6 $\mathrm{M}_\odot$ (black histogram). For both the normalisation by host total and host stellar mass, the distributions of different normalised stellar mass bins exhibit similar extents and shapes. Their scatter as $16^{\rm th}$ and $84^{\rm th}$ percentiles all range between normalised total satellite abundances of 0 and 2. Therefore, the degree of diversity in total satellite abundance remains the same regardless of the employed minimum satellite stellar mass.

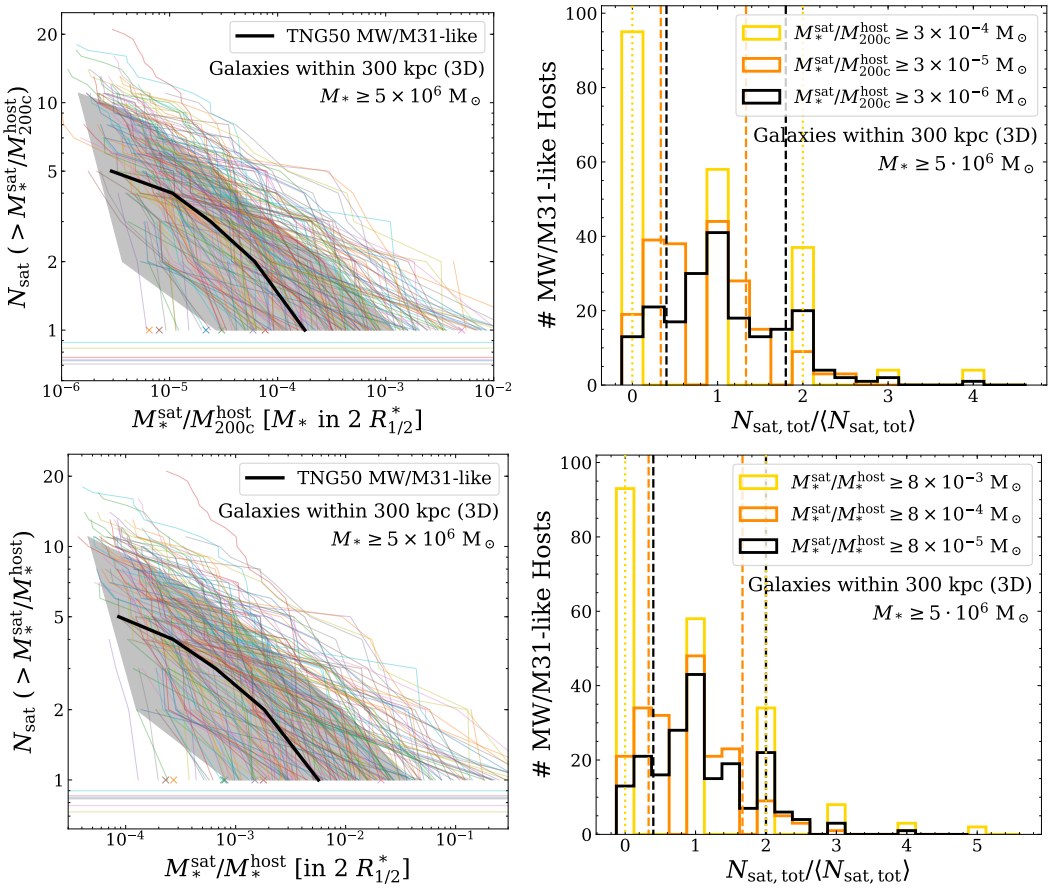

Figure D.1: As in Figure 4.4 but for the *normalised* satellite demographics around MW/M31-like galaxies in the TNG50 simulation at z = 0. In all panels, I define satellites as galaxies within 300 physical kpc (3D) of their host and with stellar masses of at least 5×10^6 M$_\odot$ (within twice the stellar half-mass radius $R_{1/2}^*$). *Left panels:* cumulative satellite abundance in terms of satellite stellar mass $M_*^{\rm sat}$ normalised by either the total virial mass of their MW/M31-like host $M_{\rm 200c}^{\rm host}$ (top left panel) or by host stellar mass $M_*^{\rm host}$ (bottom left panel). The thin, coloured curves in the background illustrate the satellite systems of individual TNG50 hosts with crosses corresponding to systems with only a single satellite and horizontal lines with $N_{\rm sat} < 1$ denoting systems with no satellites meeting the selection (6 out of 198 systems). The thick, black curve and grey shaded area depict their median and scatter as 16$^{\rm th}$ and 84$^{\rm th}$ percentiles, computed in bins of normalised satellite stellar mass. *Right panels:* distribution of normalised total satellite abundance $N_{\rm sat,tot}/\langle N_{\rm sat,tot}\rangle$ with satellite stellar masses normalised by either the total virial mass of their MW/M31-like host $M_{\rm 200c}^{\rm host}$ (top right panel) or by host stellar mass $M_*^{\rm host}$ (bottom right panel), and its dependence on the imposed minimum normalised stellar mass. These bins correspond to the stellar masses in the right panel of Figure 4.4 assuming an average host virial mass of $M_{\rm 200c} = 10^{12.1}$ M$_\odot$ and an average host stellar mass of $M_* = 10^{10.8}$ M$_\odot$.

Appendix E

Dependence of satellite abundance on host halo assembly

I examine the abundance of satellites around MW/M31-like galaxies in TNG50 and the dependence on different stages in host halo assembly in Figure E.1. Here, I cover the hosts' early, intermediate, and late time formation using z_{10}, z_{50}, and z_{90} (from top to bottom), i.e. the redshifts at which the host halo had assembled 10, 50, or 90 per cent of its present-day total mass. The results given below represent an update based on a hydrodynamical galaxy-formation simulation of previous analyses based on DM-only calculations (Gao et al. 2011; Mao et al. 2015).

The trends on satellite populations are illustrated using percentiles in stellar mass functions in terms of the assembly time in question (left panels), as well as the total number of satellites as a function of host assembly (right panels). The specific colours of percentiles vary slightly depending on the distribution of the respective host formation time. While the total number of satellites exhibits the clearest correlation at early assembly z_{10} – hosts with a more quiet early assembly tend to have more satellites at the present-day – this trend becomes less pronounced when considering later assembly times with z_{50} and z_{90}. I find (albeit I do not show) that, for lower mass hosts, earlier formation times are more clearly correlated with total host mass than later formation times. However, there is no correlation of formation time and host mass for massive hosts. While the connection of formation time and host mass influences the trend of total satellite abundance with different halo formation stages, there still seems to be an intrinsic correlation. Furthermore, I find a secondary, less pronounced correlation with the slopes of the satellite stellar mass functions, which I do not show in Figure E.1. Stellar mass function slopes exhibit the reversed development: while there is no discernible trend with early assembly z_{10}, intermediate and late assembly z_{50} and z_{90} exhibit distinct correlations.

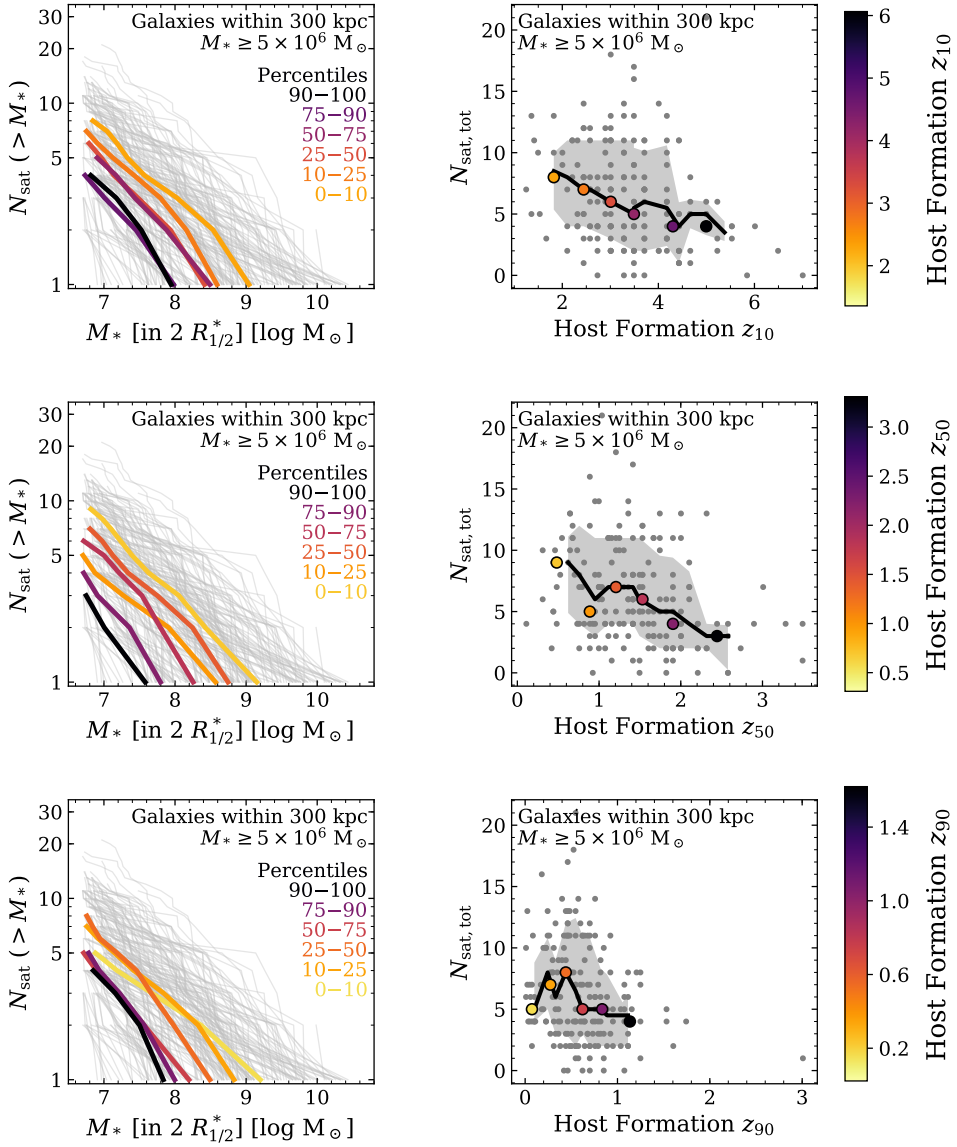

Figure E.1: Dependence of satellite abundance on different definitions of host halo formation time for satellites within 300 kpc (3D) of their MW/M31-like host and with a stellar mass of at least 5×10^6 M$_\odot$. Each row investigates a different stage of halo assembly: z_{10}, z_{50}, and z_{90} (from top to bottom), i.e. the redshifts at which the host halo had assembled 10, 50, or 90 per cent of its present-day total mass. *Left panels:* median satellite stellar mass functions in various percentiles of the assembly time in question (thick, yellow to black curves). The thin, grey curves in the background denote satellite stellar mass functions of individual TNG50 MW/M31-like hosts as a reference. *Right panels:* total number of satellites as a function host properties for the percentiles (yellow to black circles), all TNG50 MW/M31-like galaxies (grey circles), as well as their running median (black curves) and scatter (grey shaded area, 16$^{\rm th}$ and 84$^{\rm th}$ percentiles).

Appendix F

Dependence of subhalo abundance on host halo properties

To connect to earlier results based on DM-only calculations (e.g. Boylan-Kolchin et al. 2010, and references therein), I examine correlations of host halo properties and subhalo populations in Figure F.1, as opposed to satellite galaxy populations in Section 4.2.7 and Figure 4.14. Trends with subhalo abundance are illustrated using percentile stellar mass functions of the halo property in question (left panels, yellow to black curves), as well as the total number of subhaloes as a function of host halo properties (right panels). Each row of panels presents the dependence on another halo property (from top to bottom): total halo mass M_{200c}, halo assembly time z_{50}, i.e. the redshift at which the host halo had assembled 50 per cent of its present-day total mass, halo concentration c_{-2}, and halo shape as its minor-to-major axis ratio s. Overall, I find the same trends for subhalo abundances as for satellite galaxies – albeit more pronounced than in Figure 4.14. More massive host haloes and those that formed 50 per cent of their present-day total mass later in time tend to have a larger number of surviving subhaloes at $z = 0$. There are only slight trends with host halo concentration: while less concentrated MW/M31-like hosts have somewhat more subhaloes, this correlation decreases and flattens towards higher concentrations. Furthermore, there are no significant trends with the host halo's shape. As in Section 4.2.7, I did check for trends with the slope of the subhalo mass function, however, I recover no significant correlations.

Finally, I compare the correlations in the right panels to their analogues from the DM-only run TNG50-Dark (dashed, black curves). Consistent with my findings in Section 4.2.6 and Figure 4.12, I find overall larger subhalo abundances around MW/M31-like hosts in TNG50-Dark than in TNG50. I find the same qualitative trends in terms of total host halo mass and host formation time z_{50} – namely, more massive host haloes and those that formed later in time have a higher total number of subhaloes. In this respect, TNG50-Dark hosts cover a similar range in host properties as their baryonic counterparts. However, I find significant differences with host concentration c_{-2} and shape s. Hosts in TNG50-Dark are generally less concentrated and have smaller minor-to-major axis ratios: this is qualitatively consistent with the effects of baryons due to galaxy formation processes in Illustris (Chua et al. 2017;

Chua et al. 2019). While subhalo abundances exhibit a clear correlation with host concentration – more subhaloes tend to reside in less concentrated host haloes – there is still no significant trend with host shape. As in Illustris (Chua et al. 2017), TNG host concentration correlates more strongly with subhalo abundance in DM-only than in baryonic simulations of MW/M31-like hosts.

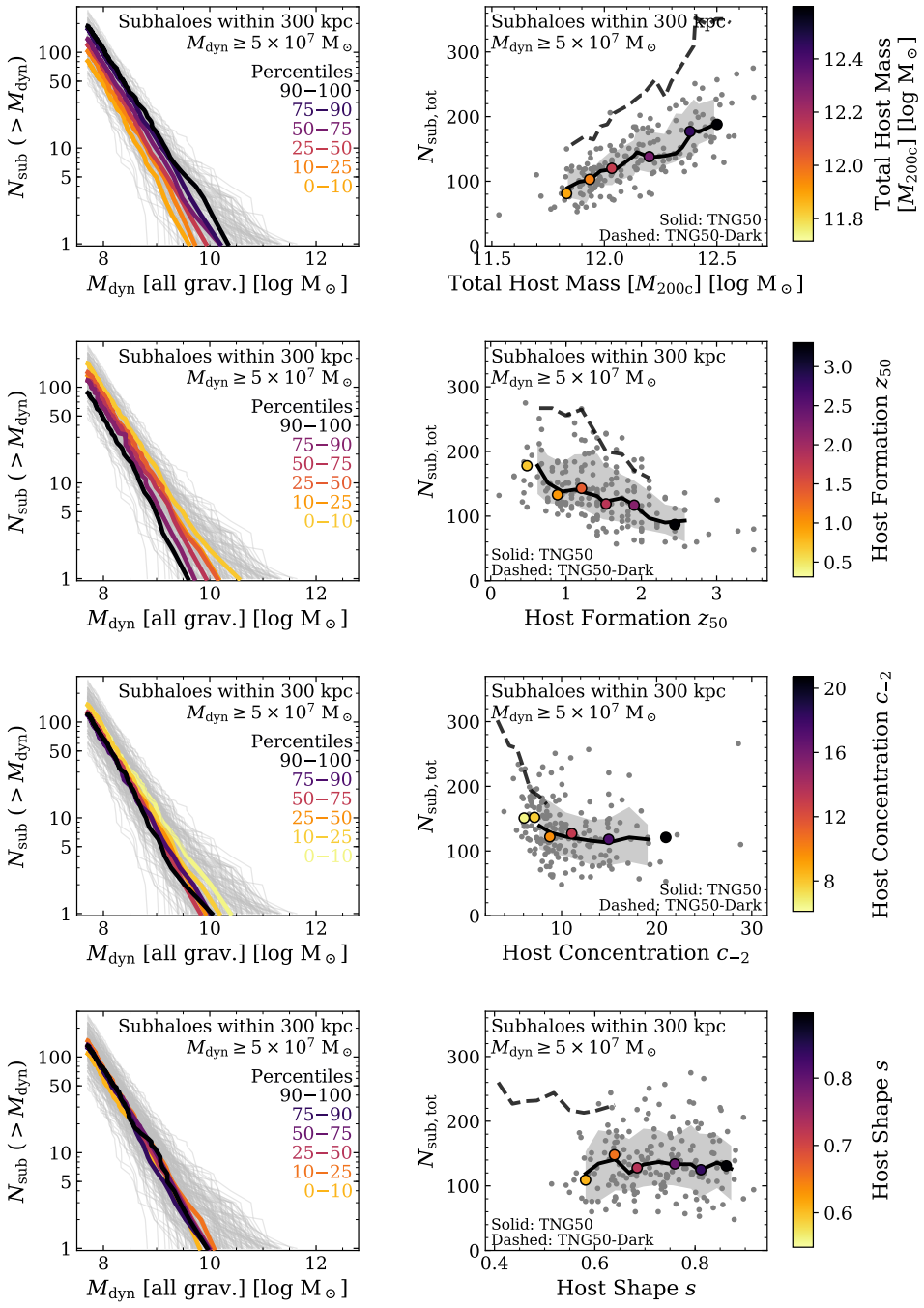

Figure F.1: Dependence of *subhalo abundance* (instead of satellite abundance as in Figure 4.14) on host halo properties for subhaloes within 300 kpc (3D) of their MW/M31-like host and with a dynamical mass of at least 5×10^7 M$_\odot$. Each row investigates a different host property (from top to bottom): total mass $M_{\rm 200c}$, halo assembly time z_{50}, i.e. the redshift at which the MW/M31-like host had assembled 50 per cent of its mass, halo concentration c_{-2}, as well as halo shape s as minor-to-major axis ratio. *Left panels:* median subhalo dynamical mass functions in various percentiles of the host property in question (thick, yellow to black curves). The thin, grey curves in the background denote subhalo dynamical mass functions of individual TNG50 MW/M31-like hosts as a reference. *Right panels:* total number of subhaloes as a function host properties for the percentiles (yellow to black circles), all TNG50 MW/M31-like galaxies (grey circles), as well as their running median (solid, black curves) and scatter (grey shaded area, 16$^{\rm th}$ and 84$^{\rm th}$ percentiles). Dashed, black curves denote the corresponding medians from the DM-only analogue simulation TNG50-Dark. Baryonic processes reduce the strength of the correlations between subhalo number and host properties – particularly with host halo concentration.

Appendix G

Comparison of quenched definitions

Throughout Chapter 5, I study the quenched fractions of satellite galaxies around TNG50 MW/M31-like hosts using both my fiducial quenched definition based on the satellites' distance to the star forming main sequence (SFMS, Pillepich et al. 2019) as well as the criterion of Wetzel et al. (2015) based on the satellites' gas fractions. In the former definition, satellites with $\Delta \log \mathrm{SFR} \leq -1$ to the SFMS are considered to be quenched, satellites with $-1 < \Delta \log \mathrm{SFR} < -0.5$ are defined as green valley galaxies, and satellites with $\Delta \log \mathrm{SFR} > -0.5$ are considered to be star-forming. In the latter definition, satellites with gas fractions of $M_{\mathrm{gas}}/M_{*} < 0.1$ are quenched while gas-richer galaxies are still star-forming.

I examine the differences between these two quenched definitions for my satellite sample in Figure G.1. The top panels employ the fiducial, star formation rate-based (SFR) quenched definition while the bottom panels define quenched states based on their gas fractions. In all panels, quenched satellites are illustrated as red dots. For the SFR-based definition, green valley galaxies are shown separately as green dots. The left panels depict the scaling relations the respective quenched definition is based on – i.e. specific star formation rate sSFR as a function of stellar mass M_{*} for the SFR-based quenched definition and gas fractions M_{gas}/M_{*} as a function of stellar mass for the gas fraction-based quenched definition of Wetzel et al. (2015) – while the right panels show the opposite scaling relation. Thus, I show the specific star formation rate as a function of stellar mass colour-coded by SFR-based quenched definition (top left panel), M_{gas}/M_{*} vs. M_{*} colour-coded by the SFR-based quenched definition (top right panel), M_{gas}/M_{*} vs. M_{*} colour-coded by the gas fraction-based quenched definition (bottom left panel), as well as sSFR vs. M_{*} colour-coded by the gas fraction-based quenched definition (bottom right panel). For TNG50 satellite galaxies with an sSFR of zero, I assign a random sSFR value of $10^{-14} - 10^{-13.5}$ yr^{-1}; those containing no gas whatsoever are assigned a random gas fraction of $10^{-5} - 10^{-4.5}$. Thus, these satellites are still shown in Figure G.1, detached from their main scaling relation.

Overall, the two quenched definitions result in a reasonable level of agreement.

While the fiducial, SFR-based quenched definition from Pillepich et al. (2019) results in 950 quenched satellites and the gas fraction-based definition of Wetzel et al. (2015) results in 956 quenched satellites, 923 of them are quenched according to both definitions. However, some satellites – particularly low-mass dwarf galaxies that are considered to be quenched based on their SFR can still hold significant amounts of gas (see top right panel), and thus be considered star-forming when employing the gas fraction-based quenched definition, despite exhibiting sSFR in the range of $10^{-14} - 10^{-13.5}$ yr^{-1} (see bottom right panel).

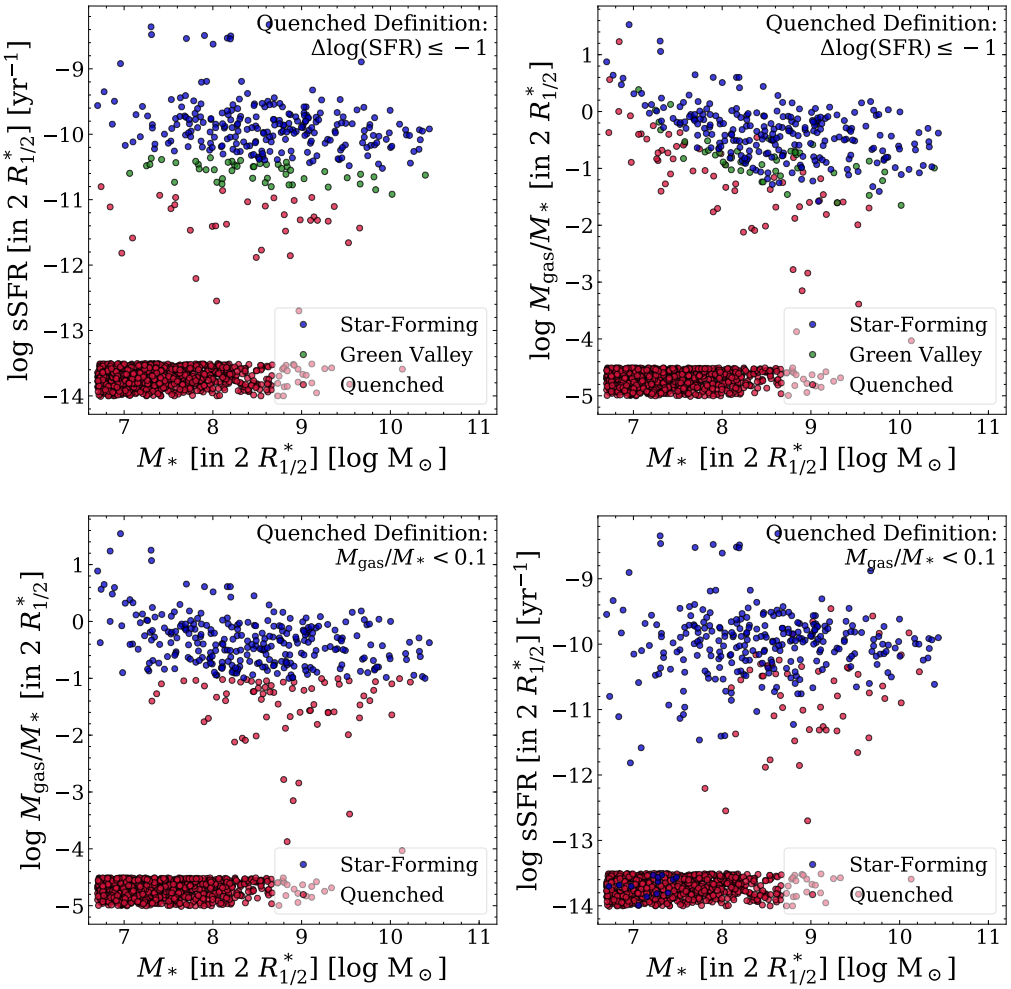

Figure G.1: Comparison of quenched definitions based on the SFMS and gas fractions, for both satellite sSFR and gas fractions as a function of stellar mass. *Top panels:* I employ the fiducial quenched definition based on the distance to the SFMS (Pillepich et al. 2019), i.e. satellites with $\Delta \log(\mathrm{SFR}) \leq -1$ are quenched (red dots), satellites with $-1 < \log(\mathrm{SFR}) < -0.5$ are defined as green valley galaxies (green dots). All other satellites with smaller distances to the SFMS are considered to be star-forming galaxies (blue dots). *Bottom panels:* quenched definition based on satellite gas fractions from Wetzel et al. (2015). Satellites with gas fractions of < 0.1 are quenched (red dots) whereas all those with larger gas fractions are considered to be star-forming (blue dots).

List of the author's publications

The results presented throughout this thesis are – as indicated in Chapter 1.4, as well as in the beginning of Chapter 3 and Chapter 4 – largely based on the following publications:

Christoph Engler et al. (Jan. 2021b). "The distinct stellar-to-halo mass relations of satellite and central galaxies: insights from the IllustrisTNG simulations". In: 500.3, pp. 3957–3975. DOI: 10.1093/mnras/staa3505. arXiv: 2002.11119 [astro-ph.GA]

Christoph Engler et al. (Nov. 2021a). "The abundance of satellites around Milky Way- and M31-like galaxies with the TNG50 simulation: a matter of diversity". In: 507.3, pp. 4211–4240. DOI: 10.1093/mnras/stab2437. arXiv: 2101.12215 [astro-ph.GA]

Furthermore, I was involved in the following publications prior to and during my PhD:

Thomas M. Jackson et al. (Oct. 2020). "The stellar mass assembly of low-redshift, massive, central galaxies in SDSS and the TNG300 simulation". In: 497.4, pp. 4262–4275. DOI: 10.1093/mnras/staa2306. arXiv: 2008.05114 [astro-ph.GA]

Thorsten Lisker et al. (Sept. 2018). "The Active Assembly of the Virgo Cluster: Indications for Recent Group Infall From Early-type Dwarf Galaxies". In: 865.1, 40, p. 40. DOI: 10.3847/1538-4357/aadae1. arXiv: 1808.04751 [astro-ph.GA]

Christoph Engler et al. (Apr. 2018). "On the Scatter of the Present-day Stellar Metallicity-Mass Relation of Cluster Dwarf Galaxies". In: *Research Notes of the American Astronomical Society* 2.2, 6, p. 6. DOI: 10.3847/2515-5172/aabcce. arXiv: 1804.05679 [astro-ph.GA]

Bibliography

Agertz, Oscar, Romain Teyssier, and Ben Moore (Jan. 2011). "The formation of disc galaxies in a ΛCDM universe". In: 410.2, pp. 1391–1408. DOI: 10.1111/j.1365-2966.2010.17530.x. arXiv: 1004.0005 [astro-ph.CO].

Agertz, Oscar et al. (June 2013). "Toward a Complete Accounting of Energy and Momentum from Stellar Feedback in Galaxy Formation Simulations". In: 770.1, 25, p. 25. DOI: 10.1088/0004-637X/770/1/25. arXiv: 1210.4957 [astro-ph.CO].

Allgood, Brandon et al. (Apr. 2006). "The shape of dark matter haloes: dependence on mass, redshift, radius and formation". In: 367.4, pp. 1781–1796. DOI: 10.1111/j.1365-2966.2006.10094.x. arXiv: astro-ph/0508497 [astro-ph].

Anbajagane, Dhayaa et al. (June 2020). "Stellar property statistics of massive haloes from cosmological hydrodynamics simulations: common kernel shapes". In: 495.1, pp. 686–704. DOI: 10.1093/mnras/staa1147. arXiv: 2001.02283 [astro-ph.GA].

Anglés-Alcázar, Daniel, Feryal Özel, and Romeel Davé (June 2013). "Black Hole-Galaxy Correlations without Self-regulation". In: 770.1, 5, p. 5. DOI: 10.1088/0004-637X/770/1/5. arXiv: 1303.5058 [astro-ph.CO].

Applebaum, Elaad et al. (Jan. 2021). "Ultrafaint Dwarfs in a Milky Way Context: Introducing the Mint Condition DC Justice League Simulations". In: 906.2, 96, p. 96. DOI: 10.3847/1538-4357/abcafa. arXiv: 2008.11207 [astro-ph.GA].

Aragón-Calvo, Miguel A., Rien van de Weygaert, and Bernard J. T. Jones (Nov. 2010). "Multiscale phenomenology of the cosmic web". In: 408.4, pp. 2163–2187. DOI: 10.1111/j.1365-2966.2010.17263.x. arXiv: 1007.0742 [astro-ph.CO].

Arrigoni Battaia, Fabrizio et al. (Jan. 2019). "QSO MUSEUM I: a sample of 61 extended Ly α-emission nebulae surrounding z $\sim$ 3 quasars". In: 482.3, pp. 3162–3205. DOI: 10.1093/mnras/sty2827. arXiv: 1808.10857 [astro-ph.GA].

Artale, M. Celeste et al. (Sept. 2017). "Small-scale galaxy clustering in the eagle simulation". In: 470.2, pp. 1771–1787. DOI: 10.1093/mnras/stx1263. arXiv: 1611.05064 [astro-ph.GA].

Ashman, Keith M., Paolo Salucci, and Massimo Persic (1993). "The mass function of spiral galaxy haloes". In: 260.3, pp. 610–616. DOI: 10.1093/mnras/260.3.610.

Aumer, Michael et al. (Oct. 2013). "Towards a more realistic population of bright spiral galaxies in cosmological simulations". In: 434.4, pp. 3142–3164. DOI: 10.1093/mnras/stt1230. arXiv: 1304.1559 [astro-ph.GA].

Ayromlou, Mohammadreza et al. (2019). "A new method to quantify environment and model ram-pressure stripping in N-body simulations". In: 487.3, pp. 4313–4331. DOI: 10.1093/mnras/stz1549. arXiv: 1903.01988 [astro-ph.GA].

Babcock, Horace W. (Jan. 1939). "The rotation of the Andromeda Nebula". In: *Lick Observatory Bulletin* 498, pp. 41–51. DOI: 10.5479/ADS/bib/1939LicOB.19.41B.

Baes, Maarten et al. (Oct. 2011). "Efficient Three-dimensional NLTE Dust Radiative Transfer with SKIRT". In: 196.2, 22, p. 22. DOI: 10.1088/0067-0049/196/2/22. arXiv: 1108.5056 [astro-ph.CO].

Bahé, Yannick M. et al. (2013). "Why does the environmental influence on group and cluster galaxies extend beyond the virial radius?" In: 430, pp. 3017–3031. DOI: 10.1093/mnras/stt109. arXiv: 1210.8407 [astro-ph.CO].

Bahé, Yannick M. et al. (Oct. 2017). "The Hydrangea simulations: galaxy formation in and around massive clusters". In: 470.4, pp. 4186–4208. DOI: 10.1093/mnras/stx1403. arXiv: 1703.10610 [astro-ph.GA].

Bahé, Yannick M. et al. (2019). "Disruption of satellite galaxies in simulated groups and clusters: the roles of accretion time, baryons, and pre-processing". In: 485.2, pp. 2287–2311. DOI: 10.1093/mnras/stz361. arXiv: 1901.03336 [astro-ph.GA].

Baldry, I. K., K. Glazebrook, and S. P. Driver (Aug. 2008). "On the galaxy stellar mass function, the mass-metallicity relation and the implied baryonic mass function". In: 388.3, pp. 945–959. DOI: 10.1111/j.1365-2966.2008.13348.x. arXiv: 0804.2892 [astro-ph].

Baldry, I. K. et al. (Dec. 2004). "Color bimodality: Implications for galaxy evolution". In: *The New Cosmology: Conference on Strings and Cosmology*. Ed. by Roland E. Allen, Dimitri V. Nanopoulos, and Christopher N. Pope. Vol. 743. American Institute of Physics Conference Series, pp. 106–119. DOI: 10.1063/1.1848322. arXiv: astro-ph/0410603 [astro-ph].

Baldry, I. K. et al. (Mar. 2012). "Galaxy And Mass Assembly (GAMA): the galaxy stellar mass function at z < 0.06". In: 421.1, pp. 621–634. DOI: 10.1111/j.1365-2966.2012.20340.x. arXiv: 1111.5707 [astro-ph.CO].

Balogh, Michael L., Julio F. Navarro, and Simon L. Morris (Sept. 2000). "The Origin of Star Formation Gradients in Rich Galaxy Clusters". In: 540.1, pp. 113–121. DOI: 10.1086/309323. arXiv: astro-ph/0004078 [astro-ph].

Balogh, Michael L. et al. (Dec. 1999). "Differential Galaxy Evolution in Cluster and Field Galaxies at z∼0.3". In: 527.1, pp. 54–79. DOI: 10.1086/308056. arXiv: astro-ph/9906470 [astro-ph].

Balogh, Michael L. et al. (Oct. 2001). "Revisiting the cosmic cooling crisis". In: 326.4, pp. 1228–1234. DOI: 10.1111/j.1365-2966.2001.04667.x. arXiv: astro-ph/0104041 [astro-ph].

Balogh, Michael L. et al. (Nov. 2004). "The Bimodal Galaxy Color Distribution: Dependence on Luminosity and Environment". In: 615.2, pp. L101–L104. DOI: 10.1086/426079. arXiv: astro-ph/0406266 [astro-ph].

Barnes, David J. et al. (Oct. 2017). "The Cluster-EAGLE project: global properties of simulated clusters with resolved galaxies". In: 471.1, pp. 1088–1106. DOI: 10.1093/mnras/stx1647. arXiv: 1703.10907 [astro-ph.GA].

Barnes, Josh and Piet Hut (Dec. 1986). "A hierarchical O(N log N) force-calculation algorithm". In: 324.6096, pp. 446–449. DOI: 10.1038/324446a0.

Barnes, Joshua E. and Lars Hernquist (1992). "Formation of dwarf galaxies in tidal tails". In: 360, pp. 715–717. DOI: 10.1038/360715a0.

Barsanti, S. et al. (Apr. 2018). "Galaxy and Mass Assembly (GAMA): Impact of the Group Environment on Galaxy Star Formation". In: 857.1, 71, p. 71. DOI: 10.3847/1538-4357/aab61a. arXiv: 1803.05076 [astro-ph.GA].

Behroozi, Peter et al. (Sept. 2019). "UNIVERSEMACHINE: The correlation between galaxy growth and dark matter halo assembly from z = 0-10". In: 488.3, pp. 3143–3194. DOI: 10.1093/mnras/stz1182. arXiv: 1806.07893 [astro-ph.GA].

Behroozi, Peter S., Charlie Conroy, and Risa H. Wechsler (July 2010). "A Comprehensive Analysis of Uncertainties Affecting the Stellar Mass-Halo Mass Relation for 0 < z < 4". In: 717.1, pp. 379–403. DOI: 10.1088/0004-637X/717/1/379. arXiv: 1001.0015 [astro-ph.CO].

Behroozi, Peter S., Risa H. Wechsler, and Hao-Yi Wu (2013). "The ROCKSTAR Phase-space Temporal Halo Finder and the Velocity Offsets of Cluster Cores". In: 762.2, 109, p. 109. DOI: 10.1088/0004-637X/762/2/109. arXiv: 1110.4372 [astro-ph.CO].

Behroozi, Peter S. et al. (2014). "Mergers and Mass Accretion for Infalling Halos Both End Well Outside Cluster Virial Radii". In: 787, 156, p. 156. DOI: 10.1088/0004-637X/787/2/156. arXiv: 1310.2239 [astro-ph.CO].

Bekki, Kenji (Feb. 2014). "Galactic star formation enhanced and quenched by ram pressure in groups and clusters". In: 438.1, pp. 444–462. DOI: 10.1093/mnras/stt2216. arXiv: 1311.3010 [astro-ph.CO].

Bekki, Kenji and Warrick J. Couch (Aug. 2011). "Transformation from spirals into S0s with bulge growth in groups of galaxies". In: 415.2, pp. 1783–1796. DOI: 10.1111/j.1365-2966.2011.18821.x. arXiv: 1105.0531 [astro-ph.CO].

Belokurov, V. et al. (Aug. 2006). "A Faint New Milky Way Satellite in Bootes". In: 647.2, pp. L111–L114. DOI: 10.1086/507324. arXiv: astro-ph/0604355 [astro-ph].

Belokurov, V. et al. (July 2018). "Co-formation of the disc and the stellar halo". In: 478.1, pp. 611–619. DOI: 10.1093/mnras/sty982. arXiv: 1802.03414 [astro-ph.GA].

Benitez-Llambay, Alejandro and Carlos Frenk (Sept. 2020). "The detailed structure and the onset of galaxy formation in low-mass gaseous dark matter haloes". In: 498.4, pp. 4887–4900. DOI: 10.1093/mnras/staa2698. arXiv: 2004.06124 [astro-ph.GA].

Bennet, P. et al. (Nov. 2017). "Discovery of Diffuse Dwarf Galaxy Candidates around M101". In: 850.1, 109, p. 109. DOI: 10.3847/1538-4357/aa9180. arXiv: 1710.01728 [astro-ph.GA].

Bennet, P. et al. (Nov. 2019). "The M101 Satellite Luminosity Function and the Halo-Halo Scatter among Local Volume Hosts". In: 885.2, 153, p. 153. DOI: 10.3847/1538-4357/ab46ab. arXiv: 1906.03230 [astro-ph.GA].

Benson, A. J. et al. (Feb. 2000). "The nature of galaxy bias and clustering". In: 311.4, pp. 793–808. DOI: 10.1046/j.1365-8711.2000.03101.x. arXiv: astro-ph/9903343 [astro-ph].

Benson, A. J. et al. (June 2002a). "The effects of photoionization on galaxy formation - I. Model and results at z=0". In: 333.1, pp. 156–176. DOI: 10.1046/j.1365-8711.2002.05387.x. arXiv: astro-ph/0108217 [astro-ph].

Benson, A. J. et al. (June 2002b). "The effects of photoionization on galaxy formation - II. Satellite galaxies in the Local Group". In: 333.1, pp. 177–190. DOI: 10.1046/j.1365-8711.2002.05388.x. arXiv: astro-ph/0108218 [astro-ph].

Berger, M. J. and P. Colella (May 1989). "Local Adaptive Mesh Refinement for Shock Hydrodynamics". In: *Journal of Computational Physics* 82.1, pp. 64–84. DOI: 10.1016/0021-9991(89)90035-1.

Berger, Marsha J. and Joseph Oliger (Mar. 1984). "Adaptive Mesh Refinement for Hyperbolic Partial Differential Equations". In: *Journal of Computational Physics* 53.3, pp. 484–512. DOI: 10.1016/0021-9991(84)90073-1.

Bertone, Serena and Joop Schaye (Jan. 2012). "Rest-frame ultraviolet line emission from the intergalactic medium at $2 \leq z \leq 5$". In: 419.1, pp. 780–798. DOI: 10.1111/j.1365-2966.2011.19742.x. arXiv: 1008.1791 [astro-ph.CO].

Bertschinger, Edmund (Nov. 2001). "Multiscale Gaussian Random Fields and Their Application to Cosmological Simulations". In: 137.1, pp. 1–20. DOI: 10.1086/322526. arXiv: astro-ph/0103301 [astro-ph].

Besla, G. et al. (Oct. 2010). "Simulations of the Magellanic Stream in a First Infall Scenario". In: 721.2, pp. L97–L101. DOI: 10.1088/2041-8205/721/2/L97. arXiv: 1008.2210 [astro-ph.GA].

Besla, Gurtina et al. (Oct. 2007). "Are the Magellanic Clouds on Their First Passage about the Milky Way?" In: 668.2, pp. 949–967. DOI: 10.1086/521385. arXiv: astro-ph/0703196 [astro-ph].

Bett, Philip et al. (Mar. 2007). "The spin and shape of dark matter haloes in the Millennium simulation of a Λ cold dark matter universe". In: 376.1, pp. 215–232. DOI: 10.1111/j.1365-2966.2007.11432.x. arXiv: astro-ph/0608607 [astro-ph].

Beygu, B. et al. (May 2016). "The void galaxy survey: Star formation properties". In: 458.1, pp. 394–409. DOI: 10.1093/mnras/stw280. arXiv: 1601.08228 [astro-ph.GA].

Bialas, D. et al. (Apr. 2015). "On the occurrence of galaxy harassment". In: 576, A103, A103. DOI: 10.1051/0004-6361/201425235. arXiv: 1503.01965 [astro-ph.GA].

Bianconi, M. et al. (Jan. 2018). "LoCuSS: pre-processing in galaxy groups falling into massive galaxy clusters at z = 0.2". In: 473.1, pp. L79–L83. DOI: 10.1093/mnrasl/slx167. arXiv: 1710.04230 [astro-ph.GA].

Bidaran, Bahar et al. (Sept. 2020). "On the accretion of a new group of galaxies on to Virgo: I. Internal kinematics of nine in-falling dEs". In: 497.2, pp. 1904–1924. DOI: 10.1093/mnras/staa2097. arXiv: 2007.05021 [astro-ph.GA].

Bigiel, F. et al. (Apr. 2011). "A Constant Molecular Gas Depletion Time in Nearby Disk Galaxies". In: 730.2, L13, p. L13. DOI: 10.1088/2041-8205/730/2/L13. arXiv: 1102.1720 [astro-ph.CO].

Binggeli, Bruno, G. A. Tammann, and Allan Sandage (1987). "Studies of the Virgo Cluster. VI. Morphological and Kinematical Structure of the Virgo Cluster". In: 94, p. 251. DOI: 10.1086/114467.

Blitz, Leo and Timothy Robishaw (Oct. 2000). "Gas-Rich Dwarf Spheroidals". In: 541.2, pp. 675–687. DOI: 10.1086/309457. arXiv: astro-ph/0001142 [astro-ph].

Blumenthal, G. R., H. Pagels, and J. R. Primack (Sept. 1982). "Galaxy formation by dissipationless particles heavier than neutrinos". In: 299.5878, pp. 37–38. DOI: 10.1038/299037a0.

Boardman, N. et al. (Sept. 2020). "Are the Milky Way and Andromeda unusual? A comparison with Milky Way and Andromeda analogues". In: 498.4, pp. 4943–4954. DOI: 10.1093/mnras/staa2731. arXiv: 2009.02576 [astro-ph.GA].

Bocquet, Sebastian et al. (Mar. 2016). "Halo mass function: baryon impact, fitting formulae, and implications for cluster cosmology". In: 456.3, pp. 2361–2373. DOI: 10.1093/mnras/stv2657. arXiv: 1502.07357 [astro-ph.CO].

Boehm, C. et al. (Nov. 2014). "Using the Milky Way satellites to study interactions between cold dark matter and radiation." In: 445, pp. L31–L35. DOI: 10.1093/mnrasl/slu115. arXiv: 1404.7012 [astro-ph.CO].

Bond, J. R., A. S. Szalay, and M. S. Turner (June 1982). "Formation of Galaxies in a Gravitino-Dominated Universe". In: 48.23, pp. 1636–1640. DOI: 10.1103/PhysRevLett.48.1636.

Bond, J. R. et al. (Jan. 1984). "Dark matter and shocked pancakes". In: *Formation and Evolution of Galaxies and Large Structures in the Universe*. Ed. by J. Audouze and J. Tran Thanh Van. Vol. 117. NATO Advanced Study Institute (ASI) Series C, p. 87.

Bond, J. R. et al. (Oct. 1991). "Excursion Set Mass Functions for Hierarchical Gaussian Fluctuations". In: 379, p. 440. DOI: 10.1086/170520.

Bond, J. Richard, Lev Kofman, and Dmitry Pogosyan (Apr. 1996). "How filaments of galaxies are woven into the cosmic web". In: 380.6575, pp. 603–606. DOI: 10.1038/380603a0. arXiv: astro-ph/9512141 [astro-ph].

Bose, Sownak et al. (Feb. 2017). "Substructure and galaxy formation in the Copernicus Complexio warm dark matter simulations". In: 464.4, pp. 4520–4533. DOI: 10.1093/mnras/stw2686. arXiv: 1604.07409 [astro-ph.CO].

Boselli, A. et al. (Oct. 2014). "The GALEX Ultraviolet Virgo Cluster Survey (GUViCS). IV. The role of the cluster environment on galaxy evolution". In: 570, A69, A69. DOI: 10.1051/0004-6361/201424419. arXiv: 1407.4986 [astro-ph.GA].

Boselli, A. et al. (Nov. 2016). "Quenching of the star formation activity in cluster galaxies". In: 596, A11, A11. DOI: 10.1051/0004-6361/201629221. arXiv: 1609.00545 [astro-ph.GA].

Boselli, Alessandro and Giuseppe Gavazzi (2006). "Environmental Effects on Late-Type Galaxies in Nearby Clusters". In: 118.842, pp. 517–559. DOI: 10.1086/500691. arXiv: astro-ph/0601108 [astro-ph].

Bournaud, F. et al. (Oct. 2004). "Kinematics of tidal tails in interacting galaxies: Tidal dwarf galaxies and projection effects". In: 425, pp. 813–823. DOI: 10.1051/0004-6361:20040394. arXiv: astro-ph/0406169 [astro-ph].

Bower, Richard G. (Jan. 1991). "The evolution of groups of galaxies in the Press-Schechter formalism". In: 248, pp. 332–352. DOI: 10.1093/mnras/248.2.332.

Boylan-Kolchin, Michael, Gurtina Besla, and Lars Hernquist (June 2011). "Dynamics of the Magellanic Clouds in a Lambda cold dark matter universe". In: 414.2, pp. 1560–1572. DOI: 10.1111/j.1365-2966.2011.18495.x. arXiv: 1010.4797 [astro-ph.GA].

Boylan-Kolchin, Michael et al. (Aug. 2010). "There's no place like home? Statistics of Milky Way-mass dark matter haloes". In: 406.2, pp. 896–912. DOI: 10.1111/j.1365-2966.2010.16774.x. arXiv: 0911.4484 [astro-ph.CO].

Bradford, Jeremy D., Marla C. Geha, and Michael R. Blanton (Aug. 2015). "A Study in Blue: The Baryon Content of Isolated Low-mass Galaxies". In: 809.2, 146, p. 146. DOI: 10.1088/0004-637X/809/2/146. arXiv: 1505.04819 [astro-ph.GA].

Brook, C. B. et al. (Aug. 2011). "Hierarchical formation of bulgeless galaxies: why outflows have low angular momentum". In: 415.2, pp. 1051–1060. DOI: 10.1111/j.1365-2966.2011.18545.x. arXiv: 1010.1004 [astro-ph.CO].

Brown, Thomas M. et al. (Dec. 2014). "The Quenching of the Ultra-faint Dwarf Galaxies in the Reionization Era". In: 796.2, 91, p. 91. DOI: 10.1088/0004-637X/796/2/91. arXiv: 1410.0681 [astro-ph.GA].

Bruzual, G. and S. Charlot (Oct. 2003). "Stellar population synthesis at the resolution of 2003". In: 344.4, pp. 1000–1028. DOI: 10.1046/j.1365-8711.2003.06897.x. arXiv: astro-ph/0309134 [astro-ph].

Bryan, Greg L. et al. (Apr. 2014). "ENZO: An Adaptive Mesh Refinement Code for Astrophysics". In: 211.2, 19, p. 19. DOI: 10.1088/0067-0049/211/2/19. arXiv: 1307.2265 [astro-ph.IM].

Buck, Tobias et al. (Feb. 2019). "NIHAO XV: the environmental impact of the host galaxy on galactic satellite and field dwarf galaxies". In: 483.1, pp. 1314–1341. DOI: 10.1093/mnras/sty2913. arXiv: 1804.04667 [astro-ph.GA].

Buckley, Matthew R. et al. (Aug. 2014). "Scattering, damping, and acoustic oscillations: Simulating the structure of dark matter halos with relativistic force carriers". In: 90.4, 043524, p. 043524. DOI: 10.1103/PhysRevD.90.043524. arXiv: 1405.2075 [astro-ph.CO].

Bullock, James S. and Michael Boylan-Kolchin (Aug. 2017). "Small-Scale Challenges to the ΛCDM Paradigm". In: 55.1, pp. 343–387. DOI: 10.1146/annurev-astro-091916-055313. arXiv: 1707.04256 [astro-ph.CO].

Bullock, James S., Andrey V. Kravtsov, and David H. Weinberg (Aug. 2000). "Reionization and the Abundance of Galactic Satellites". In: 539.2, pp. 517–521. DOI: 10.1086/309279. arXiv: astro-ph/0002214 [astro-ph].

Busha, Michael T. et al. (Dec. 2011a). "Statistics of Satellite Galaxies around Milky-Way-like Hosts". In: 743.2, 117, p. 117. DOI: 10.1088/0004-637X/743/2/117. arXiv: 1011.6373 [astro-ph.CO].

Busha, Michael T. et al. (Dec. 2011b). "The Mass Distribution and Assembly of the Milky Way from the Properties of the Magellanic Clouds". In: 743.1, 40, p. 40. DOI: 10.1088/0004-637X/743/1/40. arXiv: 1011.2203 [astro-ph.GA].

Callingham, Thomas M. et al. (Apr. 2019). "The mass of the Milky Way from satellite dynamics". In: 484.4, pp. 5453–5467. DOI: 10.1093/mnras/stz365. arXiv: 1808.10456 [astro-ph.GA].

Camps, P. and M. Baes (Mar. 2015). "SKIRT: An advanced dust radiative transfer code with a user-friendly architecture". In: *Astronomy and Computing* 9, pp. 20–33. DOI: 10.1016/j.ascom.2014.10.004. arXiv: 1410.1629 [astro-ph.IM].

Cantalupo, Sebastiano et al. (July 2005). "Fluorescent Lyα Emission from the High-Redshift Intergalactic Medium". In: 628.1, pp. 61–75. DOI: 10.1086/430758. arXiv: astro-ph/0504015 [astro-ph].

Carlsten, Scott G. et al. (June 2019). "Using Surface Brightness Fluctuations to Study nearby Satellite Galaxy Systems: The Complete Satellite System of M101". In: 878.1, L16, p. L16. DOI: 10.3847/2041-8213/ab24d2. arXiv: 1901.07578 [astro-ph.GA].

Carlsten, Scott G. et al. (Oct. 2020a). "Radial Distributions of Dwarf Satellite Systems in the Local Volume". In: 902.2, 124, p. 124. DOI: 10.3847/1538-4357/abb60b. arXiv: 2006.02444 [astro-ph.GA].

Carlsten, Scott G. et al. (Mar. 2020b). "Wide-field Survey of Dwarf Satellite Systems around 10 Hosts in the Local Volume". In: 891.2, 144, p. 144. DOI: 10.3847/1538-4357/ab7758. arXiv: 1909.07389 [astro-ph.GA].

Carlsten, Scott G. et al. (Feb. 2021). "Luminosity Functions and Host-to-host Scatter of Dwarf Satellite Systems in the Local Volume". In: 908.1, 109, p. 109. DOI: 10.3847/1538-4357/abd039. arXiv: 2006.02443 [astro-ph.GA].

Cautun, Marius, Rien van de Weygaert, and Bernard J. T. Jones (Feb. 2013). "NEXUS: tracing the cosmic web connection". In: 429.2, pp. 1286–1308. DOI: 10.1093/mnras/sts416. arXiv: 1209.2043 [astro-ph.CO].

Cautun, Marius et al. (July 2014a). "Evolution of the cosmic web". In: 441.4, pp. 2923–2973. DOI: 10.1093/mnras/stu768. arXiv: 1401.7866 [astro-ph.CO].

Cautun, Marius et al. (Dec. 2014b). "Milky Way mass constraints from the Galactic satellite gap". In: 445.2, pp. 2049–2060. DOI: 10.1093/mnras/stu1849. arXiv: 1405.7697 [astro-ph.CO].

Chang, Jiang, Andrea V. Macciò, and Xi Kang (2013). "The dependence of tidal stripping efficiency on the satellite and host galaxy morphology". In: 431.4, pp. 3533–3542. DOI: 10.1093/mnras/stt434. arXiv: 1212.3408 [astro-ph.CO].

Chen, Yen-Chi et al. (Apr. 2017). "Detecting effects of filaments on galaxy properties in the Sloan Digital Sky Survey III". In: 466.2, pp. 1880–1893. DOI: 10.1093/mnras/stw3127. arXiv: 1509.06376 [astro-ph.GA].

Chua, Kun Ting Eddie et al. (Dec. 2017). "Subhalo demographics in the Illustris simulation: effects of baryons and halo-to-halo variation". In: 472.4, pp. 4343–4360. DOI: 10.1093/mnras/stx2238. arXiv: 1611.07991 [astro-ph.GA].

Chua, Kun Ting Eddie et al. (Mar. 2019). "Shape of dark matter haloes in the Illustris simulation: effects of baryons". In: 484.1, pp. 476–493. DOI: 10.1093/mnras/sty3531. arXiv: 1809.07255 [astro-ph.GA].

Cignoni, M. et al. (Mar. 2018). "Star Formation Histories of the LEGUS Dwarf Galaxies. I. Recent History of NGC 1705, NGC 4449, and Holmberg II". In: 856.1, 62, p. 62. DOI: 10.3847/1538-4357/aab041. arXiv: 1802.06792 [astro-ph.GA].

Clauwens, Bart et al. (Aug. 2018). "The three phases of galaxy formation". In: 478.3, pp. 3994–4009. DOI: 10.1093/mnras/sty1229. arXiv: 1711.00030 [astro-ph.GA].

Codis, Sandrine, Dmitri Pogosyan, and Christophe Pichon (Sept. 2018). "On the connectivity of the cosmic web: theory and implications for cosmology and galaxy formation". In: 479.1, pp. 973–993. DOI: 10.1093/mnras/sty1643. arXiv: 1803.11477 [astro-ph.CO].

Colless, Matthew et al. (Dec. 2001). "The 2dF Galaxy Redshift Survey: spectra and redshifts". In: 328.4, pp. 1039–1063. DOI: 10.1046/j.1365-8711.2001.04902.x. arXiv: astro-ph/0106498 [astro-ph].

Corlies, Lauren et al. (June 2020). "Figuring Out Gas & Galaxies in Enzo (FOGGIE). II. Emission from the z = 3 Circumgalactic Medium". In: 896.2, 125, p. 125. DOI: 10.3847/1538-4357/ab9310. arXiv: 1811.05060 [astro-ph.GA].

Couchman, H. M. P. and M. J. Rees (July 1986). "Pregalactic evolution in cosmologies with cold dark matter". In: 221, pp. 53–62. DOI: 10.1093/mnras/221.1.53.

Cowie, L. L. and A. Songaila (1977). "Thermal evaporation of gas within galaxies by a hot intergalactic medium". In: 266, pp. 501–503. DOI: 10.1038/266501a0.

Crain, Robert A. et al. (June 2015). "The EAGLE simulations of galaxy formation: calibration of subgrid physics and model variations". In: 450.2, pp. 1937–1961. DOI: 10.1093/mnras/stv725. arXiv: 1501.01311 [astro-ph.GA].

Crnojević, D. et al. (Nov. 2014). "Discovery of a Close Pair of Faint Dwarf Galaxies in the Halo of Centaurus A". In: 795.2, L35, p. L35. DOI: 10.1088/2041-8205/795/2/L35. arXiv: 1409.4776 [astro-ph.GA].

Crnojević, D. et al. (Feb. 2019). "The Faint End of the Centaurus A Satellite Luminosity Function". In: 872.1, 80, p. 80. DOI: 10.3847/1538-4357/aafbe7. arXiv: 1809.05103 [astro-ph.GA].

Crossett, Jacob P. et al. (Jan. 2017). "Near-ultraviolet signatures of environment-driven galaxy quenching in Sloan Digital Sky Survey groups". In: 464.1, pp. 480–490. DOI: 10.1093/mnras/stw2228. arXiv: 1609.02311 [astro-ph.GA].

Cui, Weiguang et al. (Jan. 2018). "The large-scale environment from cosmological simulations - I. The baryonic cosmic web". In: 473.1, pp. 68–79. DOI: 10.1093/mnras/stx2323. arXiv: 1708.02302 [astro-ph.CO].

Dalla Vecchia, Claudio and Joop Schaye (Oct. 2012). "Simulating galactic outflows with thermal supernova feedback". In: 426.1, pp. 140–158. DOI: 10.1111/j.1365-2966.2012.21704.x. arXiv: 1203.5667 [astro-ph.GA].

Davé, Romeel, Robert Thompson, and Philip F. Hopkins (Nov. 2016). "MUFASA: galaxy formation simulations with meshless hydrodynamics". In: 462.3, pp. 3265–3284. DOI: 10.1093/mnras/stw1862. arXiv: 1604.01418 [astro-ph.GA].

Davé, Romeel et al. (May 2017). "MUFASA: Galaxy star formation, gas, and metal properties across cosmic time". In: 467.1, pp. 115–132. DOI: 10.1093/mnras/stx108. arXiv: 1610.01626 [astro-ph.GA].

Davé, Romeel et al. (June 2019). "SIMBA: Cosmological simulations with black hole growth and feedback". In: 486.2, pp. 2827–2849. DOI: 10.1093/mnras/stz937. arXiv: 1901.10203 [astro-ph.GA].

Davies, Jonathan J. et al. (Jan. 2020). "The quenching and morphological evolution of central galaxies is facilitated by the feedback-driven expulsion of circumgalactic gas". In: 491.3, pp. 4462–4480. DOI: 10.1093/mnras/stz3201. arXiv: 1908.11380 [astro-ph.GA].

Davies, L. J. M. et al. (Mar. 2019). "Galaxy and Mass Assembly (GAMA): environmental quenching of centrals and satellites in groups". In: 483.4, pp. 5444–5458. DOI: 10.1093/mnras/sty3393. arXiv: 1901.01640 [astro-ph.GA].

Davis, M. et al. (Feb. 1982). "A survey of galaxy redshifts. II. The large scale space distribution." In: 253, pp. 423–445. DOI: 10.1086/159646.

de Graaff, Anna et al. (Apr. 2019). "Probing the missing baryons with the Sunyaev-Zel'dovich effect from filaments". In: 624, A48, A48. DOI: 10.1051/0004-6361/201935159. arXiv: 1709.10378 [astro-ph.CO].

de Lapparent, V., M. J. Geller, and J. P. Huchra (Mar. 1986). "A Slice of the Universe". In: 302, p. L1. DOI: 10.1086/184625.

De Lucia, Gabriella, Michaela Hirschmann, and Fabio Fontanot (Feb. 2019). "Nature versus nurture: what regulates star formation in satellite galaxies?" In: 482.4, pp. 5041–5051. DOI: 10.1093/mnras/sty3059. arXiv: 1806.00484 [astro-ph.GA].

De Lucia, Gabriella et al. (June 2012). "The environmental history of group and cluster galaxies in a Λ cold dark matter universe". In: 423.2, pp. 1277–1292. DOI: 10.1111/j.1365-2966.2012.20983.x. arXiv: 1111.6590 [astro-ph.CO].

De Rossi, María Emilia et al. (Dec. 2017). "Galaxy metallicity scaling relations in the EAGLE simulations". In: 472.3, pp. 3354–3377. DOI: 10.1093/mnras/stx2158. arXiv: 1704.00006 [astro-ph.GA].

Dehnen, Walter (June 2000). "A Very Fast and Momentum-conserving Tree Code". In: 536.1, pp. L39–L42. DOI: 10.1086/312724. arXiv: astro-ph/0003209 [astro-ph].

Dekel, A. and J. Silk (Apr. 1986). "The Origin of Dwarf Galaxies, Cold Dark Matter, and Biased Galaxy Formation". In: 303, p. 39. DOI: 10.1086/164050.

Dekel, A. et al. (Jan. 2009). "Cold streams in early massive hot haloes as the main mode of galaxy formation". In: 457.7228, pp. 451–454. DOI: 10.1038/nature07648. arXiv: 0808.0553 [astro-ph].

Dekel, Avishai and Yuval Birnboim (May 2006). "Galaxy bimodality due to cold flows and shock heating". In: 368.1, pp. 2–20. DOI: 10.1111/j.1365-2966.2006.10145.x. arXiv: astro-ph/0412300 [astro-ph].

Di Matteo, Tiziana, Volker Springel, and Lars Hernquist (Feb. 2005). "Energy input from quasars regulates the growth and activity of black holes and their host galaxies". In: 433.7026, pp. 604–607. DOI: 10.1038/nature03335. arXiv: astro-ph/0502199 [astro-ph].

Diemand, J. et al. (Aug. 2008). "Clumps and streams in the local dark matter distribution". In: 454.7205, pp. 735–738. DOI: 10.1038/nature07153. arXiv: 0805.1244 [astro-ph].

Diemand, Jürg, Michael Kuhlen, and Piero Madau (Oct. 2007). "Formation and Evolution of Galaxy Dark Matter Halos and Their Substructure". In: 667.2, pp. 859–877. DOI: 10.1086/520573. arXiv: astro-ph/0703337 [astro-ph].

Dodelson, Scott and Lawrence M. Widrow (Jan. 1994). "Sterile neutrinos as dark matter". In: 72.1, pp. 17–20. DOI: 10.1103/PhysRevLett.72.17. arXiv: hep-ph/9303287 [hep-ph].

Dolag, K., E. Komatsu, and R. Sunyaev (Dec. 2016). "SZ effects in the Magneticum Pathfinder simulation: comparison with the Planck, SPT, and ACT results". In: 463.2, pp. 1797–1811. DOI: 10.1093/mnras/stw2035. arXiv: 1509.05134 [astro-ph.CO].

Dolag, K. et al. (Oct. 2009). "Substructures in hydrodynamical cluster simulations". In: 399, pp. 497–514. DOI: 10.1111/j.1365-2966.2009.15034.x. arXiv: 0808.3401 [astro-ph].

Dolag, K. et al. (Aug. 2015). "Constraints on the distribution and energetics of fast radio bursts using cosmological hydrodynamic simulations". In: 451.4, pp. 4277–4289. DOI: 10.1093/mnras/stv1190. arXiv: 1412.4829 [astro-ph.CO].

Dolphin, A. E. (May 2002). "Numerical methods of star formation history measurement and applications to seven dwarf spheroidals". In: 332.1, pp. 91–108. DOI: 10.1046/j.1365-8711.2002.05271.x. arXiv: astro-ph/0112331 [astro-ph].

D'Onghia, Elena et al. (Feb. 2010). "Substructure Depletion in the Milky Way Halo by the Disk". In: 709.2, pp. 1138–1147. DOI: 10.1088/0004-637X/709/2/1138. arXiv: 0907.3482 [astro-ph.CO].

Donnari, M. et al. (June 2019). "The star formation activity of IllustrisTNG galaxies: main sequence, UVJ diagram, quenched fractions, and systematics". In: 485, pp. 4817–4840. DOI: 10.1093/mnras/stz712. arXiv: 1812.07584.

Donnari, Martina et al. (July 2021a). "Quenched fractions in the IllustrisTNG simulations: comparison with observations and other theoretical models". In: DOI: 10.1093/mnras/stab1950. arXiv: 2008.00004 [astro-ph.GA].

Donnari, Martina et al. (Jan. 2021b). "Quenched fractions in the IllustrisTNG simulations: the roles of AGN feedback, environment, and pre-processing". In: 500.3, pp. 4004–4024. DOI: 10.1093/mnras/staa3006. arXiv: 2008.00005 [astro-ph.GA].

Dressler, A. (Mar. 1980). "Galaxy morphology in rich clusters - Implications for the formation and evolution of galaxies". In: 236, pp. 351–365. DOI: 10.1086/157753.

Drimmel, Ronald and David N. Spergel (July 2001). "Three-dimensional Structure of the Milky Way Disk: The Distribution of Stars and Dust beyond 0.35 R_{solar}". In: 556.1, pp. 181–202. DOI: 10.1086/321556. arXiv: astro-ph/0101259 [astro-ph].

Driver, S. P. et al. (May 2011). "Galaxy and Mass Assembly (GAMA): survey diagnostics and core data release". In: 413.2, pp. 971–995. DOI: 10.1111/j.1365-2966.2010.18188.x. arXiv: 1009.0614 [astro-ph.CO].

Driver, Simon P. et al. (Oct. 2009). "GAMA: towards a physical understanding of galaxy formation". In: *Astronomy and Geophysics* 50.5, pp. 5.12–5.19. DOI: 10.1111/j.1468-4004.2009.50512.x. arXiv: 0910.5123 [astro-ph.CO].

Drlica-Wagner, A. et al. (Nov. 2015). "Eight Ultra-faint Galaxy Candidates Discovered in Year Two of the Dark Energy Survey". In: 813.2, 109, p. 109. DOI: 10.1088/0004-637X/813/2/109. arXiv: 1508.03622 [astro-ph.GA].

Drlica-Wagner, A. et al. (Apr. 2020). "Milky Way Satellite Census. I. The Observational Selection Function for Milky Way Satellites in DES Y3 and Pan-STARRS DR1". In: 893.1, 47, p. 47. DOI: 10.3847/1538-4357/ab7eb9. arXiv: 1912.03302 [astro-ph.GA].

Dubois, Yohan et al. (Dec. 2016). "The HORIZON-AGN simulation: morphological diversity of galaxies promoted by AGN feedback". In: 463.4, pp. 3948–3964. DOI: 10.1093/mnras/stw2265. arXiv: 1606.03086 [astro-ph.GA].

Duffell, Paul C. and Andrew I. MacFadyen (Dec. 2011). "TESS: A Relativistic Hydrodynamics Code on a Moving Voronoi Mesh". In: 197.2, 15, p. 15. DOI: 10.1088/0067-0049/197/2/15. arXiv: 1104.3562 [astro-ph.HE].

Duffy, Alan R. et al. (July 2010). "Impact of baryon physics on dark matter structures: a detailed simulation study of halo density profiles". In: 405.4, pp. 2161–2178. DOI: 10.1111/j.1365-2966.2010.16613.x. arXiv: 1001.3447 [astro-ph.CO].

Dvornik, Andrej et al. (Oct. 2020). "KiDS+GAMA: The weak lensing calibrated stellar-to-halo mass relation of central and satellite galaxies". In: 642, A83, A83. DOI: 10.1051/0004-6361/202038693. arXiv: 2006.10777 [astro-ph.CO].

Efstathiou, G. (May 1992). "Suppressing the formation of dwarf galaxies via photoionization". In: 256.2, 43P–47P. DOI: 10.1093/mnras/256.1.43P.

Einasto, J. (Jan. 1965). "On the Construction of a Composite Model for the Galaxy and on the Determination of the System of Galactic Parameters". In: *Trudy Astrofizicheskogo Instituta Alma-Ata* 5, pp. 87–100.

Einasto, J. et al. (Nov. 1974). "Missing mass around galaxies - Morphological evidence". In: 252, pp. 111–113. DOI: 10.1038/252111a0.

Elahi, Pascal J. et al. (2019). "Hunting for galaxies and halos in simulations with VELOCIraptor". In: 36, e021, e021. DOI: 10.1017/pasa.2019.12. arXiv: 1902.01010 [astro-ph.CO].

Elias, Lydia M. et al. (June 2020). "Detecting the cosmic web: Lyα emission from simulated filaments at z = 3". In: 494.4, pp. 5439–5448. DOI: 10.1093/mnras/staa1059. arXiv: 2004.09518 [astro-ph.GA].

Ellis, John et al. (June 1984). "Supersymmetric relics from the big bang". In: *Nuclear Physics B* 238.2, pp. 453–476. DOI: 10.1016/0550-3213(84)90461-9.

Emerick, Andrew et al. (Aug. 2016). "Gas Loss by Ram Pressure Stripping and Internal Feedback from Low-mass Milky Way Satellites". In: 826.2, 148, p. 148. DOI: 10.3847/0004-637X/826/2/148. arXiv: 1605.02746 [astro-ph.GA].

Engler, Christoph, Thorsten Lisker, and Annalisa Pillepich (Apr. 2018). "On the Scatter of the Present-day Stellar Metallicity-Mass Relation of Cluster Dwarf Galaxies". In: *Research Notes of the American Astronomical Society* 2.2, 6, p. 6. DOI: 10.3847/2515-5172/aabcce. arXiv: 1804.05679 [astro-ph.GA].

Engler, Christoph et al. (Nov. 2021a). "The abundance of satellites around Milky Way- and M31-like galaxies with the TNG50 simulation: a matter of diversity". In: 507.3, pp. 4211–4240. DOI: 10.1093/mnras/stab2437. arXiv: 2101.12215 [astro-ph.GA].

Engler, Christoph et al. (Jan. 2021b). "The distinct stellar-to-halo mass relations of satellite and central galaxies: insights from the IllustrisTNG simulations". In: 500.3, pp. 3957–3975. DOI: 10.1093/mnras/staa3505. arXiv: 2002.11119 [astro-ph.GA].

Erickson, L. K., S. T. Gottesman, and Jr. Hunter J. H. (1987). "Mass distribution in spiral galaxies". In: 325.6107, pp. 779–782. DOI: 10.1038/325779a0.

Fakhouri, Onsi, Chung-Pei Ma, and Michael Boylan-Kolchin (Aug. 2010). "The merger rates and mass assembly histories of dark matter haloes in the two Millennium simulations". In: 406.4, pp. 2267–2278. DOI: 10.1111/j.1365-2966.2010.16859.x. arXiv: 1001.2304 [astro-ph.CO].

Falck, B. and M. C. Neyrinck (July 2015). "The persistent percolation of single-stream voids". In: 450.3, pp. 3239–3253. DOI: 10.1093/mnras/stv879. arXiv: 1410.4751 [astro-ph.CO].

Falck, Bridget L., Mark C. Neyrinck, and Alexander S. Szalay (Aug. 2012). "ORIGAMI: Delineating Halos Using Phase-space Folds". In: 754.2, 126, p. 126. DOI: 10.1088/0004-637X/754/2/126. arXiv: 1201.2353 [astro-ph.CO].

Fall, S. M. and G. Efstathiou (Oct. 1980). "Formation and rotation of disc galaxies with haloes." In: 193, pp. 189–206. DOI: 10.1093/mnras/193.2.189.

Fattahi, Azadeh et al. (Mar. 2016a). "The APOSTLE project: Local Group kinematic mass constraints and simulation candidate selection". In: 457.1, pp. 844–856. DOI: 10.1093/mnras/stv2970. arXiv: 1507.03643 [astro-ph.GA].

Fattahi, Azadeh et al. (July 2016b). "The cold dark matter content of Galactic dwarf spheroidals: no cores, no failures, no problem". In: *arXiv e-prints*, arXiv:1607.06479, arXiv:1607.06479. arXiv: 1607.06479 [astro-ph.GA].

Fattahi, Azadeh et al. (Oct. 2020). "A tale of two populations: surviving and destroyed dwarf galaxies and the build-up of the Milky Way's stellar halo". In: 497.4, pp. 4459–4471. DOI: 10.1093/mnras/staa2221. arXiv: 2002.12043 [astro-ph.GA].

Faucher-Giguère, Claude-André et al. (Dec. 2010). "Lyα Cooling Emission from Galaxy Formation". In: 725.1, pp. 633–657. DOI: 10.1088/0004-637X/725/1/633. arXiv: 1005.3041 [astro-ph.CO].

Feldmann, R., C. M. Carollo, and L. Mayer (Aug. 2011). "The Hubble Sequence in Groups: The Birth of the Early-type Galaxies". In: 736.2, 88, p. 88. DOI: 10.1088/0004-637X/736/2/88. arXiv: 1008.3386 [astro-ph.CO].

Ferriere, Katia (Feb. 2003). "Magnetic Fields in Galaxies: Their Origin and Their Impact on the Interstellar Medium". In: *Acta Astronomica Sinica* 44, pp. 115–122.

Ferrière, Katia M. (Oct. 2001). "The interstellar environment of our galaxy". In: *Reviews of Modern Physics* 73.4, pp. 1031–1066. DOI: 10.1103/RevModPhys.73.1031. arXiv: astro-ph/0106359 [astro-ph].

Fiacconi, Davide et al. (June 2016). "Cold Dark Matter Substructures in Early-type Galaxy Halos". In: 824.2, 144, p. 144. DOI: 10.3847/0004-637X/824/2/144. arXiv: 1602.03526 [astro-ph.GA].

Field, G. B., D. W. Goldsmith, and H. J. Habing (Mar. 1969). "Cosmic-Ray Heating of the Interstellar Gas". In: 155, p. L149. DOI: 10.1086/180324.

Fillingham, Sean P. et al. (2016). "Under pressure: quenching star formation in low-mass satellite galaxies via stripping". In: 463, pp. 1916–1928. DOI: 10.1093/mnras/stw2131. arXiv: 1606.07810 [astro-ph.GA].

Flores, Ricardo A. and Joel R. Primack (May 1994). "Observational and Theoretical Constraints on Singular Dark Matter Halos". In: 427, p. L1. DOI: 10.1086/187350. arXiv: astro-ph/9402004 [astro-ph].

Font, A. S. et al. (Oct. 2011). "The population of Milky Way satellites in the Λ cold dark matter cosmology". In: 417.2, pp. 1260–1279. DOI: 10.1111/j.1365-2966.2011.19339.x. arXiv: 1103.0024 [astro-ph.GA].

Font, Andreea S., Ian G. McCarthy, and Vasily Belokurov (May 2021a). "Can cosmological simulations capture the diverse satellite populations of observed Milky Way analogues?" In: DOI: 10.1093/mnras/stab1332. arXiv: 2011.12974 [astro-ph.GA].

Font, Andreea S. et al. (Sept. 2021b). "Quenching of satellite galaxies of Milky Way analogues: reconciling theory and observations". In: *arXiv e-prints*, arXiv:2109.06215, arXiv:2109.06215. arXiv: 2109.06215 [astro-ph.GA].

Forbes, Duncan A. et al. (2018). "Extending the globular cluster system-halo mass relation to the lowest galaxy masses". In: 481.4, pp. 5592–5605. DOI: 10.1093/mnras/sty2584. arXiv: 1809.07831 [astro-ph.GA].

Forero-Romero, Jaime E., Sergio Contreras, and Nelson Padilla (Sept. 2014). "Cosmic web alignments with the shape, angular momentum and peculiar velocities of dark matter haloes". In: 443.2, pp. 1090–1102. DOI: 10.1093/mnras/stu1150. arXiv: 1406.0508 [astro-ph.CO].

Foucaud, S. et al. (July 2010). "Clustering properties of galaxies selected in stellar mass: breaking down the link between luminous and dark matter in massive galaxies from z = 0 to z = 2". In: 406.1, pp. 147–164. DOI: 10.1111/j.1365-2966.2010.16682.x. arXiv: 1003.2755 [astro-ph.CO].

Frenk, C. S. and S. D. M. White (Oct. 2012). "Dark matter and cosmic structure". In: *Annalen der Physik* 524.9-10, pp. 507–534. DOI: 10.1002/andp.201200212. arXiv: 1210.0544 [astro-ph.CO].

Fujita, Yutaka (Feb. 2004). "Pre-Processing of Galaxies before Entering a Cluster". In: 56, pp. 29–43. DOI: 10.1093/pasj/56.1.29. arXiv: astro-ph/0311193 [astro-ph].

Furlanetto, Steven R. et al. (Dec. 2003). "Mapping the Cosmic Web with Lyα Emission". In: 599.1, pp. L1–L4. DOI: 10.1086/381140. arXiv: astro-ph/0311006 [astro-ph].

Furlong, M. et al. (July 2015). "Evolution of galaxy stellar masses and star formation rates in the EAGLE simulations". In: 450.4, pp. 4486–4504. DOI: 10.1093/mnras/stv852. arXiv: 1410.3485 [astro-ph.GA].

Gallart, Carme et al. (Oct. 2015). "The ACS LCID Project: On the Origin of Dwarf Galaxy Types—A Manifestation of the Halo Assembly Bias?" In: 811.2, L18, p. L18. DOI: 10.1088/2041-8205/811/2/L18. arXiv: 1507.08350 [astro-ph.GA].

Gallego, Sofia G. et al. (Apr. 2018). "Stacking the Cosmic Web in fluorescent Ly α emission with MUSE". In: 475.3, pp. 3854–3869. DOI: 10.1093/mnras/sty037. arXiv: 1706.03785 [astro-ph.CO].

Gao, L. et al. (Dec. 2004). "The subhalo populations of ΛCDM dark haloes". In: 355.3, pp. 819–834. DOI: 10.1111/j.1365-2966.2004.08360.x. arXiv: astro-ph/0404589 [astro-ph].

Gao, L. et al. (Feb. 2011). "The statistics of the subhalo abundance of dark matter haloes". In: 410.4, pp. 2309–2314. DOI: 10.1111/j.1365-2966.2010.17601.x. arXiv: 1006.2882 [astro-ph.CO].

Garrison-Kimmel, Shea et al. (Mar. 2014). "ELVIS: Exploring the Local Volume in Simulations". In: 438.3, pp. 2578–2596. DOI: 10.1093/mnras/stt2377. arXiv: 1310.6746 [astro-ph.CO].

Garrison-Kimmel, Shea et al. (Jan. 2017). "Organized chaos: scatter in the relation between stellar mass and halo mass in small galaxies". In: 464.3, pp. 3108–3120. DOI: 10.1093/mnras/stw2564. arXiv: 1603.04855 [astro-ph.GA].

Garrison-Kimmel, Shea et al. (July 2019). "The Local Group on FIRE: dwarf galaxy populations across a suite of hydrodynamic simulations". In: 487.1, pp. 1380–1399. DOI: 10.1093/mnras/stz1317. arXiv: 1806.04143 [astro-ph.GA].

Geha, Marla et al. (Sept. 2017). "The SAGA Survey. I. Satellite Galaxy Populations around Eight Milky Way Analogs". In: 847.1, 4, p. 4. DOI: 10.3847/1538-4357/aa8626. arXiv: 1705.06743 [astro-ph.GA].

Geller, Margaret J. and John P. Huchra (Nov. 1989). "Mapping the Universe". In: *Science* 246.4932, pp. 897–903. DOI: 10.1126/science.246.4932.897.

Genel, Shy et al. (Nov. 2014). "Introducing the Illustris project: the evolution of galaxy populations across cosmic time". In: 445.1, pp. 175–200. DOI: 10.1093/mnras/stu1654. arXiv: 1405.3749 [astro-ph.CO].

Genel, Shy et al. (Mar. 2018). "The size evolution of star-forming and quenched galaxies in the IllustrisTNG simulation". In: 474.3, pp. 3976–3996. DOI: 10.1093/mnras/stx3078. arXiv: 1707.05327 [astro-ph.GA].

Gheller, C. et al. (Oct. 2016). "Evolution of cosmic filaments and of their galaxy population from MHD cosmological simulations". In: 462.1, pp. 448–463. DOI: 10.1093/mnras/stw1595. arXiv: 1607.01406 [astro-ph.CO].

Gnedin, Nickolay Y. and Alexander A. Kaurov (Sept. 2014). "Cosmic Reionization on Computers. II. Reionization History and Its Back-reaction on Early Galaxies". In: 793.1, 30, p. 30. DOI: 10.1088/0004-637X/793/1/30. arXiv: 1403.4251 [astro-ph.CO].

Gnedin, Nickolay Y. and Andrey V. Kravtsov (Feb. 2011). "Environmental Dependence of the Kennicutt-Schmidt Relation in Galaxies". In: 728.2, 88, p. 88. DOI: 10.1088/0004-637X/728/2/88. arXiv: 1004.0003 [astro-ph.CO].

Gnedin, Oleg Y., Lars Hernquist, and Jeremiah P. Ostriker (1999). "Tidal Shocking by Extended Mass Distributions". In: 514.1, pp. 109–118. DOI: 10.1086/306910.

Goh, Tze et al. (Feb. 2019). "Dark matter halo properties versus local density and cosmic web location". In: 483.2, pp. 2101–2122. DOI: 10.1093/mnras/sty3153. arXiv: 1805.04943 [astro-ph.GA].

González, Roberto E., Andrey V. Kravtsov, and Nickolay Y. Gnedin (June 2013). "Satellites in Milky-Way-like Hosts: Environment Dependence and Close Pairs". In: 770.2, 96, p. 96. DOI: 10.1088/0004-637X/770/2/96. arXiv: 1301.2605 [astro-ph.CO].

Gott J. Richard, III et al. (May 2005). "A Map of the Universe". In: 624.2, pp. 463–484. DOI: 10.1086/428890. arXiv: astro-ph/0310571 [astro-ph].

Gould, Andrew and David H. Weinberg (Sept. 1996). "Imaging the Forest of Lyman Limit Systems". In: 468, p. 462. DOI: 10.1086/177707. arXiv: astro-ph/9512138 [astro-ph].

Governato, F. et al. (Feb. 2007). "Forming disc galaxies in ΛCDM simulations". In: 374.4, pp. 1479–1494. DOI: 10.1111/j.1365-2966.2006.11266.x. arXiv: astro-ph/0602351 [astro-ph].

Grand, Robert J. J. et al. (May 2017). "The Auriga Project: the properties and formation mechanisms of disc galaxies across cosmic time". In: 467.1, pp. 179–207. DOI: 10.1093/mnras/stx071. arXiv: 1610.01159 [astro-ph.GA].

Grcevich, Jana and Mary E. Putman (May 2009). "H I in Local Group Dwarf Galaxies and Stripping by the Galactic Halo". In: 696.1, pp. 385–395. DOI: 10.1088/0004-637X/696/1/385. arXiv: 0901.4975 [astro-ph.GA].

Grebel, E. K. (2011). "Satellites in the Local Group and Other Nearby Groups". In: *EAS Publications Series*. Ed. by M. Koleva, Ph. Prugniel, and I. Vauglin. Vol. 48.

EAS Publications Series, pp. 315–327. DOI: 10.1051/eas/1148074. arXiv: 1103.6234 [astro-ph.CO].

Grebel, Eva K., III Gallagher John S., and Daniel Harbeck (Apr. 2003). "The Progenitors of Dwarf Spheroidal Galaxies". In: 125.4, pp. 1926–1939. DOI: 10.1086/368363. arXiv: astro-ph/0301025 [astro-ph].

Guedes, Javiera et al. (Dec. 2011). "Forming Realistic Late-type Spirals in a ΛCDM Universe: The Eris Simulation". In: 742.2, 76, p. 76. DOI: 10.1088/0004-637X/742/2/76. arXiv: 1103.6030 [astro-ph.CO].

Gunn, James E. and III Gott J. Richard (1972). "On the Infall of Matter Into Clusters of Galaxies and Some Effects on Their Evolution". In: 176, p. 1. DOI: 10.1086/151605.

Guo, Q. and S. D. M. White (Feb. 2008). "Galaxy growth in the concordance ΛCDM cosmology". In: 384.1, pp. 2–10. DOI: 10.1111/j.1365-2966.2007.12619.x. arXiv: 0708.1814 [astro-ph].

Guo, Qi et al. (May 2011). "From dwarf spheroidals to cD galaxies: simulating the galaxy population in a ΛCDM cosmology". In: 413.1, pp. 101–131. DOI: 10.1111/j.1365-2966.2010.18114.x. arXiv: 1006.0106 [astro-ph.CO].

Guth, Alan H. (Jan. 1981). "Inflationary universe: A possible solution to the horizon and flatness problems". In: 23.2, pp. 347–356. DOI: 10.1103/PhysRevD.23.347.

Haardt, Francesco and Piero Madau (Feb. 2012). "Radiative Transfer in a Clumpy Universe. IV. New Synthesis Models of the Cosmic UV/X-Ray Background". In: 746.2, 125, p. 125. DOI: 10.1088/0004-637X/746/2/125. arXiv: 1105.2039 [astro-ph.CO].

Hahn, Oliver et al. (Feb. 2007). "Properties of dark matter haloes in clusters, filaments, sheets and voids". In: 375.2, pp. 489–499. DOI: 10.1111/j.1365-2966.2006.11318.x. arXiv: astro-ph/0610280 [astro-ph].

Haines, C. P. et al. (June 2015). "LoCuSS: The Slow Quenching of Star Formation in Cluster Galaxies and the Need for Pre-processing". In: 806.1, 101, p. 101. DOI: 10.1088/0004-637X/806/1/101. arXiv: 1504.05604 [astro-ph.GA].

Hammer, F. et al. (June 2007). "The Milky Way, an Exceptionally Quiet Galaxy: Implications for the Formation of Spiral Galaxies". In: 662.1, pp. 322–334. DOI: 10.1086/516727. arXiv: astro-ph/0702585 [astro-ph].

Helmi, Amina et al. (Oct. 2018). "The merger that led to the formation of the Milky Way's inner stellar halo and thick disk". In: 563.7729, pp. 85–88. DOI: 10.1038/s41586-018-0625-x. arXiv: 1806.06038 [astro-ph.GA].

Henriques, Bruno M. B. et al. (Aug. 2017). "Galaxy formation in the Planck cosmology - IV. Mass and environmental quenching, conformity and clustering". In: 469.3, pp. 2626–2645. DOI: 10.1093/mnras/stx1010. arXiv: 1611.02286 [astro-ph.GA].

Hernquist, Lars et al. (Feb. 1996). "The Lyman-Alpha Forest in the Cold Dark Matter Model". In: 457, p. L51. DOI: 10.1086/309899. arXiv: astro-ph/9509105 [astro-ph].

HI4PI Collaboration et al. (Oct. 2016). "HI4PI: A full-sky H I survey based on EBHIS and GASS". In: 594, A116, A116. DOI: 10.1051/0004-6361/201629178. arXiv: 1610.06175 [astro-ph.GA].

Hinshaw, G. et al. (Oct. 2013). "Nine-year Wilkinson Microwave Anisotropy Probe (WMAP) Observations: Cosmological Parameter Results". In: 208.2, 19, p. 19. DOI: 10.1088/0067-0049/208/2/19. arXiv: 1212.5226 [astro-ph.CO].

Hirschmann, Michaela et al. (Aug. 2014). "Cosmological simulations of black hole growth: AGN luminosities and downsizing". In: 442.3, pp. 2304–2324. DOI: 10.1093/mnras/stu1023. arXiv: 1308.0333 [astro-ph.CO].

Hockney, R. W. and J. W. Eastwood (1981). *Computer Simulation Using Particles*.

Hogan, Craig J. and Ray J. Weymann (Mar. 1987). "Lyman-alpha emission from the Lyman-alpha forest". In: 225, 1P–5P. DOI: 10.1093/mnras/225.1.1P.

Hogg, David W. et al. (Jan. 2004). "The Dependence on Environment of the Color-Magnitude Relation of Galaxies". In: 601.1, pp. L29–L32. DOI: 10.1086/381749. arXiv: astro-ph/0307336 [astro-ph].

Hopkins, Philip F. (June 2014). "Galaxies on FIRE: Stellar Feedback Explains Inefficient Star Formation". In: *American Astronomical Society Meeting Abstracts #224*. Vol. 224. American Astronomical Society Meeting Abstracts, p. 215.06.

Hopkins, Philip F. and Eliot Quataert (Aug. 2011). "An analytic model of angular momentum transport by gravitational torques: from galaxies to massive black holes". In: 415.2, pp. 1027–1050. DOI: 10.1111/j.1365-2966.2011.18542.x. arXiv: 1007.2647 [astro-ph.CO].

Hopkins, Philip F., Eliot Quataert, and Norman Murray (Apr. 2012). "The structure of the interstellar medium of star-forming galaxies". In: 421.4, pp. 3488–3521. DOI: 10.1111/j.1365-2966.2012.20578.x. arXiv: 1110.4636 [astro-ph.CO].

Hopkins, Philip F. et al. (Oct. 2018). "FIRE-2 simulations: physics versus numerics in galaxy formation". In: 480.1, pp. 800–863. DOI: 10.1093/mnras/sty1690. arXiv: 1702.06148 [astro-ph.GA].

Horii, Toshihiro et al. (Aug. 2017). "Can HI 21-cm lines trace the missing baryons in the filamentary structures?" In: 69.4, 73, p. 73. DOI: 10.1093/pasj/psx056. arXiv: 1702.00193 [astro-ph.CO].

Hou, Annie, Laura C. Parker, and William E. Harris (July 2014). "The pre-processing of subhaloes in SDSS groups and clusters". In: 442.1, pp. 406–418. DOI: 10.1093/mnras/stu829. arXiv: 1404.7504 [astro-ph.GA].

Huang, Song et al. (2019). "Weak Lensing Reveals a Tight Connection Between Dark Matter Halo Mass and the Distribution of Stellar Mass in Massive Galaxies". In: p. 2990. DOI: 10.1093/mnras/stz3314. arXiv: 1811.01139 [astro-ph.GA].

Huchra, J. et al. (June 2005). "The 2MASS Redshift Survey and Low Galactic Latitude Large-Scale Structure". In: *Nearby Large-Scale Structures and the Zone of Avoidance*. Ed. by Anthony P. Fairall and Patrick A. Woudt. Vol. 329. Astronomical Society of the Pacific Conference Series, p. 135.

Hudson, Michael J. et al. (2015). "CFHTLenS: co-evolution of galaxies and their dark matter haloes". In: 447, pp. 298–314. DOI: 10.1093/mnras/stu2367. arXiv: 1310.6784 [astro-ph.CO].

Hummels, Cameron B. et al. (Sept. 2019). "The Impact of Enhanced Halo Resolution on the Simulated Circumgalactic Medium". In: 882.2, 156, p. 156. DOI: 10.3847/1538-4357/ab378f. arXiv: 1811.12410 [astro-ph.GA].

Ibata, R. A., G. Gilmore, and M. J. Irwin (July 1994). "A dwarf satellite galaxy in Sagittarius". In: 370.6486, pp. 194–196. DOI: 10.1038/370194a0.

Ibata, Rodrigo A. et al. (Jan. 2014). "The Large-scale Structure of the Halo of the Andromeda Galaxy. I. Global Stellar Density, Morphology and Metallicity Properties". In: 780.2, 128, p. 128. DOI: 10.1088/0004-637X/780/2/128. arXiv: 1311.5888 [astro-ph.GA].

Jõeveer, Mikhel, Jaan Einasto, and Erik Tago (Nov. 1978). "Spatial distribution of galaxies and of clusters of galaxies in the southern galactic hemisphere". In: 185, pp. 357–370. DOI: 10.1093/mnras/185.2.357.

Jackson, Thomas M. et al. (Oct. 2020). "The stellar mass assembly of low-redshift, massive, central galaxies in SDSS and the TNG300 simulation". In: 497.4, pp. 4262–4275. DOI: 10.1093/mnras/staa2306. arXiv: 2008.05114 [astro-ph.GA].

Jenkins, A. et al. (Feb. 2001). "The mass function of dark matter haloes". In: 321.2, pp. 372–384. DOI: 10.1046/j.1365-8711.2001.04029.x. arXiv: astro-ph/0005260 [astro-ph].

Jiang, Fangzhou and Frank C. van den Bosch (May 2016). "Statistics of dark matter substructure - I. Model and universal fitting functions". In: 458.3, pp. 2848–2869. DOI: 10.1093/mnras/stw439.

Jing, Y. P. (Oct. 2002). "Intrinsic correlation of halo ellipticity and its implications for large-scale weak lensing surveys". In: 335.4, pp. L89–L93. DOI: 10.1046/j.1365-8711.2002.05899.x. arXiv: astro-ph/0206098 [astro-ph].

Joshi, Gandhali D. et al. (Feb. 2019). "The trajectories of galaxies in groups: mass-loss and preprocessing". In: 483.1, pp. 235–248. DOI: 10.1093/mnras/sty3119. arXiv: 1811.06530 [astro-ph.GA].

Joshi, Gandhali D. et al. (Aug. 2020). "The fate of disc galaxies in IllustrisTNG clusters". In: 496.3, pp. 2673–2703. DOI: 10.1093/mnras/staa1668. arXiv: 2004.01191 [astro-ph.GA].

Joshi, Gandhali D. et al. (Sept. 2021). "The cumulative star-formation histories of dwarf galaxies with TNG50. I: Environment-driven diversity and connection to quenching". In: DOI: 10.1093/mnras/stab2573. arXiv: 2101.12226 [astro-ph.GA].

Kaastra, J. S. et al. (Nov. 2006). "The O VII X-Ray Forest toward Markarian 421: Consistency between XMM-Newton and Chandra". In: 652.1, pp. 189–197. DOI: 10.1086/507835. arXiv: astro-ph/0604519 [astro-ph].

Kaastra, Jelle et al. (June 2013). "The Hot and Energetic Universe: The missing baryons and the warm-hot intergalactic medium". In: *arXiv e-prints*, arXiv:1306.2324, arXiv:1306.2324. arXiv: 1306.2324 [astro-ph.HE].

Kahn, F. D. and L. Woltjer (Nov. 1959). "Intergalactic Matter and the Galaxy." In: 130, p. 705. DOI: 10.1086/146762.

Kallivayalil, Nitya et al. (Feb. 2013). "Third-epoch Magellanic Cloud Proper Motions. I. Hubble Space Telescope/WFC3 Data and Orbit Implications". In: 764.2, 161, p. 161. DOI: 10.1088/0004-637X/764/2/161. arXiv: 1301.0832 [astro-ph.CO].

Kang, Hoyoung D. and Massimo Ricotti (Sept. 2019). "Ghostly haloes in dwarf galaxies: constraints on the star formation efficiency before reionization". In: 488.2, pp. 2673–2688. DOI: 10.1093/mnras/stz1886. arXiv: 1810.01437 [astro-ph.GA].

Katz, Neal (June 1992). "Dissipational Galaxy Formation. II. Effects of Star Formation". In: 391, p. 502. DOI: 10.1086/171366.

Katz, Neal and James E. Gunn (Aug. 1991). "Dissipational Galaxy Formation. I. Effects of Gasdynamics". In: 377, p. 365. DOI: 10.1086/170367.

Katz, Neal et al. (2003). "How Do Galaxies Get Their Gas?" In: *The IGM/Galaxy Connection. The Distribution of Baryons at z=0*. Ed. by J. L. Rosenberg and M. E. Putman. Vol. 281, p. 185. DOI: 10.1007/978-94-010-0115-1_34.

Kauffmann, G. and S. D. M. White (Apr. 1993). "The merging history of dark matter haloes in a hierarchical universe." In: 261, pp. 921–928. DOI: 10.1093/mnras/261.4.921.

Kauffmann, Guinevere et al. (May 2003). "The dependence of star formation history and internal structure on stellar mass for 10^5 low-redshift galaxies". In: 341.1, pp. 54–69. DOI: 10.1046/j.1365-8711.2003.06292.x. arXiv: astro-ph/0205070 [astro-ph].

Kauffmann, Guinevere et al. (Sept. 2004). "The environmental dependence of the relations between stellar mass, structure, star formation and nuclear activity in galaxies". In: 353.3, pp. 713–731. DOI: 10.1111/j.1365-2966.2004.08117.x. arXiv: astro-ph/0402030 [astro-ph].

Kaviraj, S. et al. (June 2017). "The Horizon-AGN simulation: evolution of galaxy properties over cosmic time". In: 467.4, pp. 4739–4752. DOI: 10.1093/mnras/stx126. arXiv: 1605.09379 [astro-ph.GA].

Kawata, Daisuke and John S. Mulchaey (Jan. 2008). "Strangulation in Galaxy Groups". In: 672.2, p. L103. DOI: 10.1086/526544. arXiv: 0707.3814 [astro-ph].

Kazantzidis, Stelios et al. (Jan. 2011). "On the Efficiency of the Tidal Stirring Mechanism for the Origin of Dwarf Spheroidals: Dependence on the Orbital and Structural Parameters of the Progenitor Disky Dwarfs". In: 726.2, 98, p. 98. DOI: 10.1088/0004-637X/726/2/98. arXiv: 1009.2499 [astro-ph.CO].

Kelley, Tyler et al. (Aug. 2019). "Phat ELVIS: The inevitable effect of the Milky Way's disc on its dark matter subhaloes". In: 487.3, pp. 4409–4423. DOI: 10.1093/mnras/stz1553. arXiv: 1811.12413 [astro-ph.GA].

Kereš, Dušan et al. (Oct. 2005). "How do galaxies get their gas?" In: 363.1, pp. 2–28. DOI: 10.1111/j.1365-2966.2005.09451.x. arXiv: astro-ph/0407095 [astro-ph].

Kleiner, Dane et al. (Apr. 2017). "Evidence for H I replenishment in massive galaxies through gas accretion from the cosmic web". In: 466.4, pp. 4692–4710. DOI: 10.1093/mnras/stw3328. arXiv: 1701.03467 [astro-ph.GA].

Klypin, Anatoly et al. (Sept. 1999). "Where Are the Missing Galactic Satellites?" In: 522.1, pp. 82–92. DOI: 10.1086/307643. arXiv: astro-ph/9901240 [astro-ph].

Kollmeier, Juna A. et al. (Jan. 2010). "Lyα Emission from Cosmic Structure. I. Fluorescence". In: 708.2, pp. 1048–1075. DOI: 10.1088/0004-637X/708/2/1048. arXiv: 0907.0704 [astro-ph.CO].

Koposov, Sergey E. et al. (June 2015). "Beasts of the Southern Wild: Discovery of Nine Ultra Faint Satellites in the Vicinity of the Magellanic Clouds." In: 805.2, 130, p. 130. DOI: 10.1088/0004-637X/805/2/130. arXiv: 1503.02079 [astro-ph.GA].

Kormendy, John and Luis C. Ho (Aug. 2013). "Coevolution (Or Not) of Supermassive Black Holes and Host Galaxies". In: 51.1, pp. 511–653. DOI: 10.1146/annurev-astro-082708-101811. arXiv: 1304.7762 [astro-ph.CO].

Kotera, Kumiko and Angela V. Olinto (Sept. 2011). "The Astrophysics of Ultrahigh-Energy Cosmic Rays". In: 49.1, pp. 119–153. DOI: 10.1146/annurev-astro-081710-102620. arXiv: 1101.4256 [astro-ph.HE].

Kraljic, K. et al. (Feb. 2018). "Galaxy evolution in the metric of the cosmic web". In: 474.1, pp. 547–571. DOI: 10.1093/mnras/stx2638. arXiv: 1710.02676 [astro-ph.GA].

Kravtsov, A. V., A. A. Vikhlinin, and A. V. Meshcheryakov (2018). "Stellar Mass—Halo Mass Relation and Star Formation Efficiency in High-Mass Halos". In: *Astronomy Letters* 44, pp. 8–34. DOI: 10.1134/S1063773717120015. arXiv: 1401.7329 [astro-ph.CO].

Krumholz, Mark R., Avishai Dekel, and Christopher F. McKee (Jan. 2012). "A Universal, Local Star Formation Law in Galactic Clouds, nearby Galaxies, High-redshift Disks, and Starbursts". In: 745.1, 69, p. 69. DOI: 10.1088/0004-637X/745/1/69. arXiv: 1109.4150 [astro-ph.CO].

Kuutma, Teet, Antti Tamm, and Elmo Tempel (Apr. 2017). "From voids to filaments: environmental transformations of galaxies in the SDSS". In: 600, L6, p. L6. DOI: 10.1051/0004-6361/201730526. arXiv: 1703.04338 [astro-ph.GA].

Lacey, Cedric and Shaun Cole (June 1993). "Merger rates in hierarchical models of galaxy formation". In: 262.3, pp. 627–649. DOI: 10.1093/mnras/262.3.627.

Lagos, Claudia del P. et al. (June 2018). "The connection between mass, environment, and slow rotation in simulated galaxies". In: 476.4, pp. 4327–4345. DOI: 10.1093/mnras/sty489. arXiv: 1712.01398 [astro-ph.GA].

Laine, Mikko and Mikhail Shaposhnikov (June 2008). "Sterile neutrino dark matter as a consequence of νMSM-induced lepton asymmetry". In: 2008.6, 031, p. 031. DOI: 10.1088/1475-7516/2008/06/031. arXiv: 0804.4543 [hep-ph].

Larson, R. B., B. M. Tinsley, and C. N. Caldwell (1980). "The evolution of disk galaxies and the origin of S0 galaxies". In: 237, pp. 692–707. DOI: 10.1086/157917.

Larson, Richard B. (Nov. 1974). "Effects of supernovae on the early evolution of galaxies". In: 169, pp. 229–246. DOI: 10.1093/mnras/169.2.229.

Laursen, Peter, Alexei O. Razoumov, and Jesper Sommer-Larsen (May 2009). "Lyα Radiative Transfer in Cosmological Simulations Using Adaptive Mesh Refinement". In: 696.1, pp. 853–869. DOI: 10.1088/0004-637X/696/1/853. arXiv: 0805.3153 [astro-ph].

Lee, Khee-Gan et al. (Nov. 2014). "Lyα Forest Tomography from Background Galaxies: The First Megaparsec-resolution Large-scale Structure Map at z > 2". In: 795.1, L12, p. L12. DOI: 10.1088/2041-8205/795/1/L12. arXiv: 1409.5632 [astro-ph.CO].

Lee, Khee-Gan et al. (Aug. 2018). "First Data Release of the COSMOS Lyα Mapping and Tomography Observations: 3D Lyα Forest Tomography at 2.05 < z < 2.55". In: 237.2, 31, p. 31. DOI: 10.3847/1538-4365/aace58. arXiv: 1710.02894 [astro-ph.CO].

Lewis, Ian et al. (2002). "The 2dF Galaxy Redshift Survey: the environmental dependence of galaxy star formation rates near clusters". In: 334, pp. 673–683. DOI: 10.1046/j.1365-8711.2002.05558.x. arXiv: astro-ph/0203336 [astro-ph].

Li, Cheng and Simon D. M. White (Oct. 2009). "The distribution of stellar mass in the low-redshift Universe". In: 398.4, pp. 2177–2187. DOI: 10.1111/j.1365-2966.2009.15268.x. arXiv: 0901.0706 [astro-ph.CO].

Lianou, S. et al. (Nov. 2019). "Dust properties and star formation of approximately a thousand local galaxies". In: 631, A38, A38. DOI: 10.1051/0004-6361/201834553. arXiv: 1906.02712 [astro-ph.GA].

Libeskind, Noam I. et al. (Mar. 2012). "The cosmic web and the orientation of angular momenta". In: 421.1, pp. L137–L141. DOI: 10.1111/j.1745-3933.2012.01222.x. arXiv: 1201.3365 [astro-ph.CO].

Licquia, Timothy C., Jeffrey A. Newman, and Jarle Brinchmann (Aug. 2015). "Unveiling the Milky Way: A New Technique for Determining the Optical Color and Luminosity of Our Galaxy". In: 809.1, 96, p. 96. DOI: 10.1088/0004-637X/809/1/96. arXiv: 1508.04446 [astro-ph.GA].

Lin, Yen-Ting and Joseph J. Mohr (2004). "K-band Properties of Galaxy Clusters and Groups: Brightest Cluster Galaxies and Intracluster Light". In: 617.2, pp. 879–895. DOI: 10.1086/425412. arXiv: astro-ph/0408557 [astro-ph].

Lin, Yen-Ting, Joseph J. Mohr, and S. Adam Stanford (2003). "Near-Infrared Properties of Galaxy Clusters: Luminosity as a Binding Mass Predictor and the State of Cluster Baryons". In: 591.2, pp. 749–763. DOI: 10.1086/375513. arXiv: astro-ph/0304033 [astro-ph].

Linde, A. D. (Feb. 1982). "A new inflationary universe scenario: A possible solution of the horizon, flatness, homogeneity, isotropy and primordial monopole problems". In: *Physics Letters B* 108.6, pp. 389–393. DOI: 10.1016/0370-2693(82)91219-9.

Lisker, Thorsten, Eva K. Grebel, and Bruno Binggeli (2008). "Virgo Cluster Early-Type Dwarf Galaxies with the Sloan Digital Sky Survey. Iv. The Color-Magnitude

Relation". In: 135, pp. 380–399. DOI: 10.1088/0004-6256/135/1/380. arXiv: 0710.4135 [astro-ph].

Lisker, Thorsten et al. (2007). "Virgo Cluster Early-Type Dwarf Galaxies with the Sloan Digital Sky Survey. III. Subpopulations: Distributions, Shapes, Origins". In: 660, pp. 1186–1197. DOI: 10.1086/513090. arXiv: astro-ph/0701429 [astro-ph].

Lisker, Thorsten et al. (June 2013). "Dwarf galaxy populations in present-day galaxy clusters - II. The history of early-type and late-type dwarfs". In: 432.2, pp. 1162–1177. DOI: 10.1093/mnras/stt549. arXiv: 1303.0928 [astro-ph.CO].

Lisker, Thorsten et al. (Sept. 2018). "The Active Assembly of the Virgo Cluster: Indications for Recent Group Infall From Early-type Dwarf Galaxies". In: 865.1, 40, p. 40. DOI: 10.3847/1538-4357/aadae1. arXiv: 1808.04751 [astro-ph.GA].

Liu, Lulu et al. (May 2011). "How Common are the Magellanic Clouds?" In: 733.1, 62, p. 62. DOI: 10.1088/0004-637X/733/1/62. arXiv: 1011.2255 [astro-ph.CO].

Lovell, Mark R. et al. (Mar. 2012). "The haloes of bright satellite galaxies in a warm dark matter universe". In: 420.3, pp. 2318–2324. DOI: 10.1111/j.1365-2966.2011.20200.x. arXiv: 1104.2929 [astro-ph.CO].

Lovell, Mark R. et al. (Sept. 2016). "Satellite galaxies in semi-analytic models of galaxy formation with sterile neutrino dark matter". In: 461.1, pp. 60–72. DOI: 10.1093/mnras/stw1317. arXiv: 1511.04078 [astro-ph.CO].

Lovell, Mark R. et al. (Dec. 2018). "The fraction of dark matter within galaxies from the IllustrisTNG simulations". In: 481.2, pp. 1950–1975. DOI: 10.1093/mnras/sty2339. arXiv: 1801.10170 [astro-ph.GA].

Lubimov, V. A. et al. (July 1980). "An estimate of the ν_e mass from the β-spectrum of tritium in the valine molecule". In: *Physics Letters B* 94.2, pp. 266–268. DOI: 10.1016/0370-2693(80)90873-4.

Lucy, L. B. (Dec. 1977). "A numerical approach to the testing of the fission hypothesis." In: 82, pp. 1013–1024. DOI: 10.1086/112164.

Macciò, Andrea V. et al. (June 2007). "Concentration, spin and shape of dark matter haloes: scatter and the dependence on mass and environment". In: 378.1, pp. 55–71. DOI: 10.1111/j.1365-2966.2007.11720.x. arXiv: astro-ph/0608157 [astro-ph].

Mandelbaum, Rachel et al. (2006). "Galaxy halo masses and satellite fractions from galaxy-galaxy lensing in the Sloan Digital Sky Survey: stellar mass, luminosity, morphology and environment dependencies". In: 368.2, pp. 715–731. DOI: 10.1111/j.1365-2966.2006.10156.x. arXiv: astro-ph/0511164 [astro-ph].

Mao, Yao-Yuan, Marc Williamson, and Risa H. Wechsler (Sept. 2015). "The Dependence of Subhalo Abundance on Halo Concentration". In: 810.1, 21, p. 21. DOI: 10.1088/0004-637X/810/1/21. arXiv: 1503.02637 [astro-ph.CO].

Mao, Yao-Yuan et al. (Feb. 2021). "The SAGA Survey. II. Building a Statistical Sample of Satellite Systems around Milky Way-like Galaxies". In: 907.2, 85, p. 85. DOI: 10.3847/1538-4357/abce58. arXiv: 2008.12783 [astro-ph.GA].

Marinacci, Federico, Rüdiger Pakmor, and Volker Springel (Jan. 2014). "The formation of disc galaxies in high-resolution moving-mesh cosmological simulations". In: 437.2, pp. 1750–1775. DOI: 10.1093/mnras/stt2003. arXiv: 1305.5360 [astro-ph.CO].

Marinacci, Federico et al. (Nov. 2018). "First results from the IllustrisTNG simulations: radio haloes and magnetic fields". In: 480.4, pp. 5113–5139. DOI: 10.1093/mnras/sty2206. arXiv: 1707.03396 [astro-ph.CO].

Marsh, David J. E. (July 2016). "Axion cosmology". In: 643, pp. 1–79. DOI: 10.1016/j.physrep.2016.06.005. arXiv: 1510.07633 [astro-ph.CO].

Martin, G. et al. (Oct. 2018). "The role of mergers in driving morphological transformation over cosmic time". In: 480.2, pp. 2266–2283. DOI: 10.1093/mnras/sty1936. arXiv: 1807.08761 [astro-ph.GA].

Martin, Nicolas F. et al. (Oct. 2013). "The PAndAS View of the Andromeda Satellite System. I. A Bayesian Search for Dwarf Galaxies Using Spatial and Color-Magnitude Information". In: 776.2, 80, p. 80. DOI: 10.1088/0004-637X/776/2/80. arXiv: 1307.7626 [astro-ph.GA].

Martin, Nicolas F. et al. (Dec. 2016). "The PAndAS View of the Andromeda Satellite System. II. Detailed Properties of 23 M31 Dwarf Spheroidal Galaxies". In: 833.2, 167, p. 167. DOI: 10.3847/1538-4357/833/2/167. arXiv: 1610.01158 [astro-ph.GA].

Martínez, Héctor J., Hernán Muriel, and Valeria Coenda (Jan. 2016). "Galaxies infalling into groups: filaments versus isotropic infall". In: 455.1, pp. 127–135. DOI: 10.1093/mnras/stv2295. arXiv: 1510.00390 [astro-ph.GA].

Martizzi, Davide et al. (July 2019). "Baryons in the Cosmic Web of IllustrisTNG - I: gas in knots, filaments, sheets, and voids". In: 486.3, pp. 3766–3787. DOI: 10.1093/mnras/stz1106. arXiv: 1810.01883 [astro-ph.CO].

Martizzi, Davide et al. (Feb. 2020). "Baryons in the Cosmic Web of IllustrisTNG - II. The connection among galaxies, haloes, their formation time, and their location in the Cosmic Web". In: 491.4, pp. 5747–5758. DOI: 10.1093/mnras/stz3418. arXiv: 1907.04333 [astro-ph.GA].

McCarthy, I. G. et al. (Apr. 2011). "Gas expulsion by quasar-driven winds as a solution to the overcooling problem in galaxy groups and clusters". In: 412.3, pp. 1965–1984. DOI: 10.1111/j.1365-2966.2010.18033.x. arXiv: 1008.4799 [astro-ph.CO].

McConnachie, Alan W. (July 2012). "The Observed Properties of Dwarf Galaxies in and around the Local Group". In: 144.1, 4, p. 4. DOI: 10.1088/0004-6256/144/1/4. arXiv: 1204.1562 [astro-ph.CO].

McConnachie, Alan W. et al. (Nov. 2018). "The Large-scale Structure of the Halo of the Andromeda Galaxy. II. Hierarchical Structure in the Pan-Andromeda Archaeological Survey". In: 868.1, 55, p. 55. DOI: 10.3847/1538-4357/aae8e7. arXiv: 1810.08234 [astro-ph.GA].

McGee, Sean L. et al. (Dec. 2009). "The accretion of galaxies into groups and clusters". In: 400.2, pp. 937–950. DOI: 10.1111/j.1365-2966.2009.15507.x. arXiv: 0908.0750 [astro-ph.CO].

Meneux, B. et al. (Feb. 2008). "The VIMOS-VLT Deep Survey (VVDS). The dependence of clustering on galaxy stellar mass at z ∼1". In: 478.2, pp. 299–310. DOI: 10.1051/0004-6361:20078182. arXiv: 0706.4371 [astro-ph].

Merritt, D. (1983). "Relaxation and tidal stripping in rich clusters of galaxies. I. Evolution of the mass distribution." In: 264, pp. 24–48. DOI: 10.1086/160571.

Meszaros, P. (Dec. 1974). "The behaviour of point masses in an expanding cosmological substratum." In: 37.2, pp. 225–228.

Metuki, Ofer et al. (Jan. 2015). "Galaxy properties and the cosmic web in simulations". In: 446.2, pp. 1458–1468. DOI: 10.1093/mnras/stu2166. arXiv: 1405.0281 [astro-ph.GA].

Mo, H. J., Shude Mao, and Simon D. M. White (Apr. 1998). "The formation of galactic discs". In: 295.2, pp. 319–336. DOI: 10.1046/j.1365-8711.1998.01227.x. arXiv: astro-ph/9707093 [astro-ph].

Mocz, Philip et al. (Nov. 2017). "Galaxy formation with BECDM - I. Turbulence and relaxation of idealized haloes". In: 471.4, pp. 4559–4570. DOI: 10.1093/mnras/stx1887. arXiv: 1705.05845 [astro-ph.CO].

Moore, Ben (Aug. 1994). "Evidence against dissipation-less dark matter from observations of galaxy haloes". In: 370.6491, pp. 629–631. DOI: 10.1038/370629a0.

Moore, Ben, George Lake, and Neal Katz (1998). "Morphological Transformation from Galaxy Harassment". In: 495, pp. 139–151. DOI: 10.1086/305264. arXiv: astro-ph/9701211 [astro-ph].

Moore, Ben et al. (1996). "Galaxy harassment and the evolution of clusters of galaxies". In: 379, pp. 613–616. DOI: 10.1038/379613a0. arXiv: astro-ph/9510034 [astro-ph].

Moore, Ben et al. (Oct. 1999a). "Dark Matter Substructure within Galactic Halos". In: 524.1, pp. L19–L22. DOI: 10.1086/312287. arXiv: astro-ph/9907411 [astro-ph].

Moore, Ben et al. (Apr. 1999b). "On the survival and destruction of spiral galaxies in clusters". In: 304.3, pp. 465–474. DOI: 10.1046/j.1365-8711.1999.02345.x. arXiv: astro-ph/9811127 [astro-ph].

Mori, Masao, Andrea Ferrara, and Piero Madau (May 2002). "Early Metal Enrichment by Pregalactic Outflows. II. Three-dimensional Simulations of Blow-Away". In: 571.1, pp. 40–55. DOI: 10.1086/339913. arXiv: astro-ph/0106107 [astro-ph].

Moster, B. P., T. Naab, and S. D. M. White (Feb. 2013). "Galactic star formation and accretion histories from matching galaxies to dark matter haloes". In: 428, pp. 3121–3138. DOI: 10.1093/mnras/sts261. arXiv: 1205.5807.

Moster, B. P. et al. (Feb. 2010). "Constraints on the Relationship between Stellar Mass and Halo Mass at Low and High Redshift". In: 710, pp. 903–923. DOI: 10.1088/0004-637X/710/2/903. arXiv: 0903.4682 [astro-ph.CO].

Müller, Oliver, Helmut Jerjen, and Bruno Binggeli (Jan. 2017). "New low surface brightness dwarf galaxies in the Centaurus group". In: 597, A7, A7. DOI: 10.1051/0004-6361/201628921. arXiv: 1605.04130 [astro-ph.GA].

Müller, Oliver et al. (Sept. 2019). "The dwarf galaxy satellite system of Centaurus A". In: 629, A18, A18. DOI: 10.1051/0004-6361/201935807. arXiv: 1907.02012 [astro-ph.GA].

Myeong, G. C. et al. (Apr. 2018). "Halo substructure in the SDSS-Gaia catalogue: streams and clumps". In: 475.2, pp. 1537–1548. DOI: 10.1093/mnras/stx3262. arXiv: 1712.04071 [astro-ph.GA].

Myeong, G. C. et al. (Sept. 2019). "Evidence for two early accretion events that built the Milky Way stellar halo". In: 488.1, pp. 1235–1247. DOI: 10.1093/mnras/stz1770. arXiv: 1904.03185 [astro-ph.GA].

Naiman, Jill P. et al. (June 2018). "First results from the IllustrisTNG simulations: a tale of two elements - chemical evolution of magnesium and europium". In: 477.1, pp. 1206–1224. DOI: 10.1093/mnras/sty618. arXiv: 1707.03401 [astro-ph.GA].

Navarro, J. F. et al. (Apr. 2004). "The inner structure of ΛCDM haloes - III. Universality and asymptotic slopes". In: 349.3, pp. 1039–1051. DOI: 10.1111/j.1365-2966.2004.07586.x. arXiv: astro-ph/0311231 [astro-ph].

Navarro, Julio F. and Willy Benz (Oct. 1991). "Dynamics of Cooling Gas in Galactic Dark Halos". In: 380, p. 320. DOI: 10.1086/170590.

Navarro, Julio F., Carlos S. Frenk, and Simon D. M. White (May 1996). "The Structure of Cold Dark Matter Halos". In: 462, p. 563. DOI: 10.1086/177173. arXiv: astro-ph/9508025 [astro-ph].

— (Dec. 1997). "A Universal Density Profile from Hierarchical Clustering". In: 490.2, pp. 493–508. DOI: 10.1086/304888. arXiv: astro-ph/9611107 [astro-ph].

Navarro, Julio F. et al. (Feb. 2010). "The diversity and similarity of simulated cold dark matter haloes". In: 402.1, pp. 21–34. DOI: 10.1111/j.1365-2966.2009.15878.x. arXiv: 0810.1522 [astro-ph].

Nelson, D. et al. (Nov. 2015). "The illustris simulation: Public data release". In: *Astronomy and Computing* 13, pp. 12–37. DOI: 10.1016/j.ascom.2015.09.003. arXiv: 1504.00362 [astro-ph.CO].

Nelson, Dylan et al. (Aug. 2016). "Zooming in on accretion - I. The structure of halo gas". In: 460.3, pp. 2881–2904. DOI: 10.1093/mnras/stw1191. arXiv: 1503.02665 [astro-ph.CO].

Nelson, Dylan et al. (Mar. 2018a). "First results from the IllustrisTNG simulations: the galaxy colour bimodality". In: 475.1, pp. 624–647. DOI: 10.1093/mnras/stx3040. arXiv: 1707.03395 [astro-ph.GA].

Nelson, Dylan et al. (June 2018b). "The abundance, distribution, and physical nature of highly ionized oxygen O VI, O VII, and O VIII in IllustrisTNG". In: 477.1, pp. 450–479. DOI: 10.1093/mnras/sty656. arXiv: 1712.00016 [astro-ph.GA].

Nelson, Dylan et al. (2019a). "First results from the TNG50 simulation: galactic outflows driven by supernovae and black hole feedback". In: 490.3, pp. 3234–3261. DOI: 10.1093/mnras/stz2306. arXiv: 1902.05554 [astro-ph.GA].

Nelson, Dylan et al. (2019b). "The IllustrisTNG simulations: public data release". In: *Computational Astrophysics and Cosmology* 6.1, 2, p. 2. DOI: 10.1186/s40668-019-0028-x. arXiv: 1812.05609 [astro-ph.GA].

Nelson, Dylan et al. (Oct. 2020). "Resolving small-scale cold circumgalactic gas in TNG50". In: 498.2, pp. 2391–2414. DOI: 10.1093/mnras/staa2419. arXiv: 2005.09654 [astro-ph.GA].

Newton, Oliver et al. (Aug. 2021). "Constraints on the properties of warm dark matter using the satellite galaxies of the Milky Way". In: 2021.8, 062, p. 062. DOI: 10.1088/1475-7516/2021/08/062. arXiv: 2011.08865 [astro-ph.CO].

Nicastro, F. et al. (June 2018). "Observations of the missing baryons in the warm-hot intergalactic medium". In: 558.7710, pp. 406–409. DOI: 10.1038/s41586-018-0204-1. arXiv: 1806.08395 [astro-ph.GA].

Nicastro, Fabrizio, Smita Mathur, and Martin Elvis (Jan. 2008). "Missing Baryons and the Warm-Hot Intergalactic Medium". In: *Science* 319.5859, p. 55. DOI: 10.1126/science.1151400. arXiv: 0712.2375 [astro-ph].

Nicastro, Fabrizio et al. (Feb. 2005). "The mass of the missing baryons in the X-ray forest of the warm-hot intergalactic medium". In: 433.7025, pp. 495–498. DOI: 10.1038/nature03245.

Nickerson, S. et al. (July 2011). "Mechanisms of baryon loss for dark satellites in cosmological smoothed particle hydrodynamics simulations". In: 415.1, pp. 257–270. DOI: 10.1111/j.1365-2966.2011.18700.x. arXiv: 1103.3285 [astro-ph.CO].

Niemiec, Anna et al. (2017). "Stellar-to-halo mass relation of cluster galaxies". In: 471, pp. 1153–1166. DOI: 10.1093/mnras/stx1667. arXiv: 1703.03348 [astro-ph.CO].

Niemiec, Anna et al. (2019). "Dark matter stripping in galaxy clusters: a look at the stellar-to-halo mass relation in the Illustris simulation". In: 487.1, pp. 653–666. DOI: 10.1093/mnras/stz1318. arXiv: 1811.04996 [astro-ph.GA].

Ocvirk, P., C. Pichon, and R. Teyssier (Nov. 2008). "Bimodal gas accretion in the Horizon-MareNostrum galaxy formation simulation". In: 390.4, pp. 1326–1338. DOI: 10.1111/j.1365-2966.2008.13763.x. arXiv: 0803.4506 [astro-ph].

Ocvirk, Pierre et al. (Aug. 2020). "Cosmic Dawn II (CoDa II): a new radiation-hydrodynamics simulation of the self-consistent coupling of galaxy formation and reionization". In: 496.4, pp. 4087–4107. DOI: 10.1093/mnras/staa1266. arXiv: 1811.11192 [astro-ph.GA].

Oemler Augustus, Jr. (1974). "The Systematic Properties of Clusters of Galaxies. Photometry of 15 Clusters". In: 194, pp. 1–20. DOI: 10.1086/153216.

Okamoto, Takashi et al. (Nov. 2005). "Effects of feedback on the morphology of galaxy discs". In: 363.4, pp. 1299–1314. DOI: 10.1111/j.1365-2966.2005.09525.x. arXiv: astro-ph/0503676 [astro-ph].

Ostriker, J. P. and P. J. E. Peebles (Dec. 1973). "A Numerical Study of the Stability of Flattened Galaxies: or, can Cold Galaxies Survive?" In: 186, pp. 467–480. DOI: 10.1086/152513.

Ostriker, J. P., P. J. E. Peebles, and A. Yahil (Oct. 1974). "The Size and Mass of Galaxies, and the Mass of the Universe". In: 193, p. L1. DOI: 10.1086/181617.

Pagels, H. and J. R. Primack (Jan. 1982). "Supersymmetry, cosmology, and new physics at teraelectronvolt energies". In: 48, pp. 223–226. DOI: 10.1103/PhysRevLett.48.223.

Pakmor, R. and V. Springel (June 2013). "Simulations of magnetic fields in isolated disc galaxies". In: 432, pp. 176–193. DOI: 10.1093/mnras/stt428. arXiv: 1212.1452 [astro-ph.CO].

Pakmor, R. et al. (June 2016). "Galactic Winds Driven by Isotropic and Anisotropic Cosmic-Ray Diffusion in Disk Galaxies". In: 824.2, L30, p. L30. DOI: 10.3847/2041-8205/824/2/L30. arXiv: 1605.00643 [astro-ph.GA].

Pallero, Diego et al. (Sept. 2019). "Tracing the quenching history of cluster galaxies in the EAGLE simulation". In: 488.1, pp. 847–858. DOI: 10.1093/mnras/stz1745. arXiv: 1812.08802 [astro-ph.GA].

Panter, Benjamin et al. (July 2007). "The star formation histories of galaxies in the Sloan Digital Sky Survey". In: 378.4, pp. 1550–1564. DOI: 10.1111/j.1365-2966.2007.11909.x. arXiv: astro-ph/0608531 [astro-ph].

Pasquali, A. et al. (Apr. 2019). "Physical properties of SDSS satellite galaxies in projected phase space". In: 484.2, pp. 1702–1723. DOI: 10.1093/mnras/sty3530. arXiv: 1901.04238 [astro-ph.GA].

Patel, Ekta, Gurtina Besla, and Sangmo Tony Sohn (Feb. 2017). "Orbits of massive satellite galaxies - I. A close look at the Large Magellanic Cloud and a new orbital history for M33". In: 464.4, pp. 3825–3849. DOI: 10.1093/mnras/stw2616. arXiv: 1609.04823 [astro-ph.GA].

Peek, J. E. G. et al. (June 2011). "The GALFA-HI Survey: Data Release 1". In: 194.2, 20, p. 20. DOI: 10.1088/0067-0049/194/2/20. arXiv: 1101.1879 [astro-ph.GA].

Peek, J. E. G. et al. (Jan. 2018). "The GALFA-H I Survey Data Release 2". In: 234.1, 2, p. 2. DOI: 10.3847/1538-4365/aa91d3.

Peeples, Molly S. et al. (Mar. 2019). "Figuring Out Gas & Galaxies in Enzo (FOGGIE). I. Resolving Simulated Circumgalactic Absorption at $2 \leq z \leq 2.5$". In: 873.2, 129, p. 129. DOI: 10.3847/1538-4357/ab0654. arXiv: 1810.06566 [astro-ph.GA].

Peng, Eric W., Holland C. Ford, and Kenneth C. Freeman (2004). "The Planetary Nebula System and Dynamics in the Outer Halo of NGC 5128". In: 602.2, pp. 685–704. DOI: 10.1086/381160. arXiv: astro-ph/0311236 [astro-ph].

Peng, Ying-jie et al. (Sept. 2010). "Mass and Environment as Drivers of Galaxy Evolution in SDSS and zCOSMOS and the Origin of the Schechter Function". In: 721.1, pp. 193–221. DOI: 10.1088/0004-637X/721/1/193. arXiv: 1003.4747 [astro-ph.CO].

Phillips, John I. et al. (Feb. 2015). "The mass dependence of satellite quenching in Milky Way-like haloes". In: 447.1, pp. 698–710. DOI: 10.1093/mnras/stu2192. arXiv: 1407.3276 [astro-ph.GA].

Pichon, C. et al. (Dec. 2011). "Rigging dark haloes: why is hierarchical galaxy formation consistent with the inside-out build-up of thin discs?" In: 418.4, pp. 2493–2507. DOI: 10.1111/j.1365-2966.2011.19640.x. arXiv: 1105.0210 [astro-ph.CO].

Pillepich, A. et al. (Mar. 2018a). "First results from the IllustrisTNG simulations: the stellar mass content of groups and clusters of galaxies". In: 475, pp. 648–675. DOI: 10.1093/mnras/stx3112. arXiv: 1707.03406.

Pillepich, A. et al. (Jan. 2018b). "Simulating galaxy formation with the IllustrisTNG model". In: 473, pp. 4077–4106. DOI: 10.1093/mnras/stx2656. arXiv: 1703.02970.

Pillepich, Annalisa et al. (2019). "First results from the TNG50 simulation: the evolution of stellar and gaseous discs across cosmic time". In: 490.3, pp. 3196–3233. DOI: 10.1093/mnras/stz2338. arXiv: 1902.05553 [astro-ph.GA].

Pillepich, Annalisa et al. (May 2021). "X-ray bubbles in the circumgalactic medium of TNG50 Milky Way- and M31-like galaxies: signposts of supermassive black hole activity". In: *arXiv e-prints*, arXiv:2105.08062, arXiv:2105.08062. arXiv: 2105.08062 [astro-ph.GA].

Pisano, D. J. and Eric M. Wilcots (May 1999). "Gas-Rich Companions of Isolated Galaxies". In: 117.5, pp. 2168–2176. DOI: 10.1086/300846. arXiv: astro-ph/9901326 [astro-ph].

Planck Collaboration et al. (Sept. 2016). "Planck 2015 results. I. Overview of products and scientific results". In: 594, A1, A1. DOI: 10.1051/0004-6361/201527101.

Planelles, S. et al. (Feb. 2014). "On the role of AGN feedback on the thermal and chemodynamical properties of the hot intracluster medium". In: 438.1, pp. 195–216. DOI: 10.1093/mnras/stt2141. arXiv: 1311.0818 [astro-ph.CO].

Pontzen, Andrew and Fabio Governato (Feb. 2014). "Cold dark matter heats up". In: 506.7487, pp. 171–178. DOI: 10.1038/nature12953. arXiv: 1402.1764 [astro-ph.CO].

Popping, Gergö et al. (Sept. 2019). "The ALMA Spectroscopic Survey in the HUDF: the Molecular Gas Content of Galaxies and Tensions with IllustrisTNG and the Santa Cruz SAM". In: 882.2, 137, p. 137. DOI: 10.3847/1538-4357/ab30f2. arXiv: 1903.09158 [astro-ph.GA].

Popping, Gergö et al. (Jan. 2021). "The dust-continuum size of TNG50 galaxies at $z = 1 - 5$: a comparison with the distribution of stellar light, stars, dust and H_2". In: *arXiv e-prints*, arXiv:2101.12218, arXiv:2101.12218. arXiv: 2101.12218 [astro-ph.GA].

Porter, Scott C. et al. (Aug. 2008). "Star formation in galaxies falling into clusters along supercluster-scale filaments". In: 388.3, pp. 1152–1160. DOI: 10.1111/j.1365-2966.2008.13388.x. arXiv: 0804.4177 [astro-ph].

Pozzetti, L. et al. (Nov. 2010). "zCOSMOS - 10k-bright spectroscopic sample. The bimodality in the galaxy stellar mass function: exploring its evolution with redshift". In: 523, A13, A13. DOI: 10.1051/0004-6361/200913020. arXiv: 0907.5416 [astro-ph.CO].

Prescott, Matthew et al. (2011). "Galaxy and Mass Assembly (GAMA): the red fraction and radial distribution of satellite galaxies". In: 417, pp. 1374–1386. DOI: 10.1111/j.1365-2966.2011.19353.x. arXiv: 1107.0141 [astro-ph.CO].

Preskill, John, Mark B. Wise, and Frank Wilczek (Jan. 1983). "Cosmology of the invisible axion". In: *Physics Letters B* 120.1-3, pp. 127–132. DOI: 10.1016/0370-2693(83)90637-8.

Presotto, V. et al. (Mar. 2012). "A journey from the outskirts to the cores of groups. I. Color- and mass-segregation in 20K-zCOSMOS groups". In: 539, A55, A55. DOI: 10.1051/0004-6361/201118293. arXiv: 1201.1673 [astro-ph.CO].

Press, William H. and Paul Schechter (Feb. 1974). "Formation of Galaxies and Clusters of Galaxies by Self-Similar Gravitational Condensation". In: 187, pp. 425–438. DOI: 10.1086/152650.

Price, D. J. and J. J. Monaghan (Feb. 2007). "An energy-conserving formalism for adaptive gravitational force softening in smoothed particle hydrodynamics and N-body codes". In: 374.4, pp. 1347–1358. DOI: 10.1111/j.1365-2966.2006.11241.x. arXiv: astro-ph/0610872 [astro-ph].

Price, Daniel J. (Feb. 2012). "Smoothed particle hydrodynamics and magnetohydrodynamics". In: *Journal of Computational Physics* 231.3, pp. 759–794. DOI: 10.1016/j.jcp.2010.12.011. arXiv: 1012.1885 [astro-ph.IM].

Primack, J. R. and G. R. Blumenthal (Jan. 1984). "What is the dark matter ? Implications for galaxy formation and particle physics". In: *Formation and Evolution of Galaxies and Large Structures in the Universe*. Ed. by J. Audouze and J. Tran Thanh Van. Vol. 117. NATO Advanced Study Institute (ASI) Series C, p. 163.

Prole, D. J. et al. (2019). "Halo mass estimates from the globular cluster populations of 175 low surface brightness galaxies in the Fornax cluster". In: 484.4, pp. 4865–4880. DOI: 10.1093/mnras/stz326. arXiv: 1901.09648 [astro-ph.GA].

Purcell, Chris W., James S. Bullock, and Andrew R. Zentner (Sept. 2007). "Shredded Galaxies as the Source of Diffuse Intrahalo Light on Varying Scales". In: 666.1, pp. 20–33. DOI: 10.1086/519787. arXiv: astro-ph/0703004 [astro-ph].

Putman, Mary E. et al. (May 2021). "The Gas Content and Stripping of Local Group Dwarf Galaxies". In: 913.1, 53, p. 53. DOI: 10.3847/1538-4357/abe391. arXiv: 2101.07809 [astro-ph.GA].

Rasia, E. et al. (Nov. 2015). "Cool Core Clusters from Cosmological Simulations". In: 813.1, L17, p. L17. DOI: 10.1088/2041-8205/813/1/L17. arXiv: 1509.04247 [astro-ph.CO].

Rasmussen, Andrew P. et al. (Feb. 2007). "On the Putative Detection of z > 0 X-Ray Absorption Features in the Spectrum of Mrk 421". In: 656.1, pp. 129–138. DOI: 10.1086/509865. arXiv: astro-ph/0604515 [astro-ph].

Reddick, Rachel M. et al. (July 2013). "The Connection between Galaxies and Dark Matter Structures in the Local Universe". In: 771.1, 30, p. 30. DOI: 10.1088/0004-637X/771/1/30. arXiv: 1207.2160 [astro-ph.CO].

Reed, Darren et al. (Dec. 2003a). "Evolution of the mass function of dark matter haloes". In: 346.2, pp. 565–572. DOI: 10.1046/j.1365-2966.2003.07113.x. arXiv: astro-ph/0301270 [astro-ph].

— (Dec. 2003b). "Evolution of the mass function of dark matter haloes". In: 346.2, pp. 565–572. DOI: 10.1046/j.1365-2966.2003.07113.x. arXiv: astro-ph/0301270 [astro-ph].

Rhee, Jinsu et al. (July 2017). "Phase-space Analysis in the Group and Cluster Environment: Time Since Infall and Tidal Mass Loss". In: 843.2, 128, p. 128. DOI: 10.3847/1538-4357/aa6d6c. arXiv: 1704.04243 [astro-ph.GA].

Roberts, I. D. et al. (Aug. 2021). "LoTSS jellyfish galaxies. II. Ram pressure stripping in groups versus clusters". In: 652, A153, A153. DOI: 10.1051/0004-6361/202141118. arXiv: 2106.06315 [astro-ph.GA].

Rodriguez-Gomez, Vicente et al. (May 2015). "The merger rate of galaxies in the Illustris simulation: a comparison with observations and semi-empirical models". In: 449.1, pp. 49–64. DOI: 10.1093/mnras/stv264. arXiv: 1502.01339 [astro-ph.GA].

Rodriguez-Gomez, Vicente et al. (May 2016). "The stellar mass assembly of galaxies in the Illustris simulation: growth by mergers and the spatial distribution of accreted stars". In: 458.3, pp. 2371–2390. DOI: 10.1093/mnras/stw456. arXiv: 1511.08804 [astro-ph.GA].

Rodriguez-Gomez, Vicente et al. (May 2017). "The role of mergers and halo spin in shaping galaxy morphology". In: 467.3, pp. 3083–3098. DOI: 10.1093/mnras/stx305. arXiv: 1609.09498 [astro-ph.GA].

Rodriguez-Gomez, Vicente et al. (Mar. 2019). "The optical morphologies of galaxies in the IllustrisTNG simulation: a comparison to Pan-STARRS observations". In: 483.3, pp. 4140–4159. DOI: 10.1093/mnras/sty3345. arXiv: 1809.08239 [astro-ph.GA].

Rodríguez-Puebla, A., V. Avila-Reese, and N. Drory (Apr. 2013). "The Galaxy-Halo/Subhalo Connection: Mass Relations and Implications for Some Satellite Occupational Distributions". In: 767.1, 92, p. 92. DOI: 10.1088/0004-637X/767/1/92. arXiv: 1302.0005 [astro-ph.CO].

Rodríguez-Puebla, A., N. Drory, and V. Avila-Reese (Sept. 2012). "The Stellar-Subhalo Mass Relation of Satellite Galaxies". In: 756.1, 2, p. 2. DOI: 10.1088/0004-637X/756/1/2. arXiv: 1204.0804 [astro-ph.CO].

Rodríguez-Puebla, Aldo et al. (Sept. 2017). "Constraining the galaxy-halo connection over the last 13.3 Gyr: star formation histories, galaxy mergers and structural properties". In: 470.1, pp. 651–687. DOI: 10.1093/mnras/stx1172. arXiv: 1703.04542 [astro-ph.GA].

Rodriguez Wimberly, M. K. et al. (Mar. 2019). "The suppression of star formation on the smallest scales: what role does environment play?" In: 483.3, pp. 4031–4039. DOI: 10.1093/mnras/sty3357. arXiv: 1806.07891 [astro-ph.GA].

Rojas, Randall R. et al. (Dec. 2004). "Photometric Properties of Void Galaxies in the Sloan Digital Sky Survey". In: 617.1, pp. 50–63. DOI: 10.1086/425225. arXiv: astro-ph/0307274 [astro-ph].

Rosdahl, J. and J. Blaizot (June 2012). "Extended Lyα emission from cold accretion streams". In: 423.1, pp. 344–366. DOI: 10.1111/j.1365-2966.2012.20883.x. arXiv: 1112.4408 [astro-ph.CO].

Rosdahl, Joakim et al. (Sept. 2018). "The SPHINX cosmological simulations of the first billion years: the impact of binary stars on reionization". In: 479.1, pp. 994–1016. DOI: 10.1093/mnras/sty1655. arXiv: 1801.07259 [astro-ph.GA].

Rubin, Vera C. and Jr. Ford W. Kent (Feb. 1970). "Rotation of the Andromeda Nebula from a Spectroscopic Survey of Emission Regions". In: 159, p. 379. DOI: 10.1086/150317.

Sacchi, E. et al. (Apr. 2018). "Star Formation Histories of the LEGUS Dwarf Galaxies. II. Spatially Resolved Star Formation History of the Magellanic Irregular NGC 4449". In: 857.1, 63, p. 63. DOI: 10.3847/1538-4357/aab844. arXiv: 1803.08041 [astro-ph.GA].

Safarzadeh, Mohammadtaher and Abraham Loeb (2019). "Explaining the enhanced star formation rate of Jellyfish galaxies in galaxy clusters". In: 486.1, pp. L26–L30. DOI: 10.1093/mnrasl/slz053. arXiv: 1904.05900 [astro-ph.GA].

Sakamoto, T. and T. Hasegawa (Dec. 2006). "Discovery of a Faint Old Stellar System at 150 kpc". In: 653.1, pp. L29–L32. DOI: 10.1086/510332. arXiv: astro-ph/0610858 [astro-ph].

Sales, Laura V. et al. (Aug. 2007). "Satellites of simulated galaxies: survival, merging and their relationto the dark and stellar haloes". In: 379.4, pp. 1464–1474. DOI: 10.1111/j.1365-2966.2007.12024.x. arXiv: 0704.1770 [astro-ph].

Sales, Laura V. et al. (Jan. 2013). "Satellites and haloes of dwarf galaxies". In: 428.1, pp. 573–578. DOI: 10.1093/mnras/sts054. arXiv: 1208.2027 [astro-ph.CO].

Sawala, Till et al. (Apr. 2015). "Bent by baryons: the low-mass galaxy-halo relation". In: 448.3, pp. 2941–2947. DOI: 10.1093/mnras/stu2753. arXiv: 1404.3724 [astro-ph.GA].

Sawala, Till et al. (Apr. 2016a). "The APOSTLE simulations: solutions to the Local Group's cosmic puzzles". In: 457.2, pp. 1931–1943. DOI: 10.1093/mnras/stw145. arXiv: 1511.01098 [astro-ph.GA].

Sawala, Till et al. (Feb. 2016b). "The chosen few: the low-mass haloes that host faint galaxies". In: 456.1, pp. 85–97. DOI: 10.1093/mnras/stv2597. arXiv: 1406.6362 [astro-ph.CO].

Schaefer, A. L. et al. (Mar. 2019). "The SAMI Galaxy Survey: observing the environmental quenching of star formation in GAMA groups". In: 483.3, pp. 2851–2870. DOI: 10.1093/mnras/sty3258. arXiv: 1811.11676 [astro-ph.GA].

Schaye, Joop et al. (2015). "The EAGLE project: simulating the evolution and assembly of galaxies and their environments". In: 446, pp. 521–554. DOI: 10.1093/mnras/stu2058. arXiv: 1407.7040 [astro-ph.GA].

Schechter, P. (Jan. 1976). "An analytic expression for the luminosity function for galaxies." In: 203, pp. 297–306. DOI: 10.1086/154079.

Schewtschenko, J. A. et al. (June 2015). "Dark matter-radiation interactions: the impact on dark matter haloes". In: 449.4, pp. 3587–3596. DOI: 10.1093/mnras/stv431. arXiv: 1412.4905 [astro-ph.CO].

Schmalzing, Jens et al. (Dec. 1999). "Disentangling the Cosmic Web. I. Morphology of Isodensity Contours". In: 526.2, pp. 568–578. DOI: 10.1086/308039. arXiv: astro-ph/9904384 [astro-ph].

Schulz, Sebastian et al. (Oct. 2020). "A redshift-dependent IRX-β dust attenuation relation for TNG50 galaxies". In: 497.4, pp. 4773–4794. DOI: 10.1093/mnras/staa1900. arXiv: 2001.04992 [astro-ph.GA].

Schulze, Felix et al. (Nov. 2018). "Kinematics of simulated galaxies - I. Connecting dynamical and morphological properties of early-type galaxies at different redshifts". In: 480.4, pp. 4636–4658. DOI: 10.1093/mnras/sty2090. arXiv: 1802.01583 [astro-ph.GA].

Shao, Shi et al. (Sept. 2018). "Evolution of LMC/M33-mass dwarf galaxies in the EAGLE simulation". In: 479.1, pp. 284–296. DOI: 10.1093/mnras/sty1470. arXiv: 1803.07269 [astro-ph.GA].

Shaposhnikov, Mikhail (Nov. 2008). "Sterile neutrinos in cosmology and how to find them in the lab". In: *Journal of Physics Conference Series*. Vol. 136. Journal of Physics Conference Series, p. 022045. DOI: 10.1088/1742-6596/136/2/022045. arXiv: 0809.2028 [hep-ph].

Shen, Sijing et al. (Sept. 2014). "The Baryon Cycle of Dwarf Galaxies: Dark, Bursty, Gas-rich Polluters". In: 792.2, 99, p. 99. DOI: 10.1088/0004-637X/792/2/99. arXiv: 1308.4131 [astro-ph.CO].

Shi, Jingjing et al. (Apr. 2020). "The Formation History of Subhalos and the Evolution of Satellite Galaxies". In: 893.2, 139, p. 139. DOI: 10.3847/1538-4357/ab8464. arXiv: 2001.04090 [astro-ph.GA].

Shi, Xiangdong and George M. Fuller (Apr. 1999). "New Dark Matter Candidate: Nonthermal Sterile Neutrinos". In: 82.14, pp. 2832–2835. DOI: 10.1103/PhysRevLett.82.2832. arXiv: astro-ph/9810076 [astro-ph].

Shimwell, T. W. et al. (Feb. 2017). "The LOFAR Two-metre Sky Survey. I. Survey description and preliminary data release". In: 598, A104, A104. DOI: 10.1051/0004-6361/201629313. arXiv: 1611.02700 [astro-ph.IM].

Shimwell, T. W. et al. (Feb. 2019). "The LOFAR Two-metre Sky Survey. II. First data release". In: 622, A1, A1. DOI: 10.1051/0004-6361/201833559. arXiv: 1811.07926 [astro-ph.GA].

Shlosman, Isaac, Juhan Frank, and Mitchell C. Begelman (Mar. 1989). "Bars within bars: a mechanism for fuelling active galactic nuclei". In: 338.6210, pp. 45–47. DOI: 10.1038/338045a0.

Sick, Jonathan et al. (Apr. 2015). "The Stellar Mass of M31 as inferred by the Andromeda Optical & Infrared Disk Survey". In: *Galaxy Masses as Constraints of Formation Models*. Ed. by Michele Cappellari and Stéphane Courteau. Vol. 311. IAU Symposium, pp. 82–85. DOI: 10.1017/S1743921315003440. arXiv: 1410.0017 [astro-ph.GA].

Sifón, Cristóbal et al. (2018). "The galaxy-subhalo connection in low-redshift galaxy clusters from weak gravitational lensing". In: 478, pp. 1244–1264. DOI: 10.1093/mnras/sty1161. arXiv: 1706.06125 [astro-ph.GA].

Sijacki, Debora et al. (Sept. 2007). "A unified model for AGN feedback in cosmological simulations of structure formation". In: 380.3, pp. 877–900. DOI: 10.1111/j.1365-2966.2007.12153.x. arXiv: 0705.2238 [astro-ph].

Sijacki, Debora et al. (Sept. 2015). "The Illustris simulation: the evolving population of black holes across cosmic time". In: 452.1, pp. 575–596. DOI: 10.1093/mnras/stv1340. arXiv: 1408.6842 [astro-ph.GA].

Simionescu, Aurora et al. (May 2021). "Voyage through the hidden physics of the cosmic web". In: *Experimental Astronomy*. DOI: 10.1007/s10686-021-09720-0. arXiv: 1908.01778 [astro-ph.CO].

Simpson, Christine M. et al. (Aug. 2016). "The Role of Cosmic-Ray Pressure in Accelerating Galactic Outflows". In: 827.2, L29, p. L29. DOI: 10.3847/2041-8205/827/2/L29. arXiv: 1606.02324 [astro-ph.GA].

Simpson, Christine M. et al. (July 2018). "Quenching and ram pressure stripping of simulated Milky Way satellite galaxies". In: 478.1, pp. 548–567. DOI: 10.1093/mnras/sty774. arXiv: 1705.03018 [astro-ph.GA].

Skillman, Evan D. et al. (Mar. 2017). "The ISLAndS Project. II. The Lifetime Star Formation Histories of Six Andromeda dSphS". In: 837.2, 102, p. 102. DOI: 10.3847/1538-4357/aa60c5. arXiv: 1606.01207 [astro-ph.GA].

Skrutskie, M. F. et al. (Feb. 2006). "The Two Micron All Sky Survey (2MASS)". In: 131.2, pp. 1163–1183. DOI: 10.1086/498708.

Slater, Colin T. and Eric F. Bell (Sept. 2014). "The Mass Dependence of Dwarf Satellite Galaxy Quenching". In: 792.2, 141, p. 141. DOI: 10.1088/0004-637X/792/2/141. arXiv: 1407.6006 [astro-ph.GA].

Smercina, Adam et al. (Aug. 2018). "A Lonely Giant: The Sparse Satellite Population of M94 Challenges Galaxy Formation". In: 863.2, 152, p. 152. DOI: 10.3847/1538-4357/aad2d6. arXiv: 1807.03779 [astro-ph.GA].

Smith, Aaron et al. (Mar. 2019a). "The physics of Lyman α escape from high-redshift galaxies". In: 484.1, pp. 39–59. DOI: 10.1093/mnras/sty3483. arXiv: 1810.08185 [astro-ph.GA].

Smith, Matthew C., Debora Sijacki, and Sijing Shen (May 2019b). "Cosmological simulations of dwarfs: the need for ISM physics beyond SN feedback alone". In: 485.3, pp. 3317–3333. DOI: 10.1093/mnras/stz599. arXiv: 1807.04288 [astro-ph.GA].

Smith, R. et al. (2013). "The impact of galaxy harassment on the globular cluster systems of early-type cluster dwarf galaxies". In: 429, pp. 1066–1079. DOI: 10.1093/mnras/sts395. arXiv: 1211.2802 [astro-ph.CO].

Smith, R. et al. (2015). "The sensitivity of harassment to orbit: mass loss from early-type dwarfs in galaxy clusters". In: 454, pp. 2502–2516. DOI: 10.1093/mnras/stv2082. arXiv: 1509.02537 [astro-ph.GA].

Smith, Rory et al. (2016). "The Preferential Tidal Stripping of Dark Matter versus Stars in Galaxies". In: 833, 109, p. 109. DOI: 10.3847/1538-4357/833/1/109. arXiv: 1610.04264 [astro-ph.GA].

Smith, Rory et al. (May 2019c). "Investigating the Stellar Mass Growth Histories of Satellite Galaxies as a Function of Infall Time Using Phase-space". In: 876.2, 145, p. 145. DOI: 10.3847/1538-4357/ab1917. arXiv: 1904.07340 [astro-ph.GA].

Snyder, Gregory F. et al. (2015). "Galaxy morphology and star formation in the Illustris Simulation at z = 0". In: 454.2, pp. 1886–1908. DOI: 10.1093/mnras/stv2078. arXiv: 1502.07747 [astro-ph.GA].

Somerville, Rachel S. (June 2002). "Can Photoionization Squelching Resolve the Substructure Crisis?" In: 572.1, pp. L23–L26. DOI: 10.1086/341444. arXiv: astro-ph/0107507 [astro-ph].

Somerville, Rachel S. and Romeel Davé (Aug. 2015). "Physical Models of Galaxy Formation in a Cosmological Framework". In: 53, pp. 51–113. DOI: 10.1146/annurev-astro-082812-140951. arXiv: 1412.2712 [astro-ph.GA].

Sonnenfeld, Alessandro, Wenting Wang, and Neta Bahcall (2019). "Hyper Suprime-Cam view of the CMASS galaxy sample. Halo mass as a function of stellar mass, size, and Sérsic index". In: 622, A30, A30. DOI: 10.1051/0004-6361/201834260. arXiv: 1811.04934 [astro-ph.GA].

Sousbie, T. (June 2011). "The persistent cosmic web and its filamentary structure - I. Theory and implementation". In: 414.1, pp. 350–383. DOI: 10.1111/j.1365-2966.2011.18394.x. arXiv: 1009.4015 [astro-ph.CO].

Sousbie, T., S. Colombi, and C. Pichon (Feb. 2009). "The fully connected N-dimensional skeleton: probing the evolution of the cosmic web". In: 393.2, pp. 457–477. DOI: 10.1111/j.1365-2966.2008.14244.x. arXiv: 0809.2423 [astro-ph].

Sousbie, T., C. Pichon, and H. Kawahara (June 2011). "The persistent cosmic web and its filamentary structure - II. Illustrations". In: 414.1, pp. 384–403. DOI: 10.1111/j.1365-2966.2011.18395.x. arXiv: 1009.4014 [astro-ph.CO].

Spekkens, Kristine et al. (Nov. 2014). "The Dearth of Neutral Hydrogen in Galactic Dwarf Spheroidal Galaxies". In: 795.1, L5, p. L5. DOI: 10.1088/2041-8205/795/1/L5. arXiv: 1410.0028 [astro-ph.GA].

Spergel, David N. and Paul J. Steinhardt (Apr. 2000). "Observational Evidence for Self-Interacting Cold Dark Matter". In: 84.17, pp. 3760–3763. DOI: 10.1103/PhysRevLett.84.3760. arXiv: astro-ph/9909386 [astro-ph].

Spindler, Ashley et al. (2018). "SDSS-IV MaNGA: the spatial distribution of star formation and its dependence on mass, structure, and environment". In: 476, pp. 580–600. DOI: 10.1093/mnras/sty247. arXiv: 1710.05049 [astro-ph.GA].

Spitler, L. R. and D. A. Forbes (2009). "A new method for estimating dark matter halo masses using globular cluster systems". In: 392.1, pp. L1–L5. DOI: 10.1111/j.1745-3933.2008.00567.x. arXiv: 0809.5057 [astro-ph].

Springel, V. et al. (Dec. 2001). "Populating a cluster of galaxies - I. Results at [formmu2]z=0". In: 328, pp. 726–750. DOI: 10.1046/j.1365-8711.2001.04912.x. eprint: astro-ph/0012055.

Springel, V. et al. (Dec. 2008). "The Aquarius Project: the subhaloes of galactic haloes". In: 391.4, pp. 1685–1711. DOI: 10.1111/j.1365-2966.2008.14066.x. arXiv: 0809.0898 [astro-ph].

Springel, Volker (Dec. 2005). "The cosmological simulation code GADGET-2". In: 364.4, pp. 1105–1134. DOI: 10.1111/j.1365-2966.2005.09655.x. arXiv: astro-ph/0505010 [astro-ph].

— (Jan. 2010a). "E pur si muove: Galilean-invariant cosmological hydrodynamical simulations on a moving mesh". In: 401.2, pp. 791–851. DOI: 10.1111/j.1365-2966.2009.15715.x. arXiv: 0901.4107 [astro-ph.CO].

— (Sept. 2010b). "Smoothed Particle Hydrodynamics in Astrophysics". In: 48, pp. 391–430. DOI: 10.1146/annurev-astro-081309-130914. arXiv: 1109.2219 [astro-ph.CO].

Springel, Volker, Tiziana Di Matteo, and Lars Hernquist (Aug. 2005a). "Modelling feedback from stars and black holes in galaxy mergers". In: 361.3, pp. 776–794. DOI: 10.1111/j.1365-2966.2005.09238.x. arXiv: astro-ph/0411108 [astro-ph].

Springel, Volker, Carlos S. Frenk, and Simon D. M. White (Apr. 2006). "The large-scale structure of the Universe". In: 440.7088, pp. 1137–1144. DOI: 10.1038/nature04805. arXiv: astro-ph/0604561 [astro-ph].

Springel, Volker and Lars Hernquist (2003). "Cosmological smoothed particle hydrodynamics simulations: a hybrid multiphase model for star formation". In: 339.2, pp. 289–311. DOI: 10.1046/j.1365-8711.2003.06206.x. arXiv: astro-ph/0206393 [astro-ph].

Springel, Volker et al. (June 2005b). "Simulations of the formation, evolution and clustering of galaxies and quasars". In: 435.7042, pp. 629–636. DOI: 10.1038/nature03597. arXiv: astro-ph/0504097 [astro-ph].

Springel, Volker et al. (Mar. 2018). "First results from the IllustrisTNG simulations: matter and galaxy clustering". In: 475.1, pp. 676–698. DOI: 10.1093/mnras/stx3304. arXiv: 1707.03397 [astro-ph.GA].

Starkenburg, Else et al. (Feb. 2013). "The satellites of the Milky Way - insights from semi-analytic modelling in a ΛCDM cosmology". In: 429.1, pp. 725–743. DOI: 10.1093/mnras/sts367. arXiv: 1206.0020 [astro-ph.GA].

Starobinsky, A. A. (Nov. 1982). "Dynamics of phase transition in the new inflationary universe scenario and generation of perturbations". In: *Physics Letters B* 117.3-4, pp. 175–178. DOI: 10.1016/0370-2693(82)90541-X.

Stevens, Adam R. H. et al. (Mar. 2019). "Atomic hydrogen in IllustrisTNG galaxies: the impact of environment parallelled with local 21-cm surveys". In: 483.4, pp. 5334–5354. DOI: 10.1093/mnras/sty3451. arXiv: 1810.12158 [astro-ph.GA].

Stierwalt, S. et al. (May 2015). "TiNy Titans: The Role of Dwarf-Dwarf Interactions in Low-mass Galaxy Evolution". In: 805.1, 2, p. 2. DOI: 10.1088/0004-637X/805/1/2. arXiv: 1412.4796 [astro-ph.GA].

Stinson, G. S. et al. (Jan. 2013). "Making Galaxies In a Cosmological Context: the need for early stellar feedback". In: 428.1, pp. 129–140. DOI: 10.1093/mnras/sts028. arXiv: 1208.0002 [astro-ph.CO].

Strateva, Iskra et al. (Oct. 2001). "Color Separation of Galaxy Types in the Sloan Digital Sky Survey Imaging Data". In: 122.4, pp. 1861–1874. DOI: 10.1086/323301. arXiv: astro-ph/0107201 [astro-ph].

Suárez, Abril, Victor H. Robles, and Tonatiuh Matos (Jan. 2014). "A Review on the Scalar Field/Bose-Einstein Condensate Dark Matter Model". In: *Accelerated Cosmic Expansion*. Vol. 38, p. 107. DOI: 10.1007/978-3-319-02063-1_9. arXiv: 1302.0903 [astro-ph.CO].

Suresh, Joshua et al. (Mar. 2019). "Zooming in on accretion - II. Cold circumgalactic gas simulated with a super-Lagrangian refinement scheme". In: 483.3, pp. 4040–4059. DOI: 10.1093/mnras/sty3402. arXiv: 1811.01949 [astro-ph.GA].

Sybilska, A. et al. (Sept. 2017). "The hELENa project - I. Stellar populations of early-type galaxies linked with local environment and galaxy mass". In: 470, pp. 815–838. DOI: 10.1093/mnras/stx1138. arXiv: 1706.00014.

Tacchella, Sandro et al. (Aug. 2019). "Morphology and star formation in IllustrisTNG: the build-up of spheroids and discs". In: 487.4, pp. 5416–5440. DOI: 10.1093/mnras/stz1657. arXiv: 1904.12860 [astro-ph.GA].

Tanimura, Hideki et al. (Feb. 2019). "A search for warm/hot gas filaments between pairs of SDSS Luminous Red Galaxies". In: 483.1, pp. 223–234. DOI: 10.1093/mnras/sty3118. arXiv: 1709.05024 [astro-ph.CO].

Taylor, Christopher L. et al. (Mar. 1994). "Star Formation Threshold in H II Galaxies With H I Companions". In: 107, p. 971. DOI: 10.1086/116910.

Tegmark, Max et al. (May 2004). "The Three-Dimensional Power Spectrum of Galaxies from the Sloan Digital Sky Survey". In: 606.2, pp. 702–740. DOI: 10.1086/382125. arXiv: astro-ph/0310725 [astro-ph].

Terrazas, Bryan A. et al. (Feb. 2020). "The relationship between black hole mass and galaxy properties: Examining the black hole feedback model in IllustrisTNG". In: DOI: 10.1093/mnras/staa374. arXiv: 1906.02747 [astro-ph.GA].

Teyssier, R. (Apr. 2002). "Cosmological hydrodynamics with adaptive mesh refinement. A new high resolution code called RAMSES". In: 385, pp. 337–364. DOI: 10.1051/0004-6361:20011817. arXiv: astro-ph/0111367 [astro-ph].

Thoul, Anne A. and David H. Weinberg (July 1996). "Hydrodynamic Simulations of Galaxy Formation. II. Photoionization and the Formation of Low-Mass Galaxies". In: 465, p. 608. DOI: 10.1086/177446. arXiv: astro-ph/9510154 [astro-ph].

Tielens, A. G. G. M. (2010). *The Physics and Chemistry of the Interstellar Medium*.

Tinker, Jeremy L. et al. (2013). "Evolution of the Stellar-to-dark Matter Relation: Separating Star-forming and Passive Galaxies from z = 1 to 0". In: 778, 93, p. 93. DOI: 10.1088/0004-637X/778/2/93. arXiv: 1308.2974 [astro-ph.CO].

Tojeiro, Rita et al. (Sept. 2017). "Galaxy and Mass Assembly (GAMA): halo formation times and halo assembly bias on the cosmic web". In: 470.3, pp. 3720–3741. DOI: 10.1093/mnras/stx1466. arXiv: 1612.08595 [astro-ph.CO].

Tollerud, Erik J. and J. E. G. Peek (Apr. 2018). "Where Are All of the Gas-bearing Local Dwarf Galaxies? Quantifying Possible Impacts of Reionization". In: 857.1, 45, p. 45. DOI: 10.3847/1538-4357/aab3e4. arXiv: 1711.00485 [astro-ph.GA].

Tollerud, Erik J. et al. (Sept. 2011). "Small-scale Structure in the Sloan Digital Sky Survey and ΛCDM: Isolated $_*$ Galaxies with Bright Satellites". In: 738.1, 102, p. 102. DOI: 10.1088/0004-637X/738/1/102. arXiv: 1103.1875 [astro-ph.CO].

Tonnesen, Stephanie, Greg L. Bryan, and J. H. van Gorkom (Dec. 2007). "Environmentally Driven Evolution of Simulated Cluster Galaxies". In: 671.2, pp. 1434–1445. DOI: 10.1086/523034. arXiv: 0709.1720 [astro-ph].

Toomre, Alar and Juri Toomre (Dec. 1972). "Galactic Bridges and Tails". In: 178, pp. 623–666. DOI: 10.1086/151823.

Torrealba, G. et al. (July 2016). "The feeble giant. Discovery of a large and diffuse Milky Way dwarf galaxy in the constellation of Crater". In: 459.3, pp. 2370–2378. DOI: 10.1093/mnras/stw733. arXiv: 1601.07178 [astro-ph.GA].

Torrealba, G. et al. (Apr. 2018). "Discovery of two neighbouring satellites in the Carina constellation with MagLiteS". In: 475.4, pp. 5085–5097. DOI: 10.1093/mnras/sty170. arXiv: 1801.07279 [astro-ph.GA].

Torrealba, G. et al. (Sept. 2019). "The hidden giant: discovery of an enormous Galactic dwarf satellite in Gaia DR2". In: 488.2, pp. 2743–2766. DOI: 10.1093/mnras/stz1624. arXiv: 1811.04082 [astro-ph.GA].

Torrey, P. et al. (Mar. 2014). "A model for cosmological simulations of galaxy formation physics: multi-epoch validation". In: 438, pp. 1985–2004. DOI: 10.1093/mnras/stt2295. arXiv: 1305.4931.

Torrey, Paul et al. (June 2018). "Similar star formation rate and metallicity variability time-scales drive the fundamental metallicity relation". In: 477.1, pp. L16–L20. DOI: 10.1093/mnrasl/sly031. arXiv: 1711.11039 [astro-ph.GA].

Torrey, Paul et al. (Apr. 2019). "The evolution of the mass-metallicity relation and its scatter in IllustrisTNG". In: 484.4, pp. 5587–5607. DOI: 10.1093/mnras/stz243. arXiv: 1711.05261 [astro-ph.GA].

Trayford, James W. et al. (Sept. 2015). "Colours and luminosities of z = 0.1 galaxies in the EAGLE simulation". In: 452.3, pp. 2879–2896. DOI: 10.1093/mnras/stv1461. arXiv: 1504.04374 [astro-ph.GA].

Tremmel, M. et al. (Mar. 2019). "Introducing ROMULUSC: a cosmological simulation of a galaxy cluster with an unprecedented resolution". In: 483.3, pp. 3336–3362. DOI: 10.1093/mnras/sty3336. arXiv: 1806.01282 [astro-ph.GA].

Truong, Nhut et al. (May 2020). "X-ray signatures of black hole feedback: hot galactic atmospheres in IllustrisTNG and X-ray observations". In: 494.1, pp. 549–570. DOI: 10.1093/mnras/staa685. arXiv: 1911.11165 [astro-ph.GA].

Tully, R. B. and J. R. Fisher (Feb. 1977). "Reprint of 1977A&A....54..661T. A new method of determining distance to galaxies." In: 500, pp. 105–117.

Turner, Michael S. and Frank Wilczek (Jan. 1991). "Inflationary axion cosmology". In: 66.1, pp. 5–8. DOI: 10.1103/PhysRevLett.66.5.

Uhlig, M. et al. (July 2012). "Galactic winds driven by cosmic ray streaming". In: 423.3, pp. 2374–2396. DOI: 10.1111/j.1365-2966.2012.21045.x. arXiv: 1203.1038 [astro-ph.CO].

Umehata, H. et al. (Oct. 2019). "Gas filaments of the cosmic web located around active galaxies in a protocluster". In: *Science* 366.6461, pp. 97–100. DOI: 10.1126/science.aaw5949. arXiv: 1910.01324 [astro-ph.GA].

van de Voort, Freeke et al. (July 2011). "The rates and modes of gas accretion on to galaxies and their gaseous haloes". In: 414.3, pp. 2458–2478. DOI: 10.1111/j.1365-2966.2011.18565.x. arXiv: 1011.2491 [astro-ph.CO].

van de Voort, Freeke et al. (Jan. 2019). "Cosmological simulations of the circumgalactic medium with 1 kpc resolution: enhanced H I column densities". In: 482.1, pp. L85–L89. DOI: 10.1093/mnrasl/sly190. arXiv: 1808.04369 [astro-ph.GA].

van den Bosch, Frank C. and Go Ogiya (2018). "Dark matter substructure in numerical simulations: a tale of discreteness noise, runaway instabilities, and artificial disruption". In: 475.3, pp. 4066–4087. DOI: 10.1093/mnras/sty084. arXiv: 1801.05427 [astro-ph.GA].

van den Bosch, Frank C. et al. (2004). "Probing dark matter haloes with satellite kinematics". In: 352.4, pp. 1302–1314. DOI: 10.1111/j.1365-2966.2004.08021.x. arXiv: astro-ph/0404033 [astro-ph].

van den Bosch, Frank C. et al. (2008). "The importance of satellite quenching for the build-up of the red sequence of present-day galaxies". In: 387.1, pp. 79–91. DOI: 10.1111/j.1365-2966.2008.13230.x. arXiv: 0710.3164 [astro-ph].

van der Wel, Arjen et al. (2010). "The Physical Origins of the Morphology-Density Relation: Evidence for Gas Stripping from the Sloan Digital Sky Survey". In: 714, pp. 1779–1788. DOI: 10.1088/0004-637X/714/2/1779. arXiv: 1004.0319 [astro-ph.CO].

van Uitert, Edo et al. (2016). "The stellar-to-halo mass relation of GAMA galaxies from 100 deg^2 of KiDS weak lensing data". In: 459, pp. 3251–3270. DOI: 10.1093/mnras/stw747. arXiv: 1601.06791 [astro-ph.GA].

Vandenbroucke, B. and S. De Rijcke (July 2016). "The moving mesh code SHADOWFAX". In: *Astronomy and Computing* 16, pp. 109–130. DOI: 10.1016/j.ascom.2016.05.001. arXiv: 1605.03576 [astro-ph.IM].

Vazza, F. et al. (Feb. 2016). "Detecting the cosmic web with radio surveys". In: *arXiv e-prints*, arXiv:1602.07526, arXiv:1602.07526. arXiv: 1602.07526 [astro-ph.CO].

Villalobos, Á. et al. (Aug. 2012). "Simulating the evolution of disc galaxies in a group environment - I. The influence of the global tidal field". In: 424.4, pp. 2401–2428. DOI: 10.1111/j.1365-2966.2012.20667.x. arXiv: 1202.0550 [astro-ph.CO].

Vogelsberger, M. et al. (Dec. 2013). "A model for cosmological simulations of galaxy formation physics". In: 436, pp. 3031–3067. DOI: 10.1093/mnras/stt1789. arXiv: 1305.2913.

Vogelsberger, M. et al. (May 2014a). "Properties of galaxies reproduced by a hydrodynamic simulation". In: 509.7499, pp. 177–182. DOI: 10.1038/nature13316. arXiv: 1405.1418 [astro-ph.CO].

Vogelsberger, Mark et al. (Oct. 2014b). "Introducing the Illustris Project: simulating the coevolution of dark and visible matter in the Universe". In: 444.2, pp. 1518–1547. DOI: 10.1093/mnras/stu1536. arXiv: 1405.2921 [astro-ph.CO].

Vogelsberger, Mark et al. (Aug. 2016). "ETHOS - an effective theory of structure formation: dark matter physics as a possible explanation of the small-scale CDM problems". In: 460.2, pp. 1399–1416. DOI: 10.1093/mnras/stw1076. arXiv: 1512.05349 [astro-ph.CO].

Vogelsberger, Mark et al. (2018). "The uniformity and time-invariance of the intracluster metal distribution in galaxy clusters from the IllustrisTNG simulations". In: 474.2, pp. 2073–2093. DOI: 10.1093/mnras/stx2955. arXiv: 1707.05318 [astro-ph.CO].

Vogelsberger, Mark et al. (Jan. 2020a). "Cosmological simulations of galaxy formation". In: *Nature Reviews Physics* 2.1, pp. 42–66. DOI: 10.1038/s42254-019-0127-2. arXiv: 1909.07976 [astro-ph.GA].

Vogelsberger, Mark et al. (2020b). "High-redshift JWST predictions from IllustrisTNG: dust modelling and galaxy luminosity functions". In: 492.4, pp. 5167–5201. DOI: 10.1093/mnras/staa137. arXiv: 1904.07238 [astro-ph.GA].

von der Linden, Anja et al. (May 2010). "Star formation and AGN activity in SDSS cluster galaxies". In: 404.3, pp. 1231–1246. DOI: 10.1111/j.1365-2966.2010.16375.x. arXiv: 0909.3522 [astro-ph.CO].

Vulcani, Benedetta et al. (2018). "Enhanced Star Formation in Both Disks and Ram-pressure-stripped Tails of GASP Jellyfish Galaxies". In: 866.2, L25, p. L25. DOI: 10.3847/2041-8213/aae68b. arXiv: 1810.05164 [astro-ph.GA].

Wadsley, James W., Benjamin W. Keller, and Thomas R. Quinn (Oct. 2017). "Gasoline2: a modern smoothed particle hydrodynamics code". In: 471.2, pp. 2357–2369. DOI: 10.1093/mnras/stx1643. arXiv: 1707.03824 [astro-ph.IM].

Wang, J. et al. (May 2011). "Assembly history and structure of galactic cold dark matter haloes". In: 413.2, pp. 1373–1382. DOI: 10.1111/j.1365-2966.2011.18220.x. arXiv: 1008.5114 [astro-ph.CO].

Wang, Jie et al. (Aug. 2012). "The missing massive satellites of the Milky Way". In: 424.4, pp. 2715–2721. DOI: 10.1111/j.1365-2966.2012.21357.x. arXiv: 1203.4097 [astro-ph.GA].

Wang, Liang et al. (Nov. 2015a). "NIHAO project - I. Reproducing the inefficiency of galaxy formation across cosmic time with a large sample of cosmological hydrodynamical simulations". In: 454.1, pp. 83–94. DOI: 10.1093/mnras/stv1937. arXiv: 1503.04818 [astro-ph.GA].

— (Nov. 2015b). "NIHAO project - I. Reproducing the inefficiency of galaxy formation across cosmic time with a large sample of cosmological hydrodynamical simulations". In: 454.1, pp. 83–94. DOI: 10.1093/mnras/stv1937. arXiv: 1503.04818 [astro-ph.GA].

Wang, Wenting and Simon D. M. White (Aug. 2012). "Satellite abundances around bright isolated galaxies". In: 424.4, pp. 2574–2598. DOI: 10.1111/j.1365-2966.2012.21256.x. arXiv: 1203.0009 [astro-ph.CO].

Watson, William A. et al. (Aug. 2013). "The halo mass function through the cosmic ages". In: 433.2, pp. 1230–1245. DOI: 10.1093/mnras/stt791. arXiv: 1212.0095 [astro-ph.CO].

Weinberger, R. et al. (Mar. 2017). "Simulating galaxy formation with black hole driven thermal and kinetic feedback". In: 465, pp. 3291–3308. DOI: 10.1093/mnras/stw2944. arXiv: 1607.03486.

Weinberger, Rainer et al. (Sept. 2018). "Supermassive black holes and their feedback effects in the IllustrisTNG simulation". In: 479.3, pp. 4056–4072. DOI: 10.1093/mnras/sty1733. arXiv: 1710.04659 [astro-ph.GA].

Weisz, Daniel R. et al. (Dec. 2011a). "How Typical Are the Local Group Dwarf Galaxies?" In: 743.1, 8, p. 8. DOI: 10.1088/0004-637X/743/1/8. arXiv: 1101.1301 [astro-ph.CO].

Weisz, Daniel R. et al. (Sept. 2011b). "The ACS Nearby Galaxy Survey Treasury. VIII. The Global Star Formation Histories of 60 Dwarf Galaxies in the Local Volume". In: 739.1, 5, p. 5. DOI: 10.1088/0004-637X/739/1/5. arXiv: 1101.1093 [astro-ph.CO].

Weisz, Daniel R. et al. (July 2014). "The Star Formation Histories of Local Group Dwarf Galaxies. I. Hubble Space Telescope/Wide Field Planetary Camera 2 Observations". In: 789.2, 147, p. 147. DOI: 10.1088/0004-637X/789/2/147. arXiv: 1404.7144 [astro-ph.GA].

Weisz, Daniel R. et al. (Nov. 2019). "Comparing the Quenching Times of Faint M31 and Milky Way Satellite Galaxies". In: 885.1, L8, p. L8. DOI: 10.3847/2041-8213/ab4b52. arXiv: 1909.11036 [astro-ph.GA].

Wetzel, Andrew R., Jeremy L. Tinker, and Charlie Conroy (July 2012). "Galaxy evolution in groups and clusters: star formation rates, red sequence fractions and the persistent bimodality". In: 424.1, pp. 232–243. DOI: 10.1111/j.1365-2966.2012.21188.x. arXiv: 1107.5311 [astro-ph.CO].

Wetzel, Andrew R., Erik J. Tollerud, and Daniel R. Weisz (July 2015). "Rapid Environmental Quenching of Satellite Dwarf Galaxies in the Local Group". In: 808.1, L27, p. L27. DOI: 10.1088/2041-8205/808/1/L27. arXiv: 1503.06799 [astro-ph.GA].

Wetzel, Andrew R. et al. (June 2013). "Galaxy evolution in groups and clusters: satellite star formation histories and quenching time-scales in a hierarchical Universe". In: 432.1, pp. 336–358. DOI: 10.1093/mnras/stt469. arXiv: 1206.3571 [astro-ph.CO].

Wetzel, Andrew R. et al. (Aug. 2016). "Reconciling Dwarf Galaxies with ΛCDM Cosmology: Simulating a Realistic Population of Satellites around a Milky Way-mass Galaxy". In: 827.2, L23, p. L23. DOI: 10.3847/2041-8205/827/2/L23. arXiv: 1602.05957 [astro-ph.GA].

White, Martin (Dec. 2002). "The Mass Function". In: 143.2, pp. 241–255. DOI: 10.1086/342752. arXiv: astro-ph/0207185 [astro-ph].

White, S. D. M., C. S. Frenk, and M. Davis (Nov. 1983). "Clustering in a neutrino-dominated universe". In: 274, pp. L1–L5. DOI: 10.1086/184139.

White, S. D. M. and M. J. Rees (May 1978). "Core condensation in heavy halos: a two-stage theory for galaxy formation and clustering." In: 183, pp. 341–358. DOI: 10.1093/mnras/183.3.341.

White, Simon D. M. and Carlos S. Frenk (Sept. 1991). "Galaxy Formation through Hierarchical Clustering". In: 379, p. 52. DOI: 10.1086/170483.

Wiersma, Robert P. C., Joop Schaye, and Britton D. Smith (Feb. 2009a). "The effect of photoionization on the cooling rates of enriched, astrophysical plasmas". In: 393.1, pp. 99–107. DOI: 10.1111/j.1365-2966.2008.14191.x. arXiv: 0807.3748 [astro-ph].

Wiersma, Robert P. C. et al. (Oct. 2009b). "Chemical enrichment in cosmological, smoothed particle hydrodynamics simulations". In: 399.2, pp. 574–600. DOI: 10.1111/j.1365-2966.2009.15331.x. arXiv: 0902.1535 [astro-ph.CO].

Willman, Beth (Jan. 2010). "In Pursuit of the Least Luminous Galaxies". In: *Advances in Astronomy* 2010, 285454, p. 285454. DOI: 10.1155/2010/285454. arXiv: 0907.4758 [astro-ph.CO].

Winkel, N. et al. (Aug. 2021). "The imprint of cosmic web quenching on central galaxies". In: 505.4, pp. 4920–4934. DOI: 10.1093/mnras/stab1562. arXiv: 2105.13368 [astro-ph.GA].

Yang, Xiaohu et al. (2007). "Galaxy Groups in the SDSS DR4. I. The Catalog and Basic Properties". In: 671.1, pp. 153–170. DOI: 10.1086/522027. arXiv: 0707.4640 [astro-ph].

Yun, Kiyun et al. (2019). "Jellyfish galaxies with the IllustrisTNG simulations - I. Gas-stripping phenomena in the full cosmological context". In: 483.1, pp. 1042–1066. DOI: 10.1093/mnras/sty3156. arXiv: 1810.00005 [astro-ph.GA].

Yurin, Denis and Volker Springel (Sept. 2015). "The stability of stellar discs in Milky Way-sized dark matter haloes". In: 452.3, pp. 2367–2387. DOI: 10.1093/mnras/stv1454. arXiv: 1411.3729 [astro-ph.GA].

Zabludoff, Ann I. et al. (July 1996). "The Environment of "E+A" Galaxies". In: 466, p. 104. DOI: 10.1086/177495. arXiv: astro-ph/9512058 [astro-ph].

Zanisi, Lorenzo et al. (Feb. 2020). "Galaxy sizes and the galaxy-halo connection - I. The remarkable tightness of the size distributions". In: 492.2, pp. 1671–1690. DOI: 10.1093/mnras/stz3516. arXiv: 1912.02831 [astro-ph.GA].

Zappacosta, L. et al. (July 2010). "Studying the WHIM Content of Large-scale Structures Along the Line of Sight to H 2356-309". In: 717.1, pp. 74–84. DOI: 10.1088/0004-637X/717/1/74. arXiv: 1004.5359 [astro-ph.CO].

Zel'Dovich, Y. B. (Mar. 1970). "Reprint of 1970A&A.....5...84Z. Gravitational instability: an approximate theory for large density perturbations." In: 500, pp. 13–18.

Zhu, Qirong et al. (May 2016). "Baryonic impact on the dark matter distribution in Milky Way-sized galaxies and their satellites". In: 458.2, pp. 1559–1580. DOI: 10.1093/mnras/stw374. arXiv: 1506.05537 [astro-ph.CO].

Zinger, Elad et al. (2018). "Quenching of satellite galaxies at the outskirts of galaxy clusters". In: 475, pp. 3654–3681. DOI: 10.1093/mnras/stx3329.

Zinger, Elad et al. (Aug. 2020). "Ejective and preventative: the IllustrisTNG black hole feedback and its effects on the thermodynamics of the gas within and around galaxies". In: DOI: 10.1093/mnras/staa2607. arXiv: 2004.06132 [astro-ph.GA].

Zucker, D. B. et al. (Oct. 2006). "A Curious Milky Way Satellite in Ursa Major". In: 650.1, pp. L41–L44. DOI: 10.1086/508628. arXiv: astro-ph/0606633 [astro-ph].

Zwicky, F. (Jan. 1933). "Die Rotverschiebung von extragalaktischen Nebeln". In: *Helvetica Physica Acta* 6, pp. 110–127.